

Dynamic material behaviour related to security applications (material and structural response to blast)

16th Technical Meeting, 2005
Brussels, Belgium

ISL Research on Protective Footwear against AP Blast Mines

Fabien Rondot, Pascal Magnan, Sebastien De Mezzo

ISL, French German Research Institute of Saint-Louis, PO Box 70034, F-68301 Saint-Louis, France

In order to propose blast protective footwear concepts, it is first necessary to characterize the threat, which is determined from the pressure fields in the immediate environment of the mine. Pointed out are the strong directionality of the blast due to soil confinement and the differences in pattern of gas expansion depending on whether the mine is flush-buried or buried under a layer of soil.

Based upon linked Euler/Lagrange simulations, the second step deals with the velocity of a rigid mass driven by the detonation of a blast mine. The standoff distance appears to be a driving contributor to reducing the threat. Correlations with the loading charge, the depth of burial and the exposed surface are also discussed.

Studies on deflecting soles are in progress. Various shapes and materials (aluminium foam, rubber, air inserts, and hybrid) are reviewed. Supported by simulations, tests are conducted using a simplified mechanical leg to ensure reproducibility.

INTRODUCTION

To address the hazards posed to soldiers, deminers and peacekeepers by AP mines around the world, a R&D program on the protection of the lower limbs against AP blast mines has been started at ISL¹.

In order to propose blast protective footwear concepts, it is first necessary to characterize the threat, which is determined from the pressure fields in the immediate environment of the mine. To achieve this task, ISL has combined experimental and numerical tools [2]. The numerical simulation allows to overcome the experimental limits of the transducers, which are rapidly saturated by the huge pressures released in the near-field, i.e., within a radius of 30 cm around the mine. But in order to gain confidence in the numerical predictions, comparisons with trials are necessary in a zone where the transducers are known to work well, the area ranging from 30 cm to 70 cm from the soil surface in this instance.

The second step consisted in examining how several parameters can affect the fling of a rigid mass due to the detonation of a surrogate blast mine. This task was achieved by means of numerical simulations, coupling Euler and Lagrange methods [3]. Different parameters were reviewed such as weight, exposed surface, explosive loading, depth of burial, type of soil, standoff distance...

The ongoing step deals with deflecting sole. In parallel to trials featuring a mechanical leg, numerical simulations are carried out to draw major trends.

MAPPING OF AIR OVERPRESSURE AROUND SURROGATE AP BLAST MINES

¹ ISL has been a member of the NATO Task Group 024 "Test Methodology for Personal Protective Equipment Against Anti-Personnel Mine Blast" (Human Factors & Medicine 089 Panel) [1]

Experimental protocol

The threat consists of cylindrical surrogate mines ranging from 25 grams to 200 grams of C-4 explosive, a RDX based pyrotechnic composition widely used in AP blast mines. The explosive is moulded in a disk-shaped plastic container. An aperture in the lower part makes it possible to place the detonator for an ignition at the geometric centre of the charge. The charge is flush-buried or buried under 3 cm of a calibrated artificial medium of dry silica sand with grain size ranging from 200 to 500 μm . The Depth Of Burial (DOB) is measured from the soil surface to the top of the plastic container.

The mapping of air overpressure is obtained by using probes with conical tips as shown in Figure 1. The surrogate mine is placed into a bucket of sand. Axial measurements are performed by means of a probe equipped with 5 piezoelectric pressure transducers spaced every 20 cm from 30 cm to 110 cm above the soil surface. To deal with radial expansion and to consider the contra-lateral leg positioning, the measurement axis is shifted by 15 cm.

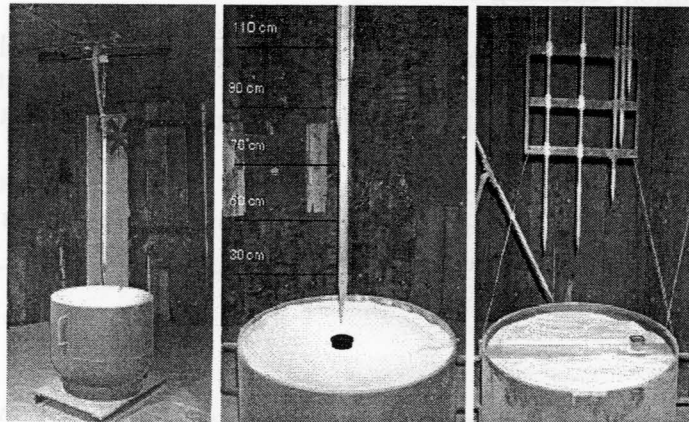


Figure 1: General view of the setup (left), axial device (centre), device for 15-cm shifted measurements (right)

Numerical approach

The numerical simulations are carried out using the Euler module of the OTI*HULL software [4]. This multi-materials hydrodynamic computer code features a second order numerical scheme to solve dynamic continuum mechanics problems in finite difference form. The geometry investigated is two-dimensional axisymmetric. The detonation products are described using a Jones-Wilkins-Lee (JWL) equation of state, air is regarded as a perfect gas and the behaviour of sand is treated via a tabulated equation that takes into account various stages of compaction of the medium. Space surrounding the charge is discretized using about 500 000 cells. A fine mesh of $0.66 \times 0.66 \text{ mm}^2$ cells is used for the explosive and for a part of the soil and air near the explosive, i.e., from 3 cm below the charge to 50 cm above the soil surface and 20 cm around the axis of symmetry. The mesh is gradually coarsened in the region away from the explosive. The numerical grid covers a radius of 1 meter around the axis of symmetry and ranges from 50 cm below the ground level to 1 meter above. Particles are inserted in the explosive to follow the expansion of the detonation products. The pressure time histories are recorded at several Eulerian stations (fixed in space).

Air overpressure generated by the explosion of a buried mine is lower than for a flush-buried charge. When the charge is buried, the soil cover moves upwards, creating a bubble of sand that thins out until the detonation products break through. Figure 2 illustrates the gas spread at 30 cm above the ground. The particulate and vectorial representations reveal the strong directionality of the blast due to soil confinement. The critical zone is at the vertical of the threat. A burial of 3 cm into sand enhances this directionality but reduces considerably the velocity of expansion of the detonation products.

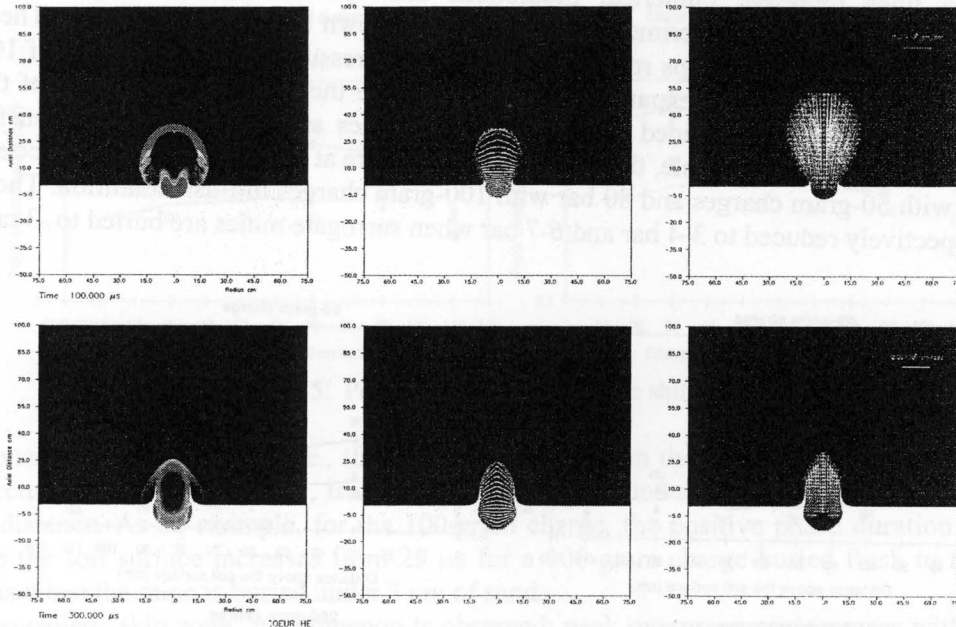


Figure 2: Air overpressure, particles and velocity vectors at 30 cm above the soil surface. 100-gram charge flush-buried (top) or buried under 3 cm of sand (bottom)

To validate the numerical predictions, comparisons with the experimental measurements are made at points ranging between 30 cm and 70 cm from the ground level. An example of the agreement is given by Figure 3 for a flush-buried 50-gram charge. Time offset is applied to the computational results to synchronize with the first experimental record. Beyond the simple conformity concerning the peaks of overpressure, the overall profile of the signals is captured in a very satisfactory way.

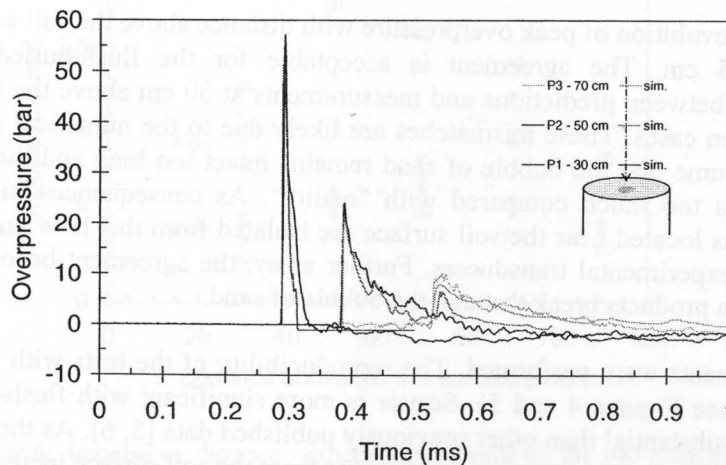


Figure 3: Pressure-Time histories with a flush-buried 50-gram charge. Comparison between experimental measurements and numerical predictions

Discussion

Agreement between Eulerian numerical predictions and experimental results for distances ranging from 30 to 70 cm above the soil surface suggests that the numerical approach has in fact been accurate in the modelling of the phenomenon and can be trusted for near-field estimation. Only peak overpressure and impulse are discussed here. A more detailed review is given in [2].

Figure 4 shows the evolution of peak overpressure along the axis with distance above the soil surface. Solid lines represent numerical predictions and symbols refer to experimental measurements. The number of experimental data points is shown between parentheses. These results emphasize that pressure drops rapidly with distance. Pressure drops by a factor of 100 within the first 10 centimetres of expansion. At 30 cm above the ground, irrespective of the charge used, the peak values obtained with flush-buried mines are 10 times higher than for mines buried to -3 cm. As an example, the levels of overpressure at 30 cm to the soil surface are about 50 bar with 50-gram charges and 80 bar with 100-gram charges in flush condition. These levels are respectively reduced to 3-4 bar and 6-7 bar when surrogate mines are buried to -3 cm.

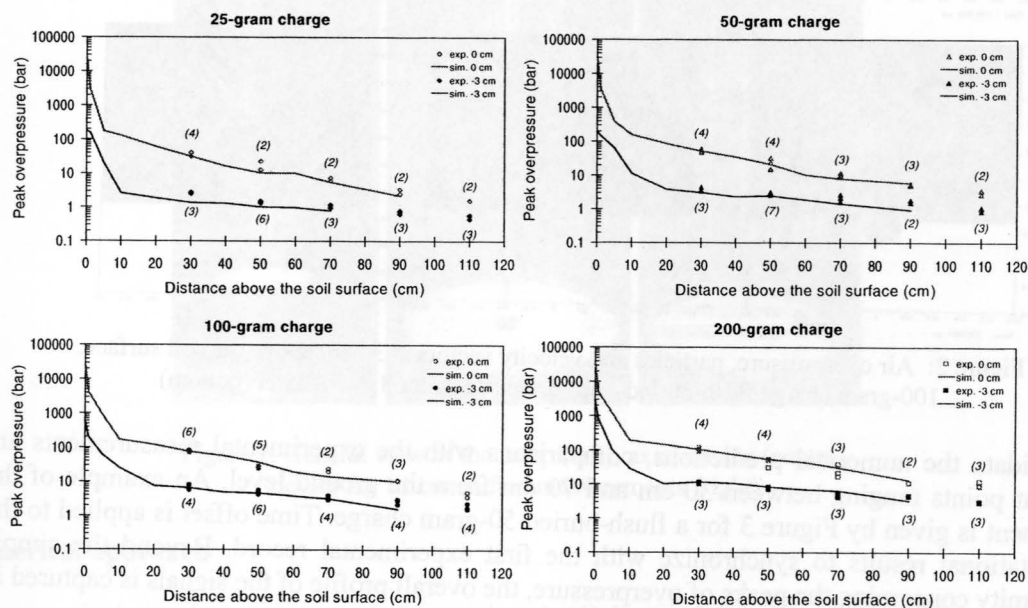


Figure 4: Peak overpressure along the vertical axis

Figure 5 shows the evolution of peak overpressure with distance above the soil surface along an axis shifted by 15 cm. The agreement is acceptable for the flush-buried charges, but discrepancies exist between predictions and measurements at 30 cm above the soil surface for the 3 cm overburden cases. These mismatches are likely due to the numerical model used for sand. One can presume that the bubble of sand remains intact too long and then channels the detonation products too much compared with "reality". As consequences in the numerical simulations, stations located near the soil surface are isolated from this flow and do not see as much pressure as experimental transducers. Further away, the agreement becomes acceptable since the detonation products break through the bubble of sand.

About 100 experiments were performed. The reproducibility of the tests with buried mines is very satisfactory (see Figures 4 and 5). Scatter is more significant with flush-buried charges, although it is less substantial than other previously published data [5, 6]. As the Canadian team did, we observe that the scatter decreases as distance from the soil surface increases.

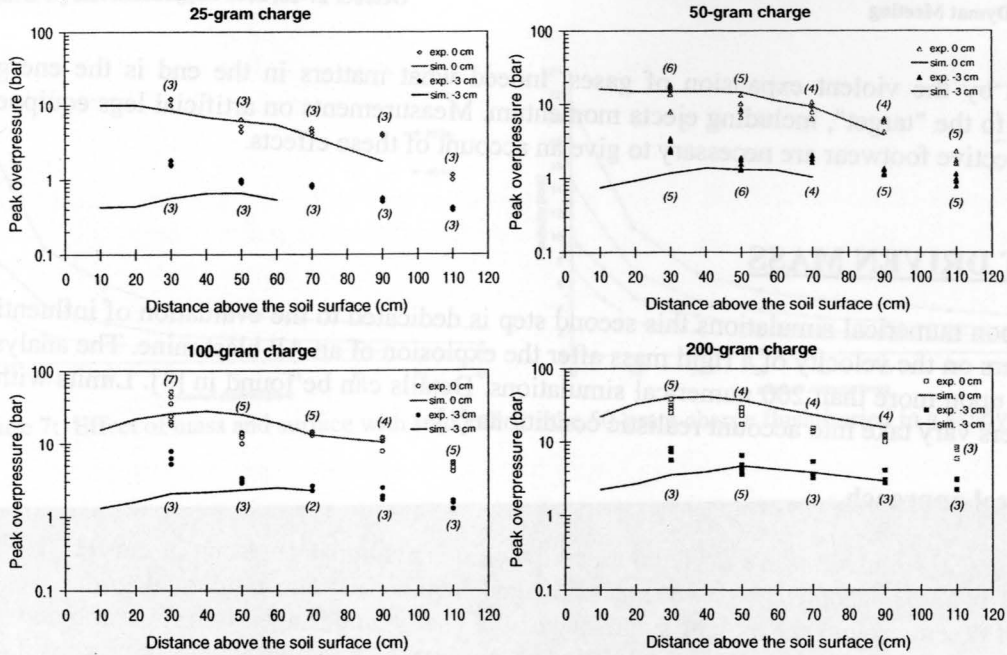


Figure 5: Peak overpressure along the shifted axis

The positive phase duration, i.e., the time interval between the initial rise in pressure and the first return to ambient pressure, is observed to be higher under buried condition and increases with distance. As an example, for the 100-gram charge, the positive phase duration at 30 cm above the soil surface increases from 25 μ s for a 100-gram charge buried flush to more than 200 μ s when the mine is buried under 3 cm of sand.

The so-called "skip zone" phenomenon is observed: peak overpressure decreases with distance but duration increases. Consequently, the positive impulse of the shock wave, i.e., the area under the overpressure curve, increases over a short distance near the explosion source and decreases afterwards. Figure 6 gives an example for the 100-gram charges for which the maximum impulse occurs between 50 cm and 70 cm above the ground level. This result agrees with previous observations [5, 6]. The distance where maximum impulse is observed increases with charge size: from 30-50 cm with 25-gram charges to 90 cm with 200-gram charges.

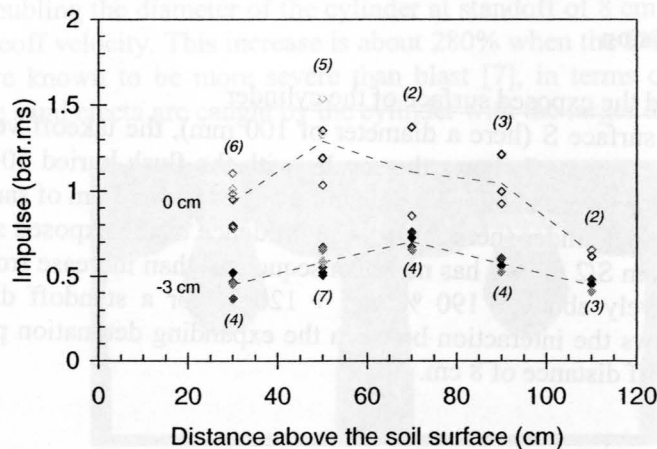


Figure 6: Impulse vs. distance - experimental results for the 100-gram charges

To summarize, as the charge is buried deeper, more explosive energy goes into compaction of the particle layer and creation of ejecta. Hence, there is less energy for the air blast. However, if the amplitude of some parameters is considerably reduced when the mine is buried, one should not neglect the "gun effect" induced by the soil confinement on the soil particles that are

propelled by the violent expansion of gases. Indeed what matters in the end is the energy imparted to the "target", including ejecta momentum. Measurements on artificial legs equipped with protective footwear are necessary to give an account of these effects.

BLAST DRIVEN MASS

Based upon numerical simulations this second step is dedicated to the evaluation of influential parameters on the velocity of a rigid mass after the explosion of an AP blast mine. The analysis is based upon more than 200 numerical simulations. Details can be found in [3]. Limits within parameters vary take into account realistic conditions [1].

Numerical approach

The numerical simulations are carried out using the Euler-Lagrange coupling of the OTI*HULL software [4]. The geometry is two-dimensional axisymmetric. The numerical grid covers a radius of 40 cm around the axis of symmetry of the charge and ranges from 50 cm below the ground level to 80 cm above. The rigid cylinder, one wants to compute the takeoff velocity, is described as a lagrangian structure put into an eulerian grid with cells of size 1,66 x 1,66 mm². A Von Mises strength model and a Mie-Gruneisen equation of state with data for tungsten are applied. Explosive, sand and air remain as in the previous step of the program.

The standard threat is a 50-gram C-4 surrogate mine placed parallel to the soil surface and initiated at the bottom dead centre. The mine can be flush-buried or buried up to a DOB of 8 cm. The standoff distance (initial distance between the cylinder base and the soil surface) ranges between 0 and 8 cm. Some calculations feature a 25-gram surrogate mine.

The velocity time history is captured by means of lagrangian stations attached to the rigid cylinder. The eulerian grid is deleted after 750 μ s; the energy transfer to the lagrangian structure is complete. Simulations run over 15 ms after the detonation, the takeoff velocity is then steady. To be rigorous, because of the gravity and the air drag the velocity will later decrease to zero (trajectory apogee) and the cylinder will fall down. The total duration of the phenomenon numbers hundreds of milliseconds, and even seconds.

Main results and discussion

Influence of the mass and the exposed surface of the cylinder

For a constant exposed surface S (here a diameter of 100 mm), the takeoff velocity varies in inverse ratio to the mass. Figure 7 shows the results with the flush-buried 50-gram surrogate mine. The same conclusions were obtained with a mine buried under 3 cm of sand.

For a constant mass of the cylinder (here 20 kg), the influence of the exposed surface was also investigated. Increase from $S/2$ to $2xS$ has more consequences than increase from S to $4xS$: the differences are respectively about + 190 % and + 120 % for a standoff distance of 8 cm (Figure 7). Figure 8 shows the interaction between the expanding detonation products and the rigid cylinder at a standoff distance of 8 cm.

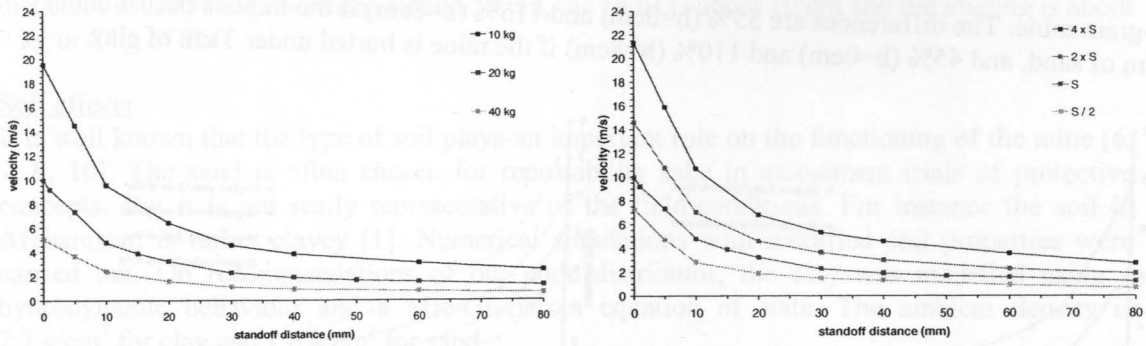


Figure 7: Effect of mass and surface with standoff for the 50-gram charge flush-buried in a sandy soil

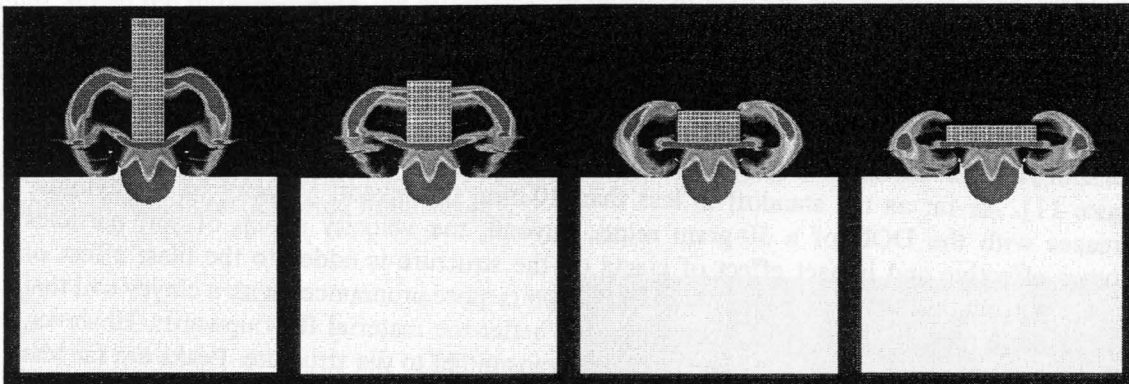


Figure 8: Fringes of air overpressure @ 100 μ s after the detonation of a 50-gram charge flush-buried into sand (red levels \geq 7 bars) - mass of 20 kg and surfaces S/2, S, 2S, 4S at a standoff of 8 cm

On the first 10 millimetres, the effect of the exposed surface was found to increase with a clayey soil. This can be attributed to the lateral confinement of detonation products which is more pronounced with clay (higher density). Beyond 20 mm, the effects are nearly the same.

The "surface" parameter is more crucial when the mine is buried: for a 50-gram mine under 8 cm of sand, doubling the diameter of the cylinder at standoff of 8 cm involves an increase of 340 % of its takeoff velocity. This increase is about 280% when the DOB is 3 cm. With buried mines, ejecta are known to be more severe than blast [7], in terms of momentum. Figure 9 shows how more sand ejecta are caught by the cylinder with the larger diameter.

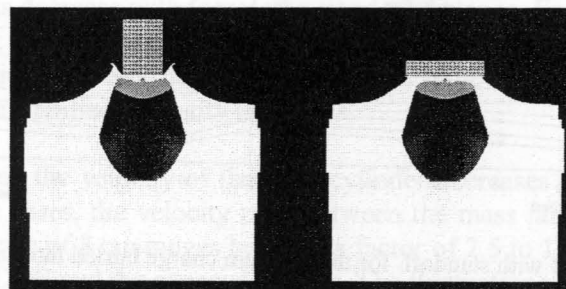


Figure 9: Fringes of air overpressure @ 1000 μ s for a 50-gram charge buried under 8 cm of sand - mass of 20 kg with exposed surface S (left) and 4S (right) at a standoff of 8 cm

Influence of the loading (amount of explosive)

This subpart concerned mines flush-buried or buried under 3 cm of sand or clay (Figure 10). The differences increase with the standoff distance. The takeoff velocity due to the explosion of a 50-gram flush-buried mine is 60% higher (h=0cm) and 160% higher (h=8cm) compared to a

25-gram mine. The differences are 55% (h=0cm) and 115% (h=8cm) if the mine is buried under 3 cm of sand, and 45% (h=0cm) and 110% (h=8cm) if the mine is buried under 3 cm of clay.

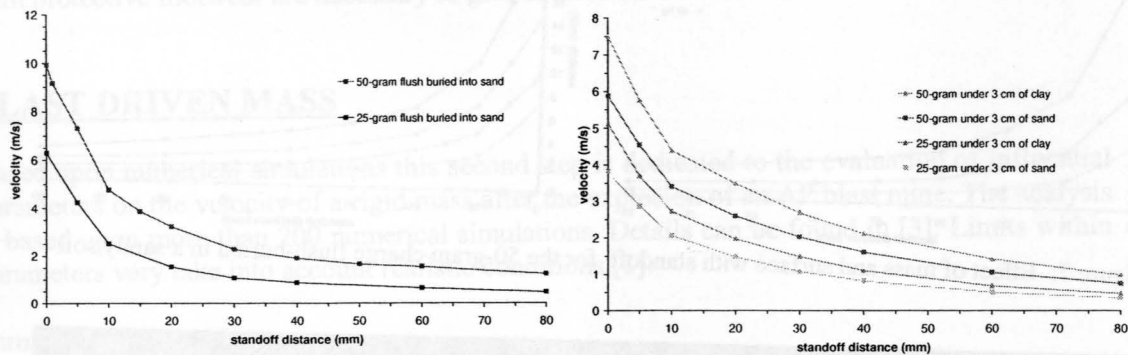


Figure 10: Loading effect with standoff for a charge flush-buried (left) or buried (right)

Influence of the depth of burial (DOB)

Depending on the standoff distance, a buried mine can be more severe than a flush-buried mine (Figure 11). As far as the standoff is less than 10 mm, the takeoff velocity of the cylinder decreases with the DOB of a 50-gram mine. Beyond, the velocity set-up of soil particles becomes effective and impact effect of ejecta on the structure is added to the blast effect of detonation products (see Figure 9). This phenomenon is more pronounced with a clayey soil that confines more (density effect) and focuses all the better the material flow upwards. However, the DOB of the mine limits the shock magnitude transmitted to the structure. Peaks are far less pronounced. For a stabilized velocity about 10 m/s, peaks of +90 m/s and -20 m/s are recorded during the first instants of interaction between the 50-gram surrogate mine flush buried and the 20-kg cylinder laid on the soil. Those peaks are about +25 m/s and -10 m/s for a final velocity of 6 m/s when the same mine is buried under 3 cm. With a DOB of 8 cm, the maxima are about +10 m/s and -1 m/s while the asymptotic velocity is close to 4 m/s.

The DOB is usually 2 or 3 cm [1]. Under such conditions and at standoff of 30 mm, a mine buried into clay has the same effects as a flush-buried mine. The thickness of a standard combat boot is about 35 mm at the heel.

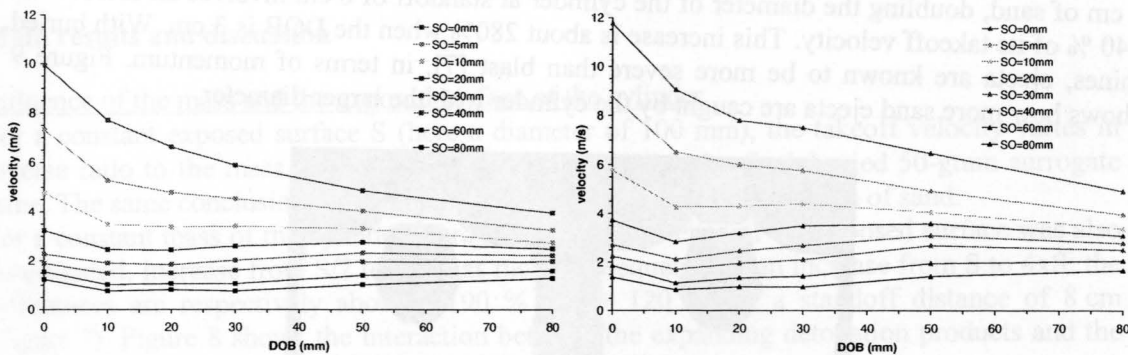


Figure 11: Effect of DOB with standoff for the 50-gram charge buried into sand (left) or clay (right)

The major role of the impact of ejecta compared to blast effects alone has been discussed, and momentum was found to prevail [6, 7, 8]. The positive effects of DOB on the functioning of mines were already pointed out using anti-tank blast mines [9, 10]. Those studies are comparables: taking into account the TNT equivalences of composition C-4, a scaling ratio of about 1:5 can be defined between our AP mine context (50-gram of C-4 buried under 2 or 3 cm of soil and standoff distance of 10 cm) and a typical AT mine configuration, where standoff

distances usually range between 40 and 50 cm, the DOB is about 10 cm and the loading is about 7 kg or 8 kg of TNT.

Soil effects

It is well known that the type of soil plays an important role on the functioning of the mine [6, 7, 9, 10]. The sand is often chosen for repeatability sake in assessment trials of protective concepts. But it is not really representative of the field-conditions. For instance the soil in Afghanistan is rather clayey [1]. Numerical simulations with modified soil properties were carried out. On recommendations of our code distributor, the clay was modelled using a hydrodynamic behaviour and a Mie-Gruneisen equation of state. The ambient density is 2.2 g/cm^3 for clay and 1.6 g/cm^3 for sand.

With a 50-gram flush-buried mine, the velocity of the rigid cylinder is 12 % to 20 % higher with clay. When the mine is buried, the differences in favour of clay are comparables in case of low DOB. They come to 30-35 % for a DOB of 3 cm (Figure 12) and reach 40 % for a DOB of 5 cm and a standoff distance of 8 cm.

The influence of the type of soil is slightly more significant with 25-gram charge.

Those orders of magnitude are subject to the validity of the models used to treat soils. An experimental validation is required. It is noteworthy that those results are consistent with published results on delivered impulses [8].

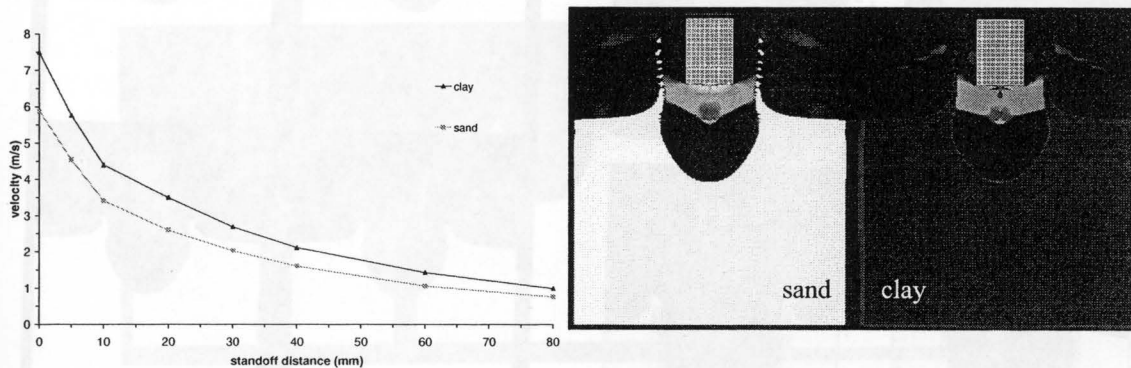


Figure 12: Soil effect with a 50-gram charge buried at 3 cm (left) Fringes of air overpressure @ $500 \mu\text{s}$ for a standoff of 8 cm (right)

Effect of the standoff distance

The first step of the program has shown that pressure drops by a factor of 100 within the first 10 centimetres of expansion. This feature is also rendered in the velocity time histories as the amplitudes of first peaks decrease with increasing standoff distance. For standoff of 8 cm peaks are nearly non-existent: for instance, maxima of +2 m/s and -0.3 m/s are recorded during the first instants of interaction between the 50-gram surrogate mine flush-buried into sand and the 20-kg cylinder while the stabilized velocity is 1.2 m/s.

For any case investigated the velocity of the rigid cylinder decreases with increasing standoff distance. For the whole cases, the velocity ratio between the mass laid on the surface and the mass at a standoff distance of 8 cm ranges between a factor of 2.5 to 13.5 depending mainly on the loading charge, the DOB and the exposed surface. The fluctuations are less when the mine is buried into sand or clay. In this case, one can argue that the reduction of the blast effect is balanced by the impact of soil ejecta.

The effects are similar for exposed surfaces of S, 2S and 4S but are emphasized with S/2: the smaller the exposed surface is the less it catches the divergent expansion of detonation products at "high" standoff distances.

ENERGY TRANSFER TO A SURROGATE LEG USING DEFLECTORS

Numerical results

To start with very simple things, cylindrical shaped blocks of different materials and various heights were inserted between the soil and the surrogate mass. Figure 13 gives some examples of results with aluminium and rubber blocks. The height of 38 mm was chosen to fit the thickness of a standard combat boot at the heel. The height of 80 mm was fixed as a limit, taken into account the functional aspect of the footwear.

Depending on the materials, the consumption of energy increases in different way with thickness of the interface. Regarding flush-buried mines, the velocity transmitted to the rigid mass is reduced from less than 5 % with aluminium but close to 60 % with rubber. Regarding charges buried under 3 cm of sand; the decrease is about 15% with aluminium and 55 % with rubber. The splash of the all-rubber blocks is obvious. Not surprising is that blocks do not deflect the flow of the detonation products ("red zones" are still visible on the pressure plots of Figure 13).

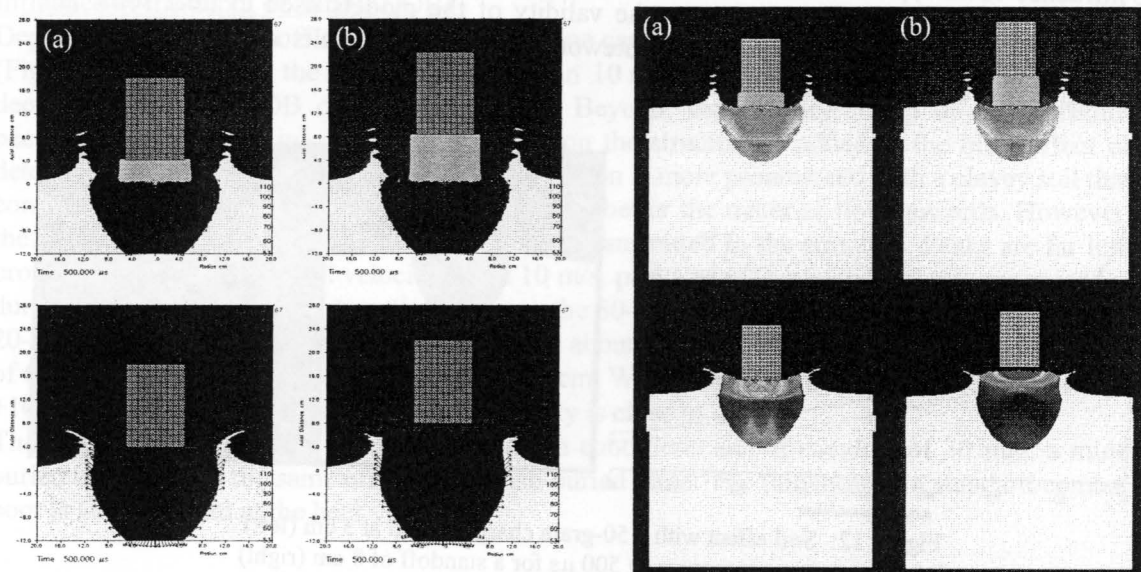


Figure 13: Flow of the detonation products (left) and fringes of overpressure @ 500 μ s (right) for a 50-gram charge buried at 3 cm and block interfaces of aluminium (top) or rubber (bottom) with a height of 38 mm (a) or 80 mm (b)

The next step included shape factors. The total height of the interface was kept constant to 80 mm. Figure 14 shows some results with 3 types of interfaces. As expected, the deflection is improved with aluminium. Concave profiles are inclined to accumulate more pressure.

Not shown here, the efficiency of V-shapes is optimal with flush-buried surrogate mines. Indeed, only the detonation products need to be deflected in this case. When the mine is buried, soil ejecta (coming from the layer initially just over the mine) impact the deflector. Those particles pick up speed during the first stage of expansion if some interval is given between the soil surface and the deflector boundaries. About that, lateral air gaps are more important with the V-shaped pod compared with the convex one.

Another argument is that V-shape is certainly more efficient when the mine is ideally located, as it is the case here, but could become the worst case when the mine is off-axis. That is the reason why a convex pod is more adapted for polyvalence aspects.

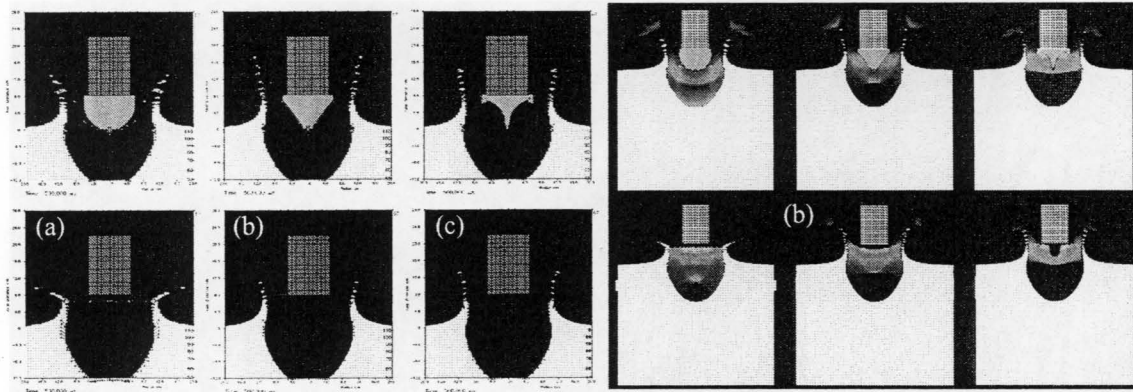


Figure 14: Flow of the detonation products (left) and fringes of overpressure @ 500 μ s (right) for a 50-gram charge buried at 3 cm and convex (a) V-shaped (b) or concave pods (c) of aluminium (top) or rubber (bottom)

To optimise the stream deflection of the detonation products by a solid part and the energy consumption by a shock-absorbing part, hybrid interfaces are now investigated (Figure 15). But to go further, the problem is that one lacks adapted constitutive laws and equations of state to model exotic materials under highly dynamic loading.

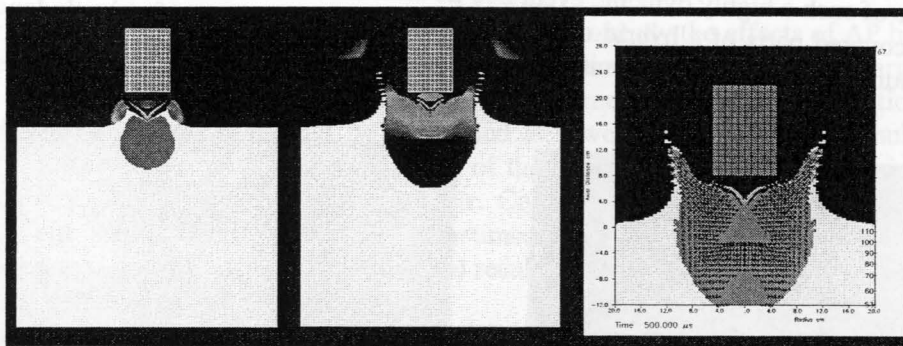


Figure 15: Fringes of overpressure @ 100 μ s (left) and 500 μ s (center) and flow of the detonation products (right) for a 50-gram charge buried under 3 cm of sand and an hybrid deflector

Experimental results

In a parallel direction with calculations, tests are carried out using a simplified mechanical leg to ensure reproducibility. The experimental measures feature a 250 kV X-ray apparatus, pressure transducers, extension gauges as well as a velocity tracking device based on graphite leads (as seen on Figure 16).

The mechanical leg is hanging on the gantry so that the base of the deflector is in contact with the calibrated artificial medium of dry silica sand without exerting pressure there.

The velocity tracking device features bars of graphite leads instead of copper wires. Indeed, copper wires exhibited a variable stiffness depending on the sticking technique so that measurements were not very reliable. The distance between the elements can be easily adjusted by studs assembled on slides.

A sharpened probe, laterally positioned at a distance of 45 cm from the soil surface, gives some information about pressure.

In addition, a numerical video makes it possible to appreciate the behaviour of the unit leg / gantry and to evaluate the rise of the leg under various conditions.

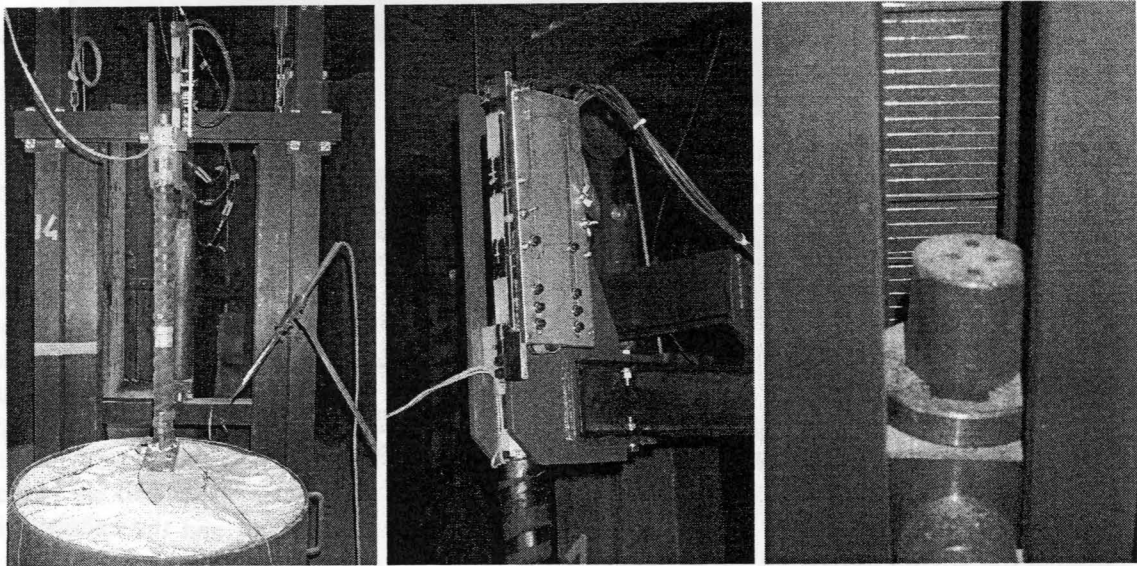


Figure 16: Experimental set-up equipped with velocity tracking device

The deflector has to play its role within a very short time, about 250 μ s. Figure 17 shows an X-ray picture of such a highly dynamic event 200 μ s after the detonation of a 50-gram surrogate mine and recovered parts of a hybrid deflector made of a hollow shape of polyethylene filled with aluminium foam and covered by a thin steel wedge.

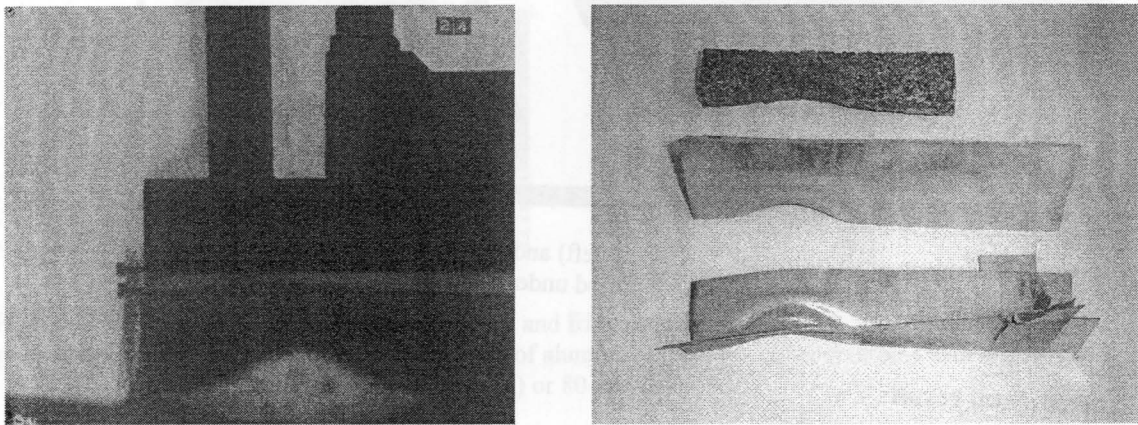


Figure 17: Example of X-ray @ 200 μ s and recovered deflector

Outlook: Now, to really benefit from more sophisticated numerical simulations (Figure 18), one would need more advanced material models and robust 3D Euler/Lagrange numerical schemes to better describe the phenomena. Also needed is a more bio-fidelic surrogate leg to make the link between the experimental data collected and the risk of human injury.

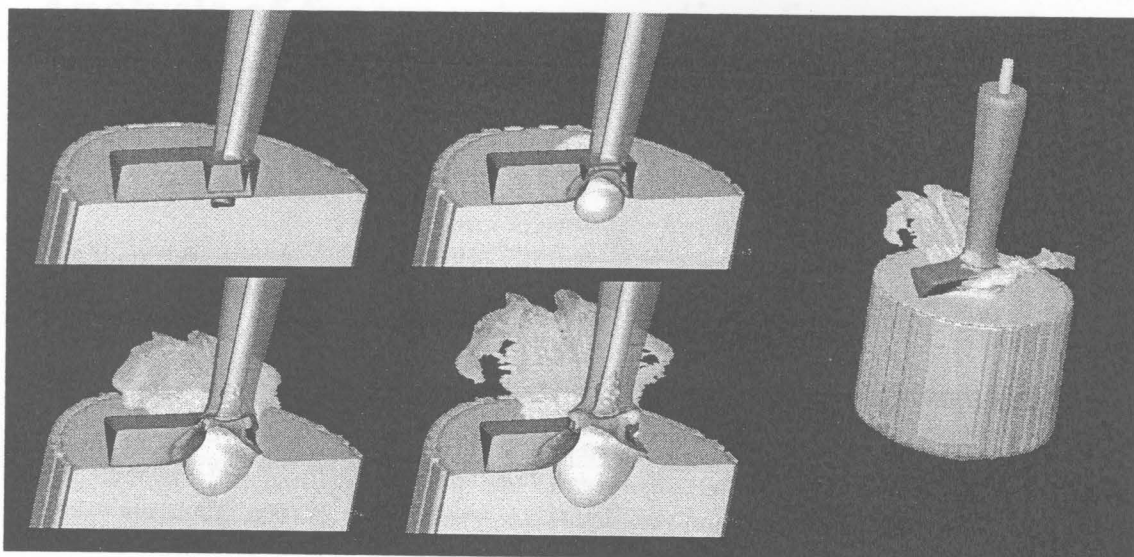


Figure 18: Snapshots of an exploratory calculation

CONCLUSIONS

This work demonstrated the relevance of numerical tools to study the effects of AP blast mines. Here, the severe conditions in the zone of interest (immediate proximity of the charge) make it difficult, even impossible, to obtain experimental measurements. Numerical simulation fills that gap so that a parametric study can be performed at lower cost. Numerical simulation also contributes to the design and the dimensioning of the tests, by facilitating the choice of some space-time sizes that are not always foreseeable. Coupled with experiments, it allows a finer analysis of the physical phenomena, and sometimes helps to explain unexpected or suspect observations, e.g., scattering of the experimental results.

Pointed out were the strong directionality of the blast due to soil confinement and the differences in pattern of gas expansion depending on whether the mine was flush-buried or buried under 3 cm of sand.

Peak overpressure decreased by a factor of 100 over the first 10 centimetres. At soil level, the surrogate mines used in these experiments generate overpressure of about 25 to 30 kbar when they are flush with the soil. Peak overpressure reduces to 130 – 200 bar at 10 cm of elevation. If the mines are buried under 3 cm of dry sand, peak overpressure values range from 200 to 2700 bar at the soil level and from 2 to 35 bar 10 cm up. Using the numerical predictions and experimental measurements, it was shown that the effect of a 3 cm soil overburden is to decrease peak overpressure by a factor of 10, vertical expansion rates by a factor of 3, but positive phase duration increases significantly.

The standoff distance appears to be a driving contributor to reducing the level of boot destruction and subsequent leg injury. But this distance must stay limited for ergonomic and operational reasons.

The burial of the mine (the most frequent field-situation) generates ejecta that add to the blast. Simultaneously, the type of the soil is an influent parameter regarding the level of aggression. Results show that several parameters must be weighed before any conclusion on the aptitudes of a concept to protect against AP blast mine threat. Some parameters are hardly controllable since they can vary radically from a person to another (weight, exposed surface...) and depend on the environment (type of soil, depth of burial of the mine...). The polyvalent aspect of any protective footwear must prevail. As an example, V-shaped deflector was found to be more

efficient when the mine is ideally located but could become the worst case when the mine is off-axis. That is the reason why a convex pod is certainly more adapted.

To summarize, the protective footwear concept has to do with 3 major functions:

- to deflect the stream of the detonation products,
- to consume the remaining energy,
- to trap the soil ejecta.

Moreover with respect to the physical equilibrium of the user (ergonomics), i.e., the standoff must be optimized.

The work presented here was the first step of a program dedicated to the standardization of experimental protocols between countries involved in PPE assessment. The aim of the program is to allow the improvement of existing protection concepts (standard boot or overboot) as well as the development of new blast protective footwear. The step in progress deals with the energy transfer to a surrogate leg. The challenge is multiple:

- one needs more advanced material models and robust 3D Euler/Lagrange numerical schemes to better describe the phenomena,
- one needs a more bio-fidelic surrogate leg to make the link between the experimental data collected and the risk of injury for human leg.

Acknowledgements

A part of this work was funded by the French Ministry of Defense (DGA/DSP/STTC/DT-SH) under contracts PEA 980823 and PEA 010809. The authors would like to thank all the technicians who were involved, for their logistical and technical support.

References

1. "Test Methodologies for Personal Protective Equipment Against Anti-Personnel Mine Blast", Final Report of the RTO Human Factors and Medicine Panel (HFM) Task Group TG-024, March 2004
2. P. Magnan, F. Rondot, "Mapping of Air Overpressure around Surrogate AP Blast Mines", NATO RTO Specialist's Meeting on Personal Protection, Koblenz, May 19-23, 2003. ISL PU 621/2003
3. F. Rondot, "Mise en vitesse d'une masse inerte rigide par explosion d'une mine antipersonnel à effet de souffle. Etude paramétrique par simulations numériques", ISL R 112/2002
4. D.A. Matuska, J.J. Osborn, E.W. Piburn, "Hull Users Manual-Version 5 OTI*HULL "
5. D. Bergeron, R. Walker, C. Coffey, "Detonation of 100-Gram Anti-Personnel Mine Surrogate Charges in Sand - A Test Case for Computer Code Validation", DRES SR 668 Report, October 1998.
6. D.M. Bergeron, J.E. Tremblay, "Canadian Research to Characterise Mine Blast Output", 16th MABS Conference, Oxford, UK, September 2000.
7. J.F. Unruh, D.C. Scheidt, D.J. Pomorenig, "Data Analysis of Scale Model Armored Vehicle Response to Ballistic Impulse", Contract Report No. 13112, US Army TACOM R&D Center, 1985.
8. G. Fairlie, D. Bergeron, "Numerical Simulation of Mine Blast Loading on Structures", 17th MABS Conference, Las Vegas, Nevada, June 2002.
9. L. Laine, O. Ranestad, A. Sandvik, A. Snekkevik, "Numerical Simulation of Anti-Tank Mine Detonations", 12th APS Topical group Conference on Shock Compression of Condensed Matter, Atlanta, USA, June 24-29 2001.
10. G.I. Kerley, "Numerical Modeling of Buried Mines Explosion", Report ARL-CR-461, March 2001

Underwater Plate holing Studies

Phil Church, Ian Cullis, Richard Townsley, W Huntington-Thresher

QinetiQ Fort Halstead, Building Q14, Sevenoaks, Kent, TN14 7BP, United Kingdom

This investigation describes a combined experimental and simulation study on the response of steel plates subjected to explosive charges in contact underwater. The experiments were designed to perforate the plate by plugging and then cause subsequent tearing or petalling of the plate. The simulations were performed using the Eulerian hydrocode GRIM to predict the plate loading and the Lagrangian hydrocode DYNA to predict the response of the plate. The failure of the plate was captured using a simple erosion criterion based on a critical damage number. The most successful techniques for transferring the loading was a simple momentum dump option and good agreement was obtained compared to the experimental data. This also demonstrated that the dynamic pressure loading from the water was a major contribution to the loading. These results are quite surprising since the loading is non-impulsive in nature.

INTRODUCTION

The defeat of underwater targets comprises a number of complex mechanisms, which are interdependent. These are shock effects, general gas loading and bubble loading, all of which can take place in different timescales and all of which have a potentially significant contribution to the defeat of a structure [1]. The simulation of these effects is also complex, since the loading and structural response is heavily influenced by the fluid/structure interaction and is therefore not a simple impulsive loading.

Qualitatively the effect of the water is to provide inertia, which inhibits the expansion of the explosive products and results in the production of an underwater bubble. In addition this provides an additional loading due to its physical motion against the plate.

The aim of this investigation was to obtain a much better appreciation of these effects and to evaluate their individual contribution to the loading and subsequent structural response. This was achieved by performing a combined experimental and numerical simulation study of controlled charges in contact with steel plates underwater. The charges were designed to perforate the plate by plugging and then the subsequent loading would cause the plate to petal. The simulations were used to isolate the contribution of the various mechanisms and determine the most robust method for simulating the loading and subsequent structural response. The simulations used advanced constitutive and fracture models.

EXPERIMENTS

The main aim of the experimental programme was to provide precise data to compare with the numerical simulations and to identify the timescale for different failure modes of the plate to operate. In order to identify the timescale for plugging and petalling and determine whether the boundary conditions on the plate influenced its response a number of highly instrumented small-scale tests were used. These comprised small cylindrical explosive (i.e. tetryl) pellets in contact with thin (i.e. 0.6mm steel plates). The plate was instrumented with a fine grid on the back, such that high speed photography captured the hole growth process. The experimental arrangement is shown in Figure 1.

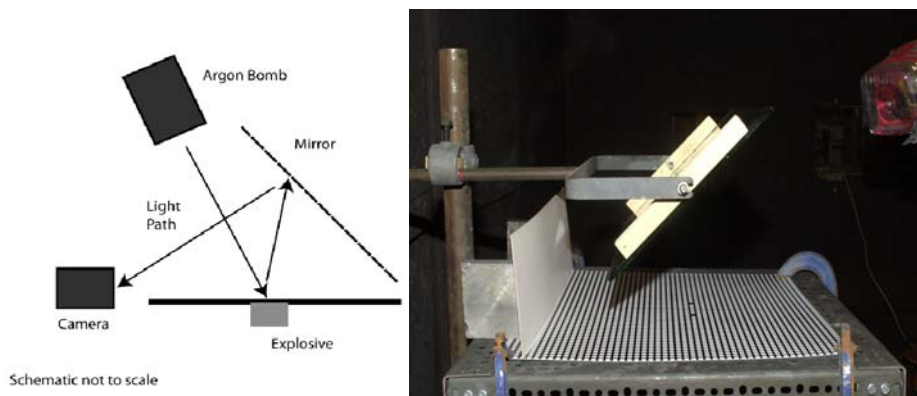


Figure 1 – Experimental Arrangement

The results demonstrated that the plugging of the plate was complete in a very short timescale (i.e. 10 μ s) and the longer time petalling was complete in about 140 μ s after detonation. In addition the petalling commenced shortly after the plugging process had completed and was a function of the localised deformation induced around the initial hole. The plate boundary conditions had no influence on the final hole size or shape. An example of the final hole produced in the experiments is shown in Figure 2.



Figure 2 – Hole in plate loaded by Tetryl pellet

The large scale trials were conducted on 4m square steel plates of different thicknesses. The explosive used was PE4 in different charge sizes. The hole growth was monitored by high speed video cameras. It should be recognised that there are some errors associated with the hole growth, since it is a subjective analysis from the photographs. The hole can be obscured by the explosive products and there was also a large skirt on the edge of the plates to help them float on the water, but was an additional barrier to the observation of the growth of the hole. An example of the hole growth for a 1.5kg charge against a 12mm thick plate is shown in Figure 3, where the accuracy for the hole size is assumed as 10%. The final hole size was in excess of 2m.

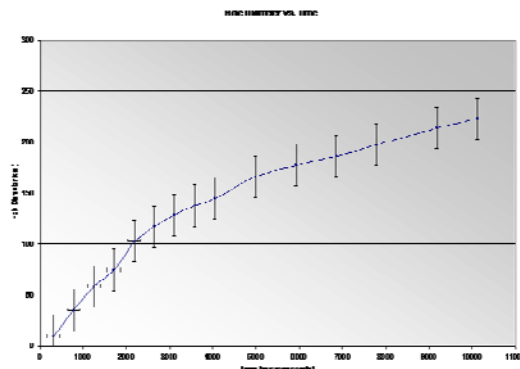


Figure 3 - Hole diameter (mm) v time (μ s) for 1.5kg PE4 loading a 12mm plate

CONSTITUTIVE AND FRACTURE MODELS

The constitutive model for the steel plate was described by the modified Armstrong-Zerilli model [2,3]. This expresses the flow stress as a function of strain, strain rate and temperature and has been demonstrated as applicable for body centred cubic (bcc) metals and some alloys. The form of the model is as follows:-

$$\sigma = (C_0 + C_1 \varepsilon^n) \mu_T / \mu_{293} + C_2 \exp(-C_3 T + C_4 T \log \dot{\varepsilon}) \quad (1)$$

Where C0 to C4 and n are constants and σ , ε , $\dot{\varepsilon}$ and T are respectively stress, strain, strain rate and temperature in °K. μ_{293} is the shear modulus at 293°K and μ_T is the shear modulus at the current temperature.

Unfortunately for this study it was not possible to characterise the actual materials and therefore models had to be constructed from specification sheets comprising hardness, yield strength and proof stress. The steel specification for the small plate trials was BS 1449 and BS 4360 43A. Extensive studies within QinetiQ have demonstrated that the rate and thermal sensitivity are similar for all bcc steels [4]. The values appropriate for each steel are given in Table 1.

Constants	BS 4360	BS 1449
C ₀ MPa	400 MPa	100 MPa
C ₁ MPa	500 MPa	420 MPa
C ₂ MPa	990 MPa	1100 MPa
C ₃	0.00515	0.00515
C ₄	0.000262	0.000262
N	0.5	0.66
Sm1	1.13	1.13
Sm2	0.000445	0.000445

Table 1 – Material Constants for Steels

The steels used in this programme fail by a ductile fracture mechanism based on the growth and coalescence of voids. The Goldthorpe Path Dependent Ductile Fracture model has been developed for ductile fracture processes [5]. It has been applied to the growth and nucleation of voids under different stress systems. The model accumulates damage according to the following relationship:-

$$dS = 0.67 \exp(1.5\sigma_n - 0.04\sigma_n^{-1.5}) d\varepsilon + A\varepsilon_s \quad (2)$$

Where

- σ_n = Stress triaxiality (Pressure/Flow Stress or P/Y)
- $d\varepsilon$ = Effective plastic strain increment
- ε_s = maximum principle shear strain
- A = Constant determined from torsion test
- S = Damage

The damage is then incremented by

$$S_{new} = S_{old} + dS \quad (3)$$

Fracture occurs when the damage reaches a critical value S_c , which is determined from a quasi-static tension test. The damage comprises a tensile component due to void growth and a shear component due to shear localisation. The shear parameter 'A' is determined from a torsion test, which measures the shear strain to failure. Thus the algorithm is a multi-mode failure model, where the tensile failure will dominate for P/Y values less than -0.3 and the shear failure will dominate for the P/Y values between -0.3 and zero. The only means of deriving the critical damage S_c value for the steels was to compare it with the existing QinetiQ database and find the closest 'fit' in terms of elongation etc. This exercise suggested that the critical S_c value for the BS1449 and BS4360 43A steels was 3.5 and 2.5 respectively. Whilst this is subjective, the only alternative is to perform a tensile test on the actual material. Therefore it is considered legitimate to allow some flexibility in fitting this parameter to the experimental results to gauge its sensitivity on the results.

SIMULATIONS

The main purpose of the simulations was to isolate the effect of the various loading mechanisms on the structural response and to perform a sensitivity study of material parameters. The basic approach adopted was to use the one-way coupling between GRIM and DYNA3D to simulate the loading on the plate and the subsequent plate response. The methodology consisted of running GRIM to simulate the explosive loading with data collection points, or stations, on the boundary of the plate to capture the loading history. These loading histories (e.g. pressure/time), are then used as input 'load curves' to the DYNA simulation to predict the subsequent plate response in terms of deformation and fracture. This approach has been used successfully on a variety of applications.

GRIM Simulations

Various methods were used to capture the loading from GRIM, ranging from using a rigid boundary to treating the structure with a real material. The simulations were performed in axisymmetric geometry and on a mesh sufficient to resolve the detonation and hence subsequent loading. The difference in the loading, between the rigid boundary definition and real material was about 50%. As a result of this a real material was used in the GRIM simulations. This resulted in the necessity for the station points to be constrained along the axis, such that the loading could be mapped into the correct zone in the DYNA3D simulations. For these scenarios, this was considered a reasonable approximation.

DYNA Simulations

The DYNA simulations took the loading histories provided by the GRIM simulations to predict the plate deformation and fracture. This was done by applying loading histories to a 'zone' of elements as opposed to individual elements having different individual loads. However, when the mesh in DYNA is changed it means that each zone has to be recalculated for a given mesh to match the loading position.

One of the important initial conclusions from this study was that petalling was never predicted with a perfectly radial mesh. The reason for this is that there is no asymmetry in the simulation and therefore there is no mechanism for localisation of tension in the plate, which causes the plate to petal by tearing. The other important conclusion was that the most robust method of transferring the loading from GRIM was through a simple momentum dump based on shock

arrival time. This is quite dramatic since the process is not just impulsive loading, but also fluid/structural interaction.

Sensitivity of Plate Response to Loading and Material Properties

Having taken the decision to use momentum dump as the means for transferring the load, the next stage was to ascertain the relative contributions of different aspects of the loading to the subsequent structural response of the plate. In this study it was demonstrated that the initial shock response was largely responsible for the plugging in the plate. Therefore there were two major effects to consider. These were the general dynamics of gas loading, which would be inhibited by the bubble growth and the inertial loading of the water itself. The effect of the bubble jetting was ignored since the result would be a jet of water passing through the hole. In addition, reflections from the side and depth of the pond were calculated as having an influence approximately 5ms after detonation. The simulations assumed semi-infinite (i.e. very deep water) for simplicity. Therefore the simulations were only run in general to 5ms. The results for the momentum loading including gaseous products only and adding the additional loading due to the inertia of the water is shown in Figure 4. In addition the results for different values of the critical damage are also illustrated in both cases.

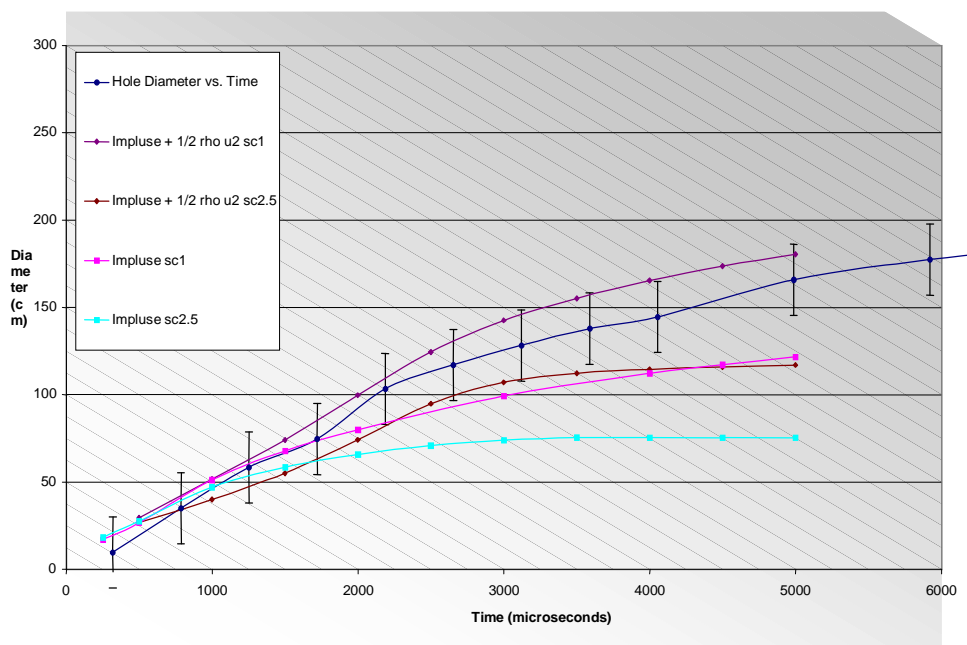


Figure 4 - Comparisons of hole size showing importance of water loading

The sensitivity of the results to critical damage are not surprising since the failure mode is tensile through ductile tearing. The two values chosen are considered the extremes for this type of steel, although it is acknowledged that without testing the material, one can never be sure. The sensitivity of the results to material properties was minimal in that a halving of the yield strength resulted in a 2% increase in the predicted hole size. However, there may well have been anisotropic effects in the actual material used (e.g. due to rolling), which were not accounted for in the analysis.

The dramatic effect of the water loading is more surprising, but easily explainable. Although the velocity of the water is small in the axial direction of the plate, its density is much greater than the detonation products, resulting in a substantial increase in the overall loading. This is also illustrated in Figure 5, which shows the hole at 5ms due to the gaseous loading compared to the gaseous + water loading.

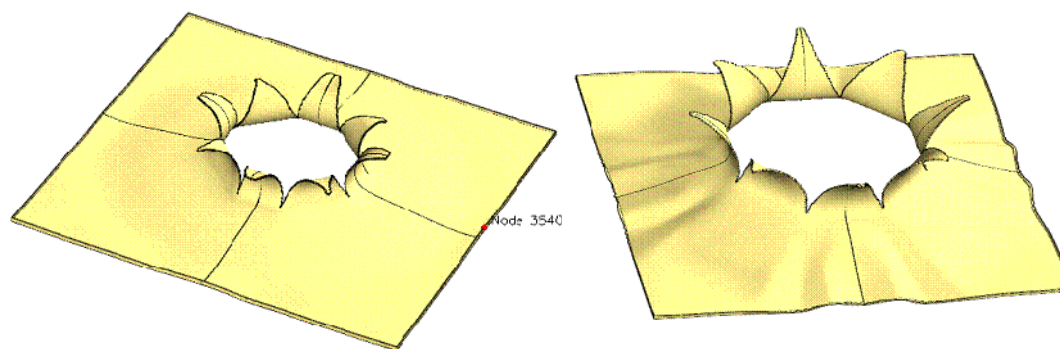


Figure 5 - Plots of hole size for impulse only and impulse + water loading

The results demonstrate that using a simple momentum deposition loading method based on impulse coupled with advanced constitutive models can adequately reproduce the experimental results. This negates the requirement for a fully coupled Euler/Lagrange hydrocode. The trends presented here were observed in the simulations of the other trials results.

CONCLUSIONS

1. 2. A simulation methodology based on momentum dump of the load into the plate between GRIM and DYNA is the most robust loading technique in these scenarios.
2. The dynamic loading of the water is crucial and can account for 30% of the total impulse delivered to the plate.
3. The use of advanced constitutive and fracture models are essential for success using this method.
4. This investigation has highlighted the strength of an integrated modelling and experimental approach in studying the response of explosively loaded structures.

References

1. 'Shock Response of Ships to Underwater Explosions', Y Wu, J Lui, B Zhao
2. 'Dislocation Mechanics Based Constitutive relations for Material Dynamics Calculations', R Armstrong, F Zerilli, Jnl de Physique 49 C3-529,1988.
3. 'Constitutive Models for Annealed and Explosively Shocked Iron for Application to High Strain rates and Large Strains', B Goldthorpe, DYMAT Conference 1991.
4. 'A Wide ranging Constitutive Model for bcc Steels', A Butler, P Church, B Goldthorpe, Jnl de Physique C8-471, 1994.
5. 'A Path Dependent Model for Ductile Fracture', B Goldthorpe, Jnl de Physique 7,C3-705, Aug 97.

Assessing the impact energy absorbing properties of composite and sandwich materials

John Dear MA PhD CEng FIMechE CPhys FInstP

Reader in Mechanical Engineering, Imperial College London, Exhibition Road, London SW7 2AZ – U.K.

The air-born pressure wave from an explosion is often accompanied by flying debris of different masses and velocities. This is a particular problem when structures need to be lightweight and there is a requirement for the structure designed to incorporate features to absorb and disperse the impact energy of flying debris. In relation to this, my group have been studying the impact effects on lightweight composite and other materials. This for a range of different types of impact threat from High Velocity / Low Mass (HV/LM) projectiles (1 g to 175 g for velocities up to 250 m s⁻¹) through to Low Velocity / High Mass (LV/HM) projectiles (3 kg up to 7 m s⁻¹). Different types of material evaluated include composite and sandwich materials having honeycomb and skin material that are metallic, composite or a mixture of both. Also, investigated are the effects of different holding and support arrangements for these materials and the effect of the different frontal profiles of impactors.

INTRODUCTION

Increasingly, there is a need for improved and new materials for structures that can survive blast loading. Often pressure blasts generated within structures or external to structures can produce high velocity debris that much adds to the damage inflicted to the structures. This is particularly so for lightweight materials required for aerospace and other structures. Modelling of the impact damage to lightweight materials and their resistance to blast damage much requires a well planned experimental research programme. For example, this is to include obtaining through-thickness impact properties of materials including types and degrees of damage inflicted as well as post-impact retained strength. There are a number of quasi-static models for studying impact failure in lightweight materials [1-10] but fewer for studying debris impact and blast pressure wave effects. For these studies, this paper concentrates on impact damage loading, impact energy absorption and penetration resistance of Carbon-Fibre Reinforced Polymers (CFRP), Sheet Moulding Compounds (SMC), Glass Mat Thermoplastics (GMT) as well as sandwich material constructions and glass-fibre polyester pultruded beams. All of these materials are used for structures that can be subject to blast loading.

CARBON-FIBRE REINFORCED POLYMERS

Carbon-fibre panels have been impacted under different conditions using a gas gun and a drop-weight rig [11]. The material used was a CFRP with an intermediate strength fibre and a high toughness matrix with a symmetrical lay-up of equal numbers of 0, +45°, -45° and 90° plies. Two types of clamping geometry were used (figure 1). The specimens were prepared using a diamond-slitting wheel and c-scanned before and after impact giving amplitude and time-of-flight information using the pulse-echo technique. One impact condition explored with the gas gun was a 1 g steel ball bearing impactor (diameter 6 mm). A plastic sabot was cleanly separated from the ball bearing prior to impact and was used for velocities up to 250 m s⁻¹ giving a High Velocity / Low Mass (HV/LM) impact. For the Low Velocity / High Mass

(LV/HM) impacts, a drop-weight rig was used. This used a 3 kg mass and a 6.35 mm (or 12.7 mm) steel hemispherical nose. The maximum drop height used was 2.5 m corresponding to a velocity of 7 m s^{-1} . Between these two extreme HV/LM and LV/HM impact conditions, a number of other impact conditions were explored. This is using the gas gun with different projectile masses from 17 g to 175 g, each having the same 6.35 mm hemispherical nose on cylindrical steel rods of different length mounted in a plastic sabot [11].

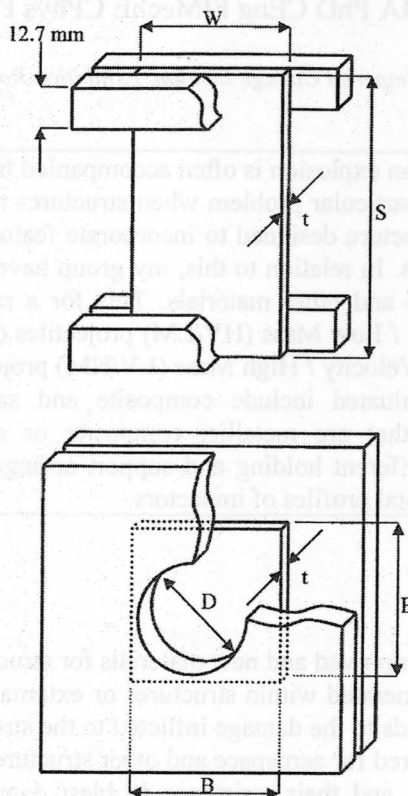


Figure 1 : Clamping arrangements.

The following were dimensions and clamping conditions:

- 126 specimens with impacts using 6.35 mm (and 12.7 mm) diameter hemispherical-nosed impactors with masses of 1, 17, 27, 37, 54, 63, 86, 122, 175 g and 3 kg.
- Panel thickness (t): 2 mm to 6 mm.
- Panel area dimensions ($W \times S$ or $B \times B$): 80 x 100, 80 x 150, 80 x 200, 50 x 200 mm, 70 x 70, 120 x 120.
- Holding conditions: rectangular specimens - rigidly secured along 80 and 50 mm sides; circular specimens - 50 and 100 mm internal diameter (D).
- Impact energy: different energies used for each configuration from 6 to 100 J.
- Impact velocities: LV: 1 to 7 m s^{-1} & HV: ca. 20 to 250 m s^{-1} .
- Measured quantities: impact velocity, rebound or perforation velocity if relevant, duration of the contact event, specimen central deflection with time, damage by visual inspection and c-scan.

Residual strength of the test panels, was measured with Compression After Impact (CAI) based on the Boeing Airbus AITM standard [11]. In general, under HV/LM conditions, for a given thickness of specimen and impact energy, the same impact damage was inflicted irrespective of specimen size or clamping arrangements. This applied providing the inflicted damage did not reach the clamps or boundary of the specimen. Under LV/HM conditions, the inflicted damage varied greatly for different specimen sizes and clamping conditions as well as for each thickness

of the specimen and impact energy. The specimens subjected to these impacting conditions showed a larger scale deformation response. Other researchers have made similar observations [6, 10]. Some sample sets of c-scan results are shown in figures 2 to 7. Figures 2 to 4 show c-scan for 2 and 6 mm thick specimens for different impact energies under LV/HM conditions. Figures 5 to 7 show c-scan for 2 and 6 mm thick specimens for different impact energies under the HV/LM condition. Under LV/HM conditions, the global compliance of the specimens had a dominant role to play in deciding the response to impact. The full set of c-scans, shown in figures 2 and 3, clearly demonstrate this point. The relationship between c-scan damage and impact energy varies with specimen span for the LV/HM condition. The 6 mm thick 200 mm span specimens show no delamination at all with only a small top surface dent for the higher impact energies. The 6 mm thick 100 mm span specimens by contrast show large areas of delamination. Delamination patterns initiated by the two different mechanisms of flexure and through thickness shock are different as shown (figure 4).

Single Specimen Impact energy

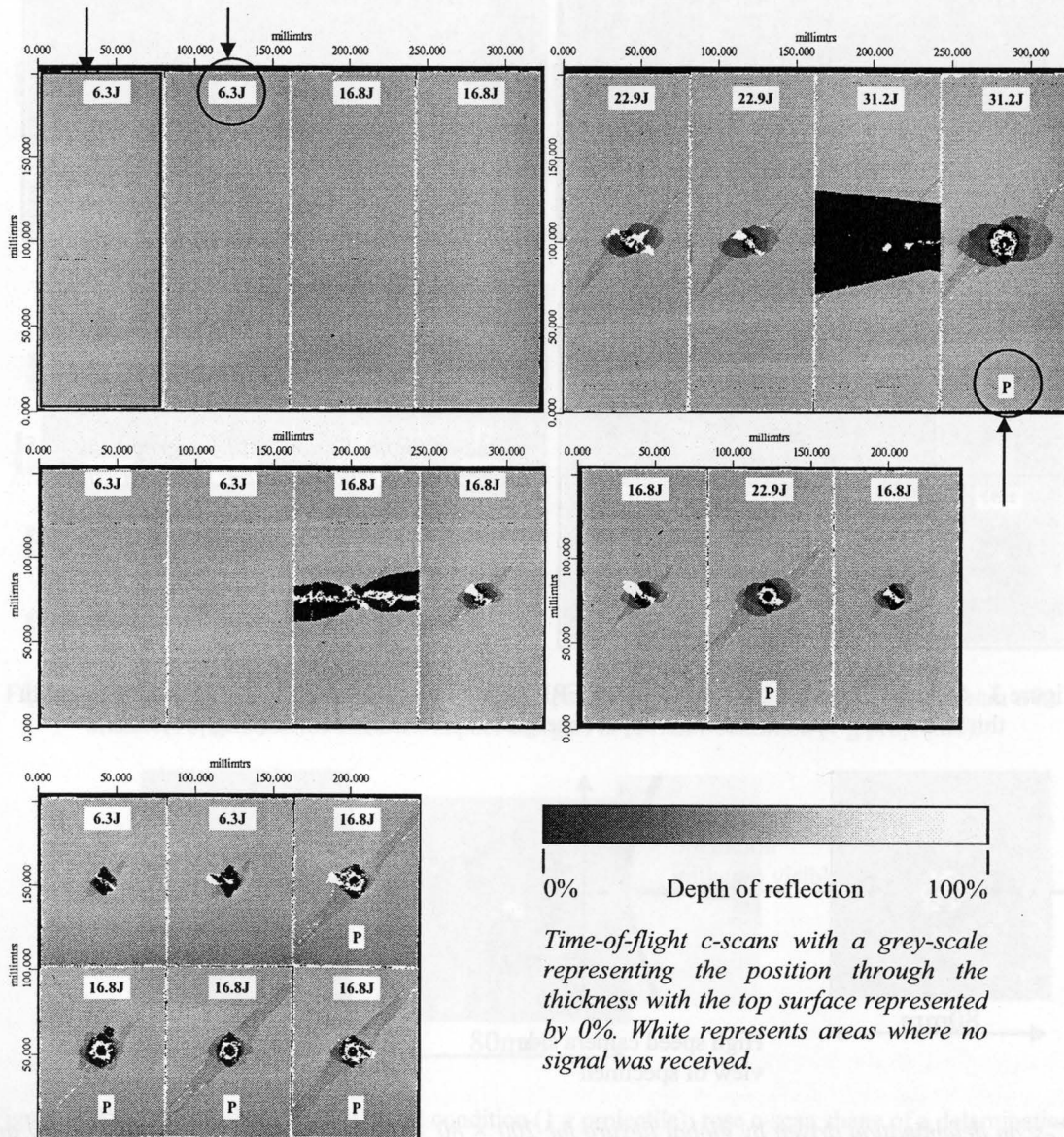


Figure 2 : C-scan showing impact damage on CFRP panels 80 x 200, 80 x 150 and 80 x 100 mm with thickness 2 mm and for different impact energies in LV/HM condition (3 kg projectile).

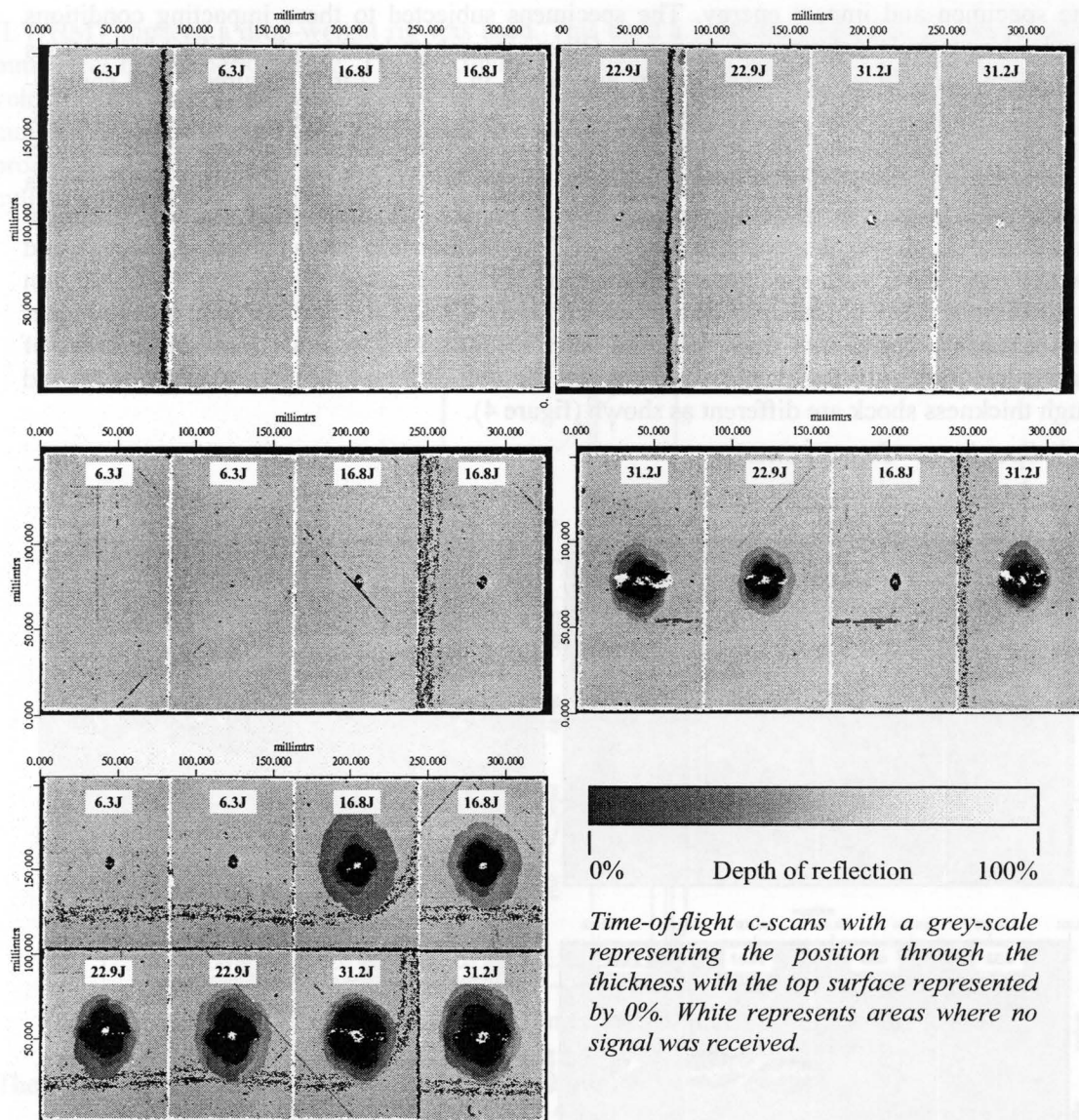
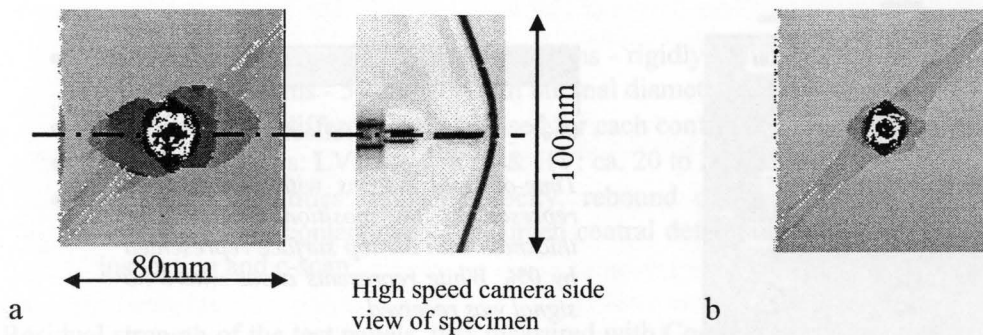


Figure 3 : C-scan showing impact damage on CFRP panels 80 x 200, 80 x 150 and 80 x 100 mm with thickness 6 mm and for different impact energies in LV/HM condition (3 kg projectile).



- a: C-scan delamination driven by global flexure for $200 \times 80 \times 2$ mm specimen at 4.56 m s^{-1} giving an impact energy of 31.2 J.
- b: C-scan delamination from a combination of shock induced delamination and rear-surface spallation for a $100 \times 80 \times 2$ mm specimen at 3.35 m s^{-1} giving an impact energy of 16.8 J.

Figure 4 : Damage mechanisms in LV/HM condition for 2mm thick specimens (3 kg projectile).

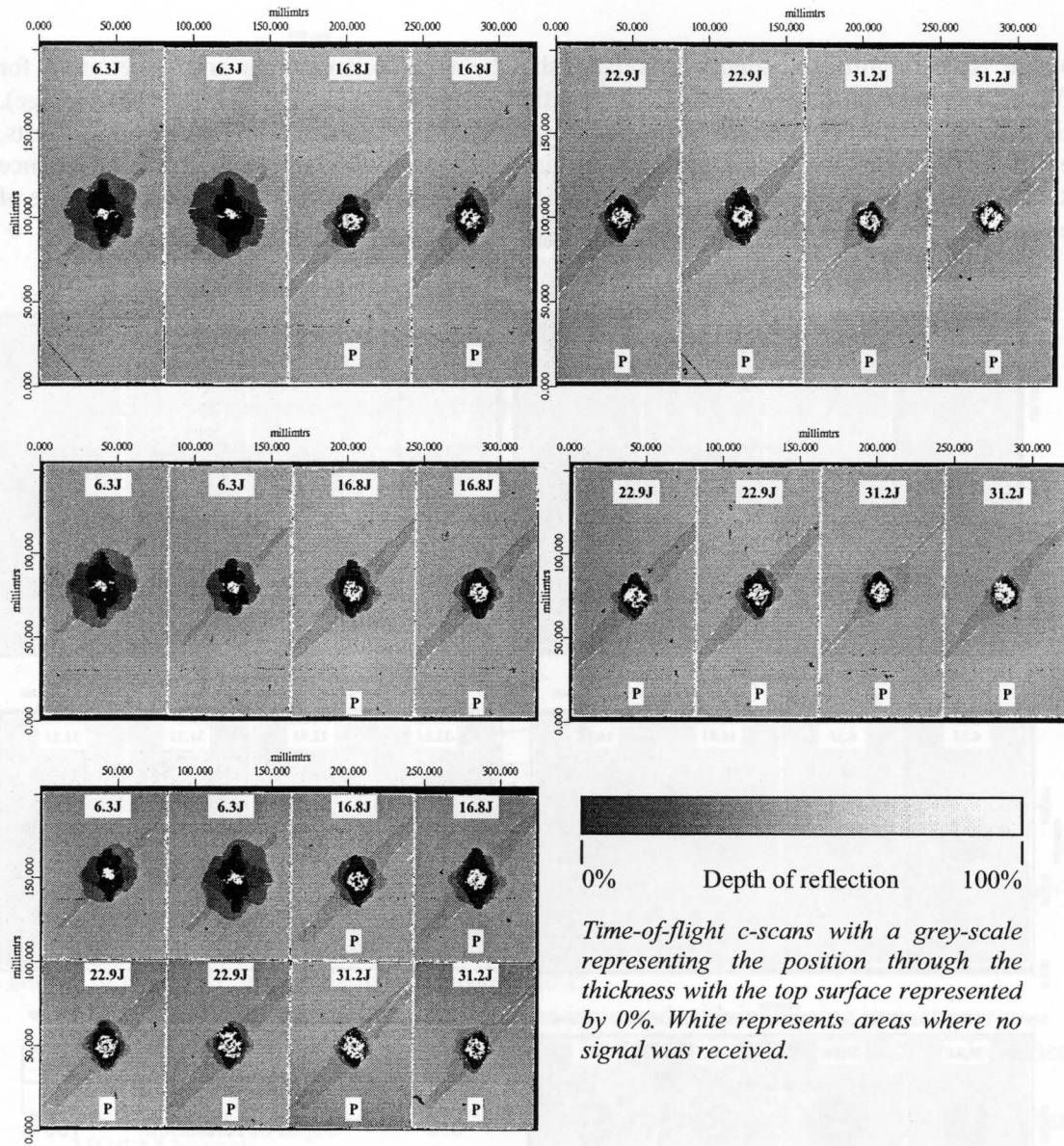


Figure 5 : C-scan showing impact damage on CFRP panels 80 x 200, 80 x 150 and 80 x 100 mm with thickness 2 mm and for different impact energies in HV/LM condition (1 g projectile).

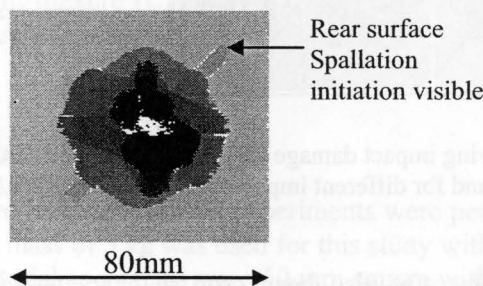


Figure 6 : Damage mechanism in HV/LM condition (1 g projectile): rose c-scan shape of a delamination driven by through thickness shock induced stress waves for a 200 x 80 x 2 mm specimen at 112 m s⁻¹ giving an impact energy of 6.3 J.

Notable is the significant change in relationship between delamination and penetration for different specimen thickness (specimen penetration by impactor labelled as P on c-scan image). This is for all impact conditions. For a given specimen thickness for the HV/LM impact tests, the full set of c-scan images for one span are similar to those of other spans and the difference between images for a given thickness is as to the extent of the damage (figures 5 & 7). Some of the characteristic features of the HV/LM condition are shown in figure 6.

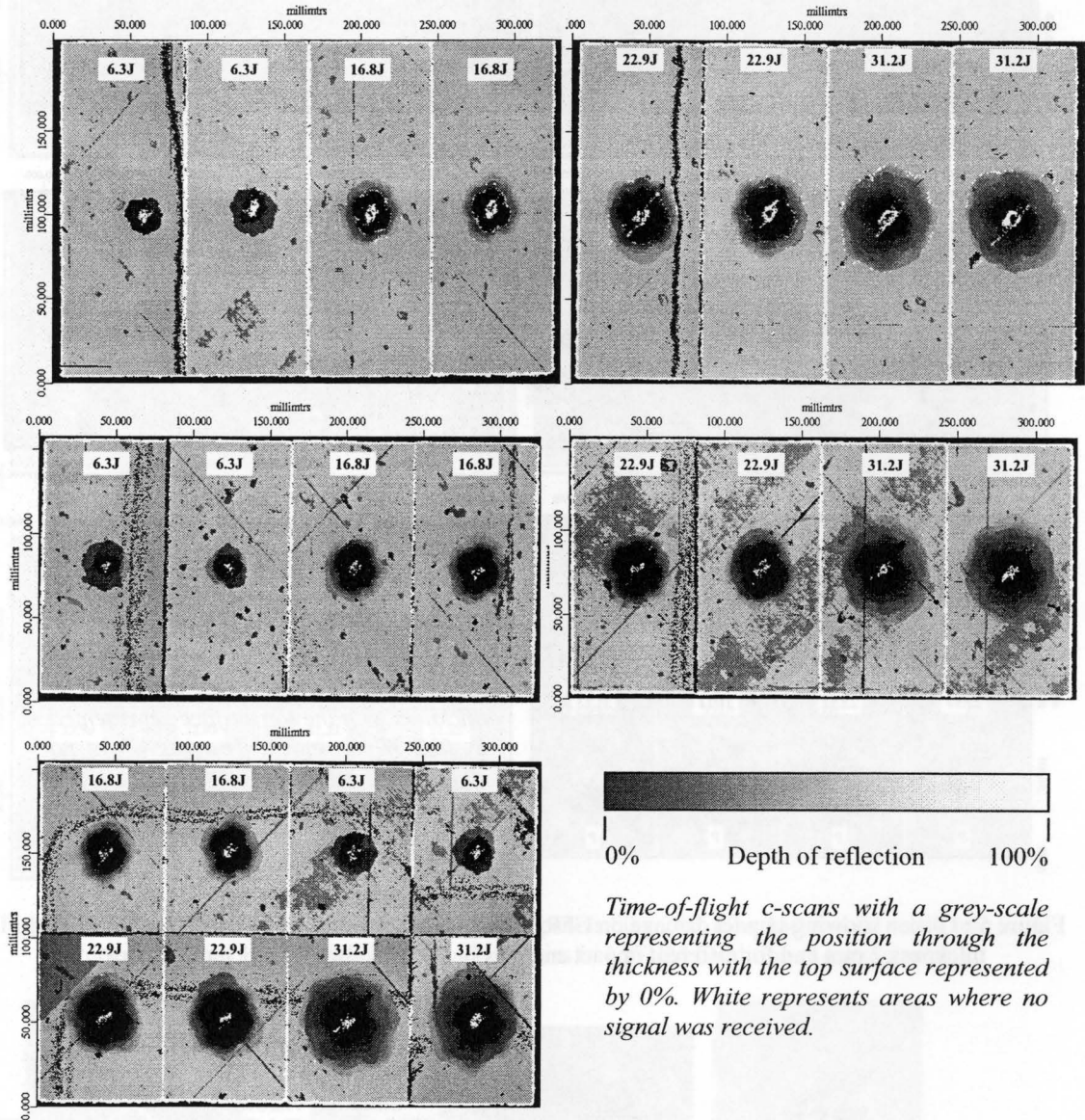


Figure 7 : C-scan showing impact damage on CFRP panels 80 x 200, 80 x 150 and 80 x 100 mm with thickness 6 mm and for different impact energies in the HV/LM condition (1 g projectile).

High-speed photography was also been used to characterise the impact events. A LV/HM impact with large-scale deformation for a 2 mm thick specimen is shown in Figure 8. Very little large-scale deformation was observed for HV/LM impacts. Compression after impact data is shown in figure 9. HV/LM impacts are more damaging than LV/HM impacts in terms of compressive residual strength at low impact energies (below 25 J).

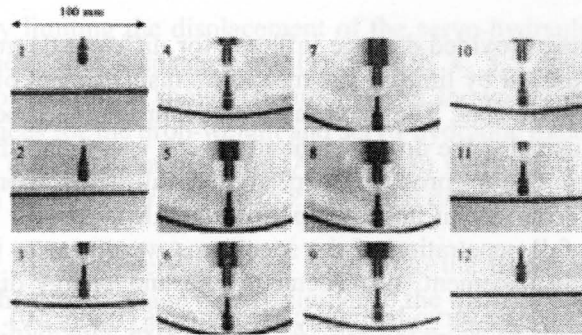


Figure 8 : HSC images of a LV/HM impact showing side view and central section of 80 x 200 x 2 mm specimen for impact energy of 22.9 J with inter-frame time of 2.5 ms (3 kg projectile).

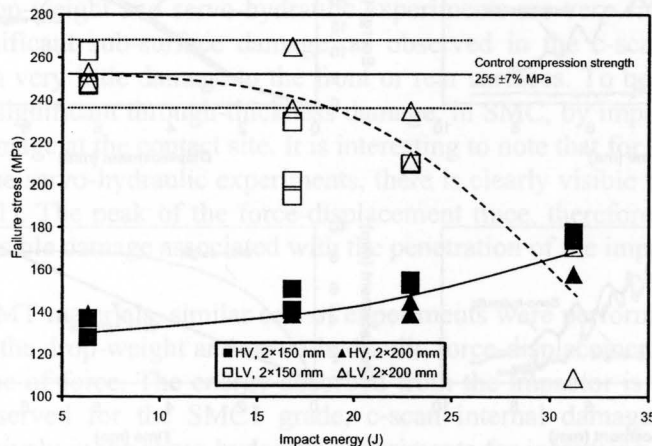


Figure 9 : Compression After Impact failure stress versus impact energy for two spans (150 and 200 mm) for HV/LM (1 g projectile) and LV/HM (3 kg projectile).

A survey of the CFRP impact damage is given below:

- For LV/HM impacts, the delamination area increased with increasing impact energy.
- For HV/LM impacts, the delamination area increased up to perforation then decreased after perforation for increasing impact energy.
- For the same impact energy, LV/HM impacts produced less delamination area than HV/LM impacts.
- For HV/LM impacts, the delamination area was less affected by specimen span.
- For HV/LM impacts, a factor is that for the thicker specimens, with many more plies, then the conical region of delamination is able to absorb more impact energy.
- Delamination dominated by flexure (LV/HM) showed a very different pattern to that dominated by through-thickness stress waves (HV/LM).

SMC AND GMT MATERIALS

Both drop-weight impact and servo-hydraulic impact experiments were performed on SMC and GMT materials [12]. An impactor mass of 5 kg was used for this study with a drop height of 1.0 m (4.4 m s^{-1}). SMC and GMT material specimens were 60 mm square with support diameter of 40 mm (figure 1(b)). Two grades of SMC were investigated: SMC1 with 62wt% E-glass, 30wt% Polyester and 8wt% CaCO_3 and other additives; SMC2 with 30wt% E-glass, 16wt% Polyester and 54wt% CaCO_3 and other additives. These were compared with GMT with 30wt% E-glass and 70wt% Polypropylene.

The servo-hydraulic machine provided damage inflicted for different degrees of penetration of the specimen. This was achieved by limiting the maximum displacement of the servo-hydraulic machine in a series of experiments. The servo-hydraulic impact machine was fitted with an impactor identical to that used for the drop-weight studies. It was found that a servo-hydraulic constant velocity impact of 1 m s^{-1} produced very similar full penetration force-displacement data as obtained with the drop-weight impact experiments. Also, the size and shape of the in-plane damage zones after full penetration of the specimens were near to identical. For SMC1 material, load-time, load-displacement, displacement-time and energy-displacement data are shown for the drop-weight and the servo-hydraulic experiments (figure 10).

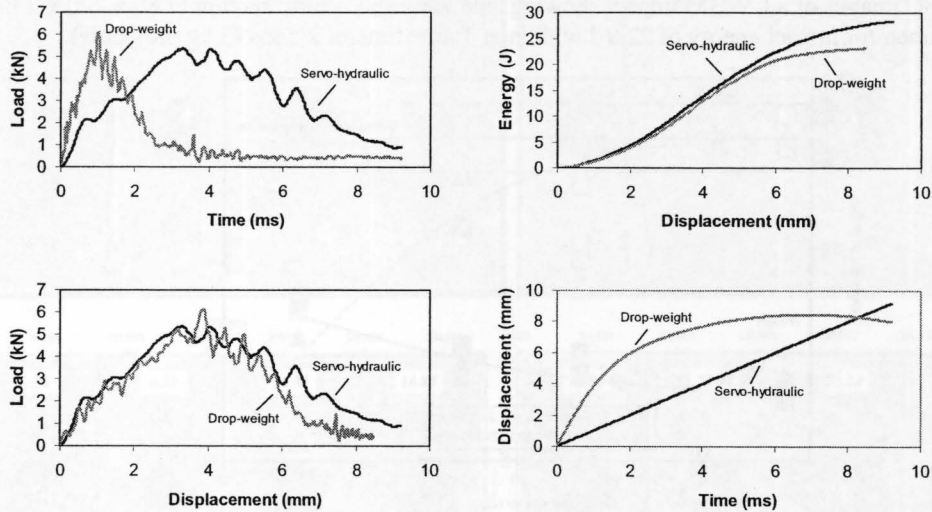


Figure 10 : Comparison of 5 kg drop-weight (4.4 m s^{-1}) and servo-hydraulic (1 m s^{-1}) results for SMC1.

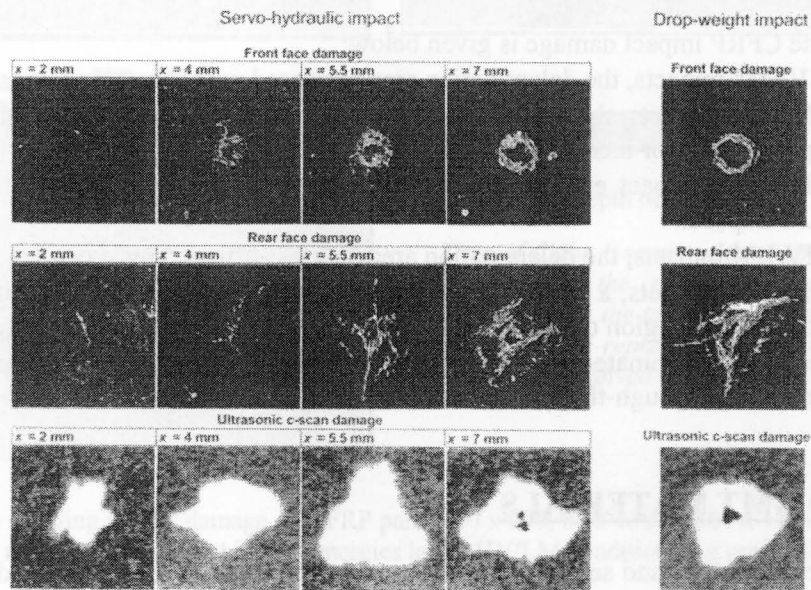


Figure 11 : Damage for 5 kg drop-weight (4.4 m s^{-1}) and servo-hydraulic (1 m s^{-1}) results for SMC1.

Figure 11 compares, for SMC, front face damage and rear face damage with the associated ultrasonic c-scan image for the drop-weight experiments (*on the right*) with the development of damage obtained in the servo-hydraulic experiments (*on the left*). The ultrasonic c-scan image shows the in-plane extension of delaminations, matrix cracks and fibre fracture as a whitened region. The servo-hydraulic experiments were performed for different degrees of deformation of

the SMC specimen by limiting the displacement of the servo-hydraulic machine in a series of four experiments. These four displacements (x) were 2, 4, 5.5 and 7 mm and the damage observed at each displacement is shown (figure 11). As shown by figure 10, the peak of the force-displacement traces for the drop-weight and servo-hydraulic experiments are both close to 6 kN for an impactor displacement of 4 mm. Also, for an impactor displacement of 8 mm, the energy absorbed from the impactor is close to 25 J (initial drop-weight kinetic energy is 50 J).

Figure 11 shows that the drop-weight impact damage to the front face and rear face and the damage revealed by the c-scan image is very similar to the damage obtained for a displacement of 7 mm in the servo-hydraulic experiments. As the force-displacement traces for drop-weight and servo-hydraulic experiments (figure 10) are nearly identical and the final penetration damage is virtually the same for SMC, it is reasonable to assume that the development of damage in the drop-weight and servo-hydraulic experiments are very similar. Figure 11 shows that there is significant sub-surface damage, as observed in the c-scan image, for a 2 mm displacement with very little damage to the front or rear surfaces. To be expected, therefore, is that there can be significant through-thickness damage, in SMC, by impacts albeit there is little visible surface damage at the contact site. It is interesting to note that for displacements of 4 mm (and greater) in the servo-hydraulic experiments, there is clearly visible front face and rear face damage (figure 11). The peak of the force-displacement trace, therefore, corresponds with the onset of clearly visible damage associated with the penetration of the impactor.

For SMC2 and GMT materials, similar sets of experiments were performed. For the SMC2 and GMT specimens, the drop-weight and servo-hydraulic force-displacement traces are flatter with a lower peak value of force. The energy absorbed from the impactor is also less for these two materials. As observed for the SMC1 grade, c-scan internal damage in SMC2 and GMT increases progressively in the servo-hydraulic experiments for increasing displacements (x) with visual damage most notable for displacements greater than the peak load condition. SMC2 shows the largest extent of c-scan internal damage due to the high filler content in this material. For all materials, there is significant through-thickness damage before there is notable front or rear surface damage.

There is a good correlation between the peak load (F_{peak}), the displacement at peak load (x_{peak}), total energy absorbed (E_{Total}) and the in-plane modulus (E_{11}) for SMC and GMT materials (figure 12). The in-plane tensile modulus (E_{11}) and Poisson's ratio (ν_{12}) for a uniaxial tensile test on the three materials were obtained at a displacement rate of 2 mm/min [12]. The SMC1 material has the highest fibre weight fraction twice that of the GMT material and hence the highest stiffness of the three specimens.

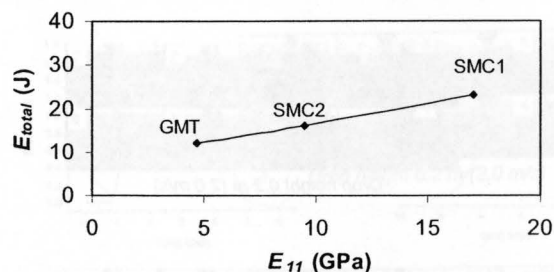


Figure 12 : Total energy absorption by SMC1, SMC2 and GMT for 5 kg drop-weight (4.4 m s^{-1}).

It has been shown for SMC and GMT materials that the in-plane modulus (E_{11}) is dominant in determining the penetration resistance of these three materials. SMC1, with its higher glass fibre weight fraction and highest in-plane modulus, absorbs most impact energy in the drop-weight experiments.

SANDWICH STRUCTURES

A drop-weight impactor mass of 1.55 kg was used for this study with drop heights of 0.2 to 1.0 m (up to 4.4 m s^{-1}) [13]. Honeycomb sandwich material specimens were 150 mm square with a support diameter of 100 mm (figure 1(b)). The sandwich panels researched were:

- Fibrelam: *Unidirectional cross-plyed fiberglass skins (S-glass) bonded to aramid (Kevlar/Phenolic) medium density core* (thickness 10 mm).
- Hexlite H620: *Woven glass fibre impregnated with epoxy resin and a lightweight aluminum honeycomb core* (thickness 14 mm).
- Hexlite H640: *Woven glass fibre impregnated with epoxy resin and a lightweight aluminum honeycomb core* (thickness 6 mm).
- Hexlite H220: *Aluminium alloy sheet bonded to lightweight aluminium honeycomb using epoxy film adhesive* (thickness 14 mm).

Figure 13 presents data on Fibrelam specimens for drop heights of 0.2, 0.6 and 1.0 m. The undamaged Fibrelam material absorbed and returned a substantial proportion of the impact energy to the striker. Figure 14 shows the behaviour for a 0.2 & 1.0 m drops with the force-time traces annotated with frame numbers from the high-speed sequences. Figure 15 shows the damage where cracking along the cross-ply directions on the front skin is visible in the Fibrelam panels at a 1.0 m drop.

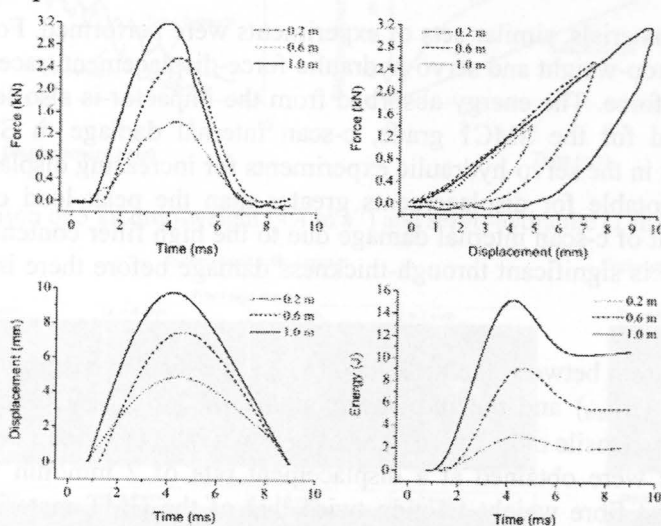


Figure 13 : Fibrelam force-displacement-energy-time data for 0.2, 0.6 and 1.0 m drops.

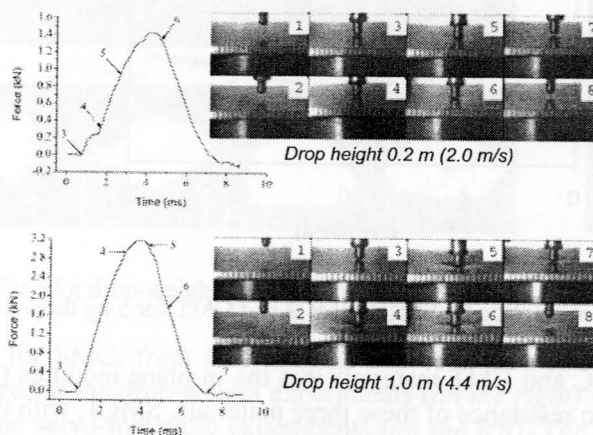


Figure 14 : Fibrelam force-time traces related to HSC sequences for 0.2 and 1.0 m drops.

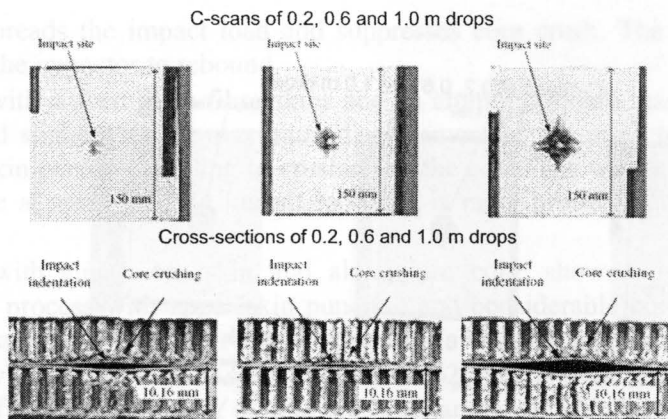


Figure 15 : Fibrelam c-scan and cross-sectional damage for 0.2, 0.6 and 1.0 m drops.

Figure 16 presents data for 0.2, 0.6 and 1.0 m drops on H220 that is an adhesively bonded aluminium honeycomb construction with aluminium skins. H220 is very effective as an energy absorbing material. Figure 17 shows the behaviour for a 0.2 & 1.0 m drop with the force-time traces annotated with frame numbers from the high-speed sequences and figure 18 shows the damage for drop heights of 0.2, 0.6 and 1.0 m with very localized penetration damage.

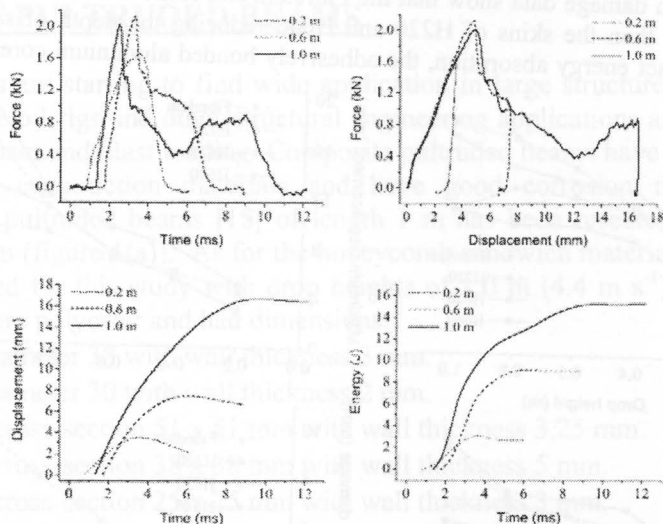


Figure 16 : H220 force-displacement-energy-time data for 0.2, 0.6 and 1.0 m drops.

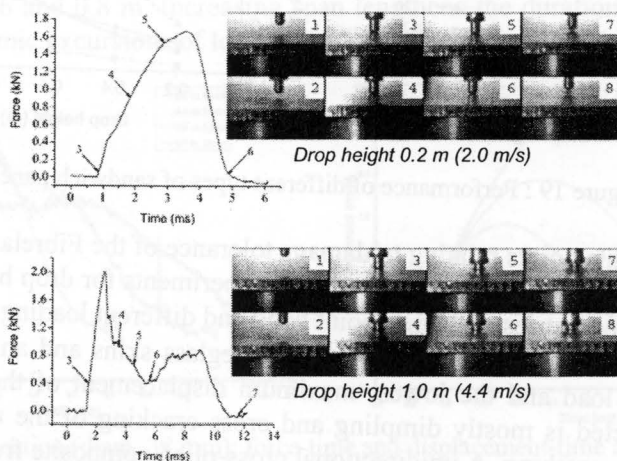


Figure 17 : H220 force-time traces related to HSC sequences for 0.2 and 1.0 m drops.

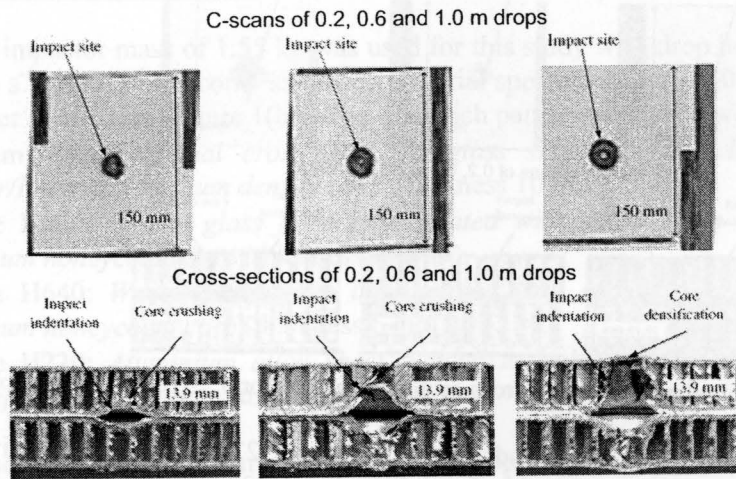


Figure 18 : H220-scan and cross-sectional damage for 0.2, 0.6 and 1.0 m drops.

Figure 19 shows that Fibrelam has the highest peak load and this is for the lowest maximum displacement of the impactor. The c-scan damage data show that the Fibrelam and H620 front skins spread the impact deformation process more than the skins of H220 and H640 reducing the depth of sectional damage. However, in terms of impact energy absorption, the adhesively bonded aluminium core and skin is very effective.

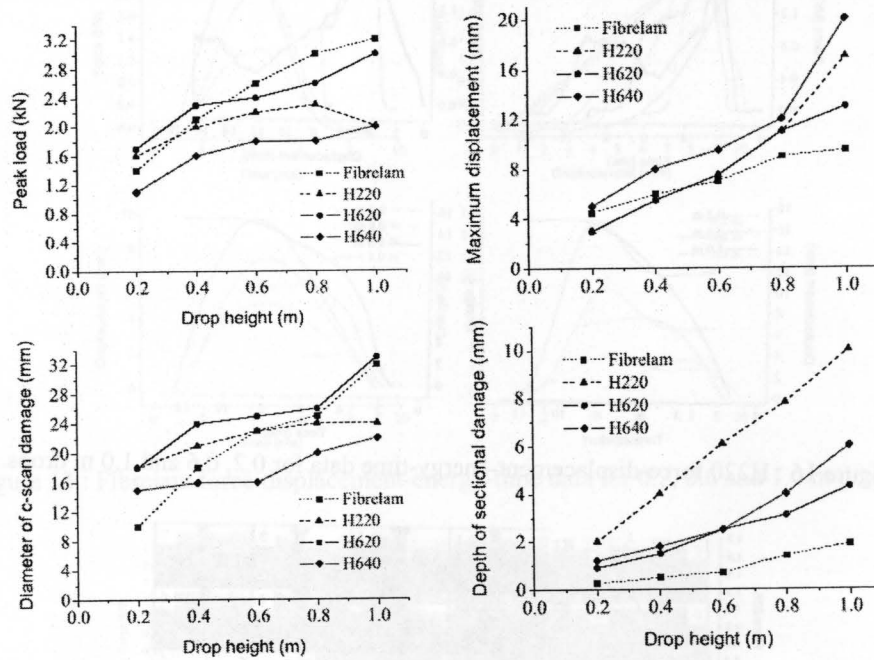


Figure 19 : Performance of different types of sandwich panel.

The following highlights points relating to damage tolerance of the Fibrelam and Hexlite (H620, H220 and H640) materials for 1.55 kg drop-weight experiments for drop heights from 0.2 to 1.0 m (for other support geometries e.g. three-point bend and different loading rates see [13]):

- Fibrelam, with unidirectional cross-plyed fibreglass skins and an aramid core, has the highest peak load and the lowest maximum displacement of the impactor. Also, the damage inflicted is mostly dimpling and cross cracking of the upper skin with some localised core crushing. A unidirectional cross-plyed composite front skin to a sandwich

panel spreads the impact load and suppresses core crush. The elasticity of the panel caused the impactor to rebound.

- H620, with woven glass fibre skins and an aluminium core, has a slightly lower peak load and slightly higher maximum displacement of the impactor and puncture of the upper skin occurred leading to crushing of the core. The woven glass fibre skin is less effective at spreading the impact load and is more prone to puncture leading to core crush.
- H220, with aluminium skin and aluminium core, showed a much more localised damage process with upper skin puncture and considerable core crush. However, this panel was effective at absorbing the impactor's kinetic energy with little rebound.
- H640, which was a similar construction as H620, but is of reduced thickness exhibited a failure, for a drop of 1.0 m, of both the upper and lower skin leading to two peaks on the force-time and force-displacement trace. The thinner panel exhibited greater overall deformation leading to cross cracking in the directions of weave. H640 was the only sandwich panel to be completely penetrated for a drop height of 1.0 m.

In addition to the round-nosed impactors described above, similar research has been performed to evaluate the impact of truncated cone impactors [14].

IMPACT OF PULTRUDED BEAMS

Pultruded beams are starting to find wide application in large structures e.g. processing plant, bridges, offshore oil-rigs and other structural engineering applications and such structures need to withstand impact and blast loading. Composite pultruded beams have the advantage that they are lightweight construction materials and have good corrosion resistance. The impact performance of pultruded beams [15] of length 1 m has been researched with support spans from 0.2 to 0.8 m (figure 1(a)). As for the honeycomb sandwich materials, an impactor mass of 1.55 kg was used for this study with drop heights of 1.0 m (4.4 m s^{-1}). The pultruded beams were E-Glass fibre polyester and had dimensions:

- Outer diameter 38 with wall thickness 3 mm.
- Outer diameter 30 with wall thickness 2 mm.
- Square cross-section 51 x 51 mm with wall thickness 3.25 mm.
- Square cross-section 38 x 38 mm with wall thickness 5 mm.
- Square cross-section 25 x 25 mm with wall thickness 3 mm.

Figures 20 present drop-weight impact data on a circular cross-section (diameter 38 mm) for spans of 0.2, 0.4, 0.6 and 0.8 m. Increasing span lengthens the duration of impact event. Also, there are more dynamic excursions of load as the longer beam is excited into oscillation.

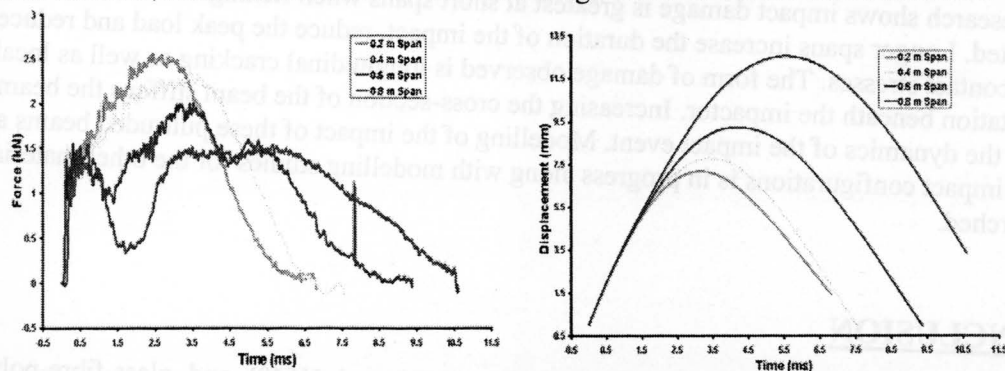


Figure 20 : Circular-section (diam. 38 mm): force-time and displacement-time impact data for spans 0.2, 0.4, 0.6 and 0.8 m.

Figure 21 shows high-speed photographic sequences for a circular-section beam of diameter 38 mm with a 0.4 m span. The upper sequence shows the flexing of the full length of supported beam during the impact and the lower sequence shows the beam local to the impact site with the indentation of the impactor visible. Figure 22 shows the variation of damage for different spans for this cross-section.

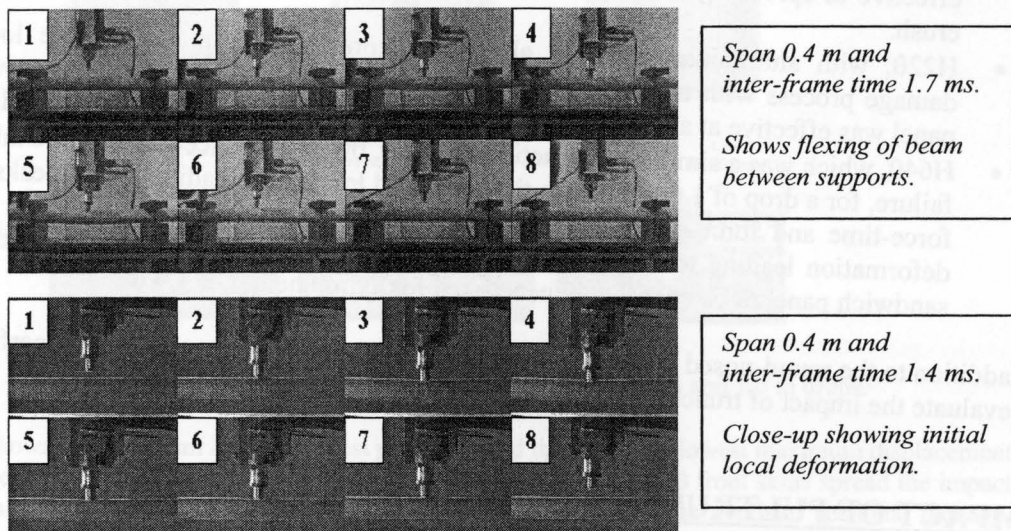


Figure 21 : Circular-section (diameter 38 mm): high-speed photographic sequences.

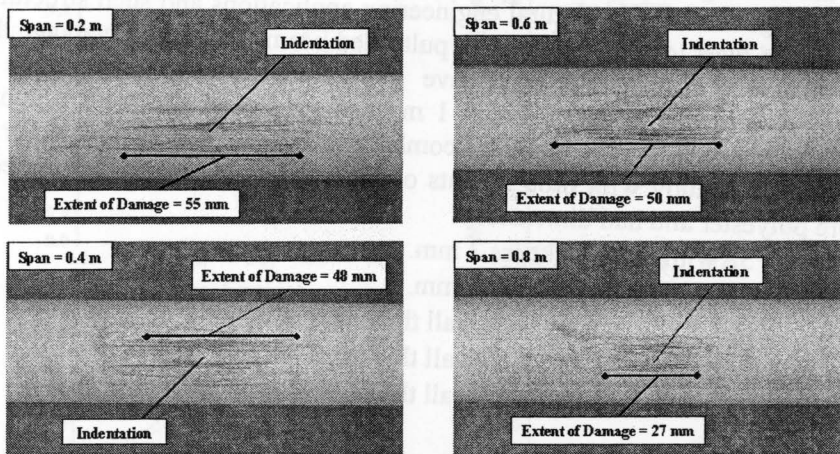


Figure 22 : Circular-section (diameter 38 mm): damage for support span 0.2, 0.4, 0.6 and 0.8 m.

The research shows impact damage is greatest at short spans when flexing of the beam is inhibited. Longer spans increase the duration of the impact, reduce the peak load and reduce local contact stresses. The form of damage observed is longitudinal cracking as well as local indentation beneath the impactor. Increasing the cross-section of the beam stiffens the beam and alters the dynamics of the impact event. Modelling of the impact of these pultruded beams and other impact configurations is in progress along with modelling studies for the other materials researched.

CONCLUSION

CFRP, SMC, GMT, Fibrelam, Hexlite (H220, H620 and H640) and glass-fibre-polyester pultruded beams have been studied in the dimensions that they are frequently used in large engineering structures. There is an increase in the wider use of these lightweight composite

materials and there is now considerable interest in the ability of these materials to survive impact and blast damage. In many structures, both sheet composites and sandwich honeycomb materials are used in the same products and in some cases aluminium skins and honeycomb core are used. Often the susceptibility to damage of these materials is an important factor. The interest in this study, therefore, was the generation of impact and blast related damage in these materials from the onset of damage to catastrophic failure.

References

1. Abrate S., "Impact on laminated composite materials", *Appl Mech Rev* 1991;44(4):155-90.
2. Abrate S., "Impact on laminated composites: recent advances", *ASME, Appl Mech Rev* 1994;47(11):517-44.
3. Davies G.A.O., Robinson P., Robson J., Eady D., "Shear driven delamination propagation in two dimensions", *Compos: Part A* 1997; 28(1):757-65.
4. Davies G.A.O., Zhang X., "Impact damage prediction in carbon composite structures", *Int J Impact Eng* 1995;16(1):149-170.
5. Olsson R., "Analytical prediction of large mass impact damage in composite laminates", *Compos: Part A* 2001;32(9):1207-1215.
6. Robinson P., Davies G.A.O., "Impactor mass and specimen geometry effects in low velocity impact of laminated composites", *Int J Impact Eng* 1992;12(2):189-207.
7. Gong S.W., Lam K.Y., "Transient response of stiffened composite plates subjected to low velocity impact", *Compos: Part B* 1999;30(5):473-484.
8. Mines R.A.W., Worrall C.M., Gibson A.G., "Low velocity performance behaviour of polymer composite sandwich panels", *Int J Impact Eng* 1998;21(10):855-879.
9. Abrate S., "Localized impact on sandwich structures with laminated facings", *Appl Mech Rev* 1997;50(1):69-82.
10. Olsson R., "Engineering method for prediction of impact response and damage in sandwich panels", *J Sandwich Struct & Mat* 2002;4:3-28.
11. Bland P.W., "Impact response and performance of carbon-fibre reinforced polymers", PhD Thesis, Imperial College of Science, Technology and Medicine, University of London, 2000.
12. Brown S.A., "Low velocity impact resistance of reinforced polymeric materials", PhD Thesis, Imperial College of Science, Technology and Medicine, University of London, 1999.
13. Lee H., "Drop-weight and ballistic impact of honeycomb composite sandwich structures", PhD Thesis, Imperial College London, University of London, 2004.
14. Maruszewska W., "Failure processes in composite sandwich structures for automotive and similar applications", PhD Thesis, Imperial College London, University of London, 2005.
15. Oh S-T., "Impact response and damage to pultruded composite beams", PhD Thesis, Imperial College London, University of London, 2005.

MAPPING OF AIR OVERPRESSURE AROUND SURROGATE AP BLAST MINES

Dr. Liu has a member of the NATO Task Group 024 "Test Methodology for Personal Protection
Equipment Against Anti-Personnel Mine Blast" (Human Factors & Medicine 029 Part 011)

Analysis of fragment generation from structures under extreme blast loads using Euler-Lagrange coupling techniques

Greg Fairlie¹, Jon Glanville¹, Xiangyang Quan²,

*1. Century Dynamics Limited, Dynamics House, Hurst Road, Horsham,
West Sussex, RH12 2DT, ENGLAND*

2 Century Dynamics, Inc., 1001 Galaxy Way, Suite 325, Concord, CA 94520, USA

This paper describes the capabilities available in the AUTODYN software for coupled analyses of structures under extreme blast loads. AUTODYN is an explicit analysis tool for modelling non-linear dynamics of solids, fluids, gases and their interaction. These capabilities are illustrated through several examples including internal loading on masonry structures, external blast loading on vehicle glazing, combined blast and fragment loading from cased munitions and blast loading on a reinforced concrete wall.

INTRODUCTION

For structures under shock and impact loading, numerical simulation software has proven to be extremely useful. It provides a rapid and cost-effective way to evaluate new design ideas and has become an important tool for understanding and predicting response of real systems and scenarios. Many prestigious companies and institutions around use the AUTODYN^[1] software to evaluate the performance of defence and security systems. This numerical tool can supply quantitative and accurate details of stress, strain, and deformation fields in systems that would be very expensive or difficult to investigate experimentally.

AUTODYN COUPLED MULTI-SOLVER APPROACH

AUTODYN is an explicit analysis tool for modelling non-linear dynamics of solids, fluids, gases and their interaction. It is based on explicit finite difference, finite volume and finite element (FE) techniques that use both mesh-based and mesh-free numerical methods. The software is based on classical continuum mechanics, which are used to describe the dynamics of a continuous media with a set of differential equations established through the application of the principles of conservation of mass, momentum and energy from a macroscopic point of view. Over the last two decades, it has been developed to handle the non-linear behaviour of fluids and structures in an integrated fashion. It provides multiple solvers such as Lagrange, Euler and SPH. Each of these solvers has unique capabilities and limitations. In terms of accuracy and efficiency there is usually not a single solver appropriate to all the regimes of a problem. For example, numerical simulation of the dynamic response of a structure to an explosive detonation can best be described using an Euler approach for the detonation and blast while the structural response is generally best modelled using a Lagrangian method. AUTODYN allows a Coupled Multi-Solver approach with different solvers combined in a single simulation with spatial and temporal coupling. Recent development work has concentrated on the implementation of a new generation of Lagrange FE solvers allowing shorter run times, bigger models and better accessibility to third-party FE pre-processors and links to CAD systems.

Coupling between Lagrangian parts is called Lagrange/Lagrange interaction and is implemented in AUTODYN using automatic impact/slide surfaces. The Coupled Multi-Solver approach with Lagrange/Lagrange interaction was successfully employed to simulate the impact of a Boeing

passenger jet to the New York World Trade Centre North Tower and the progressive collapse of the North Tower^[2]. Recent work using a similar approach investigated the impact of an F-4 Phantom jetfighter into a reinforced concrete wall^[3] where good agreement of impact force and damage area was achieved between numerical predictions and experimental measurements.

The interaction between Euler and Lagrange parts is called Euler/Lagrange coupling and is often used to simulate fluid/structure interactions. The Lagrange grids overlap the Euler mesh and provide constraints to the flow of material in the Eulerian grid. At the Euler-Lagrange interface, the Lagrange grid acts as a geometric flow boundary to the Euler grid while the Euler grid provides a pressure boundary to the Lagrange grid. As the Lagrange grid moves or distorts, it covers or uncovers the fixed Euler cells. The coupled Euler/Lagrange technique allows complex gas-structure or fluid-structure interaction problems including large displacements, deformations and changes in the topology of the structure, to be solved in a single numerical simulation. Techniques for interacting with 3D shell parts are also available. An example of this type of simulation is described in reference [4]. Page 4 of this paper shows the response of a room within a farmhouse to an internal detonation and the subsequent response of the walls and break up of the floor.

An extensive range of material models is available in both AUTODYN-2D & 3D. The equations of state include the well known Linear, Polynomial, Shock, JWL, Slow-burn, and Ideal Gas as well as Orthotropic, Porous, Tillotson, PUFF and Sesame models. Strength models include Hydrodynamic, Elastic, Piecewise hardening, Brittle, Von Mises and Mohr-Coulomb models, the Johnson-Cook, Zerilli-Armstrong and Steinberg-Guinan models which include the effects of strain and strain rate hardening and thermal softening, the AMMHIS model for non-linear shock response of composites, the Johnson-Holmquist model for ceramics and glass and the RHT model for concrete. Multiple failure models are available, including bulk failure criteria such as hydro-tensile limit, bulk strain, directional failure based on principal stress and/or strain and material stress and/or strain, as well as special models such as cumulative damage and tensile crack softening. An extensive material model library combining thermodynamic and constitutive behaviour is available.

Special techniques are available to improve the accuracy and efficiency of a range of different types of simulation. If required, the user can switch between FE and Euler solvers (or vice versa) and continue the analysis. By using the remapping functionality one can start with a 1D-spherical or 2D analysis, map the results onto a 3D mesh, and continue with it in full 3D. This approach results in higher accuracy (i.e. a 1D or 2D mesh can be more refined) at a lower CPU cost. AUTODYN includes capabilities for greatly reducing the lead-time of large 3D calculations by distributed parallel processing^{[5] [6]}. All of the 3D FE and Euler solvers, Lagrange/Lagrange contact, Lagrange/SPH, Euler-Lagrange coupling algorithms are parallelised. Parallel processing is available on a range of operating systems including MS Windows XP, NT and 2000, Linux, and Unix workstations. A parallel calculation can use a mixture of shared memory and distributed memory systems allowing efficient usage of available processing power.

AUTODYN has been applied to a wide range of blast, fragmentation and structural response simulations. Techniques for the numerical simulation of cased munitions are described in reference [7] and [8]. Blast wave propagation and interaction with rigid urban type environments was investigated and compared with small-scale experimental results in reference [9]. These techniques have been further developed and applied to large scale geometries such as blast waves propagating in city centres in [10]. Initial investigations of fragment throws from small masonry cubicles are described in [11], with more sophisticated fully coupled simulations of the same structures described in [12]. Combined blast and fragment loading and subsequent response of structures under mine blast loading including comparison with experimental results is described in reference [13]. Some recent work on blast loading and subsequent collapse of reinforced concrete buildings is described in [14].

EXAMPLES

Internal detonations in small masonry explosive stores

There is an international interest in the consequences of high explosive detonations within brick and masonry structures. The quantity and velocity of fragments produced by such an explosion is of particular concern as they determine the building separation distance for the safe storage of a given quantity of explosives. Fragment mass and velocity distributions are usually determined experimentally by detonating high explosive charges within structures. These experiments are difficult to instrument, and experimental results are mainly limited to collecting data on post-test fragment locations. If numerical modelling can be demonstrated to be effective in predicting the fragmentation behaviour of different types of structures and materials, then significant savings in cost and time may be achieved by reducing the number of field experiments conducted. The UK Ministry of Defence, Explosive Storage and Transport Support Group sponsored the programme of work reported here, and provided the experimental results used for comparison.

A typical cubicle used during the experimental programme is shown in Figure 1, before and after the detonation of a charge. The cubicle is 3m square in plan, 2.4m high and sits on concrete foundations. A reinforced concrete roof was used in place of the frangible roof in some of the trials. Spherical Composition B charges of 10, 25 and 50kg were detonated 1m above the ground at the centre of the cubicle. Four different types of wall construction were investigated. Further details of the cubicle construction, and the test configurations are given in [15].

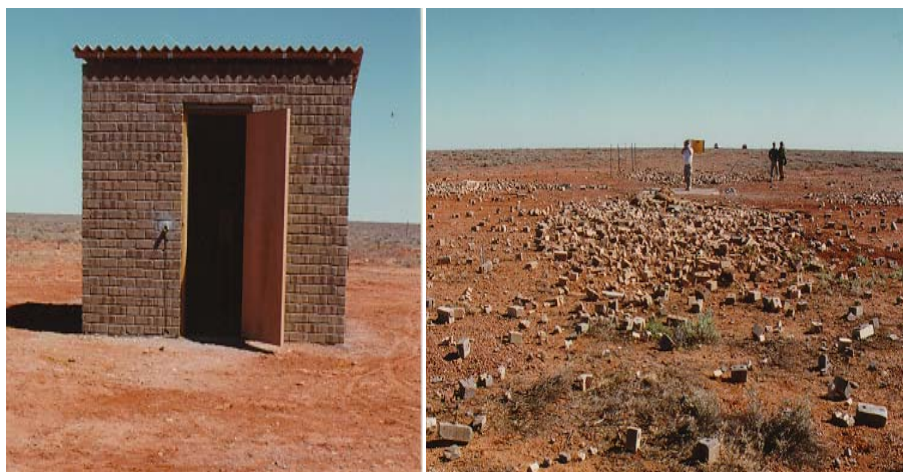


Figure 1 Brick Cubicle With Frangible Roof, Before and After Charge Detonation

This problem has been analysed in AUTODYN using two approaches:

In the first method the walls were assumed to remain rigid under the applied blast loads. For each brick the impulse was recorded and was used to calculate an initial brick velocity and the impact point of the bricks with the ground was calculated assuming simple motion under gravity. This first impact point with the ground was taken as a measure of the brick throw^[11].

A second more sophisticated set of simulations using a Lagrange representation of each brick and the roof, and full Euler/Lagrange coupling with the calculated blast loads is described in [12]. For efficiency the Euler grid was removed when the bricks had finished accelerating and they then dropped to ground level under gravity. Lagrange/Lagrange contact was specified between the bricks to allow them to interact and also between the ground surface and the bricks. Throw distances were calculated at a time of 4 seconds for the concrete roof cases and 2 seconds for the frangible roof cases. A plot of the masonry structure and the roof is shown in Figure 2 for the 50kg explosive, where half of the geometry is plotted. The velocities on

selected horizontal planes in the explosive gas flow field at the time of 0.22ms are also shown in this figure when the blast wave front has almost reached the ground.

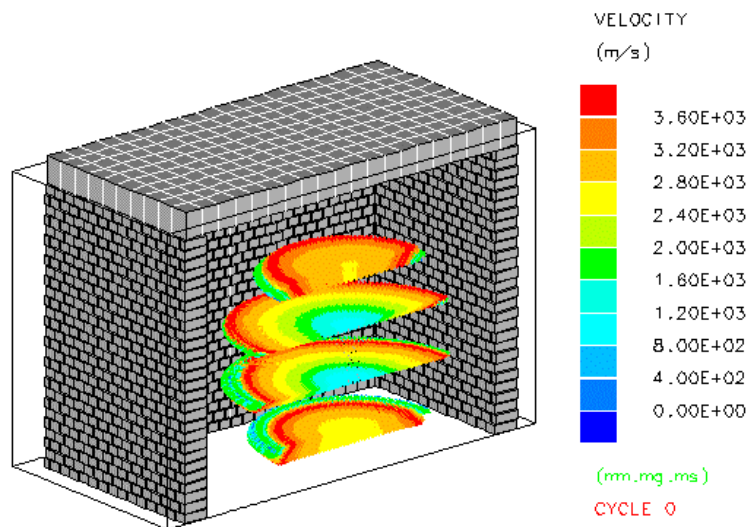


Figure 2 Brick Cubicle With Concrete Roof, and Initial Flow Velocities for 50kg Charge

An example set of fragment throw distance results for the 25kg charge with a concrete roof are shown in Figure 3. This plot shows the proportion of fragments for each case that lie within 20m wide distance bands from the initial cubicle location. The first three curves are experimental results for three different wall constructions. The light blue curve is from the earlier AUTODYN calculations referred to above and the red curve is from the coupled Euler/Lagrange simulation. The EBSD, DBCS and UK curves refer to tests with different wall constructions.

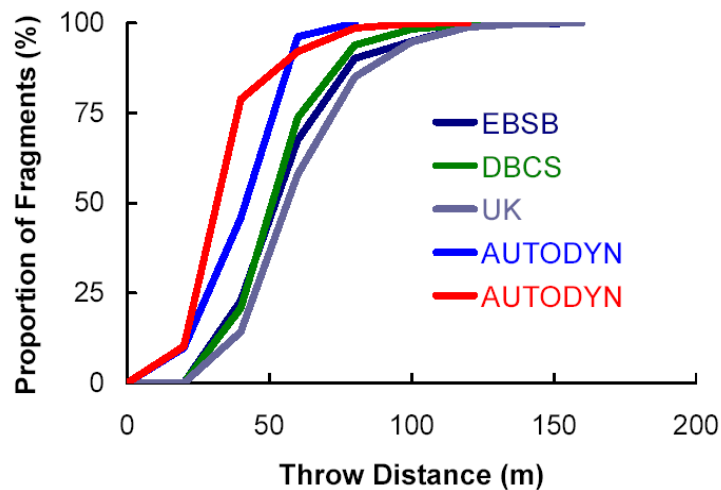


Figure 3 Test and Calculated Fragment Throw for Brick Cubicle

Blast effects on vehicle windows

It is estimated that most injuries from bomb blasts can be attributed to airborne sharp glass fragments. An example is the disastrous event in Kabul, Afghanistan, where a suicide car bomber rammed a bus carrying German peacekeepers, killing four soldiers and wounding 29 others. To reduce the hazards of flying glass shards, the German Defence Ministry tasked WTD 52 in Germany with the investigation of safety measures for bus windows. WTD 52 used both full-scale bus experiments and AUTODYN simulations^{[16] [17]}. The blast experiments on the full-scale bus were conducted in the Large Blast Simulator at WTD 52. Figure 4 shows

simulation results of a conventional glass pane design and a new polycarbonate pane design subjected to a detonation. The original glazing disintegrates into hazardous glass fragments while the polycarbonate pane does not break up but flies as a single piece into the bus compartment. The agreement between simulations and experiments has proven the usefulness of conducting further parameter studies based on simulation for other blast loadings and protective measures.



Figure 4 Comparison Between Conventional (Left) and Polycarbonate (Right) Bus Window Subjected to a Detonation

Combined blast and fragment loading on masonry walls

The storage of cased munitions introduces additional considerations in the event of an accidental detonation of the munitions because the loads applied to the structure will be a combination of blast and fragment effects. An equivalent reduced NEQ is often calculated for cased munitions based on energy used in acceleration and break up of the casing that is then not available to drive the blast wave. If the damage to a structure or the likely fragment throw distances from the structure break up are required then fragment loading on the structure should be considered. This is a highly complex problem involving a wide range of length scales from acceleration and break up of individual munition cases, interaction of fragments, individual fragment impacts with the structure resulting in local damage and acceleration and break up of the structure, potentially leading to earlier venting of explosive products. Some of the possible effects of the detonation of individual or stacked cased munitions were described in reference [18].

In some recent work sponsored by DOSG of the UK MoD Defence Procurement Agency, combined blast and fragmentation effects were investigated numerically. These calculations used a 2D cylindrical symmetry simulation of a 155mm shell detonating 1m away from a double skin brick wall. The objectives of this work were to quantify the split between blast and fragment effects on the structure and their relative timescales and compare these with effects of a bare charge. The HE and air surrounding the shell were modelled using a multi-material Euler solver with the charge detonated at the nose of the shell. The casing was represented with a Lagrange grid with failure and erosion of badly deformed cells. The inertia of eroded nodes was retained in the calculation. The double skin brick wall was represented using Lagrange parts with explicit models of the bricks and separating mortar layers. Euler/Lagrange coupling was specified between explosive products and air and the shell casing and wall. Lagrange/Lagrange contact was activated between the shell casing and the wall, and between the two skins in the wall. The material properties used for the brick and mortar were based on standard RHT^[19] material library data modified to match available material properties. The initial geometry of the shell and wall are shown in Figure 5.

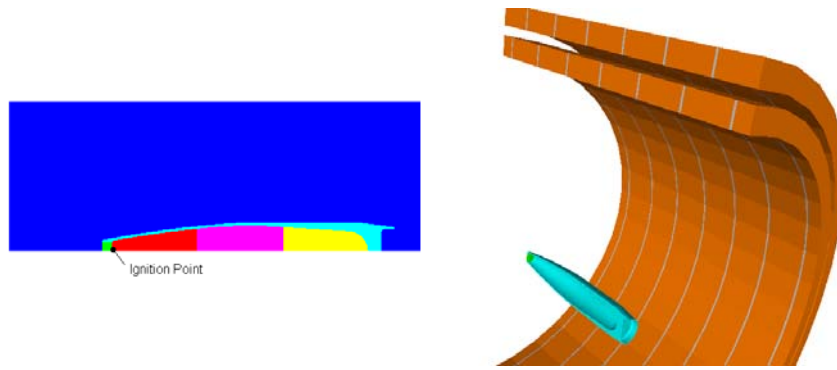


Figure 5 155mm Shell and Brick Wall Geometry

Figure 6 shows the blast wave and fragments just before they hit the wall. The light blue shows the positions of the casing and blast wave at 0.4ms. It can be seen that the blast wave is leading the fragments at this time. The casing fragment velocities are between 1200 and 2000m/s which compares well with results from the analytical SPLIT-X^[20] program giving confidence in the numerical simulation of the casing acceleration and break up.

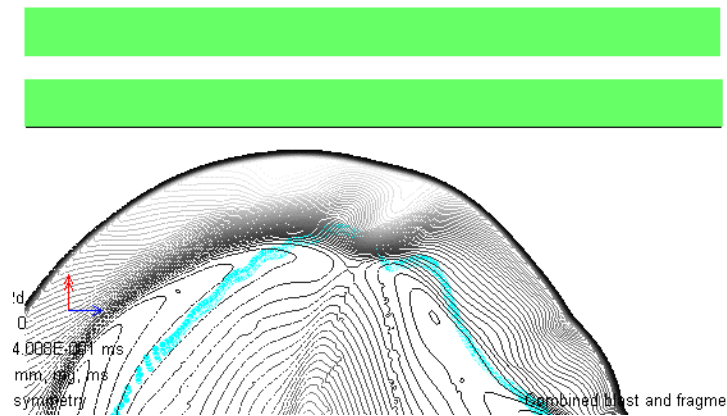
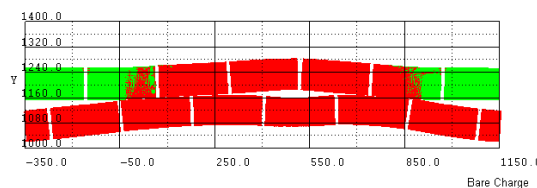


Figure 6 155mm Shell Blast Wave and Fragments About to Hit Wall

The resulting damage and deflection in the brick wall under various combinations of loading is shown in Figure 7 at 2.5ms after initiation. These plots show the material status in the wall with elastic material plotted in green and failed/damaged material shown in red. The first plot is for blast loading from a bare charge. The second plot shows damage from combined blast and fragment loading. Plots 3 and 4 used the cased shell model but in plot 3 only blast loads are applied to the wall and in plot 4 only fragment impact loads act on the wall. The reduction in the deflection of the wall with the reduced blast wave from the cased charge compared with the bare charge is obvious from comparing plots 1 and 3. Plots 2 and 4 illustrate the increased deformation of the wall under fragment loading and the bias in the fragment throw direction caused by the detonation wave propagating from left to right through the charge. The fragment loading also damages the wall earlier than the blast loading. The damage and deflection of the wall are surprisingly similar in plots 1 and 2 for the bare charge and the combined blast and fragmentation cases.



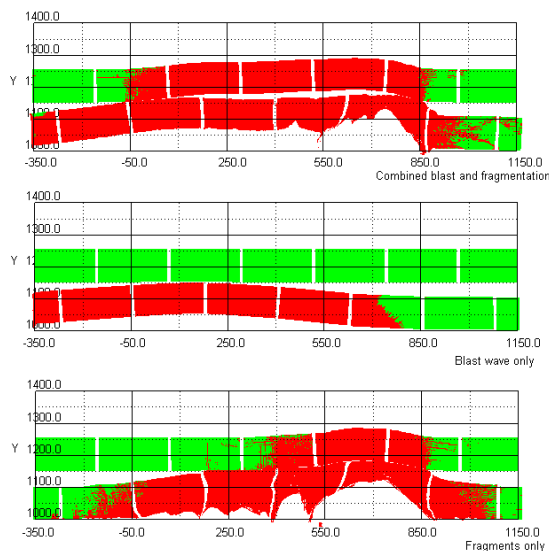


Figure 7 Wall Deflection and Damage for Different Loading Types

The combined radial momentum in both of the walls for the different loading types is shown in Figure 8. The combined blast and fragment momentum is very close to the additive amount of the two separate simulations and also to the momentum from the bare charge. For the cased charge about 60% of the wall momentum is from fragment impact loading and 40% from blast loading.

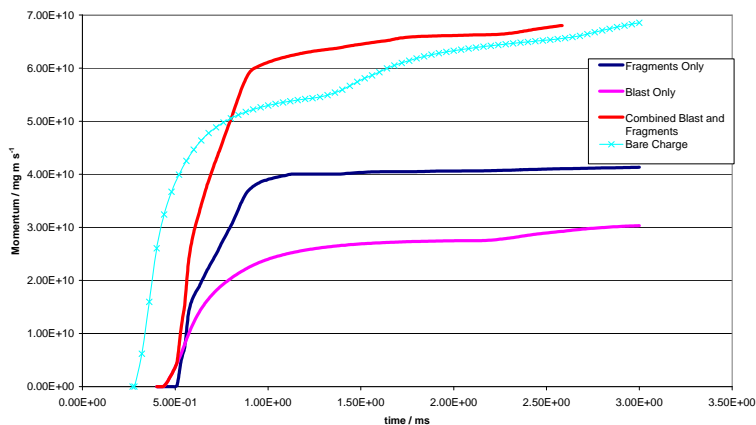


Figure 8 Wall Radial Momentum for Different Loading Types

Defence Trial 840

Defence Trial 840, conducted on 20 September 2002, employed a stack of 8 inch HE M106 projectiles giving a NEQ of 27 tonnes in an Explosive Store House (ESH) of typical reinforced concrete beam-column-slab construction with brickwork infill cavity walls. One of the main objectives of the trial was to determine the debris and primary fragment distributions around the ESH site to find the effective debris based IBD^[21].



Figure 9 ESH Layout and Internal View of Munition Stack

This section describes a scoping study of the building response to the detonating munitions using AUTODYN. The work described here was sponsored by DOSG of the UK MoD Defence Procurement Agency. The objectives of this work were to investigate the key factors and parameters affecting the building response and establish the feasibility of tracking the mass, position and velocity of the building debris. The numerical simulations of this trial were challenging and cover many different phenomena including:

- HE detonation
- Acceleration and break-up of the steel shell casings
- Complex reinforced concrete beam-column-slab structure with brick infill cavity walls
- Combined blast and fragment loading applied to the structure
- Acceleration and break-up of the structure under the applied loads

The response of the structure will also feed back into the applied loading as the building break up will allow HE products to vent to the atmosphere, leading to a reduction in the internal pressure.

Base Case Simulation Model: The model of the ESH used several different solvers as appropriate for each part of the system. For convenience two symmetry planes were utilised to reduce the size of the numerical model so that only one quarter of the system had to be represented, as shown in Figure 10. The door in the north wall of the structure and the traverses to the west, east and south were not included in the model and the ground was assumed to be rigid.

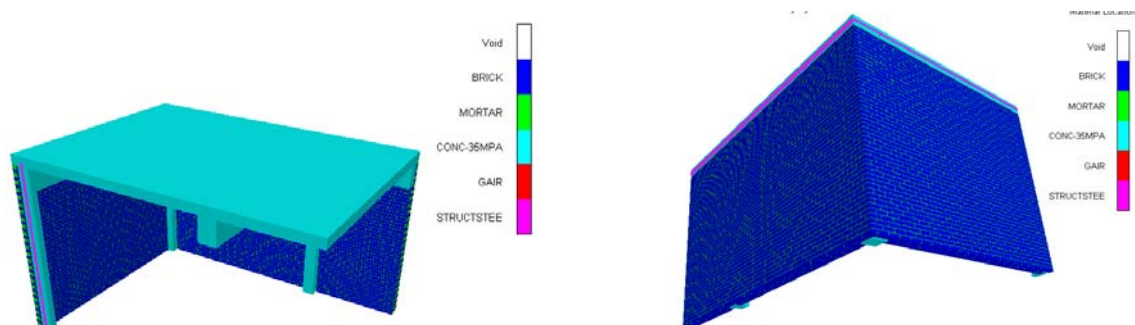


Figure 10 Model of ESH Structure

The masonry walls and the concrete parts were represented using Lagrange parts with the bricks and the mortar layers in the infill walls explicitly modelled. The steel reinforcement in the columns, beams and roof were explicitly represented using beam elements joined to the appropriate Lagrange nodes in the concrete components. The fluid surrounding the structure was represented using an Euler-FCT solver. The outline of this grid is shown by the red lines in Figure 11. This extended 3m beyond the structure in the two horizontal directions and 4m vertically above the roof.

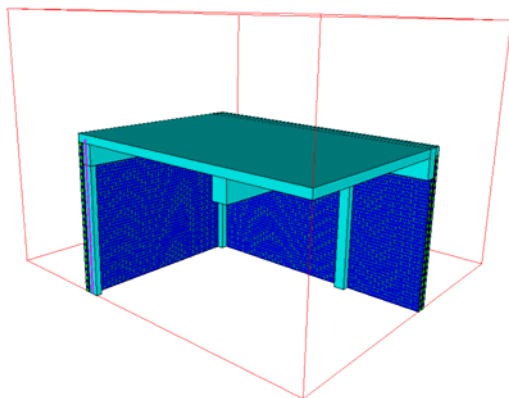


Figure 11 Euler-FCT Domain

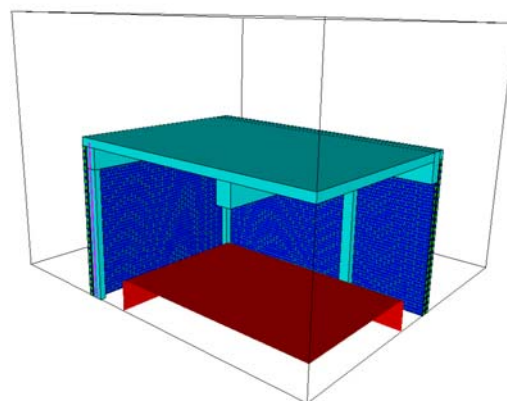


Figure 12 Initial Location of Explosive Products

The explosive products were simply represented as a high pressure gas region at the start of the simulation spread over the volume initially occupied by the shells as shown in Figure 12. The density and energy in this region was set to match the mass and detonation energy in the high explosives. The effects of this assumption compared with the trial with non-simultaneous detonation of a large number of cased munitions is complex and is the subject of ongoing research.

The pressures in the air and explosive products were transferred to the structure using Euler/Lagrange coupling. In this process the instantaneous geometry of the Lagrangian parts is used to block cells and faces in the Euler grid restricting the flow of the gases in the Euler grid and pressures in the fluid are applied to the structure. Impact between the structural components in the model was handled by AUTODYN's automatic Lagrange/Lagrange contact algorithm.

The concrete material in the columns, roof beams and roof were modelled using the RHT constitutive model which includes features to enable the capture of phenomena observed in brittle materials, including strain hardening as well as pressure hardening, third invariant dependence of the failure surface, different strain rate effects in tension and compression and coupling with p - α type compaction equations of state. The material for the steel reinforcements was based on standard AUTODYN Johnson-Cook material library data.

The bricks were assumed to remain intact during the simulation and were modelled using a simple linear elastic material model without a failure criterion. The mortar material model was adapted from standard AUTODYN material library data for concrete with modified data including a failure model that allowed fracture to occur along mortar lines.

All of the fluid in the simulation was represented using an ideal gas equation of state initialised to atmospheric conditions.

Simulation Cases. Four simulation cases were considered in this study.

1. Base case with a rigid floor and a full 27Te NEQ charge
2. Crater case with a 1m deep crater added at the start of the simulation under the shell stack to provide an upper bound estimate of how the crater formed in the experiment is likely to affect the building response. (Figure 13)
3. Reduced NEQ of 15.4Te to allow for reduced energy available for the blast wave due to energy used in accelerating, deforming and breaking the munition casing.
4. Fragment loading from munition cases applied to lower part of building walls as a momentum-time history based on 2D simulations of a single shell. This simulation also used the reduced NEQ charge as described for Case 3. (Figure 14)

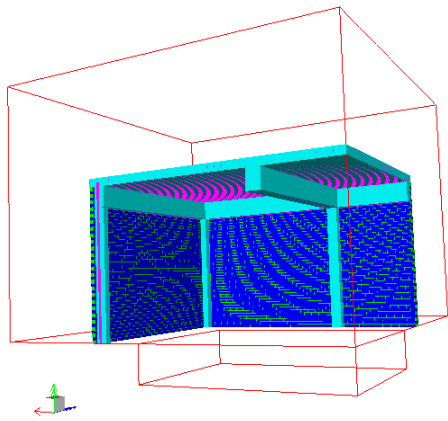


Figure 13 Case 2 Additional Crater Volume

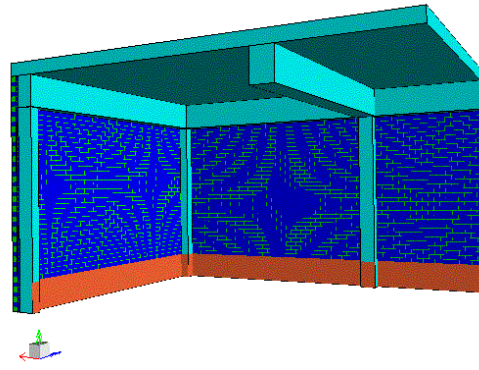


Figure 14 Case 4 Fragment Loading Region

The deformation of the ESH structure in the Case 4 simulation at 3ms and 5ms are shown in Figure 15. The effects of the additional loading at the base of the walls can be clearly seen.

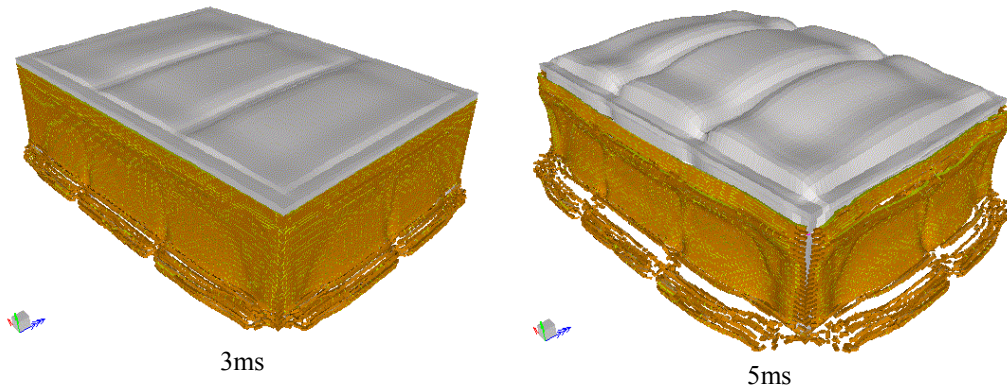


Figure 15 ESH Deformation for Case 4 (Fragment Attack and Reduced NEQ)

Figure 16 shows pressure and impulse time histories at a gauge point just under the centre of the roof for all four simulation cases. Adding the crater under the shell stack significantly changes the pressure time history and results in a 22% reduction in impulse compared to the base case. Reducing the charge NEQ lowers the peak pressure by 45% and reduces the impulse by 28%. At the centre of the roof the addition of fragment attack effects on the lower part of the walls makes no significant difference to the recorded pressure and impulse up to times of 7ms.

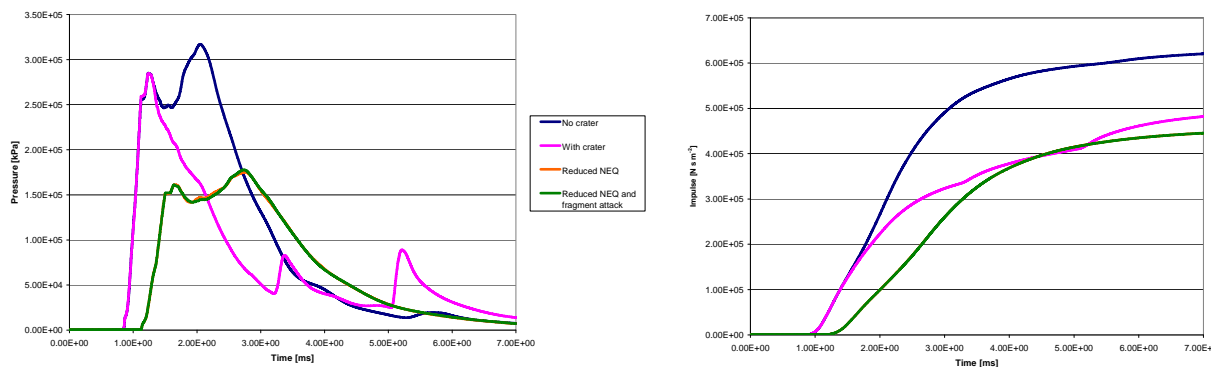


Figure 16 Pressure (Left) and Impulse (Right) at Centre of Roof

The average velocity of the outer leaf of the walls and the roof slab are shown in Figure 17 and Figure 18. Adding a 1m deep crater under the shell stack at the start of the simulation reduces the wall velocities by about 6% and the roof velocity by 12%. Some 2D investigations indicated that the crater would take several milli-seconds to form so the effect of the crater in the experiments is likely to be less than that seen in this model. The 43% reduction in NEQ due to energy loss to the munition casings gives about 25% reduction in the average speed of the walls and 20% reduction in the average speed of the roof slab. With the reduced NEQ and the addition of fragment attack a sudden step in the average velocity of both the long and short walls is evident at 0.8ms corresponding with the start of the fragments loading profile applied to the walls. This leads to slightly higher final average speeds in the walls. The addition of fragment attack on the walls gives a very small reduction of about 1% in the average speed in the roof slab.

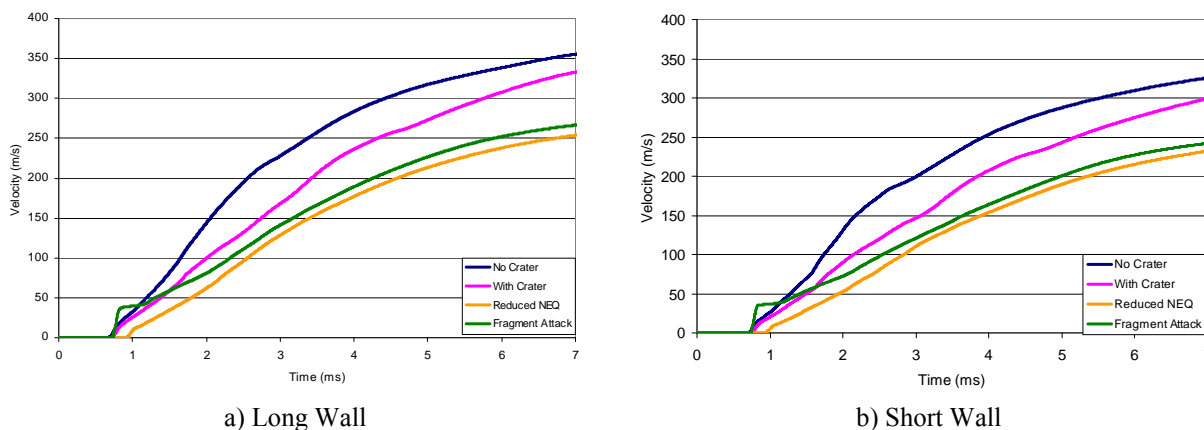


Figure 17 Average ESH Wall Speeds for the Different Simulation Cases

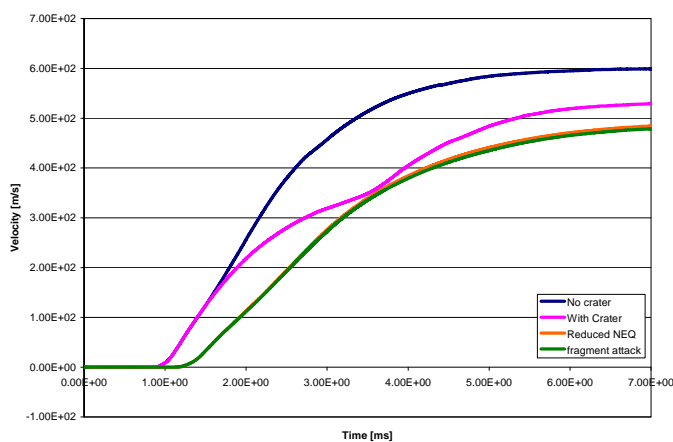


Figure 18 Average Roof Slab Speeds

Fragment Throws: At the end of each analysis a set of data files were created containing the initial position, final position and final velocities for all of the materials in each simulation. Based on this data some preliminary analysis of fragment throws has been completed using the DEBDIS program^[21].

Plots of the IBD from the trial and the simulation for the bricks in the structure are shown in Figure 19 based on an assumed sub-sonic drag coefficient of 1.5 and a super-sonic drag coefficient of 1.7. There is good correspondence between the experiment and the calculation to the north. Note that the east (0°), west (180°), and south walls (270°) of the ESH were traversed and this has had a strong effect on the debris patterns in these directions. These traverses were not included in the ESH simulation models.

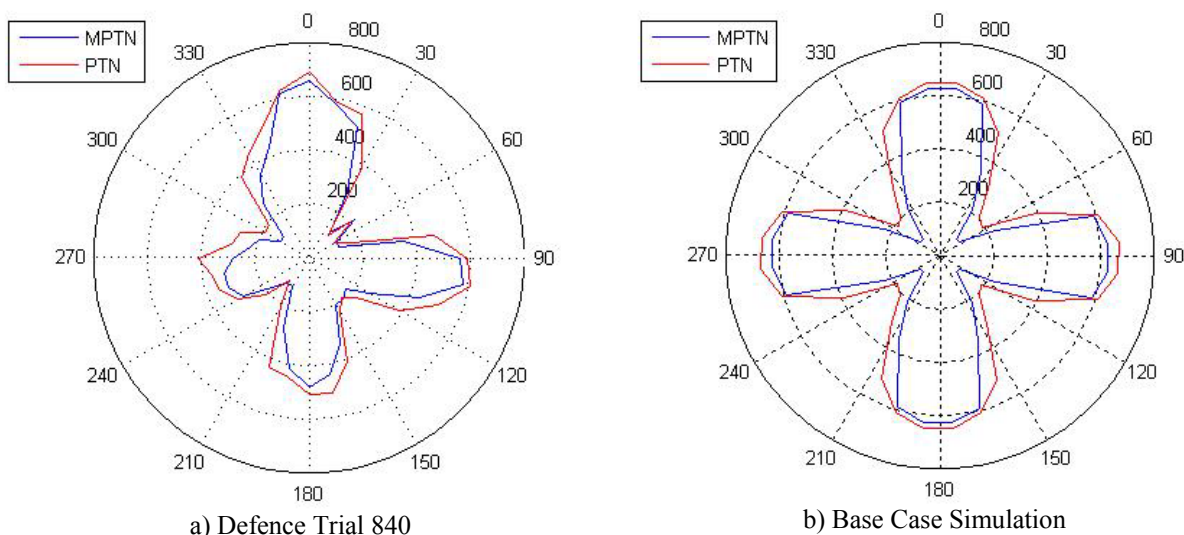


Figure 19 Brick Based IBD for Defence Trial 840

Similar data for the concrete in the ESH is shown in Figure 20. It is apparent that the IBD from the simulation data is greater than in the experiment. The reasons for this are under investigation.

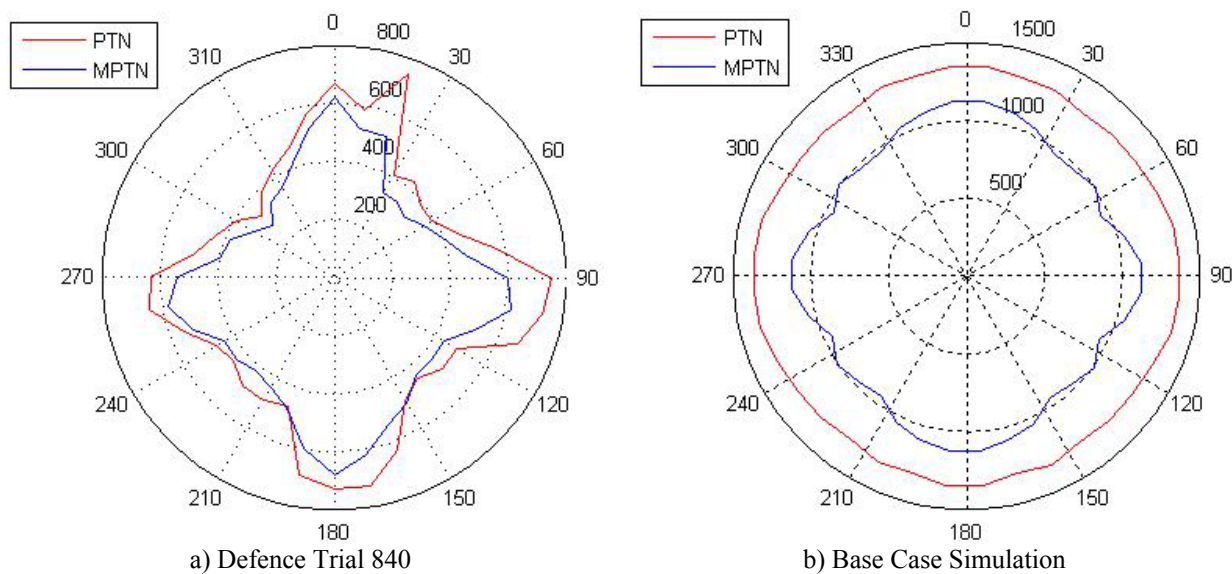


Figure 20 Concrete Based IBD for Defence Trial 840

Blast Loads on a Reinforced Concrete Wall

Sabotage from terrorist actions threatens the safety of nuclear power plants and materials. Physical barriers, usually made of steel reinforced concrete (RC) must be constructed around areas to be protected and must have adequate structural strength to prevent failure from terrorist threats. Two hypothetical terrorist threats are considered in reference [22]: blast from the detonation of a hypothetical truck bomb and impact from a Boeing 747 passenger jet. This section describes the simulations of the truck bomb detonation.

The physical barrier studied in the simulation was a 60m wide, 30m high, and 1m thick rectangular steel-reinforced concrete wall. The concrete material was modelled using Lagrange

brick elements and the steel reinforcing bars were explicitly represented using beam elements joined to the concrete. The wall was restrained from lateral motion at the bottom using a boundary condition.

The RHT strength and failure model was used for the concrete in the present simulations. A Von Mises strength model is used to represent the steel reinforcing bars. An erosion criterion was specified to allow severely deformed elements to be automatically removed from the calculation.

In the present simulations, a hypothetical truck loaded with 5,000 Kg TNT was assumed. Calculations were performed with the TNT detonating in contact with and at distances of 5m, 10m and 20m from the reinforced concrete wall as shown in Figure 21.

For efficiency and accuracy the bomb detonation and early stages of the blast wave propagation for the 5, 10 and 20m locations were simulated using a 1D spherically symmetric Euler model. Just before the blast wave reached the wall it was automatically remapped into a 3D Euler-FCT grid. Full Euler/Lagrange coupling was specified to allow the blast wave to interact with the deforming wall structure.

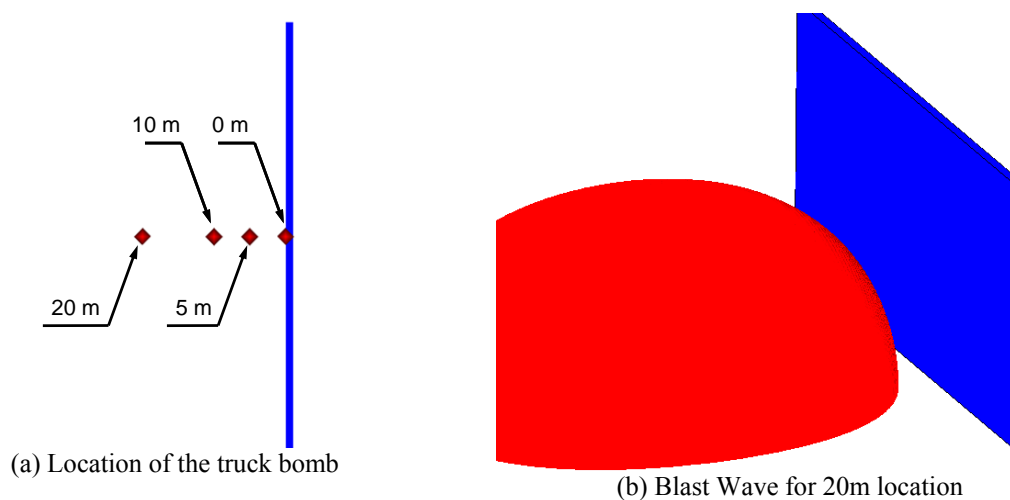


Figure 21 Truck bomb location

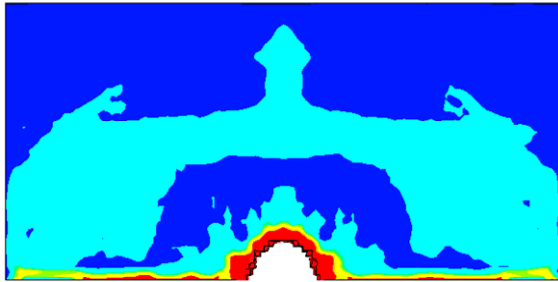
The damage to the reinforced concrete wall one second after the detonation is shown in Figure 22(a-f) for the different locations. The damage in the concrete is measured by the ratio of the plastic (unrecoverable) strain to the ultimate strain limit of the material. In Figure 22, red shows areas where the material has completely failed (damage=1). The light blue colour denotes partially damaged areas ($0 < \text{damage} < 1$). In the blast simulations, the back surface at the bottom of the concrete wall is damaged for all four cases. The magnitude of the damage decreases with the distance between the bomb and the wall.

For the contact detonation extensive damage occurs on both front and back surfaces of the wall. The wall is completely perforated by a 12m wide by 6m high opening. Thus this reinforced concrete wall fails to provide protections as a physical barrier against a contact charge.

When the truck bomb detonates at 5m the wall remains intact although significant damage is evident on both the front and the back surfaces. The partially damaged area on the rear surface of the concrete wall is 10m wide and 6m tall. At distances of 10m and 20m there is very little damage to the rear surface of the wall. Most of damage that does occur is on the front surface of the wall. Thus, the wall does indeed protect personnel and equipment from the blast.

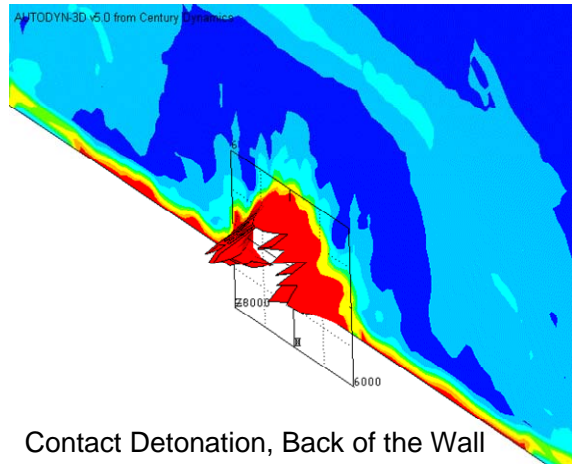
It should be noted that the damage shown in Figure 22 is caused only by the bare explosives. The effects of fragments of the truck engine and body as well as weakening of the steel reinforcing bars by possible fire are not considered in the present analyses.

AUTODYN-3D v5.0 from Century Dynamics



Contact Detonation, Front of the Wall

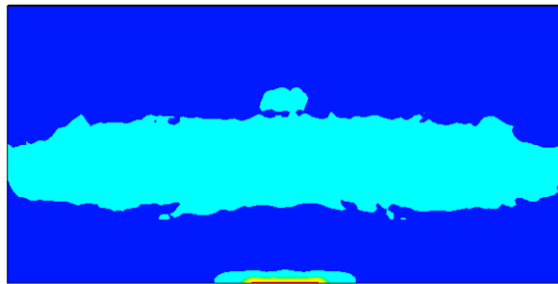
a)



Contact Detonation, Back of the Wall

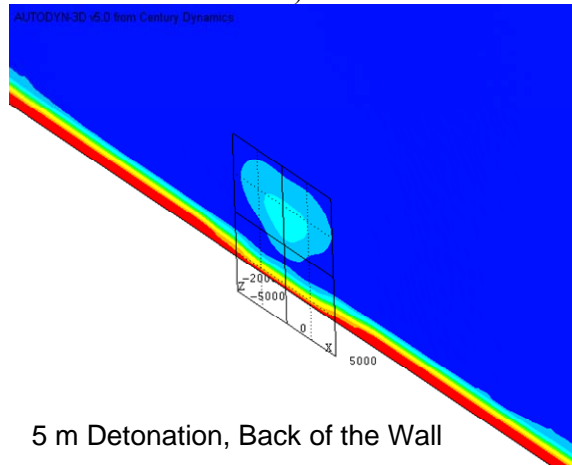
b)

AUTODYN-3D v5.0 from Century Dynamics



5 m Detonation, Front of the Wall

c)



5 m Detonation, Back of the Wall

d)

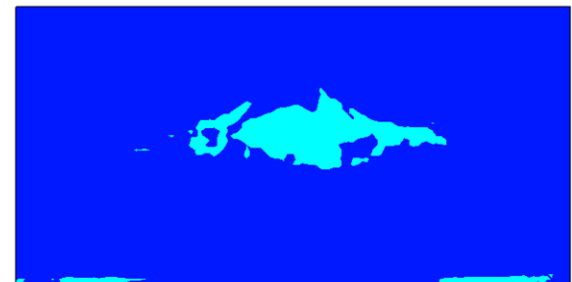
AUTODYN-3D v5.0 from Century Dynamics



10 m Detonation, Front of the Wall

e)

AUTODYN-3D v5.0 from Century Dynamics



20 m Detonation, Front of the Wall

f)

Figure 22 The Damage of the Reinforced Concrete Wall One Second After the Explosive Detonation.

CONCLUSION

The example simulations described in this paper have illustrated the application of AUTODYN's coupling capabilities to a wide range of structures responding under blast loads.

Two examples of masonry explosive store houses with internal HE detonations have been described including comparisons with experimental data. These simulations have shown that it is practicable to analyse the blast loading and break up of masonry buildings under extreme internal blast loading.

Simulations of two designs of a bus window were described. The behaviour and damage to the windows showed good agreement with full-scale experiments that means that the simulations can be confidently used to conduct parametric studies.

Simulations of combined blast and fragment loading on masonry walls from a 155mm shell showed some surprising results. The overall size of the damage region, magnitude of deflections and momentum in the wall were similar for bare and cased charges although the fragment loading did result in more severe localised damage at the impact sites. For the 155mm shell considered in the combined blast and fragment loading case, about 60% of the wall momentum was from fragment loading and 40% from blast loading.

Large fully coupled simulations of an ESH with reinforced concrete roof and columns and double skin brick infill walls have been completed using detailed models of $\frac{1}{4}$ of the structure and full coupling between blast loads calculated in an Euler grid and the structural components. These simulations showed that:

- The crater formed under the munition stack when it detonates is unlikely to have a large effect on the ESH fragment velocities
- Reducing the charge NEQ by the energy likely to be absorbed by the munition casings has a significant effect on the predicted fragment velocities reducing the average speed of the walls by about 20% and the roof slab by 25%
- Adding the effects of fragment loading on the walls actually increases the average speed of the walls with the speed of the affected region of the wall rising by up to 40%. The additional venting of the blast wave through the affected parts of the walls leads to a 1% reduction in the average speed of the roof slab.

The damage and failure of a typical physical barrier of reinforced concrete wall, subjected to blast from the detonation of a bomb was simulated using a coupled approach with Lagrange/Lagrange interaction and Euler/Lagrange coupling. The relationship between damage of the reinforced concrete wall and the distance of the truck bomb from the wall was investigated and ranged from perforation for a contact charge with reducing damage levels at increased ranges with little damage with a stand-off of 20m. The ability to simulate various threats against a variety of protection systems provides insight into the most important physical phenomena taking place.

References

- [1] AUTODYN-2D & 3D User Documentation, Century Dynamics, 2005.
- [2] X. Quan, N. K. Birnbaum, (2002), Computer Simulation of Impact and Collapse of the New York World Trade Center on September 11. Proceedings of the 20th International Symposium on Ballistics, pp 721-728, Orlando, FL, September 23-27.
- [3] M. Itoh, M. Katayama, R. Rainsberger, (2005), Computer Simulation of an F-4 Phantom Crashing into a Reinforced Concrete Wall, the 2nd International Conference on Computational Ballistics, Cordoba, Spain, May 18-20.
- [4] M. Dorn, M. Nash, A. Kesby and G. Anderson, "Urban Conflict And The Modelling Response Of Complex Masonry Structures To Internal Explosions", 20th International Symposium On Ballistics Orlando, FL, 23-27 September 2002
- [5] C. J. Hayhurst, R. A. Clegg, M. S. Cowler, "New generation 3D Hydrocode Developments including Advanced Visualisation, Parallelisation and Coupled Solvers", New Models and Hydrocodes for Shock Wave Processes in Condensed Matter, Edinburgh, Scotland, 19-24 May 2002.
- [6] M. S. Cowler, O. La'adan, T. Ohta, "High Performance Computing using AUTODYN-3D", 6th International Conference on Applications of High-Performance Computers HPC 2000, Maui, Hawaii, 26-28 January 2000.
- [7] J. P. Glanville, G. E. Fairlie, C. J. Hayhurst, N. J. Robertson, "Numerical Simulation of Fragmentation using AUTODYN-2D & 3D in Explosive Ordnance Safety Assessment", 6th PARARI International Explosive Ordnance Symposium Canberra, Australia, 29 - 31 October 2003
- [8] Q. B. Diep, J. F. Moxnes, G. Nevstad, "Fragmentation Of Projectiles And Steel Rings Using Numerical 3D Simulations", 21st International Symposium of Ballistics 19-23 April 2004 Adelaide, Australia
- [9] G.E. Fairlie, "Efficient Analysis of High Explosive Air Blast in Complex Urban Geometries Using the AUTODYN-2D & 3D Hydrocodes, Analytical and Experimental Methods", 15th Military Aspects of Blast Symposium, Banff, Canada, 15-19 September 1997
- [10] M.S. Cowler X. Quan G. E. Fairlie, "A Computational Approach To Assessing Blast Damage In Urban Centers Using AUTODYN2, Proceedings of ASME PVP: Structures Under Extreme Loadings Symposium July 25-29, 2004, San Diego, California
- [11] G. E. Fairlie, I. H. G. Livingston, "Analysis of Fragment Throw Distances from High Explosive Detonations in Masonry Structures", IEMS Conference, 1997.
- [12] N. K. Birnbaum, G. E. Fairlie, X. Quan, "Coupled Fluid-Structure Analysis of High Explosive Detonations in Masonry Structures", 29th DOD Explosives Safety Seminar, New Orleans, USA, July 2000
- [13] G.E. Fairlie, "Numerical Simulation of Combined Blast and Fragment Loading on Structures", 11th International Symposium on Interaction of the Effects of Munitions with Structures, Mannheim, May 2003
- [14] B.M. Luccioni, R.D. Ambrosini R.F. Danesi, "Analysis of Building Collapse Under Blast Loads", Engineering Structures 26, pp63-71
- [15] M. J. A. Gould, K. Cuthbertson, "UK/Australian Small Quantity Explosion Effects Tests and Their Analysis", Australasian Explosives Ordnance Symposium, PARARI '97
- [16] F. Landmann, "Numerical and Experimental Simulations of Terroristic Attacks (in German: Numerische und experimentelle Simulation terroristischer Anschläge)", Workshop Bau- Protect, Fraunhofer-Institut fuer Kurzzeitdynamik, Ernst-Mach-Institut, Freiburg, Germany, October 27-28, 2004.
- [17] R. Gündisch, "Effectiveness of Reinforcement Measures for Bus Windows", 18th International Symposium on Military Aspects of Blast and Shock, Oberjettenberg, Germany, September 27 – October 1, 2004.
- [18] N. J. Robertson, G. E. Fairlie, J.P. Glanville, I. Barnes, C. A. Hoing, "Hydrocode Modelling of Debris from Explosions", NATO Debris From Explosions Technical Meeting, San Antonio, USA, 27 August 2004
- [19] K. Thoma, W. Riedel, S. Hiermaier, "Mesomechanical Modeling of Concrete Shock Response Experiments and Linking to Macromechanics by Numerical Analysis", ECCM'99, Munchen, Germany
- [20] Split-X User Documentation, Numerics GmbH, Mozartring 6, 85238 Petershausen, Germany
- [21] G. E. Fairlie, J. P. Glanville, I. Barnes, C. Hoing, P. Norman, "Fully Coupled Simulation of Explosive Store House Response to Internal Detonations", 12th ISIEMS 2005, Sept 26-30, New Orleans
- [22] X. Quan, M. Itoh, M. Cowler, M. Katayama, N. Birnbaum, B. Gerber, G. Fairlie, "Applications of a Coupled Multi-solver Approach in evaluating damage of reinforced concrete walls from shock and impact", 18th International Conference on Structural Mechanics in Reactor Technology (SMiRT 18), Beijing, China, August 7-12, 2005, SMiRT18-J04-4

Resistance Analysis of Steel and Mixed Steel-Concrete Columns Subjected to Close-Contact Explosions

F. Halleux, J. Art, J.-M. Ndambi, J. Vantomme

Royal Military Academy, Avenue de la Renaissance 30, 1000 Brussels – Belgium

Building designers may take into account the problem of terrorist explosions in their design. In contrast to external explosions where it is sometimes possible to reduce explosion effects by application of stand-off distances between buildings and public spaces, the case of close-contact explosions is completely different. Because of the instantaneous characteristic of close-contact explosions and their local effects, this kind of explosion cannot be treated by the well known conventional methods, but by specific methods. This paper compares the behaviour of columns made with steel bars (or profiled steel bars) and the columns made with mixed steel-concrete material and subjected to close-contact explosions. Within the framework of this study, an explosive charge of 20kg equivalent TNT is considered. Experimental and simulation results on scaled models are compared. The numerical simulations are carried out using the Autodyn software.

The obtained results show that the numerical simulations may allow to qualitatively predict the experimental results and that the addition of a concrete envelope on a steel beam allows to increase its resistance to close-contact explosions.

INTRODUCTION

Nowadays, the designers of important buildings have not only to consider classical loads in their calculations but also the abnormal loads which can occur from terrorist attacks. Research has been carried out in this domain in order to study the behaviour of structural element such as beams, plates, glazing and columns subjected to blast load [1]. This paper examines the case of steel and mixed steel-concrete columns subjected to close-contact explosions. Only qualitative results are described.

THEORETICAL BACKGROUND

In the case of a close contact explosion, the structure is essentially loaded by the explosion gases and the explosive material itself. The blast effect has practically no effect on the structure.

When an explosive material is put into contact with a structural element, the arrival of the detonation wave on the surface of the explosive generates intense stresses in the element causing crushing and fragmentation or disintegration of the material.

The dynamic pressure at the front wave p expressed in kilobars, can be calculated using the following empirical equation [2]:

$$p = 2.5 \cdot 10^{-9} \rho D^2 \quad (1)$$

where ρ [kg/m³] is the explosive density and D the detonation wave velocity.

The values of these pressures are very high and may cause the failure of the concrete structure if the compressive dynamic resistance of the concrete material is exceeded (cratering). On the other hand, the reflected tensile wave may also cause the rupture of concrete and the ejection of

fragments at the back of the structure if the tensile dynamic resistance of the concrete material is exceeded (spalling or scabbing). Also, the stress wave confined between the cracks and the free surface projects concrete parts at a certain velocity called spalling velocity [3]. Next to these three phenomena, the punching phenomenon is also observed, where the concrete material is punched by a high energetic flux of concrete particles coming from the concrete part directly loaded by the explosive front wave.

Equation (1) applied to the case of C4 explosive (plastic explosive) ($\rho=1601 \text{ kg/m}^3$, $D=8193 \text{ m/s}$) leads to the following pressure:

$$p_{C4} = 2.5 \cdot 10^{-9} \rho D^2 = 26867 \text{ MPa} \quad (2)$$

This value of pressure is by far higher than the concrete dynamic resistance and should cause the cratering of the concrete specimen.

EXPERIMENTAL WORK

Material Description

The column that has to be analysed is made of a steel beam embedded in concrete. In general, the concrete envelope is used in constructions for two reasons: first, to increase the fire protection of the steel beam and second, to increase the bearing capacity of the obtained final mixed element. In this study, only the resistance of the mixed concrete-steel element to close-contact explosions is analysed. Since the lateral resistance of columns is limited, because this element is designed to withstand vertical loads, the concrete envelope also allows to increase the inertia of the final mixed column and therefore also its resistance. Moreover, the concrete permits to increase the stand-off distance between the steel and the explosive [4].

A. Concrete material

The final objective of the experiments being also the validation of numerical simulations, it is important to use materials that can be easily modelled. Because of its heterogeneous and its complex behaviour, the concrete material is replaced in the specimens by micro concrete. Micro concrete is a concrete whose components are brought back to the level of the scale of the model. The normal stone aggregates are replaced by fine granulates. In this work the composition A of Kavyrchine is adopted (see table 1) [5].

Designation	Granulates [kg]				Cement [kg/m ³]	Water [l/m ³]	Collapse to slump test [cm]	Cylindrical resistance at 28 days [N/mm ²]	Elastic modulus [N/mm ²]
	0	0.5	1.6	2.					
	/	/	/	5					
A	506	307	721	-	450	240	7 to 5	30	25 to 27000

Table 1: Kavyrchine composition [5]

B. Steel material

The steel type S235 is used. Its characteristics are presented in table 2.

f_y [N/mm ²]	f_u [N/mm ²]	E [N/mm ²]	G [N/mm ²]	α [1/°C]	ρ [kg/m ³]	ν [-]
235	400	210000	81000	12E-6	7850	0.3

Table 2: Characteristics of the steel material

f_y : steel yield stress; f_u : steel failure stress; E: elastic modulus; G: shear modulus

α : thermal dilatation coefficient; ρ : steel density; ν : Poisson ratio

Description of the specimens

Experiments are performed on reduced models, because of the imposed limitations of the maximum explosive charges which can be used in our testing facilities. The dimensions of these models are determined from usable explosive charges and the dimensions of the shooting field. This study focuses on wide flange columns of the type HD400x237, HD400x262 and HD400x347. The length of the real columns is 3600 mm.

For experiments, the height of the specimens is chosen to be less than 100mm. Since these dimensions do not exist in commerce, a decision was made to build specimen in our laboratory. The “H” shape is then obtained from two “U” steel beams welded together. Working as described before, a steel beam “H” of dimension 50x50x10mm is obtained (figure 1).



Figure 1: “H” profiled steel bar

The height of the reduced model is determined from the Hopkinson-Cranz law [6, 7, 8]. This law uses the reduced distance (Z) in function of the stand off distance (R) and the explosive weight (W).

$$Z = \frac{R}{W^{\frac{1}{3}}} \geq 0.16m / kg^{\frac{1}{3}} \quad (3)$$

As this analysis focuses on close-contact explosions, the reduced distance Z is zero and this law is strictly speaking not really applicable. Yet it can lead to some starting values. The distance scale factor λ_L is determined by the height proportion between real and model columns: $\lambda_L = (50/400) = (1/8)$. This factor leads to specimens of 450mm height. From this distance scale factor, the explosive charge scale factor can also be estimated as follows: $\lambda_W = \lambda_L^3 = (1/512)$.

In this study, only the case of package bombs is considered. The literature shows that in this case, explosive charges from 5 to 40 kg equivalent TNT can be considered [9]. In this work, only the cases of 10 and 20 kg are considered. The experimental charges are then determined from these real charges and the charge scale factor λ_W . The calculated reduced charges are mentioned in the second column of table 3.

Real explosive charge [kg]	Experiment explosive charge[g]
20	40
10	20

Table 3: real and reduced explosive charges

Experimental set-up

The final shape and dimensions of specimens used during experiments are determined by taking into account the following prerequisites:

- position of specimen during tests (vertical or horizontal),
- support system,
- workability (weight, transportability),
- shooting field dimensions.

A. Position of the specimen

Table 4 presents advantages and disadvantages of the two test positions (vertical and horizontal).

Vertical position	
Advantages	Disadvantages
This position is close to reality	Risk of swinging
The own weight of the column is taken into account	All round fragment projections
The column can be easily prestressed	
Reduced influence of ground reflection during tests	
Horizontal position	
Advantages	Disadvantages
Working facility	More ground reflections
No risk of swinging	Not realistic
Less fragment projection	The column cannot easily be prestressed

Table 4: Advantage and disadvantages of the specimen positions

B. Support system

As the real columns are fixed at the two ends, the reduced models should be tested preferably in the same conditions, while avoiding difficulties in the realisation. Two solutions are applied and tested out:

- first, two holes are drilled in advance with the column dimensions in two reinforced concrete (RC) bases. The column is then afterward inserted in the bases;
- second, the steel beams are welded to steel plates and these plates are afterwards bolted to the RC bases.

In the two cases, the bases are manufactured with classical concrete material.

As none of the two forgoing solutions seem to give satisfaction, the final choice is then to build the specimen in three successive phases: first, the construction of the inferior RC base, next, the realisation of the column itself and the third phase consists in the realisation of the superior RC base.

The RC bases of 30x30x15cm are chosen for two reasons: they are not too large, so not too heavy in order to facilitate the transportation and not too small, in order to avoid the problem of swinging during experiments. The bases are reinforced with cylindrical steel bars (S235) with

5mm diameter welded into a grid of 5x5cm and distributed over the tension and compression side as shown in figure 2. Figure 3 shows an example of a complete specimen.

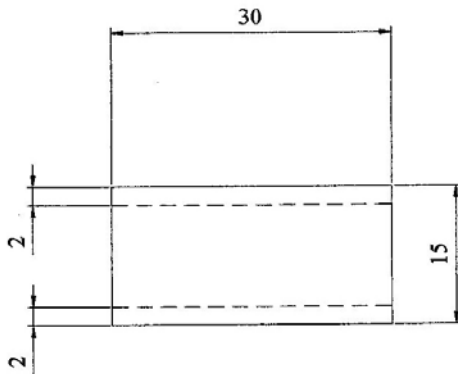


Figure 2: position of the steel bars in the RC bases

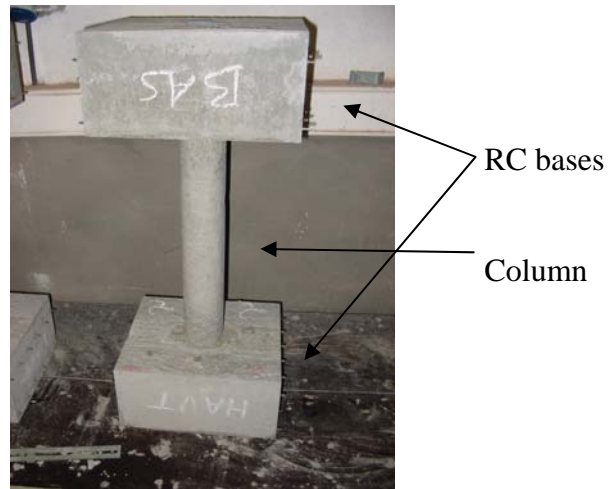


Figure 3: mixed steel-concrete column made RC bases with a cylindrical steel bar

Table 5 summarizes the mechanical characteristics of the micro concrete and concrete used in the specimens.

	Micro concrete	Concrete
ρ [kg/m ³]	2150	2350
E [N/m ²]	17000E6	35000E6
G [N/m ²]	7500E6	14500E6
f_c [N/m ²]	12.8E6	33E6
f_t [N/m ²]	2E6	6.6E6

Table 5: Mechanical properties of concrete and micro concrete used for the construction of the specimens.

ρ : density; E : elastic modulus; G : shear modulus; f_c : limit compression resistance, f_t : limit tensile resistance

Experimental tests

The experimental tests are prepared and performed in the shooting range of the Centre for evaluation and testing of materials and equipment (CEM) of the Belgian Army. These tests intend to study the phenomenon of close-contact explosions and to examine closely the effects of this kind of explosions on mixed steel-concrete columns.

The test campaign is performed in two steps:

- preliminary tests are performed on steel bars in order to make a phenomenological and qualitative study of this kind of explosions. For this step no measurements are performed; the obtained results will be compared to the results obtained from the mixed steel-concrete columns;
- next, the close-contact explosion tests are performed on two kinds of mixed steel-concrete columns.

A. Preliminary tests

Preliminary tests are performed on two kinds of specimens: cylindrical steel bars with 35mm diameter and H shaped profiles with 5cm height. These specimens are in fact the core elements used in the construction of the mixed steel-concrete columns. The purpose of these tests is to collect reference phenomena which will be compared with the results from the mixed steel-

concrete specimens. Sixteen shots are programmed for the specimens mentioned in table 6; 20 and 40 g of equivalent TNT are used.

Specimen type	H shaped profile		Cylindrical bar	
	length [cm]	Number	length [cm]	number
	45	2	45	6
	75	4	75	2
	100	0	100	2

Table 6: Dimensions of the tested specimens

As already shown before (section 3.2), the specimens should have 45cm length in order to respect the similitude principle. The specimen of 75 and 100 cm are used only in order to see what happens with long specimens.

A.1. Test configuration

For facility reasons, the specimens are tested in the horizontal position. At the ends of each specimen, a T profiled steel bar is welded. The fixed supports are then simulated by inserting these T profiled steel bars in RC blocs of 200 kg each. The explosive charge is placed on the specimen near one of the two supports, in as order to simulate the real terrorist attack.

Figure 5 presents this test configuration. Two video cameras are used to register the phenomena.



Figure 5: preliminary test configuration

A.2. Results and discussion

Nothing could be seen with the cameras because of explosive flash generated by the explosive charge; it is impossible to evaluate global and local effects by using these optical devices [10]. The presence of RC blocks does not allow a rapid dissipation of dust and reduces again the visibility. These blocks also influence the generation of this fireball.

The welding between the specimens and the T profiled steel bars does not resist to the explosion and constitutes a weak point of the specimens. This observation gives good lessons for the

construction of the specimen used in the final tests. This phenomenon is more observed in the case of the H profiled steel bars where the welded surface is less than in the case of cylindrical steel bars. The used support system works correctly. But, after some shots, some of the RC blocks have to be replaced because of damage due to the cratering effect.

Some conclusions can be drawn:

- for the same steel surface, the cylindrical steel bars resist to a more important explosive charge than the H ones;
- the welded surfaces are more resistant in the case of cylindrical steel bars than in the case of the H profiled steel bars; this can be explained by the difference in the dimension of the surface that can be welded to supports (less surface for the H profiled steel bars);
- the shape of the H profiled steel bars has a more confirming effect on the explosive gas and blast and leads to more damage than in the case a cylindrical steel bar;
- the supports made by welding are brittle and are not appropriate for close-contact explosive tests,
- more important transverse deformations are observed for longer specimens;
- the tests performed with 20g of equivalent TNT lead to very limited effects;
- the cratering effect is not affected by the position of the explosive charge (in the mid-section or at the end of the specimen);
- a large transverse deformation is observed for the explosive charge located at the mid-section of the specimen.

B. Final tests

The objective of these tests is first to validate the theoretical prediction and next to validate the numerical simulations. The specimens used are those described in section 3.3.

B.1. Set-up

For these tests, the set-up configuration should respect the following prerequisites:

- the specimens should be tested in the vertical position,
- the specimens should be prestressed during tests,
- the specimen should not swing during tests,
- only the ground reflection should be allowed.

These prerequisites lead to the set-up configuration presented in figure 6: the specimens are placed vertically in the centre of an armour-plate of 1m² and 3cm width. Four small steel bars are welded on the armour-plate in order to avoid the sliding of the specimens during the experiments. On the upper RC base, a smaller armour-plate is placed. The two armour-plates are connected by removable oblique bars which allow the prestressing of the specimens by tightening the bolts located at their ends. This prestressing load does not correspond to the real compression on building's columns. The real loads are too important and cannot be simulated by this simple loading system. Indeed, the load on real columns varies between 3870 kN and 5400 kN; this load corresponds to a reduced load varying between 7.6 kN and 10.6 kN for our specimens. This should require a complex loading system which is not used in this work.





Figure 6: Final test configuration

B.2. Measurement system

Two measurement systems are used: strain gauges and the copper-crush cylinder system. The strain gauges used are the 3% type (3000 μ m/m). These gauges are placed in the mid-section of the specimens at the opposite side from the explosive charge. The rapid X60 glue is used to assure a perfect adhesion of the strain gauges onto the specimens. The crusher system is used in order to measure the instantaneous lateral displacement of the specimen during the explosion. This device is placed in contact with the specimen at 5cm from the upper surface of the lower RC base. Figure 7 presents the measurement system.



Figure 7: measurement system: crusher and strain gauges

B.3. Results and discussions

Comparing results from sections 3.4.1 and section 3.4.2, it appears that:

- the steel bars in the mixed steel-concrete columns are less damaged than the simple steel columns. The concrete envelope is completely torn off the steel bar. The concrete envelope offers a real protection of the steel bar because it allows to avoid the shock wave confinement and it absorbs a great part of the shock wave energy;
- the measurements obtained from the crushers are not satisfactory. Indeed, the crushing of the crusher is caused by two phenomena: the displacement of the column itself on one hand and by the concrete parts projected at the back side of the specimen on the other hand. These phenomena are acting at the same time and it is the impossible to know what is the column displacement ;

- the results from strain gauges are not usable, because they are destroyed or torn out by the explosion and projected with the concrete parts.

NUMERICAL SIMULATIONS

The numerical simulations have as objective the simulation of the experimental tests in order to better understand the close-contact explosion phenomenon. In this work, the numerical simulations are performed using the AUTODYN software [11]. Only experiments on mixed steel-concrete specimens are simulated. Lagrangian, Smooth particle Hydrodynamics (SPH) and Eulerian (2D and 3D) processors are used in this work. More information about these different solvers can be found in [11, 12 and 13].

Only 3D models are described in this paper. Indeed, in 2D models, the influence of the geometry of the specimens and the explosive charges on the obtained results, is ignored. Two 3D models are considered.

A. Model 1: Cylindrical steel bar embedded in micro concrete

Figure 8 presents the first 3D model.

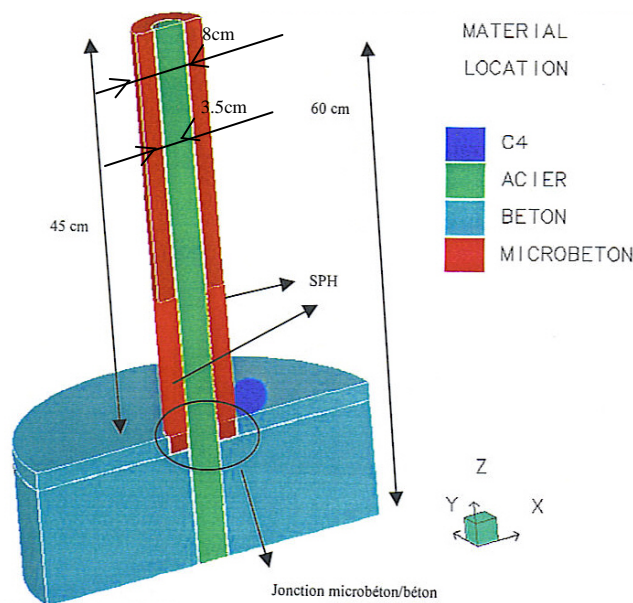


Figure 8: the first 3D model: mixed steel-concrete column with cylindrical steel bar

In order to minimize the number of cells in the analysis, only half of the specimen is modelled by considering a symmetry plane through the centre of the specimen (plane Y). The upper base is not modelled but is replaced in the model by equivalent boundary conditions.

Because of the large deformations observed during experiments and the phenomena of cratering, spalling and cracking observed in the concrete and micro concrete parts of the specimens, the Lagrangian solver cannot be used to model the behaviour of these materials, because this solver is not suited for large deformations. Concrete and micro concrete are modelled using the SPH solver. On the other hand, because of the problem of no interaction between the SPH and the Eulerian solvers, the explosive charge should also be modelled using the SPH solver.

In order to reduce the simulation time, SPH cells micro concrete are only considered in a zone limited to 15cm from the lower base (figure 8); this is justified by the fact that during experiments, important damages are only observed in this part of the specimens.

In contrast to the experiments, the bases in the model are not reinforced with steel bars, but are only made in simple concrete material. Indeed, the reinforcement of the bases is not necessary, because they do not influence the results for the columns. In addition, the bases are cylindrical and not rectangular, but their shape does not affect the columns behaviour.

The lower surface of the lower base is fixed in the direction of the Z axis: $V_z=0$; movements are possible in the X and Y directions. The upper surface of the column is fixed in the 3 directions (X, Y and Z) in order to simulate the behaviour of the upper base. An explosive charge of 40 g of C4 is represented by a half sphere located on the upper surface of the lower base and in contact with lower part of the column (figure 8). The detonation point is located in the centre of the sphere.

B. Model 2: H steel profile embedded in the micro concrete material

As for the first model, only the half of the specimen is modelled. Again, the upper base is not represented, but replaced by boundary conditions. This model is essentially equivalent to the one described in section 4.1, but only the shape of the reinforcement is different (H profiled steel bar instead of cylindrical steel bar). Figure 9 shows the considered model.

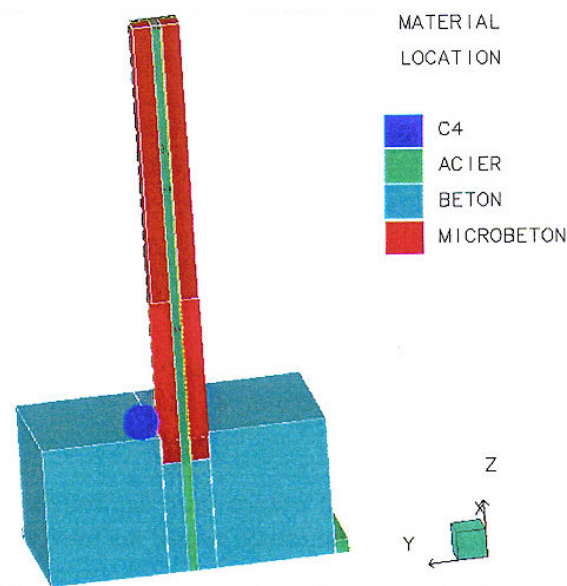


Figure 9: the second 3D model: mixed steel-concrete column with the H profiled steel bar

The boundary conditions and the explosive charge remain the same as for the first model described in section 4.1

C. Results

Figure 10a shows the results obtained from the model 1. The bases and columns are damaged where parts are in contact with the explosive charge. A good similitude is observed between the numerical and experimental results for the columns (figure 10b). Figure 11a shows the results obtained from the model 2. Again, the bases and columns are damaged on their external parts. Again, a good similitude is observed between the numerical and experimental results for the columns (figure 11b). On the other hand, the numerical results show a more severe destruction of the base, but this can be explained by the absence of reinforcement in the bases in the numerical model.



numerical
On the other
destruction

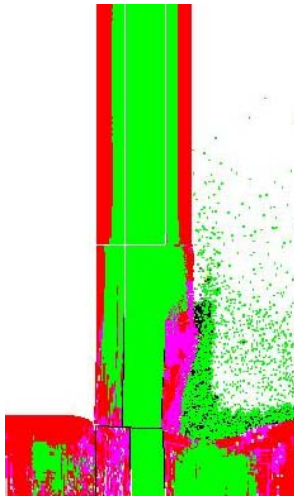


Figure 10a: Damage pattern on the mixed steel-concrete column (numerical model 1)

Figure 10b: Damage pattern on the mixed steel-concrete column (experiments)

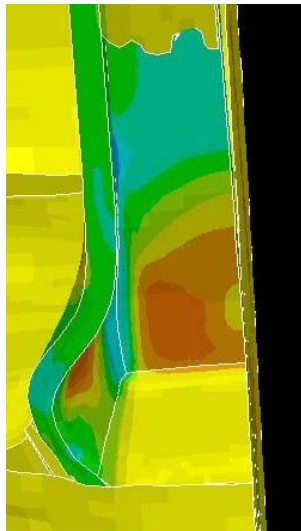


Figure 11a: Damage pattern in the mixed steel-concrete column (numerical model 2)



Figure 11b: Damage pattern in the mixed steel-concrete column (experiments)

D. Comparison between simulations and experiments

Only qualitative comparisons can be made because of the lack of experimental measurements:

- it is very difficult to make a good comparison between experiments and calculations for columns reinforced with cylindrical steel bars (model 1). Indeed, for this kind of specimens one observes a complete tearing out of the micro concrete and very small deformations. The shape of the cylindrical steel bar does not support the adherence between the two materials. Figure 10b corresponds to the case where only 20g of equivalent TNT is used;
- for the model 2 (column reinforced with H profiled steel bars), a very good similitude between experiment and simulation is observed (figures 11a and figure 11b). A good qualitative prediction of the phenomenon could be done using the Autodyn Software.

GENERAL CONCLUSIONS

This paper describes experiments and numerical simulations performed in order to better understand the close-contact explosion phenomenon. The objective is to study the behaviour of the columns made with steel bars (or profiled steel bars) and the columns made with mixed steel-concrete material and subjected to close-contact explosions.

The obtained results can be summarized as follows:

- the numerical simulations allow to qualitatively reproduce the experimental results;
- a very good similitude between experiment and simulations is observed for the mixed steel- concrete columns made with the H profiled steel bar. In the case of the cylindrical steel bar, the results are very different; this can be explained by the shape of the steel bar which does not support the adherence between the steel bar and the concrete envelope;
- experiments show that the addition of a concrete envelop on a steel beam allows to increase its resistance to close-contact explosions, because of the increased stand-off distance.

ACKNOWLEDGMENTS

This work was performed within the framework of the project Scientific and Technology Research for defence MX-01 “Analysis of explosion effect of structures”.

References

1. Luccioni B.M., Ambrosini R.D., Danesi R.F., “Analysis of building collapse under blast loading”, in Engineering Structures, 26, 2004, pp 63-71.
2. SMITH P. D. and HETHERINGTON J. G., “Blast and ballistic loading of structures”, Oxford, Butterworth-Heinemann, 1994
3. McVAY M.K., “Spalling of concrete from nearby detonations”, in proceedings of the 3rd symposium Interaktion Konventioneller Munition mit Schutzbauten (9-13 märz), Mannheim, 1987.
4. PARMENTIER B. et al., “Normes et règlements, la construction mixte acier-béton”, in CSTC magazine (Hiver 2002), pp 33-60,
5. KAVYRCHINE M., “Études structurelles en microbéton”, in Anales de l’Institut technique du Bâtiment et des travaux publics, n° 389, paris, 1990.
6. BLAZYNSKI T.Z., “Material at high strain rate”, London-New York, Elsevier, 1987
7. KURTZEMANN B., “Similitude en pyrotechnie”, Ecole Nationale Supérieure de Techniques Avancées, 1978.
8. BAKER W.E., “Use of Similitude analysis and scale modelling in research and design”, in proceedings of the 3rd symposium Interaktion Konventioneller Munition mit Schutzbauten (9-13 märz), Mannheim, 1987.
9. HALLEUX F. and ART J., “Etude de la résistance d’une colonne à une explosion de contact”, travail de fin d’étude pour l’obtention d’un diplôme d’ingénieur civil polytechnicien’, Bruxelles, Belgique, 2003.
10. DYCKMANS G., “Balistique intérieure”, cours ERM AB4010, 2001.
11. Century dynamics Inc., Autodyn-Theory Material manual, Revision 3.0, 1998.
12. Century dynamics Inc., Autodyn-SPH user manual and tutorial, Revision 3.3, 1999.
13. Century dynamics Inc., Autodyn-Introduction, training and course, Revision 3.0, 1998.

Rapid Expansion and Fragmentation for 304 Stainless Steel Cylinders Driven by Cylindrically Expanding Detonation and the Effect of Wall Configuration and Explosive Energy

Tetsuyuki Hiroe, Kazuhito Fujiwara and Hidehiro Hata

Kumamoto University, Faculty of Engineering, Kumamoto 860-8555, Japan

Tubular specimens of 304 stainless steel steels with smooth and notched walls were explosively expanded to fragmentation. The driver was a column of high explosive PETN, inserted into the central bore and initiated by exploding a fine copper wire at the column axis. Streak and framing photos show both radially and axially symmetric expansion of cylinders at average strain rates of above 10^4 s^{-1} . Cooperative work of experimental observation and numerical simulation disclosed the details of expanding cylinders, arisen stresses and fracture criteria. Most of the fragments were successfully recovered, and the circumferential measured widths of the fragments were investigated using a fragmentation model. Smooth cylinders with thicker wall thickness or partially charged explosive expanded slower and fractured with wider spacing. Rather larger fragments were generated only near the groove or slit for notched cylinders, but overall deformation and fragmentation behavior were almost similar to those of smooth ones, except partially charged cylinders showing larger notch sensitivity in slower expansion.

INTRODUCTION

Explosively driven systems are the technique requiring least capital investment, and are suited [1] for start-up of a shock-loading program. The authors have been applied the wire-explosion techniques to develop explosive loading devices [2-4] producing planar, imploding and diverging detonation waves in powder pentaerithritoltetranitrate (PETN). The cylindrically expanding detonation waves were used to examine the dynamic response of steel cylinders at high strain rates of 10^4 s^{-1} [4], which is one-order higher strain rate than those in other similar study [5]. Most of the fragmentation models [6] for cylinders were constructed based on the exploding data detonated at one end of the cylinders.

In this study, rapid expansion and fragmentation behavior for a smooth cylinder of 304 stainless steel are compared with those for cylinders with different amount of explosive charge and wall configuration regarding thickness, surface groove or slit. The observed behavior is reproduced by the numerical simulation using Autodyn 2D, and a modified Grady's model is proposed for fragmentation of such cylinders.

EXPERIMENTAL AND NUMERICAL PROCEDURES

Experiments were conducted utilizing the explosion test facilities at the Shock Wave and Condensed Matter Research Center, Kumamoto University. The developed test assembly for uniform rapid expansion of cylinders driven by explosives is illustrated in figure 1. Tubular specimens of 18Cr-8Ni stainless steel (JIS SUS 304, dynamic proof stress: 340 MPa) were

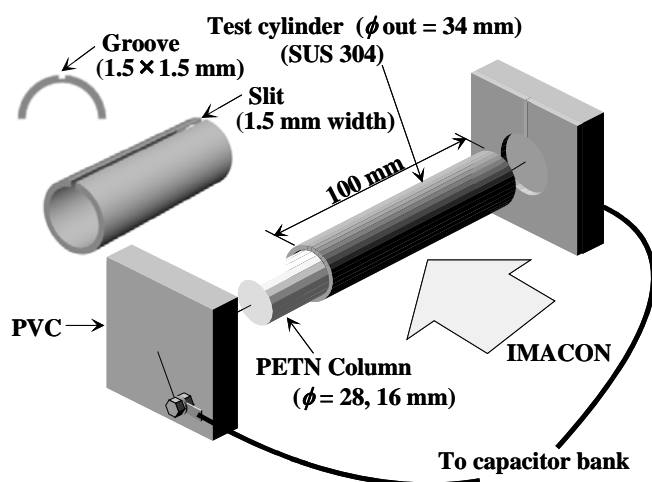


Figure 1: Schematics of test assembly for uniform explosion of metal cylinders

explosively expanded to fragmentation. A column of the high explosive PETN (charged density: 0.90-0.95 g/cc) was inserted into the central bore and initiated by exploding a bundle of three copper wires (diameter 175 μ m) set along the central axis of the column using a discharge current from a high-voltage capacitor bank (40kV, 12.5 μ F). The generated cylindrical diverging detonation wave becomes the driver for the specimens. Test specimens were machined from 304 stainless steel tubes to the cylinders of 100 mm length, outer diameter (D_o) 34 mm and wall (t) 3 mm as a standard test specimen. Other type cylinders with varying wall thickness t : 1.65 mm, 6 mm (D_o : 40 mm) and notched cylinders (GR, SL) with single axial groove (1.5 mm width and depth) or slit (1.5 mm width, space: filled with paste) in the walls were also provided for comparison with smooth wall cylinder (SM). The PETN column of 28mm diameter (fully charged) or 16 mm diameter (partially charged) was placed inside the steel tubes. So in latter case an air-layer 6 mm thick between the explosive and the cylinder wall is left to examine the effect of different explosive driver diameters. Deformation and crack initiation of expanding cylinders were observed with a high speed camera: IMACON 468 using a combination of lights from a xenon lamp as a back light and front lit by the use of a mirror to reflect the flash of exploding wires at the both edges of the cylinder. The fragments of exploded specimens were recovered for all the test conditions in a steel chamber filled with waste cloth. Numerical simulations were performed for all the experiments using a hydro code: Autodyn 2D, where the Steinberg-Guinan model is adopted for the constitutive equation of SUS304. The code is based on Finite Difference Method (FDM) but Smoothed Particle Hydrodynamics (SPH) processor was used with Mott's stochastic failure model for notched specimens or fragmentation analysis. Table 1 includes the test conditions.

Table 1: Summary of experimental data

Type.	Cylinder sizes, mm			PETN dia, mm	\dot{R} , m/s	$\dot{\epsilon}$, $10^4 s^{-1}$	Ave. data of fragments		
	D_o	t	L				t_f , mm	S , mm	F_f , kJ/m ²
Smooth	34	3	100	28/full	1000	3.66	1.76	6.78	173.4
Smooth	ditto (standard cylinder)			16	348	1.33	1.84	13.1	179.1
Smooth	34	1.65	100	30.7/full	1367	4.97	0.99	** (4.03)	** (62.8)
Smooth	40	6	100	28/full	450	2.00	5.12	10.6	181.4
Slit	34	3	100	28/full	1000	3.66	1.72	6.26	134.7
Slit		ditto		16	398	1.57	1.91	14.1	365.2
Groove		ditto		28/full	983	3.82	1.86	6.31	151.7
Groove		ditto		16	382	1.51	1.91	15.5	396.7

* \dot{R} , $\dot{\epsilon}$ are the data at the estimated fracture initiation period. **Very thin fragments folded at both sides

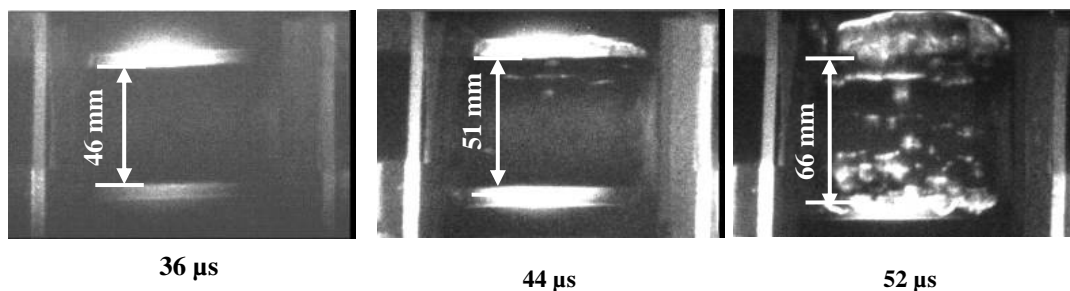


Figure 2 : Typical framing records for an exploding standard cylinder with smooth wall of 3mm thickness and partially charged PETN ($\phi=16\text{mm}$)

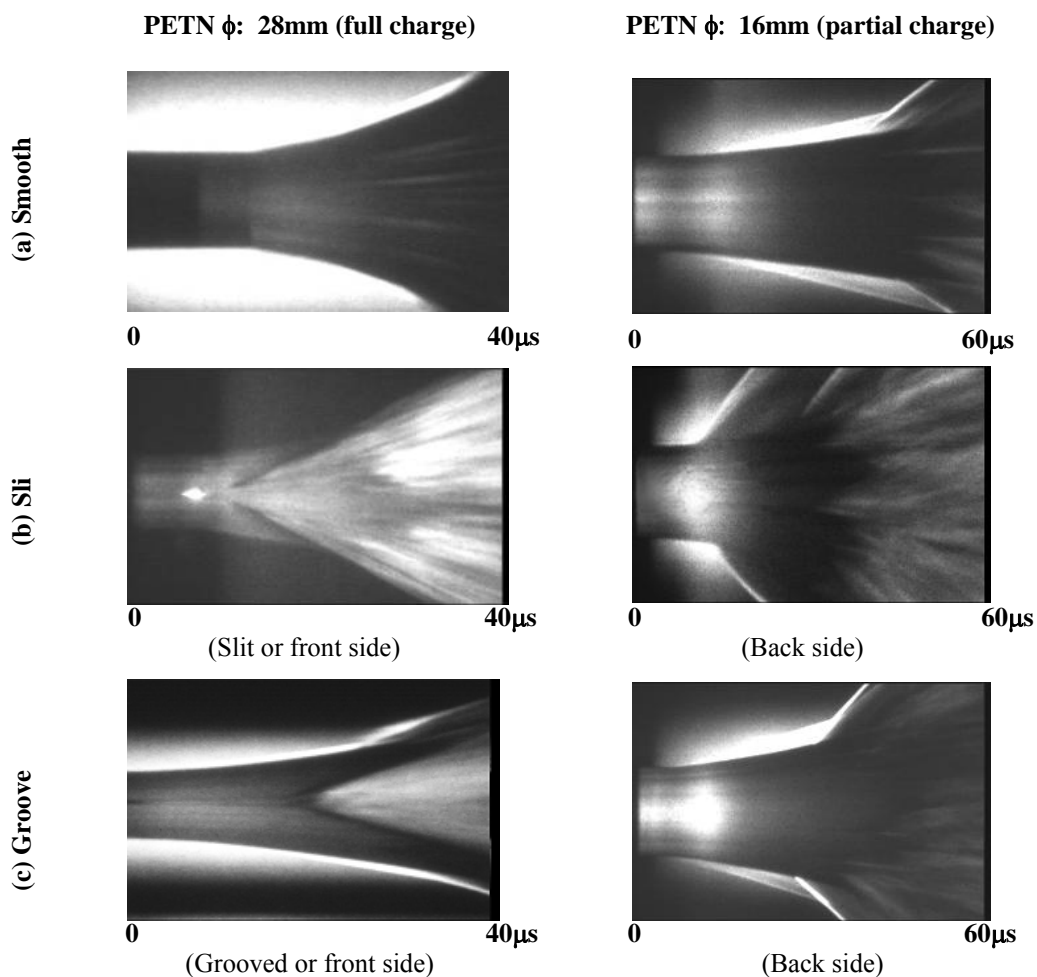


Figure 3: Streak records at the mid-length for exploding cylinders with fully or partially charged PETN and (a) smooth, (b) slit and (c) grooved walls.

EXPANDING BEHAVIOR

Figure 2 shows typical framing records for a partially charged smooth-walled cylinder expanding symmetrically and uniformly. Crack initiation and venting of detonation gas are seen at 44 and 52 μs , these features were also seen in other smooth-walled cylinders. Figure 3 shows the comparison of streak camera records at the mid-length for exploding cylinders with the different wall configuration ((a) smooth, (b) grooved and (c) slit wall) and explosive charges (full and partial). For grooved wall cylinder, early gas venting is seen at 20 μs only in the groove, and for slit wall cylinder, detonation gas starts venting at the instance of detonation arrival at the slit, but overall deformation behaviour is similar to that of the smooth wall cylinder. Figure 4 represents the comparisons of experimental and numerical time-histories of outer wall radii R of fully charged smooth wall cylinders with variation of wall thicknesses. Both results coincide well, and the disjunction radii R_f suggest the critical fracture strain ε_f of 39-50% ($=\ln(2R_f/D_o)$). Figure 5 shows typical numerical time-histories of circumferential stresses in the wall at mid-length of a fully charged standard cylinder representing that the time when all the stresses reach the value of 1.2 GPa corresponds with the disjunction time in figure 4. The similar correspondences were obtained for other cylinders. In figure 4, wall velocities \dot{R} and the circumferential logarithmic strain rates $\dot{\varepsilon}$ ($=\dot{R}/R$) at the estimated fracture initiation period are 1367, 1000, 450 m/s and 4.97, 3.66, $2.00 \times 10^4 \text{ s}^{-1}$ for cylinders with the wall thickness of 1.65, 3, 6 mm respectively. These velocity values are 48-85% of those on the Gurney equation [7], which ignores wave propagation effects and energy consumption in deformation and fracture. Figure 6 shows experimental time-histories of wall radii drawn from the streak camera records for cylinders with different (smooth, grooved, and slit) wall configuration and with different explosive charges (PETN diameter ϕ : 28, 16mm). Large effect of explosive diameter was predictable, but it is noticeable that the average expansion velocities of notched wall cylinders are almost same with that of the standard smooth wall cylinder. Abrupt radius increase region due to overall cylinder fracture is also rather similar for all the tested specimens.

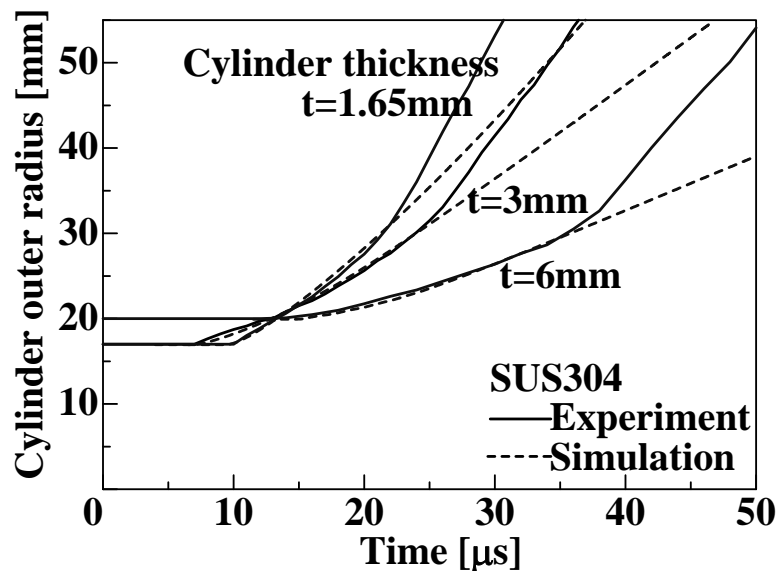


Figure 4: Experimental (solid line) and numerical (dotted line) time-histories of wall radii at the mid-length for uniformly expanding cylinders with variations of wall thicknesses (1.65, 3, 6 mm) and fully charged PETN ($\phi=28\text{mm}$)

Figure 5: An example of numerical time-histories of circumferential stresses in the wall at the mid-length for a standard cylinder (wall thickness: 3mm) with fully charged PETN

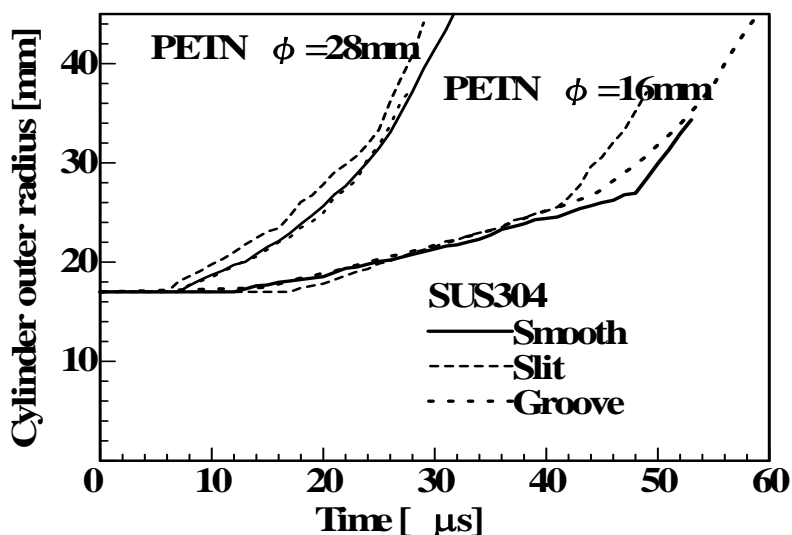
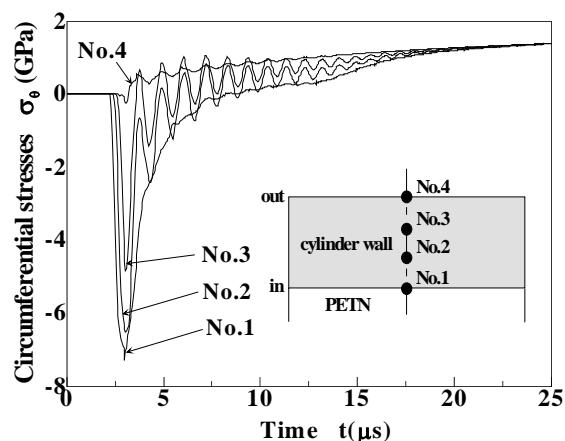


Figure 6: Experimental time-histories of wall radii at the mid-length for uniformly expanding standard cylinders with smooth (solid lines), slit (broken lines) and grooved (dotted lines) walls and fully (ϕ :28mm) and partially (ϕ :16mm) charged explosive PETN

FRAGMENTATION AND DISCUSSIONS

In the investigation on fragmentation, fragment recovery tests were performed and most fragments (81-96%) were successfully recovered for all the test conditions inside a cushion-filled chamber without secondary damage except those (61%) for the thinnest smooth wall cylinder. Figure 7 (a), (b) and (c), (d) show the comparison of recovered fragment photos for smooth wall cylinders with different initial wall thickness of 1.65, 6 mm and slit wall cylinders (3mm thickness) with different explosive charges. The fragments in the photos are placed from large to small ones except those of edge and notch part of the cylinder which are discriminated examining the machined surface of the fragments. It is generally seen that fracture of the cylinder portion is predominantly along elongated strips, with the fracture parallel to the axis. Most of the fragments are 3-6 times longer than they are wide, and shear fracture appears to be the dominant mechanism. The thinly walled or plenty charged cylinder expands more rapidly,

and its fragments apparently become smaller or narrower than those of thick walled or poorly charged one as shown here. The comparison of recovered fragments have indicated that the fragments of notched wall cylinder (SL,GR) are almost similar to those of the smooth wall cylinder except those neighbouring on the notch (groove or slit) which are notably larger than others as shown in figure 7 (c), (d). And the fragment thicknesses lead to the critical strains based on the volume constant hypothesis, and the values correspond with those estimated so far from streak records.

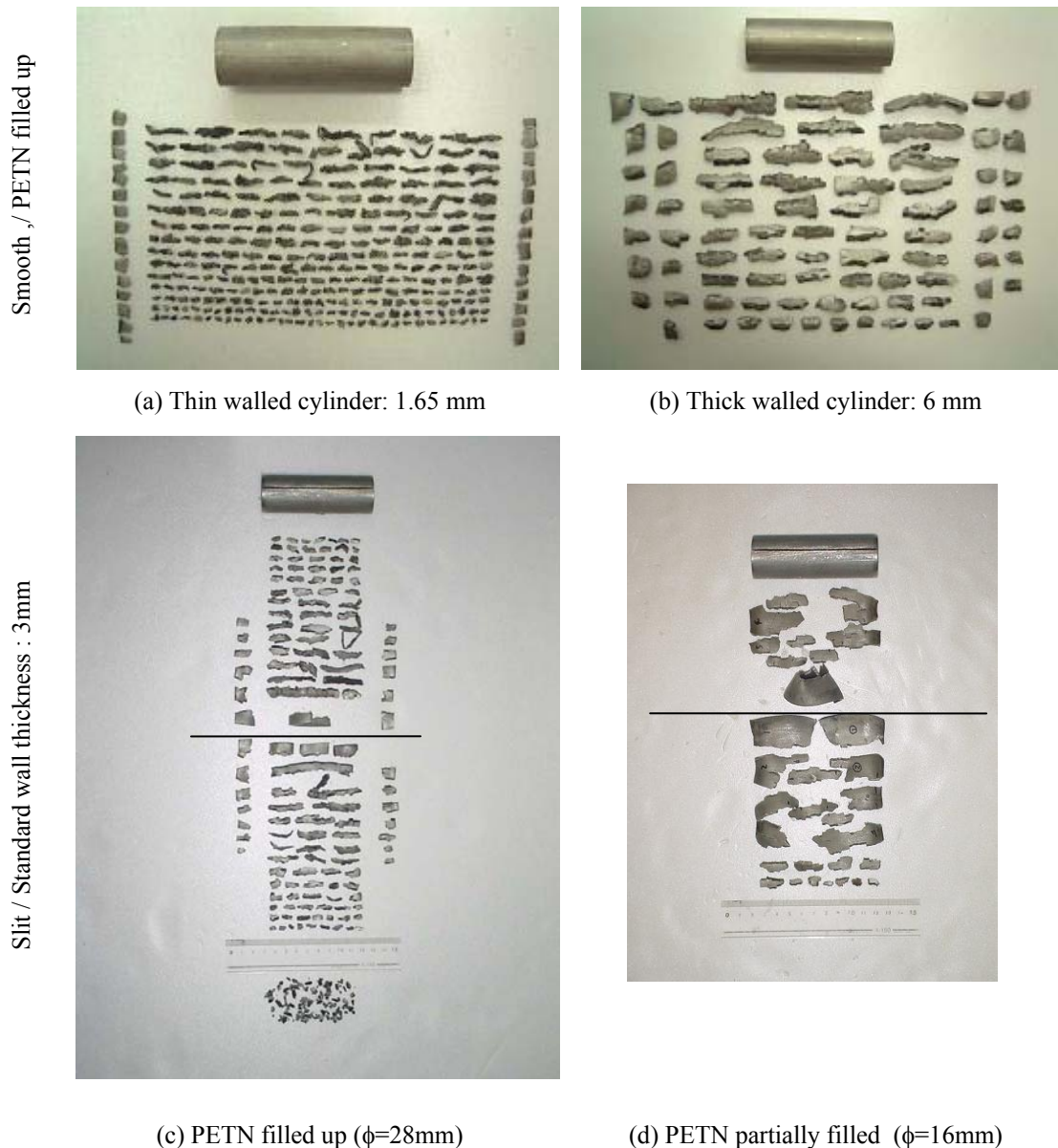


Figure 7 Typical recovered fragments of uniformly exploded cylinders (a): Smooth cylinder with thin wall (fully charged), (b): Smooth cylinder with thick wall (fully charged), (c): Slit cylinder (PETN fully charged), (d): Slit cylinder (PETN partially charged). Solid lines show the location of slits.

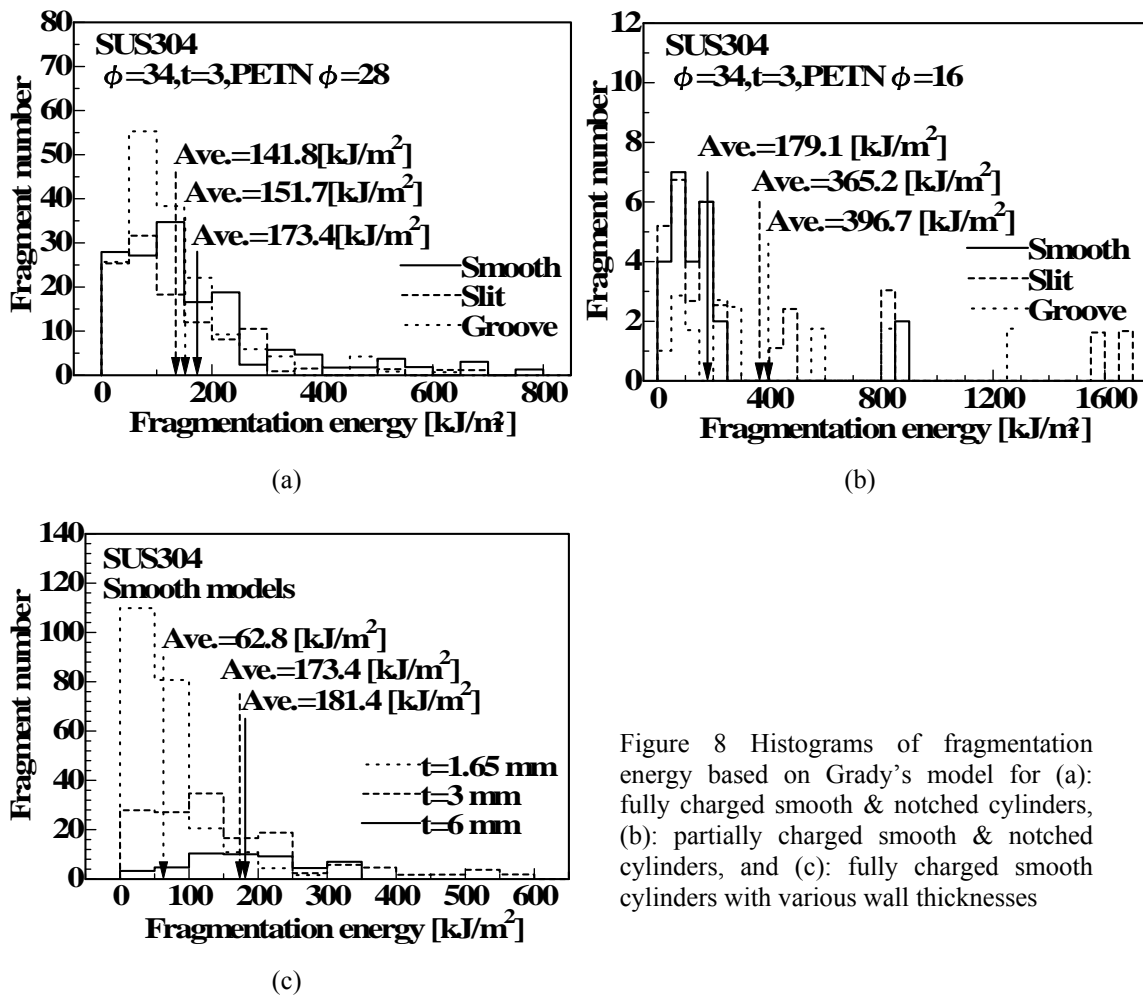


Figure 8 Histograms of fragmentation energy based on Grady's model for (a): fully charged smooth & notched cylinders, (b): partially charged smooth & notched cylinders, and (c): fully charged smooth cylinders with various wall thicknesses

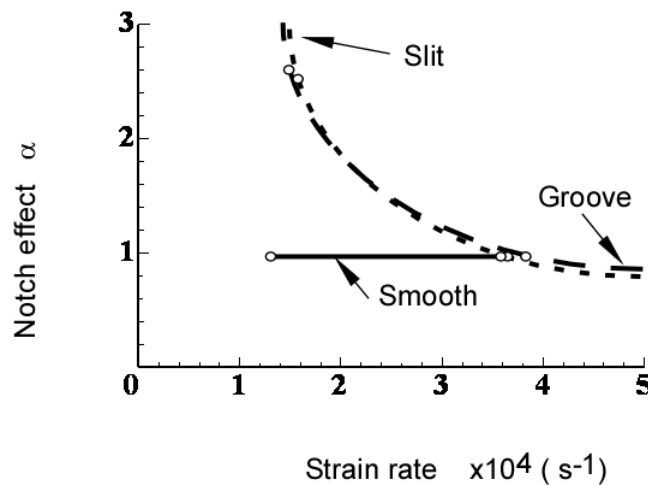


Figure 9: Relations between notch effects in the modified fragmentation model and circumferential strain rates for uniform explosion of cylinders with smooth and notched (slit or grooved) walls

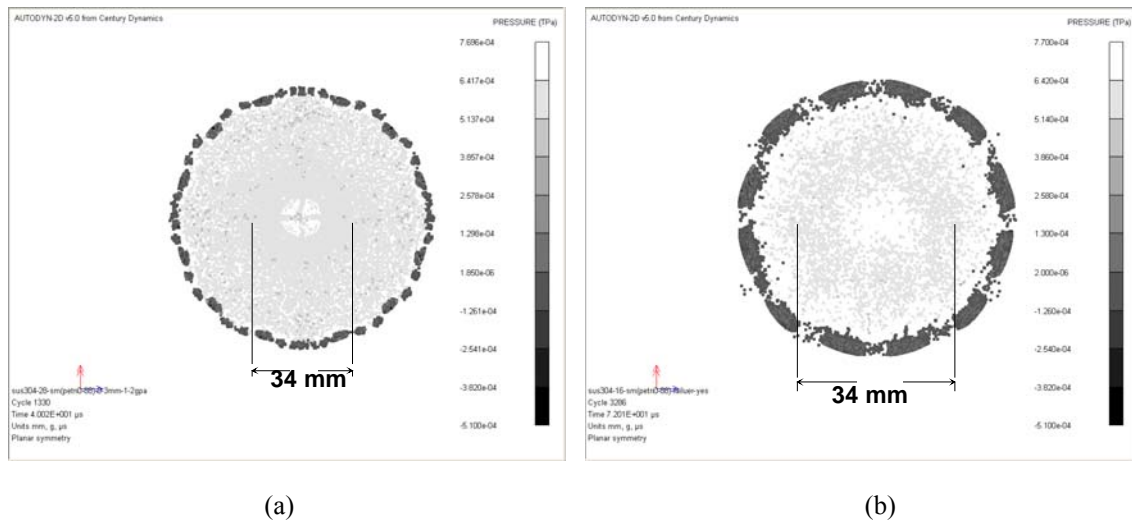


Figure 10: Numerical fragmentation examples using a Smoothed Particle Hydrodynamics processor and Mott's stochastic failure modeling in Autodyn2D for smooth cylinders with (a) fully charged (ϕ :28mm) PETN at $40\mu\text{s}$ and (b) partially charged (ϕ :16mm) PETN at $72\mu\text{s}$.

In this study, the Grady's fragmentation energy $\Gamma (= \rho \dot{\epsilon}^2 S^3/24)$ [6] where ρ : the density of stainless steel, S : circumferential width of fragments and $\dot{\epsilon}$: circumferential strain rate at estimated fracture time was derived for all the test cases. Figure 8 shows histograms of Γ values of fragments for (a): fully charged smooth and notched cylinders, (b): partially charged smooth and notched cylinders, and (c): fully charged smooth cylinders with various wall thicknesses. The average values of Γ for smooth walled cylinders remain 170-180 kJ/m² as a material constant in all the test cases except thinnest cylinder (t : 1.65mm) where the secondary deformation of thin fragments reduced accuracy in measurement. On the contrary, notch effects on Γ values become predominant in case of partially charged or slowly expanded cylinders as shown in figure 8 (b), suggesting need of a modification factor α for the notch effect in the model: $\Gamma = \alpha \rho \dot{\epsilon}^2 S^3/24$. Figure 9 shows the relations between the factor α for notch effects and strain rates for all the test cases.

Generally a stochastic failure model has to be introduced to impose some material heterogeneity or inherent microscopic flaws. In this study an investigation on numerical fragmentation is in progress using the SPH and Mott's stochastic failure model: failure probability $P = 1 - \exp(-Ce^{\gamma\sigma}/\gamma)$, σ :1.2GPa, γ :16. Figure 10 shows typical examples for smooth cylinders with (a) fully charged (ϕ :28mm) PETN at $40\mu\text{s}$ and (b) partially charged (ϕ :16mm) PETN at $72\mu\text{s}$. There still exist some discrepancies between numerical and experimental average fragment widths but such numerical fragmentation tendency coincides with experimental results as shown in figure 7 (c), (d) and table 1.

CONCLUSIONS

The cylinder specimens of 304 stainless steel with smooth, grooved or slit walls expanded at average strain rate of above 10^4 s^{-1} using a developed explosive test assembly for cylindrical uniform expansion. The smooth wall cylinders with thicker wall thickness or partially charged explosive expanded slower and fractured with wider spacing, which basically

matches the fragmentation model. Rather larger fragments were generated only near the groove or slit for notched cylinders, but overall deformation and fragmentation behavior were almost similar to those of smooth ones, except partially charged cylinders showing larger notch sensitivity for fragmentation in slower expansion. Some demonstrative numerical results have shown a possibility of simulation for fragmentation using the SPH processor and a stochastic failure model.

References

1. Meyer, M. A., "Dynamic Behavior of Materials", John Wiley & sons, Inc., 1994
2. Tetsuyuki Hiroe, Hideo Matsuo, Kazuhito Fujiwara, et al., "A Study on Generation of Plane Detonation and Strong Imploding Shocks by Wire-row Explosion", J. of the Japan Explosive Society, Vol. 57, No. 2, 49-54
3. Tetsuyuki Hiroe, Hideo Matsuo, Kazuhito Fujiwara, et al., "Spall in Metals Induced by Explosive Shock Loadings and Protective Measures Using Momentum Traps", Trans. Japan Society of Mechanical Engineers, Ser. A, Vol. 62, 2026-2031
4. Tetsuyuki Hiroe, Hideo Matsuo, Kazuhito Fujiwara, Takayuki Abe and Kazuhiro Kusumegi, "Uniform Expansion of Cylinders at High Strain Rates Using an Explosive Loading", Proc. Int. Conf. on Condensed Matter under High Pressures, National Institute of Science Communication, New Delhi, 1998, 458-465
5. Forrestal, M. J., Duggin, B. W., and Butler, R. I., "An Explosive Loading Technique for the Uniform Expansion of 304 Stainless Steel Cylinders at High Strain Rates", Trans. ASME J. of Applied Mechanics, Vol. 47, 17-20
6. Grady, D. E., and Hightower, M. M., "Natural Fragmentation of Expanding Cylinders", in Shock-wave and High-strain -rate Phenomena in Material, Marcel Dekker, Inc., 1992, 713-721
7. Gurney, R., "The Initial velocities of Fragments from Bombs Shells and Grenades", Report No. 405, Ballistic Research Laboratory, 1943

Dynamic Deformation, Spallation and Fragmentation for Casing Model Vessels Driven by Axially Propagating Explosive Detonation

Tetsuyuki Hiroe, Kazuhito Fujiwara and Hidehiro Hata

Kumamoto University, Faculty of Engineering, Kumamoto 860-8555, Japan

Casing model cylinder specimens of carbon steel and 304 stainless steel were expanded by axially propagating explosive detonation to fracture. Tested casing model cylinder vessels with welded plates at the one ends were fully filled with high explosive PETN, and initiated at the other end explosive surfaces by exploding fine copper wire-rows. Streak and framing photos showed the radial wall velocity of 1043-1143m/s at the fracture initiation slightly larger than that of the uniformly expanded cylinder and the initial breaking fracture at the welded joint. Observed VISAR signals indicated only initial cyclic reflection signals of stress waves for the cylinder wall and a pullback signal of spallation for the end plate, which was compared with the preliminary spall test results of plates induced by planar detonation of PETN. Numerical results reproduced such observed deformation and spallation successfully. Most of the fragments were recovered and they showed the cylinder portion elongated to thinner fragments in comparison with the uniformly expanded cylinder, which suggests relationship with applicability of the fragmentation model.

INTRODUCTION

The explosion hazards can be hardly overrated in modern industrial society, and the research on dynamic responses of structural members and materials is of great concern in fractural control and safety evaluation for explosion of high energy storage containers and explosive wastes. The authors have developed explosive loading devices using the wire explosion techniques to produce planar and diverging detonation waves in powder pentaerithritoltetranitrate (PETN). The plane wave generator was applied to spall tests [1, 2], where slab-like installed PETN was initiated by the simultaneous explosion of parallel copper wire rows over the entire outer surface using an impulsive discharge current from a capacitor bank. The generated planar detonation wave transfers a one-dimensional triangular pressure pulse to the plane specimen in contact with the PETN. It reflects back as a release wave at the free surface, interacting with another release waves coming from the inner surface of the explosive and finally generates internal tensile stress, producing spalling failure in the plate specimen. The cylindrical diverging detonation wave was applied to uniform expansion and fragmentation of steel cylinders [3, 4] including notched wall ones [5] at high speed strain rates of 10^4 s^{-1} , where a PETN column was installed coaxially inside the cylinder specimen and initiated at the central axis by the explosion of a bundle of copper wires. Most of the fragmentation models [6] for cylinders were developed based on the exploding data initiated at a point of the cylinder end.

In this paper, casing model vessel specimens were expanded driven by axially propagating explosive detonation to fracture, and their rapid deformation, spallation and fragmentation are reported comparing with the results for uniform expansion of cylinders and preliminary spall test [2]. The observed behaviour is successfully reproduced and examined by the numerical simulation using Autodyn 2D.

EXPERIMENTAL AND NUMERICAL PROCEDURES

Experiments were conducted utilizing the explosion test facilities at the Shock Wave and Condensed Matter Research Center, Kumamoto University. The developed test assembly for rapid expansion of cylinder vessels driven by axially propagating explosive detonation is illustrated in figure 1. Tested casing model vessels of 100 mm length, 34 or 38 mm outer diameter and 3 or 3.5 mm wall thickness with welded endplates of 6 mm thickness (11mm side-cap length for carbon steel) and 48 and 50 mm diameter at the one ends were fully filled with low density powder of high explosive PETN (charged density: 0.90-0.95 g/cc) and initiated at the other end surfaces by exploding fine copper wire (diameter: 175 μ m) rows using a discharge current from a high-voltage capacitor bank (40kV, 12.5 μ F). They were made of carbon steels (cylinder: JIS SGP-E-G/25A95, static yield stress: 190 MPa / endplate: JIS S55C, static yield stress: 400 MPa) or 304 stainless steel (JIS SUS 304, static proof stress: 220 MPa). Smooth cylinder specimens made of the same materials were also provided for uniform cylindrical expansion tests, where an inserted fully-charged PETN column was initiated at its central axis also using wire explosion techniques as shown in previous tests [5]. Table 1 includes the test

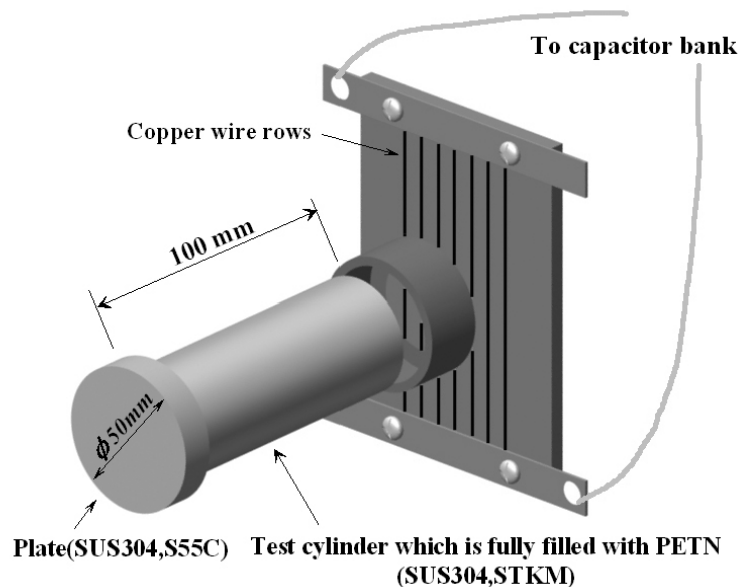


Figure 1 : Schematics of test assembly for axially phased expansion of casing model vessels

Table 1: Summary of experimental data

Type ***	Cylinder-sizes** mm		Material	* \dot{R} , m/s	* $\dot{\epsilon}$, 10^4s^{-1}	Ave. data of fragments			
	D_o	t				L , mm	t_f , mm	S , mm	Γ , kJ/m^2
Casing	34	3	SUS304	1143	3.97	21.4	1.66	6.06	173
Casing	38	3.5	C. Steel	1043	3.12	38.5	1.49	10.18	291
Cylinder	34	3	SUS304	1030	3.77	16.3	1.76	6.31	163
Cylinder	38	3.5	C. Steel	863	2.53	31.0	2.27	8.16	194

* \dot{R} , $\dot{\epsilon}$ are the data at the center part of casings and cylinders in the estimated fracture initiation period.

**Welded endplate sizes for casing models: 48 ϕ x 6t mm, cap length: 11mm (carbon steel), 50 ϕ x 6t mm (stainless steel)

***VISAR was applied for a casing model of 304 stainless steel, cylinders of carbon steel with fully and partially charged PETN. PETN was filled up for all other tests.

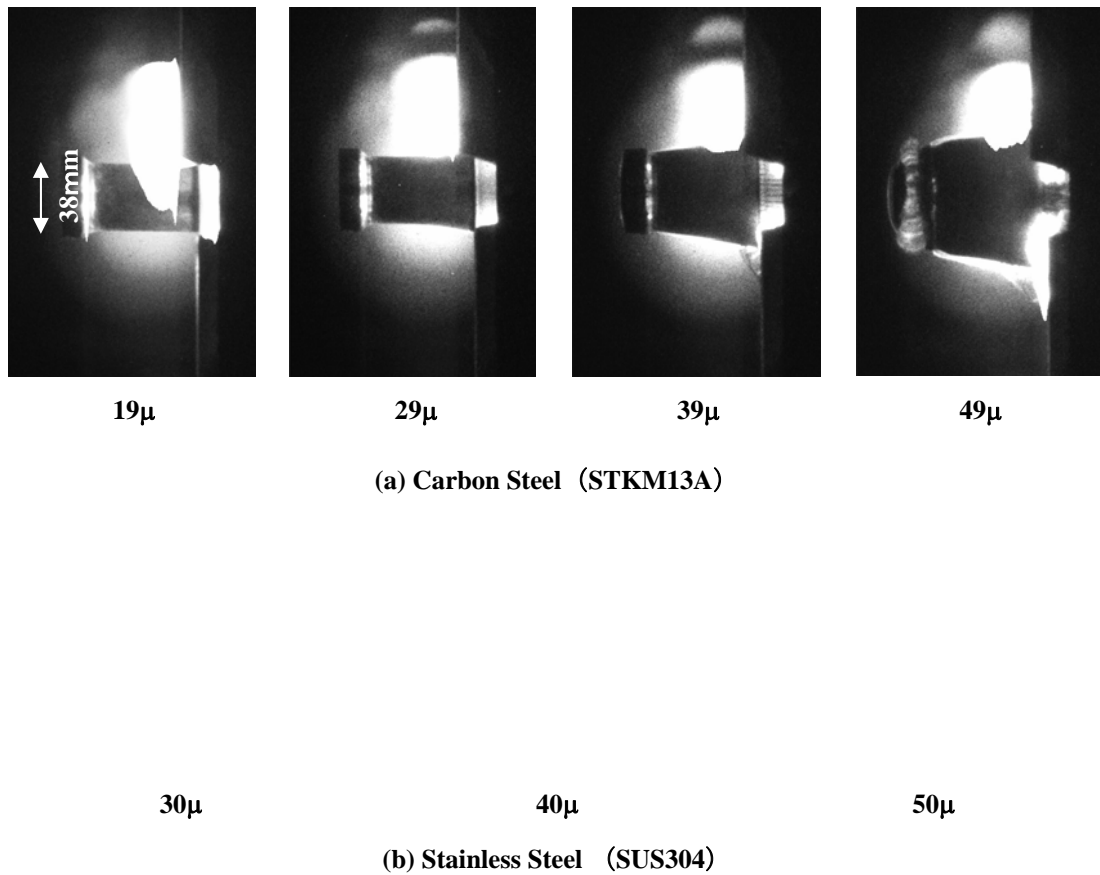


Figure 2 : Framing records for exploding casing model vessels of carbon steel (a) and stainless steel (b)

conditions. Axially phased expansions of casing models were observed with a high speed



Numerical simulations were performed for all the experiments using a hydro code: Autodyn 2D, where the Steinberg-Guinan, Johnson-Cook and JWS models were adopted for the constitutive equations of 304 stainless steel and carbon steels, and equation of state for PETN. The code is based on Finite Difference Method (FDM), Lagrange-Euler coupling.

EXPANDING BEHAVIOR, FRAGMENTATION AND VISAR SIGNALS

Figure 2 shows framing records for casing models of carbon steel and stainless steel. In both cases expansion is propagating symmetrically to the endplate. The fracture at the welded joint of a cylinder and an endplate occurs at rather early time. Time histories of wall radii at mid-length of cylinder parts obtained from the framing and streak records for casing models and cylinder models are shown in figure 3 where R'_{out} is the outer radius at the failure occurrence estimated

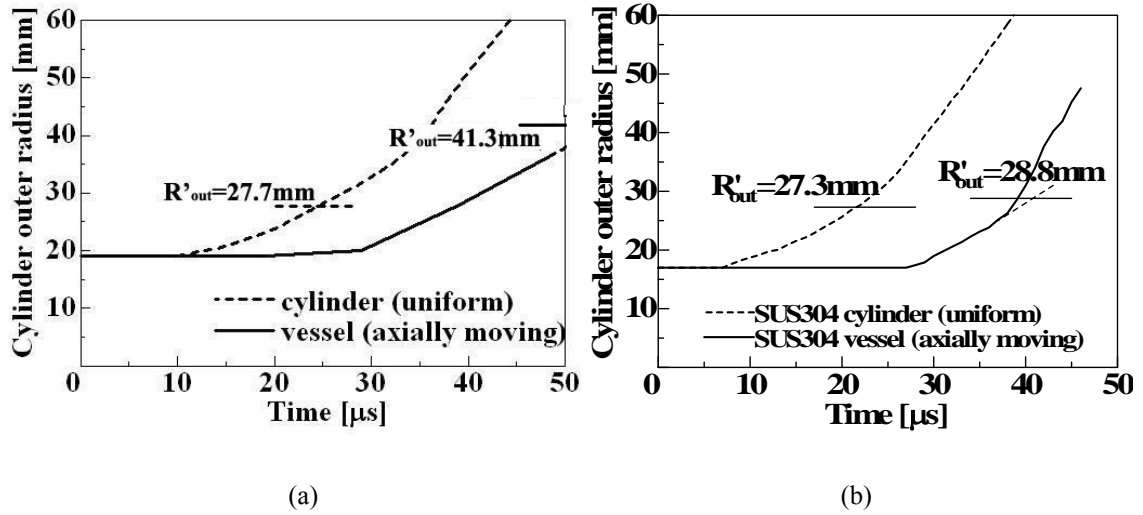


Figure 3 : Time-histories of wall radii at mid-length of cylinders and model vessels, made of carbon steel (a) and stainless steel (b)



Figure 4 : Recovered fragments of axially-phased expanded casing model vessels of carbon steel (a) and stainless steel (b)

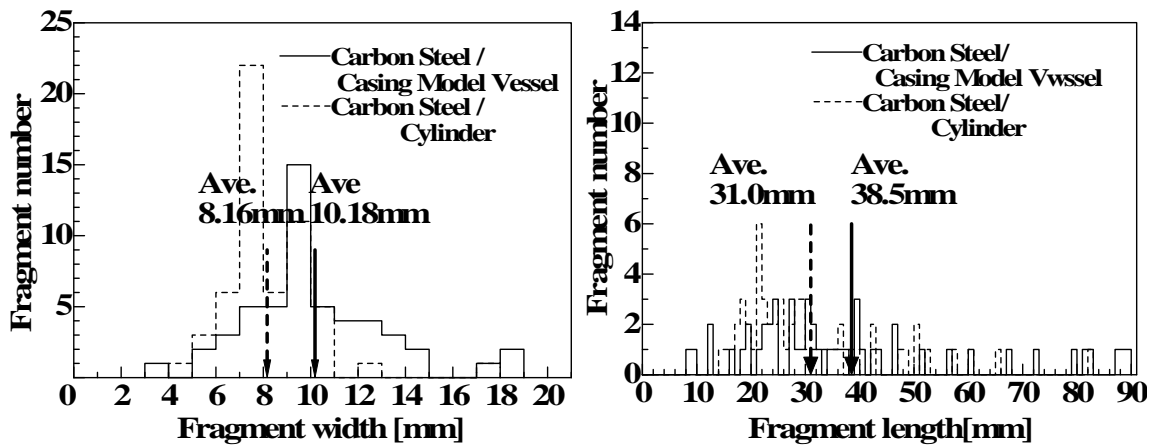


Figure 5: Statistics of fragment width (a) and length (b) for an exploded casing model vessel and a cylinder made of carbon steel

from the abrupt increase of observed radius, the disjunction from the numerical radius growth and the thicknesses of recovered fragments. The stainless steel specimen starts expanding and final fracture rather earlier than carbon steel specimen but the average expansion velocity are almost similar. It seems related to the dynamic stress-strain behaviour of both materials.

Most of the fragments were recovered without secondary damage for all the tests. Photos in figure 4 are recovered fragments for casing models, which easily classified into four groups: separated endplate, welded joint parts, cylinder edge parts and main cylinder parts examining the surface states of fragments. Fracture of the cylinder portion is predominantly along elongated strips, with the fracture parallel to the axis. Most of the fragments are 3-10 times longer than they are wide, and shear fracture appears to be the dominant mechanism. It is seen that the average width of carbon steel casing model is apparently larger than that of stainless steel. Figure 5 shows statistics of the fragment width and length for casing model vessel and the uniformly expanded cylinder made of carbon steel. The fragments of casing model are wider and longer than those of cylinder for specimens of carbon steel. Fragment data in this study are summarized in table 1 including thickness data which are smaller (thinner) for casing model as predicted from expansion behaviour. In case of 304 stainless steel, the fragments of casing model are longer but as wide and thin as those of cylinder.

In figure 6, VISAR signals (time histories of free surface velocity) are typically shown (a): for uniform expansions of carbon steel cylinders with fully charged and partially charged PETN, (b): for the endplate of the exploded casing model vessel of SUS304 with numerical velocity history, and (c): for a direct-explosive impact test of SUS304 plate previously performed [2]. Figure 6 (a) expresses observed VISAR signals during the acceleration terms, and the vibration signal especially with use of sensitive delay unit II indicates the initial cyclic reflections of stress waves in the cylinder wall and wave length corresponds with wall thickness, which designates no occurrence of spall in the cylinder wall 3mm thick. The VISAR signal in figure 6 (b) represents a time-history of the velocity at the outer surface center of the endplate for fully charged casing model vessels of 304 stainless steel. The pullback signal just after the initial shock reflection indicates spall occurrence in the endplate 6mm thick, and the pullback velocity range corresponds with that in figure 6 (c), where a circular plate 20mm thick and 50mm diameter was touch with PETN slab 15mm thick.

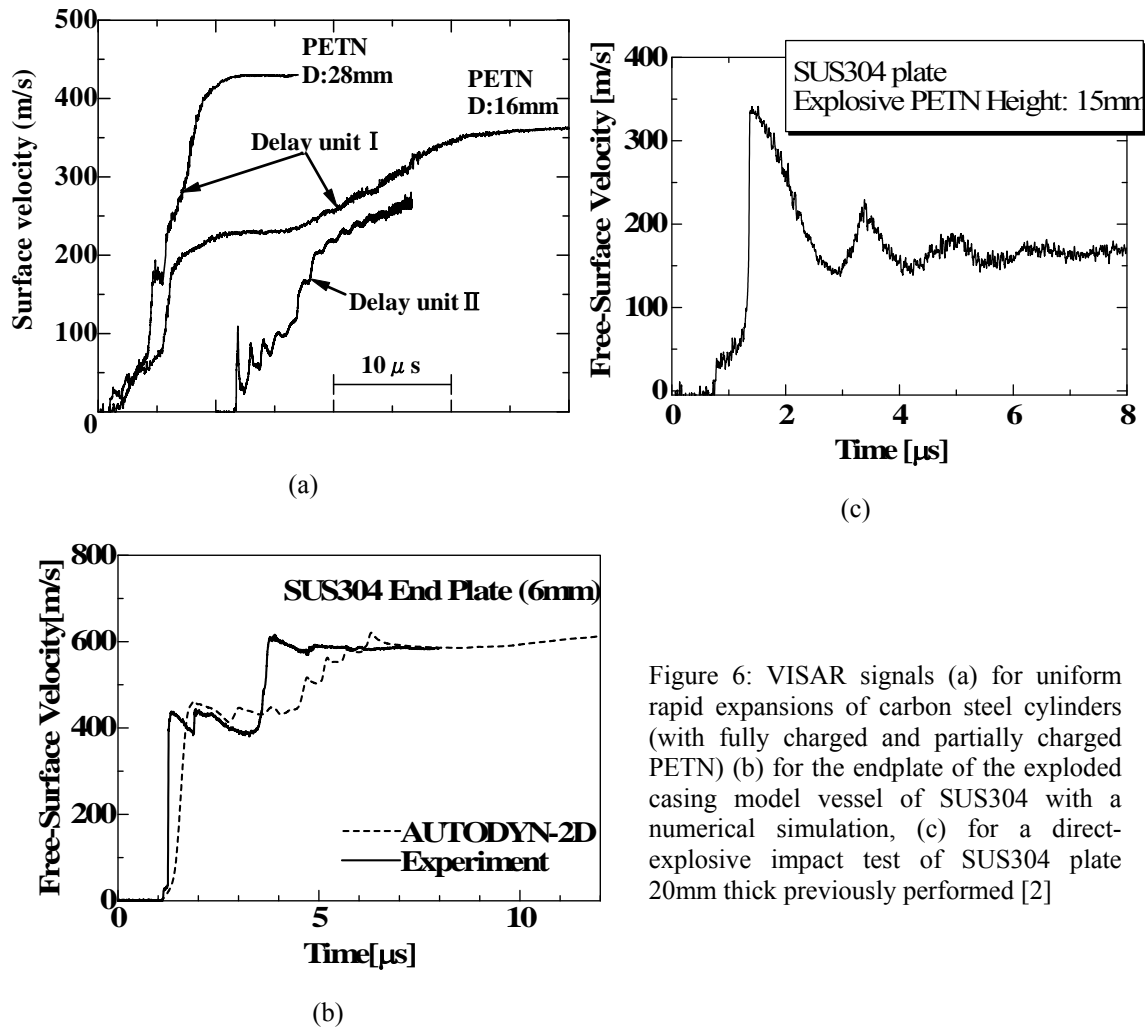


Figure 6: VISAR signals (a) for uniform rapid expansions of carbon steel cylinders (with fully charged and partially charged PETN) (b) for the endplate of the exploded casing model vessel of SUS304 with a numerical simulation, (c) for a direct-explosive impact test of SUS304 plate 20mm thick previously performed [2]

NUMERICAL SIMULATION AND DISCUSSIONS

Numerical simulations reproduced observed deformation behaviour shown in figures 2 and 3 except the responses after crack propagation and venting of detonation gas. Wall velocities \dot{R} and the circumferential logarithmic strain rates $\dot{\epsilon}$ ($=\dot{R}/R$) at the estimated fracture initiation period are 1143-863 m/s and 3.97 - $2.53 \times 10^4 \text{ s}^{-1}$ for PETN filled specimens as shown in table 1. These velocity values are 75-92% of those on the Gurney equation [7]. The radius growth rates \dot{R} for casing models are a little larger than those of cylinders. The disjunction radii of numerical and experimental radius growth coincide with R'_{out} in figure 3, which suggest the critical fracture strain ϵ_f ($=\ln(2R_f/D_o)$) of 37.7-47.4% for cylinders and 52.7-77.6% for casing models. In the numerical simulations, biaxial stress conditions are generated in the expanding walls and figure 7 shows typical numerical time-histories of predominant circumferential stresses in the wall at mid-length of the cylinder parts for casing models. The axial stresses in casing models are a little larger than those of uniformly expanded cylinders. In case of casing models of stainless steel, critical stress values can be decided as the stress at the damage observed time; 1.2 GPa should be a failure criterion. But for carbon steel model, the stresses stay nearly constant, and then there seems critical strain value for carbon steel specimens. Such characteristics are similar for cylinder models, and they are understandable from loading mode differences and dynamic stress-strain relations especially on work-hardening for both materials.

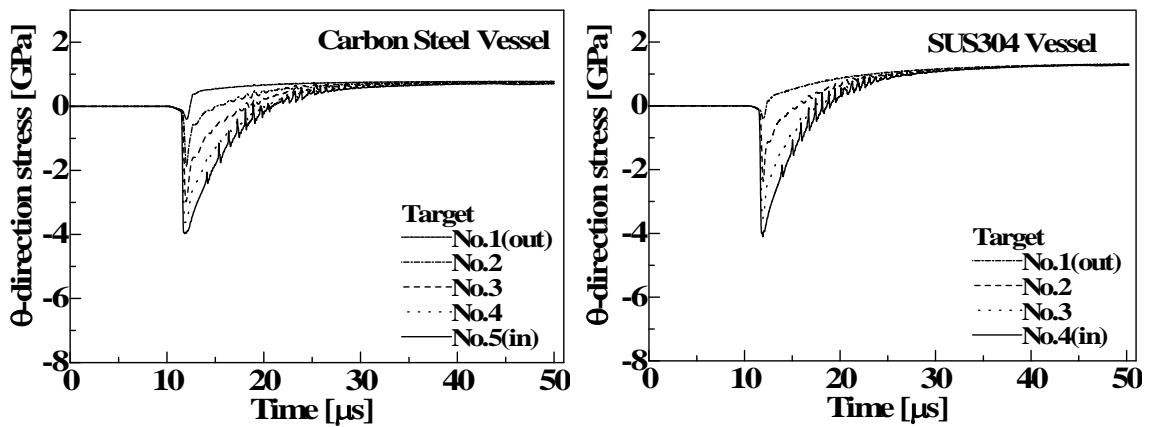


Figure 7: Numerical time-histories of circumferential stresses in the wall, at the mid-length for casing model vessels of carbon steel and SUS304 stainless steel

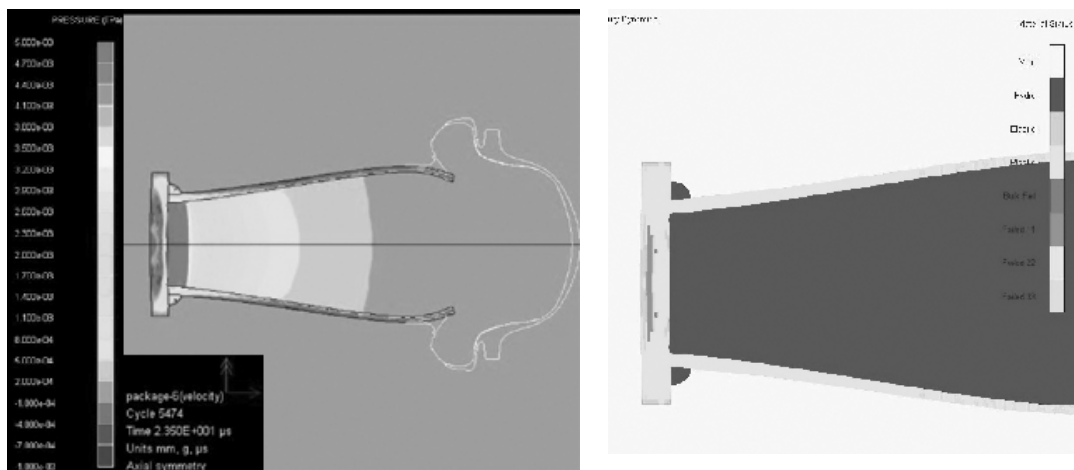


Figure 8: Numerical simulation of (a) pressure and (b) failure distributions at 23.5 μs for casing model vessel of SUS304 stainless steel. Those are the situation just after the spallation has been generated.

In this study, the Grady's fragmentation energy $\Gamma (= \rho \dot{\epsilon}^2 S^3 / 24)$ [6] where ρ : the density of stainless steel, S : circumferential width of fragments and $\dot{\epsilon}$: circumferential strain rate at estimated fracture time was calculated for all the test cases. The average Γ values based on the configuration data of recovered fragments are listed in table 1, where the values of 304 stainless steel show a little influence of expansion modes but for those of carbon steel there exists apparent influences of loading modes. This also seems related to mechanical properties of the materials.

A numerical time-history of free surface velocity at the center of 304 stainless steel endplate is compared with the VISAR signal in figure 6, using critical spall stress value 1.0 GPa. Numerical velocity shows some blunt increase, but both overall results represent similar responses including the pullback signal and following step-up increase. Figure 8 shows the numerical pressure and failure distributions at 23.5 μ s for casing model of 304 stainless steel just after the spallation has been generated, indicating negative pressure distribution and the occurrence of spallation in the endplate numerically. The step-up increase of surface velocity due to wave interactions was also known in the simulation.

CONCLUSIONS

The casing model vessels of carbon steel and stainless steel expanded to fracture being driven by axially propagating explosive detonation, comparing with the uniformly expanded cylinders. Casing models expanded a little faster than cylinder models and the stainless steel specimens starts expanding and final fracture rather earlier than carbon steel ones, which seems related to mechanical behaviour of both materials. The statistics of recovered fragments show that the fragments of carbon steel casing model are wider, longer and thinner than those of cylinder model, and the loading modes gave some influence on the fragmentation energy, but those of stainless steel specimens which seems to have stress criterion showed little influences of expansion modes. VISAR signals and numerical simulation results indicated no occurrence of spall in cylinder wall, but the endplate of casing models generated spallation after the initial shock reflection.

References

1. Tetsuyuki Hiroe, Hideo Matsuo, Kazuhito Fujiwara, et al., "Spall in Metals Induced by Explosive Shock Loadings and Protective Measures Using Momentum Traps", Trans. Japan Society of Mechanical Engineers, Ser. A, Vol. 62, 2026-2031
2. Tetsuyuki Hiroe, Kazuhito Fujiwara, Hideo Matsuo, and Naresh N. Thadhani, "Explosively Produced Spalling in Metals and Its Loading Effects", Proc. of the 4th International Symposium on Impact Engineering, 16-18 July, Kumamoto, Japan, 2001, 851-856.
3. Tetsuyuki Hiroe, Hideo Matsuo, Kazuhito Fujiwara, Takayuki Abe and Kazuhiro Kusumegi, "Uniform Expansion of Cylinders at High Strain Rates Using an Explosive Loading", Proc. Int. Conf. on Condensed Matter under High Pressures, National Institute of Science Communication, New Delhi, 1998, 458-465
4. Tetsuyuki Hiroe, Kazuhito Fujiwara, Takayuki Abe and Masatake Yoshida, "Rapid Expansion and Fracture of Metallic Cylinders Driven by Explosive Loads", Proc. of 13th Biennial International Conference of the APS Topical Group on Shock Compression of Condensed Matter, July 20-25, Portland OR, USA, 2003, 465-472
5. Tetsuyuki Hiroe, Kazuhito Fujiwara and Hidehiro Hata, "Dynamic Deformation, Spallation and Fragmentation for Casing Model Vessels Driven by Axially Propagating Explosive Detonation", to be presented at 16th DYMAT technical meeting on dynamic material behaviour related to security applications, Brussels, 27-28 October, 2005
6. Grady, D. E., and Hightower, M. M., "Natural Fragmentation of Expanding Cylinders", in Shock-wave and High-strain -rate Phenomena in Material, Marcel Dekker, Inc., 1992, 713-721
7. Gurney, R., "The Initial velocities of Fragments from Bombs Shells and Grenades", Report No. 405, Ballistic Research Laboratory, 1943

Behaviour of metallic plates subjected to explosions.

Experiments and modelling in the field of large deformations and rupture.

Olivier Pennetier¹, Krzysztof Woznica¹, Martial Mosnier¹, Benjamin Daudonnet¹, Jérôme Renard¹, Frédéric M. B. Mercier²

¹*Laboratoire Energétique Explosions Structures, EA 1205 Université d'Orléans et ENSIB
63 Av de Lattre de Tassigny, 18020 Bourges Cedex - France*

²*INERIS, Accidental Risk Department, BP 2, Verneuil en Halatte, 60550, France*

An experimental and numerical study of metallic circular plates subjected to dynamic loads leading to rupture is presented. Various loads have been produced by different kinds of explosions: deflagrations or detonations of stoichiometric hydrogen-oxygen mixtures. A sample response modelling is implemented with the MSC MARC software, using axisymmetrical shell elements and elasto-viscoplastic laws and including damage.

INTRODUCTION

Metallic thin walled pressure vessels or pipes are of common use in the industrial field. They can contain fluids at various thermodynamic states (gas, liquid or liquefied gas). Some phenomena, e.g. explosion ignition, uncontrolled chemical reaction..., can drive a sudden pressure wave to travel across those vessels, to reflect on its walls and finally to result either in their bursting or in the splitting of the enclosure into big pieces. This event finally results, in the first case in torn structures and fragments, while, in the second case, it can lead to the projections of entire parts of the vessel in its environment. The dynamics of the whole phenomenon, from its beginning to its final state, still remains very difficult to describe and explain.

For a better quantification of the potential effects of a capacity bursting on its environment, a preliminary characterisation of both the possible loading pressure and the structure response is required. Moreover, the load and the response seem to be generally coupled.

An underlying problem is to know whether two systems with similar initial conditions can produce the same response. If it was possible to show that the phenomenon is deterministic, it would be the proof that a real way of prediction is worth exploring.

Numerous experimental studies have already been done on the subject of circular metallic plates responses to dynamic loads. The first studies dealt with the permanent central deflection of circular plates. Florence (1966) compared his experimental results to those theoretically

obtained by Wang (1955). Jones (1968) took into account membrane stresses in his study of simply supported circular plates. Wierzbicki (1954), Perrone (1967), and, later, Jones (1968), Kelley and Wilshaw (1968), investigated the influence of the deformation ratio. The displacement of the plate centre as a function of time was examined by Duffey and Key (1967, 1968) for circular plate samples equipped with strain gauges and observed by means of a high-speed camera. Bodner and Symonds (1979), Nurick (1989), Teeling-Smith (1991) and later Olson (1993) experimentally studied plates with a condenser microphone placed near the middle of the sample. Nurick et al. (1985, 1987) measured deflection versus time with an interferometer technology. More recently, the dynamic response of plates, subjected to a shock wave, was investigated by Pennetier and Renard (1998), Klosowski et al. (2000) and Woznica et al. (2001).

Cracking and bursting have mostly been studied through research applied to pipelines: Emery and Kobayashi (1986) provided values for strain rate and crack growth rate. Beltman et al. (1999) investigated the structural response of cylindrical preflaw samples to a detonation loading.

A few years ago, the bursting, the strain and the bursting surface of aluminium pipes with different preflaws sizes, loaded with a detonation, have been reported (Chao and Shepherd, 2002).

On a numerical point of view, different models dedicated to the general subject of vessel rupture already exist. Some of them, for example those of Qiu et al. (2003), Recho (1995), Su et al. (1999), insist on the mechanical aspects (for example crack propagation) and others on fluid mechanics, like Haque et al. (1990), Leung (1990), Woodward and Mudan (1991), Fthenakis et al. (2003). Few models take both aspects into account. Most studies are dedicated to pipelines, as presented in Lung (1994) and Rivalin (1998) works.

In this paper, the following strategy is adopted to investigate the problem:

1. experimental study on the simplest possible structures, viz. circular metallic plates, subjected to various well controlled dynamic excitations (explosions) ;
2. numerical modelling of the phenomenon with a finite element software ;
3. Comparison of experimental results with numerical ones.

Thus the current work focuses on the accuracy of the modelling of metallic plates subjected to dynamic loads in regard to their experimental responses.

EXPERIMENTS

Set-up

The experimental device is presented figure 1. Two stainless steel tubes, are used. The tube 1 is 800 mm long (tube 1), the other, 400 mm (tube 2). Both have a 194 mm internal diameter and are 12.5 mm thick. The plates at the ends of the tubes are maintained by means of 4 rods. Using this system, no welding is required.

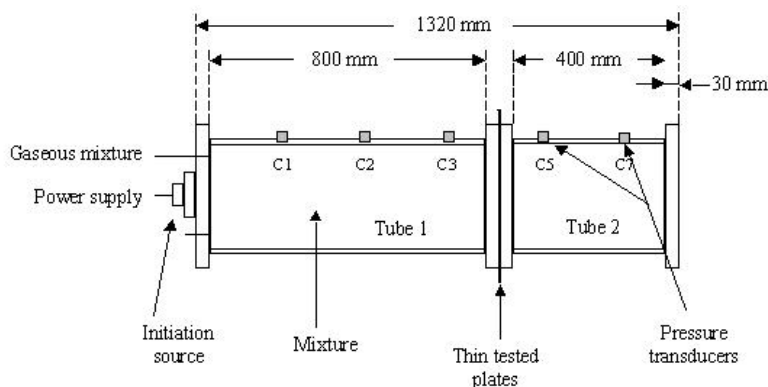


Figure 1: Experimental device

For the test, the sample is tightened between both tubes using 4 strong screws and massive flanges and the explosion is produced in the longer tube. The experimental device has been designed to withstand very high pressure, since the reactive media explosions present overpressure up to 150 bar.

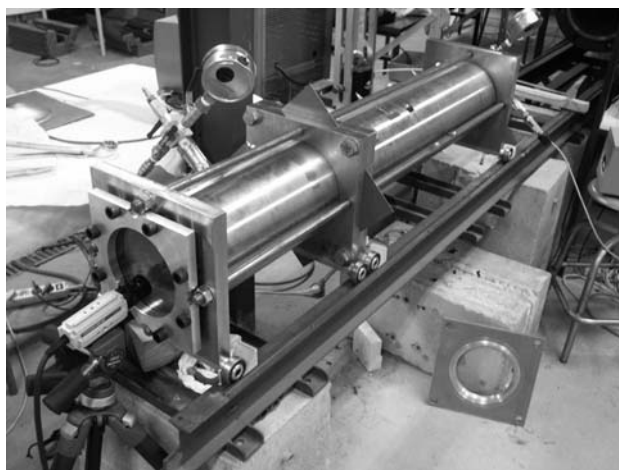


Figure 2: Photograph of the whole set-up

Figure 2 displays the whole set-up. In addition to the different elements that have already been described above, a high speed camera is shown in the foreground. It is used to follow the cracking / bursting of the tested plates ($\Delta t: 10^{-4}$ s).

A typical experiment is conducted as follows. A testing plate is clamped between tubes 1 and 2, using 4 screws and a system of double rings. The vacuum is simultaneously realised in tubes 1 and 2. A predefined gaseous mixture is then introduced in tube 1, at the same time as air is introduced in tube 2, so that the plate remains unloaded, due to the balance of pressures in the two tubes. At the time of fire, the pressures are the same on both side of the sample, in each tube.

Two kinds of explosion can be produced:

- the deflagration, a subsonic wave, is ignited by a low energy discharge (some mJ). An electric spark can easily generate such a phenomenon.
- the detonation needs a stronger ignition energy (50 J in our experiment). This energy is generated by the capacitors discharge through a thin copper wire. The wire instantaneously melts, which creates a plasma. Details about this set-up can be found in Pennetier et al.

(1998). The subsequent shock wave is supersonic and very stable. It is a deterministic and transient phenomenon, whereas a deflagration is partially stochastic.

In these experiments, it was observed that an explosion initiated in the deflagration mode generally evolved towards the detonation mode. Nevertheless, when the shock wave reaches the tested plate, its celerity and overpressure peak are not those of a real detonation. To summarise and to simplify this complex phenomenon, in this context, the term of deflagration will be used for an explosion obtained with the lowest energy ignition. Actually, it corresponds to the transition of a deflagration to a detonation, which explains that supersonic velocities could be reached.

On the contrary, for low initial pressures (less than 0.5 bar), a strong energy ignition does not immediately initiate a detonation. The explosion, at its beginning, is a deflagration. It quickly accelerates but the tube is not long enough to permit a well established stationary detonation. So, the velocity can remain subsonic.

In short, the terms of deflagration and detonation are not really appropriate to describe the two explosion modes that have been experimentally observed. Nevertheless, in this context, by convenience and to simplify, these terms will be respectively associated to the explosions originated by low and high ignition energies.

Loading on the plate sample

The reactive medium is a stoichiometric hydrogen-oxygen mixture ($2\text{H}_2+\text{O}_2$). It has been employed at different initial pressure levels in order to get detonations as well as deflagrations. As an example, the figure 3 illustrates the pressure evolution as a function of time for a detonation corresponding to an initial pressure of 1.2 bar. This signal was recorded by closing the first tube with a thick rigid plate equipped with pressure transducers. This modified device has permitted to investigate the shape of the pressure loads as well as to check their reproducibility through various tests for detonations as well as for deflagrations. The curve of figure 3 is typical of a detonation: it exhibits a main overpressure peak of which duration is less than 5 microseconds. The other peaks represent the multiple reflections of the shock wave.

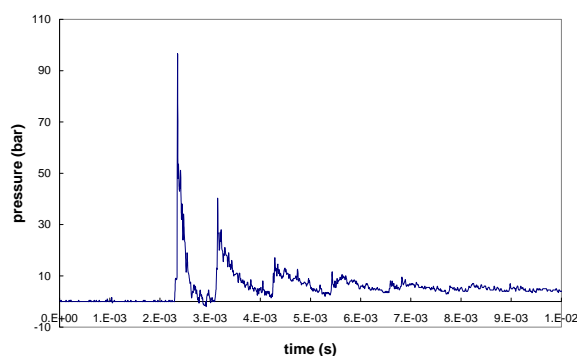


Figure 3 : Pressure record as function of time - detonation - ($P_i=1.2$ bar)

According to the kind of loading (deflagration or detonation), both the duration and the amplitude of the pressure are different. In a detonation, the pressure peak has a more important amplitude but a shorter duration than in a deflagration. The notion of impulse, linking pressure and time, is of great importance for the effects of explosion on a structure. Tables 1 and 2 summarise the impulse on the tested plate and the value of the initial pressure peak in a deflagration and in a detonation. It can be noticed that, for the same initial pressure, the impulse values in a deflagration and in a detonation are close, only about 8 % higher for a detonation than for a deflagration. The pressure wave velocity is also reported, deduced from pressure gauges.

In a long tube, a detonation evolves towards a stationary solution. In this condition, the pressure front travels at the Chapman-Jouguet velocity, depending on the mixture and on its initial pressure. In these experiments, the tube 1 is too short to allow the Chapman-Jouguet condition to be reached.

Initial pressure (bar)	Impulse (N.s)	Pressure peak (bar)	Wave velocity (m.s ⁻¹)
0.4	35	4.4	181
0.6	68	7.5	200
0.8	98	40	309
1	130	62	345
1.2	171	92	419
1.4	177	120	453
1.6	220	125	503

Table 1: Deflagration loading parameters

Initial pressure (bar)	Impulse (N.s)	Pressure peak (bar)	Wave velocity (m.s ⁻¹)
0.4	44	6.3	233
0.6	97	42.5	351
0.8	135	76.1	417
1	158	94.2	503
1.2	216	96	580
1.4	230	104	640
1.6	244	133	645

Table 2 : Detonation loading parameters

Test results

Experimental tests were conducted on 1 mm thick Al 5754 plates, subjected to the loads previously described. The properties of this aluminium alloy have been evaluated from tensile tests and are given below, in table 3.

	Young modulus (GPa)	max. tensile stress (MPa)	yield stress at $\epsilon_{0,2\%}$ (MPa)	crack strain (%)
Al 5754	70	201,4	110	20

Table 3: Tensile properties of the Al 5754 alloy

The simplest test consists in surveying the sample shape after explosion. At a first time, whatever the load, only two kinds of behaviour were obtained: the bulging of the plate, or its splitting along its edge and ejected.

These two kinds of behaviour did not permit to follow the kinetics of the plate rupture. So, a modification of the plate clamping has been achieved in order to get large plastic deformations and the ejection of a metallic cap, instead of the entire plate ejection. To do so, a ring with rounded edges was added between the tube and the plate. It prevents the plate from being systematically cut out.

Such a modified device allows greater pressure loading to be used, without cutting out the whole plate. As a result, caps, of which diameter is dependent from the explosion intensity, could be ejected. Due to its interest, this unexpected consequence is discussed below.

For an initial pressure of 1.1 bar, the plate is highly deformed, without rupture. The associated deflection in the centre is about 7 cm. For an initial pressure of 1.2 bars, a small circular cap with a 3.5 cm diameter is ejected. The deflection measured on the rupture perimeter is of 5 cm. In this area, immediately close to the edge, the thickness of the plate is seriously reduced: 0.72 mm instead of 1 mm. For a higher initial pressure, 1.3 bar, the same phenomenon is observed, but the diameter of the cap becomes 10 cm. Finally, for an initial pressure of 1.4 bar, a larger but irregular piece of the plate is ejected. Its diameter is about 15 cm.

It must be put forward that the occurrence of these ruptures is amazingly reproducible when similar conditions of explosion are repeated.

Table 4 lists the size of the ejected metallic elements, in regard to the explosive mixture initial pressure.

Initial pressure [bar]	1.1	1.2	1.3	1.4
Cap diameter [cm]	0	3.5	10.0	15.0

Table 4 : Size of the ejected element for different initial pressures when subjected to detonation.

Figure 4 illustrates the different shapes and sizes of the ejected caps obtained for different initial pressure values.



Pi = 1.1 bar



Pi = 1.2 bar



Pi = 1.3 bar



Pi = 1.4 bar

Figure 4: Different types of plates ruptures when subjected to detonations (thickness : 1 mm, Al 5754).

Pressure changes induced by the rupture.

Although the rupture occurs, inducing some load discharge, the dynamics of the plate goes on. This results from a coupling between the load on the plate and its response.

The coupling changes the pressure evolution and this effect is visible on the pressure records, particularly near the plate, in front of (gauge 3) or behind it (gauge 5). The figure 5 shows the record of pressure gauges 3 and 5 for a detonation with an initial pressure of 1.2 bar. When the shock wave hits the plate, the overpressure peak is important (50 bars). This wave breaks a part of the plate. The time between the peak on gauge 3 and the response of gauge 5 is 150 microseconds. Then, the reflected waves are strongly reduced. The second peak of gauge 3 is about 25 bar. This wave reaches gauge 5 after the ejection of the cap. Figure 5-b shows the pressure behind the plate, which proves the cracking of the plate, with the ejection of the cap. In this experiment, the cracking appears 1 ms after the loading.

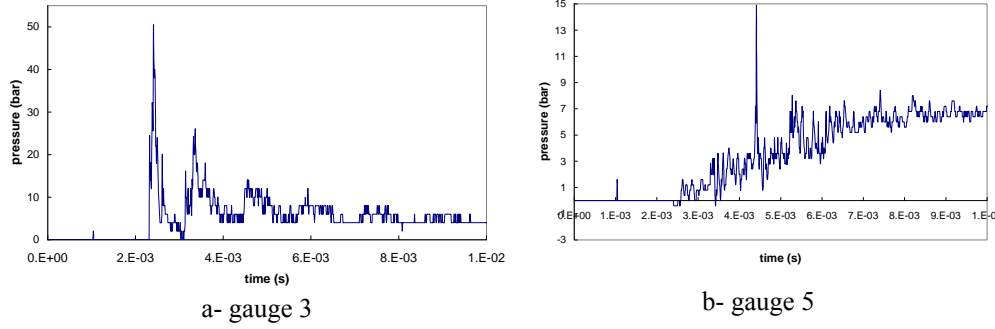


Figure 5 : Pressure record ahead and behind the plate

MODELING

Introduction

In this study, a modelling of circular plates subjected to dynamic pressure loads has been implemented with MSC.MARC finite element software, a commercial software accurate for non linear dynamic applications. The fluid contribution, that is applied to the plates, comes from experimental pressure data. The modelling focuses on the material response to these loads. It grounds on different considerations to represent the sample global dynamic behaviour as well as possible. Since the plate exhibits high rate dynamic behaviour, appropriate material properties are required. For large displacements and dynamic loading, an elasto-viscoplastic law is chosen. In addition, the crack initiation has to be described with a damage law.

Material behaviour: the Chaboche constitutive law

As the system is subjected to high strain rate and displacement, the elasto-viscoplastic property of materials must be taken into account. The Chaboche elasto-viscoplastic law has been chosen to describe the material behaviour. Woznica et al. (2001) have already verified that this law provide accurate results by comparison with experiments.

The relations introduced in this law are, for the inelastic strain rate $\dot{\mathbf{E}}^I$

$$\dot{\mathbf{E}}^I = \frac{3}{2} \dot{p} \frac{\mathbf{s}' - \mathbf{X}'}{J(\mathbf{s}' - \mathbf{X}')} \quad (1)$$

where \dot{p} is the accumulated inelastic strain rate

$$\dot{p} = \gamma \left\langle \frac{J(\mathbf{s}' - \mathbf{X}') - R - k}{K} \right\rangle^n \quad (2)$$

and K , n are viscous parameters, $\gamma=1$ [s^{-1}]. The parameter k is the initial yield limit.

\mathbf{s}' denotes the deviator of stress tensor \mathbf{s} , $J(\dots)$ is the scalar equivalent of deviatoric stress invariant. R is a drag stress.

Such a law introduces an isotropic hardening:

$$\dot{R} = b(R_1 - R) \dot{p} \quad (3)$$

where R_1 and b are material parameters.

A cinematic hardening is expressed through the evolution of the back stress \mathbf{X} ,

$$\dot{\mathbf{X}} = \frac{2}{3} a \dot{\mathbf{E}}^I - c \mathbf{X} \dot{p} \quad (4)$$

where a and c are the law parameters.

A method to determine these parameters has been presented by Woznica and Klosowski (2000).

The following material data, validated for Al 5457 at $T = 20^\circ\text{C}$ (Woznica et al. (2001)), have been used in the Chaboche elasto-viscoplastic model:

$E = 71.11 \text{ GPa}$, $\gamma = 1 \text{ s}^{-1}$, $n = 8.9$; $K = 13.97 \text{ MPa}$, $k = 101.64 \text{ MPa}$, $c_1 = 2478.3$, $a_1 = 54049 \text{ GPa}$, $b = 14.68$, $R_1 = 178.45 \text{ MPa}$;

Damage law: the Lemaitre - Chaboche model

A fully coupled model of damage is proposed by Lemaitre and Chaboche (1988), relying on the following damage parameter:

$$D = \frac{S_D}{S} = \frac{S - \bar{S}}{S} \quad (6)$$

where S is the surface of a representative element of the material and \bar{S} represents the effective surface (taking into account cavities). $D=0$ corresponds to a non-damaged material, while $D=1$ indicates a fully damaged material and so, leads to the failure of the representative element.

The law parameters can be determined with loading and unloading tensile tests. Indeed, the damage parameter can be expressed through:

$$\dot{D} \times (1-D)^{2\beta} \times \left(\frac{2E\alpha}{Cte} \right)^\beta = \dot{p} \quad (7)$$

with $\dot{D} = \frac{dD}{dt}$, E Young modulus, α and β , parameters determined experimentally. Integrating (7), one obtains:

$$D(p) = 1 - \left[1 - (p - p_0) \times (2\beta + 1) \times \left(\frac{2E\alpha}{Cte} \right)^{-\beta} \right]^{\frac{1}{2\beta+1}} \quad (8)$$

As $D = 1 - E'/E$ (where E' represents the Young modulus modified by damage), the α and β parameters can be easily determined with relation (8) from loading and unloading cyclic tensile tests.

Numerical simulation

It has been assumed that the material includes both isotropic and cinematic hardening.

The modelled samples are 1 mm thick, with a radius of 97 mm. Two shell elements models were chosen to mesh the plate: 4 node shell elements and axisymmetrical shell elements.

Different computations have been realised:

- First, the plate is supposed to strain without rupture (case A). The plate turns into a shell after the loading, as long as the initial pressure of the reactive medium does not exceed a given value (1.1 bar). In this case, the computation provides a good agreement with experiments.
- For higher pressures, as it is reported above, a cap with an explosion intensity dependent diameter is ejected (case B). Different initial conditions have been introduced in the model. According to the results, the discussion is not closed.

Case A : Plate swelling

Simulation results of a deflagration with an initial 0.8 bar pressure on a plate are presented. In the compared experiment, the plate is clamped and the rounded edge ring is not used. The associated pressure signal leads to large displacements but no rupture occurs. Figure 6 presents the calculated displacement of the plate centre. Simulations have been conducted for both elemental representations. The dotted line represents the measured final experimental displacement of the plate centre.

Figure 7 presents the calculated plate shape evolution with time. While time increases, the simulated final shape becomes closer and closer to the experimental final deflection.

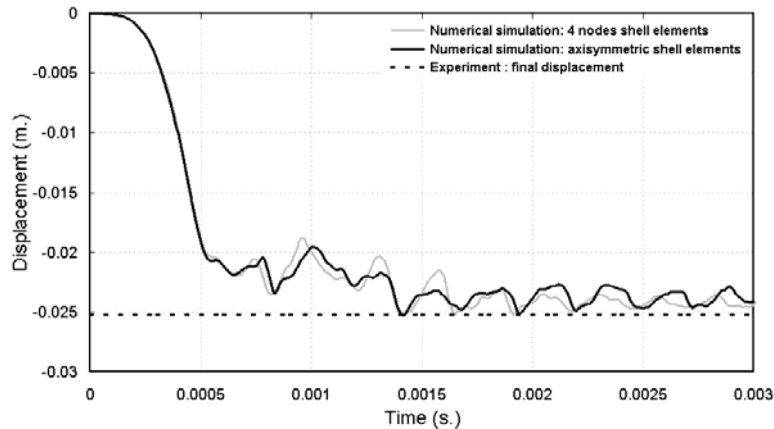


Figure 6 : Numerical and experimental results for the plate centre displacement
Case of a deflagration at 0.8 bar

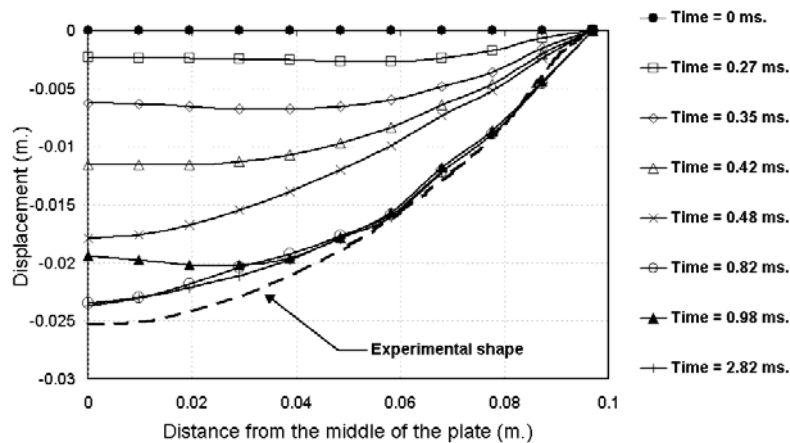


Figure 7 : Evolution of the plate shape with time

As a conclusion, numerical simulations provide a good assessment with experiments: the difference between the mean simulated value and the final measured displacement is less than 5%. The plate central part deflection is lightly underestimated. After the bulging of the plate, high frequencies vibration of low amplitudes appear numerically, as in the experiment.

It has been above underlined that the implementation of a rounded edge ring for the clamping of the plate could change the response of the plate. A series of experiments have been performed with this device that enables the plate to be subjected to higher pressure loading. Consequently, larger displacements and deformations have been obtained, without splitting the plate on its

edge. The modelling of a sample with those different boundary conditions has been achieved, and compared with the associated experiments.

Figure 8 illustrates the plate centre displacement in regard to the experimental displacement. The model proves to be accurate.

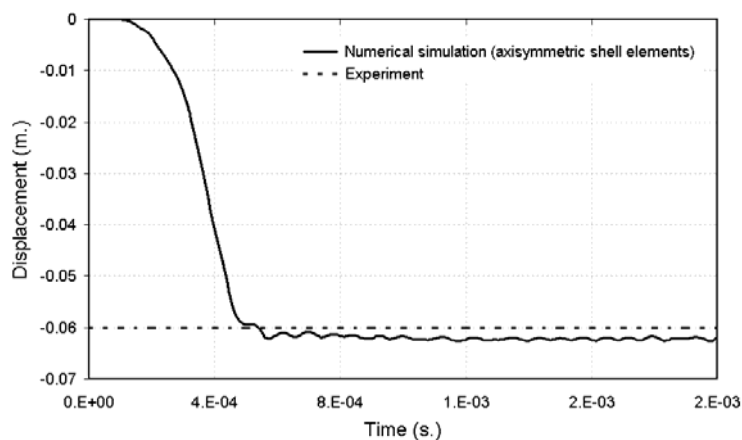


Figure 8. Numerical and experimental results for the plate centre displacement using a rounded ring. (Case of a detonation at 0.8 bar)

Case B : Plate rupture

The main problem is to define the most accurate pressure loading. The loads initially used come from the pressure signals that have been recorded on a rigid plate, as explained before. Consequently, this signal does not take into account any coupling between fluid and structure. When the displacements of the plate are not very large, the difference with the real loading is not significant. However when large displacements occur, the plate movement modifies the pressure signal. This coupling phenomenon can even be amplified by the discharge produced by a plate failure that reduces the initial loading on the plate. In this case, the coupling cannot be neglected.

The main difficulty is to choose an appropriate pressure on the plate, as no pressure transducer can be set on the plate itself. Different pressure gauges that are located along the tube (figure 1), can be used to replace the exact and missing pressure signal, according to some hypotheses. Associated simulations are discussed thereafter.

Modelling details

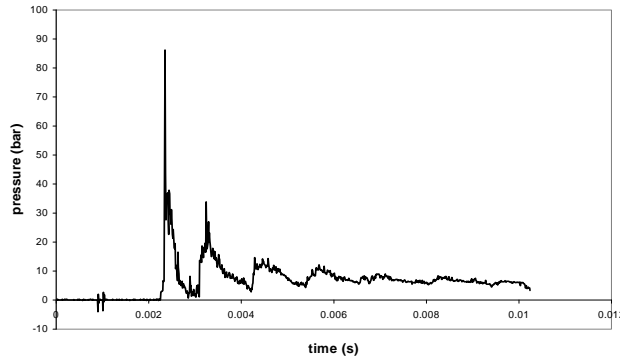
a- Pressure obtained on a rigid plate.

In the first modelling the assertion is done that the plate swells without fracture. Under this condition, the loading experimentally obtained on a rigid plate can be introduced. It corresponds to a detonation with an initial pressure of 1.2 bar. According to the duration of the solicitation, the response of the plate is transient and the calculation limited to 1 ms.

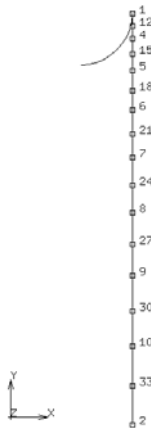
Looking at the computed deformations in the plate, it is important to note that their maximum is not in the plate centre, but evolves along the radius. The modelling has been realised with 16 elements. Figure 9 presents the total computed deformation for different nodes (their numbers

are not sorted according the position). The meshing presented figure 9-b is valid for the 3 different computations.

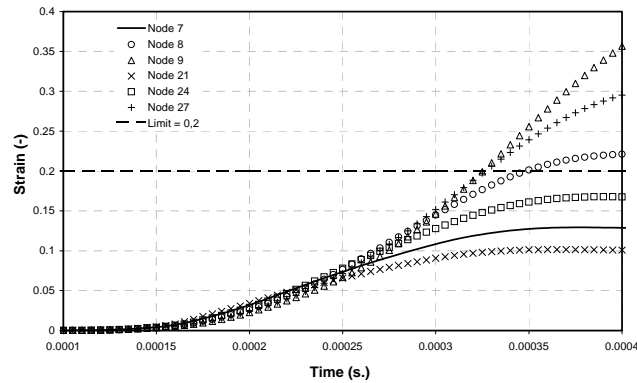
This result confirms qualitatively that, for appropriate conditions, a different diameter cap can be ejected, as observed experimentally when the presence of a round edge device avoid the whole plate from being ejected.



9-a : Pressure on the plate (detonation: 1.2 bar)



9-b: meshing of a radius (node 2: centre)



9-c: total strain variation induced in different nodes (case a)

Figure 9: The case of a 1.2 bar detonation : Pressure and strains induced

Using a strain value limit (arbitrarily 20 %), it is possible to find the location of the first node where the criterion is reached. Figure 9 shows that its position is approximately at 35 mm from the plate centre. Consequently, for this load , the ejected cap would be 70 mm in diameter. The experiment gives a lower value of 37 mm. Therefore, the cap size is overestimated by the model. This can result from the choice of an inappropriate criterion.

This can also result from a too important numerical loading. Once again, it must be emphasised that the pressure signals comes from an experimental recording on a rigid plate. Actually this load does not take into account the pressure discharge that is produced by the plate movement. Therefore, the real load has to be investigated.

b- Pressure obtained just before the plate (gauge C3).

The use of a pressure load issued from the gauge C3 has the advantage of injecting a load that account for the plate movement. However it has the negative aspect that the gauge is not at the real sample position.

In this particular case, considering the same strain value limit as previously (20 %), the first node to be reached is at 26 mm from the plate centre (figure 10). Using this second possible loading, the ejected cap would be 52 mm in diameter, whereas the experimental value is of 37 mm. The cap size is still overestimated, but the result is better than for the previous loading. The computed final deflection of the plate is 65 mm.

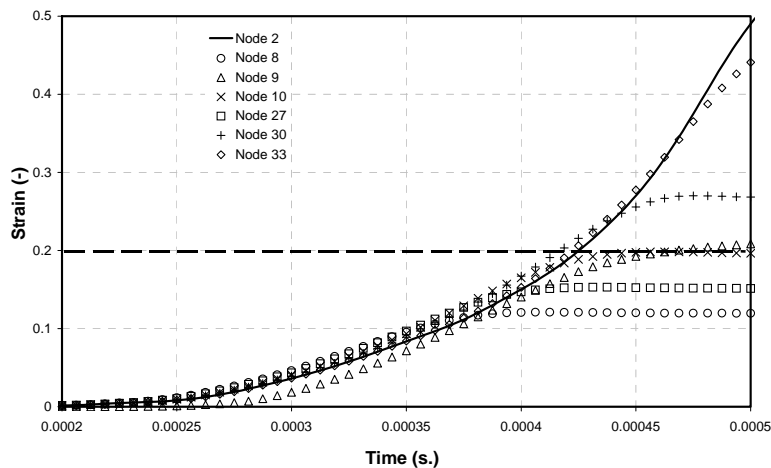


Figure 10: Total strain variation induced in different nodes
Case b: Pressure obtained just before the plate

c- Difference of pressure between front and back signals

Figures 5a and 5b show that the influence of plate rupture does not immediately appear on the pressure signals. It can be stated that the signal is correct, while the plate is not opened. After the rupture, the pressure ahead of the plate quickly decreases. The global signal can be seen as the difference between the signals ahead and behind the plate, using records from pressure gauges C3 and C5. Figure 11 displays this global pressure signal.. As presented on figure 12, the associated simulation shows that the first node to reach the criterion value of 20 % corresponds to a 54 mm diameter cap, which is closer to the experiments.

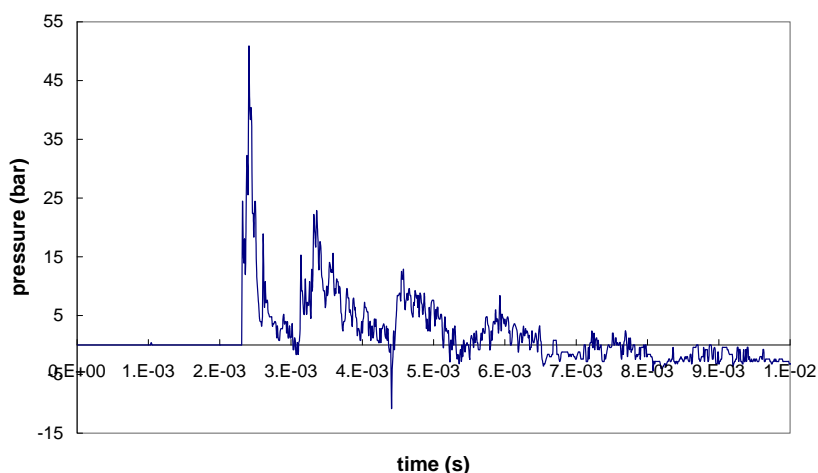


Figure 11. Difference between front and back pressure signals

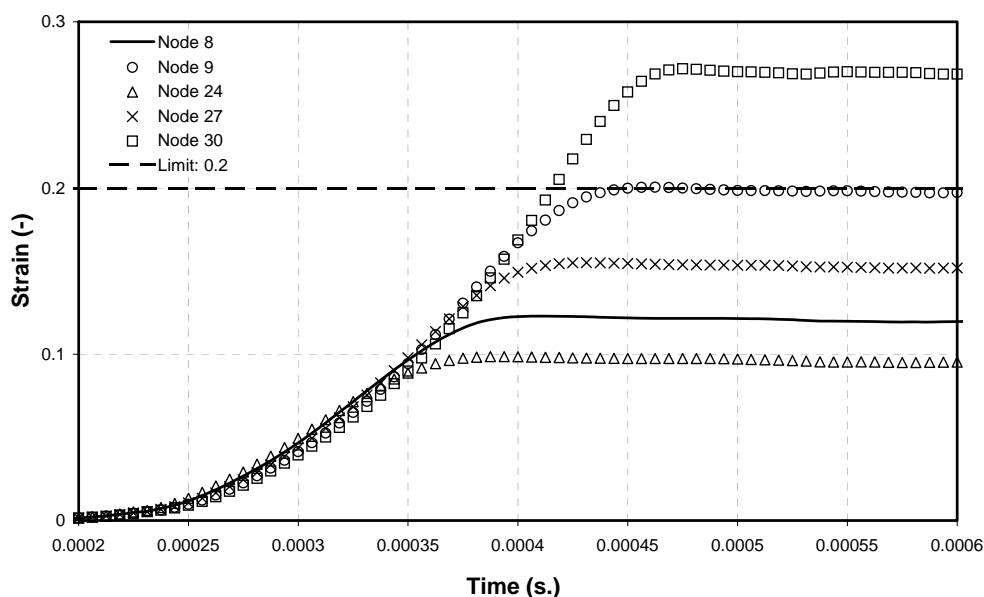


Figure 12: Total strain variation induced in different nodes.
Case c: Difference of pressure between front and back signal

Numerical simulations have been realised in the case of a detonation for a 1.4 bar initial pressure. Results corresponding to this case of loading are summarised in table 5. The strain damage criterion previously defined has been used for these computations.

Comparison Experiments – Numerical simulations

Table 5 compares the numerical and experimental ejected caps sizes for detonation associated with two different initial pressures (1.2 and 1.4 bar). The influence of the three different pressure loads have also been investigated.

		Detonation (1.2 bar)	Detonation (1.4 bar)
Experimental cap diameter		37.50 mm	150 mm
Numerical simulations:	a)- Rigid plate pressure signal	70.2 mm	113 mm
	b)- Pressure obtained just before the plate (gauge C3).	52 mm	98 mm
	c)- Pressure difference between front and back signals	54 mm	/

Table 5 : Ejected caps sizes evolution - Experimental and numerical results

CONCLUSION

This paper compares experimental results and numerical simulations of metallic plates subjected to dynamic pressure loads.

The experimental device consists in a shock tube in which metallic plates are subjected to explosions. The pressure loads are realised by the ignition of a H₂/O₂ stoichiometric mixture. The incoming pressure signals on the samples depends on the initial conditions in the mixture: ignition energy, initial pressure. For the same initial conditions, the pressure signals in front of and behind the plate are amazingly reproducible. Furthermore, this reproducibility is also found in the response of the samples. The ejected caps sizes are identical for explosions of a given value.

The numerical study consists in an axisymmetric modelling of a metallic plate subjected to a dynamic load. The material is described with a Chaboche elasto-viscoplastic law, where the material characteristics have been identified from tensile tests. They have been implemented into the model in order to determine the failure zone. The maximal equivalent stress and the total strain value criteria have been used to predict the rupture area. The first results seems to confirm that a strain criterion is more relevant than a stress criterion. Another simple criterion, which could be studied, is the strain energy density. The model proves to be accurate when the sample only suffers swelling. However details about the plate rupture models have still to be investigated: some difficulties remain to obtain the real pressure signal. Moreover, in the modelling, the formulation of an accurate criterion is necessary for the prediction of the rupture.

Nevertheless, the test device proves to be perfectly appropriate to analyse the appearance and propagation of rupture phenomenon in dynamically loaded samples.

References

- Beltman W., Burcsu E., Shepherd J., Zuhail L., "The structural response of cylindrical shells to internal shock loading", *J. Pressure Vessel Technology*, 121, 315-322 (1999)
- Bodner S.R., Symonds P.S., Experiments on dynamic plastic loading of frames, *Int. J. Solids Struct.*, 15, 1-13 (1979)
- Bodner S.R., Symonds P.S., Experiments on viscoplastic response of circular plates to impulsive loading, *J. Mech. Phys. Solids*, 27, 91-113 (1979)
- Chao T.W., Shepherd J.E., 2002, Fracture response of externally-flawed cylindrical shells to internal gaseous detonation loading, In ASME Pressure Vessels and Piping Conference.
- Dragon A., Hild F., Rota L., Trumel H., Modélisation du comportement et de la rupture des matériaux sous sollicitations dynamiques, *Mec. Ind.*, 521-537 (2000)
- Duffey T.A., The large deflexion dynamic response of clamped circular plates subject to explosive loading, Sandia Laboratories Research Report SC-RR-67-532 (1967)
- Duffey T.A., Key S.W., Experimental-theoretical correlation of impulsively loaded clamped circular plates, Sandia Laboratories Research Report SC-RR-68-210 (1968)
- Emery A.F., Kobayashi A.S., Love W.J., Place B.W., Lee C., Chao Y.H., An experimental and analytical investigation of axial crack propagation in long pipes, *Engineering Fracture Mechanics*, 23, 1, 215-226 (1986)
- Florence A.L., Circular plate under a uniformly distributed impulse, *Int. J. Solids Struct.* 2, 37-47 (1966)
- Fthenakis, V.M., Rohatgi, U.S., Chung, B.D. 2003. A simple model for predicting the release of a liquid-vapor mixture from a large break in a pressurized container. *J. Loss Prev. Process Ind.*, 16, 1, 61-72.
- Haque, A., Richardson, S., Saville, G., Chamberlain, G. 1990. Rapid depressurization of pressure vessels. *J. Loss Prev. Process Ind.*, 3, 1, 4-7.
- Iung, T. 1994. Propagation rapide et arrêt des fissures dans les aciers pour gazoducs. Rupture par clivage et rupture ductile, *Thèse de l'Ecole Nationale Supérieure des Mines de Paris*.
- Johnson W., Impact strength of materials. Edward Arnold, London (1972)
- Jones N., Impulsive loading of a simply supported rigid-plastic circular plate, *J. Appl. Mech.* 35, 59-65 (1968)
- Jones N., Finite deflections of a rigid-viscoplastic strain-hardening annular plate loaded impulsively, *J. Appl. Mech.* 35, 349-356 (1968)

- Kelly J.M. and Wilshaw T.R., A theoretical and experimental study of projectile impact on clamped circular plates, *Proc. R. Soc. A* 306, 435-447 (1968)
- Klosowski, P. 1999. Nieliniowa analiza numeryczna i badania doswiadczone drgan sprzysto-plastycznych plyt i powlok, Politechnika Gdanska
- Klosowski P., Woznica K., Weichert D., Comparison of numerical modelling and experiments for the dynamic response of circular elasto-viscoplastic plates, *Eur. J. Mech. A/Solids* 19, 343-359 (2000)
- Lemaitre, J., Chaboche, J.-L. 1998. Mécanique des matériaux solides, *Dunod*
- Leung, J.C. 1990. Two-phase flow discharge in nozzles and pipes – a unified approach. *J. Loss Prev.Process Ind.*, 3, 1, 27-32.
- Mott, N.F., 1943, Fragmentation of H.E. shells: a theoretical formula for the distribution of weight of fragments, A.O.R.G. Memorandum 24, also NOS-AC-3642
- Nurick G.N., Martin J.B., Deformation of thin plates subjected to impulsive loading – a review – Part II: Eperimental studies, *Int. J. Impact Engng*, 8, 2, 171-186 (1989)
- Nurick G.N., A new technique to measure the deflexion-time history of a material subjected to high strain rates, *Int. J. Impact Engng*, 3, 17-26 (1985)
- Nurick G.N., Pearce H.T., Martin J.B., The deformation of thin plates subjected to impulsive loading, In *Inelastic Behaviour of Plates and Shells* (Ed. L. Bevilacqua). Springer-Verlag, Berlin (1986)
- Nurick G.N., The measurement of the deformation response of a structure subjected to an explosive load using a light interference technique. *Proc. 1986 SEM Spring Conf. Exp. Mech.*, 105-114. The society for experimental mechanics (1986)
- Olson M.D., Nurick G.N., Fagnan J.R., Deformation and rupture of blast loaded square plates – Prediction and experiments, *Int. J. Impact Engng*, 13, 2, 279-291 (1993)
- Pennetier O., Renard J., Structures minces face à une explosion, application à la gestion de risques industriels, *Mécanique Industrielle et Matériaux* 51, 2, 67-69 (1998)
- Perrone N., Impulsively loaded strain-rate sensitive plates, *J. Appl. Mech.* 34, 2 (1967)
- Qiu, H., Enoki, M., Kawaguchi, Y., Kishi, T. 2003. A model for the dynamic fracture toughness of ductile structural steel. *Eng. Frac. Mech.*, 70, 5, 589-598
- Recho, N., 1995. *Rupture par fissuration des structures*. Hermès
- Rivalin, F. 1998. Développement d'aciers pour gazoducs à haute limite d'élasticité et ténacité élevée: mécanique et mécanismes de la rupture ductile a grande vitesse, *PHD Thesis of the Ecole Nationale Supérieure des Mines de Paris*.
- Rivalin, F., Besson, J., Pineau, A., Di Fant, M., 2001, Ductile tearing of pipeline-steel wide plates II. Modeling of in-plane crack propagation, *Eng. Fract. Mech.*, 68, 347-364
- Su, B., Bhuyan, G.S. 1999. Elastic fracture properties of all-steel gas cylinders with different axial crack types. *Int. J. Press. Vessels and Piping*, 76, 1, 23-33
- Symonds P.S., Survey of methods of analysis for plastic deformation of structures under dynamic loading. Division of Engineering, Brown University Report BU/NSRDC, 1-67 (1967)
- Teeling-Smith R.G., Nurick G.N., The deformation and tearing of thin circular plates subjected to impulsive loads, *Int. J. Impact Engng*, 11, 1, 77-91 (1991)
- Tvergaard, V., Needleman, A. 1984. Analysis of cup-cone fracture in a round tensile bar. *Acta Metall.*, 32, 1, 157-169
- Wang A.J., The permanent deflection of a plastic plate under blast loading, *J. Appl. Mech.* 22, 375-376 (1955)
- Wierzbicki T., Viscoplastic flow of rotationally symmetric shells with particular application to dynamic loading, *J. Mech. Phys. Solids* 3, 22-37 (1954)
- Wierzbicki T., Florence A.L., A theoretical and experimental investigation of impulsively loaded clamped circular viscoplastic plates, *Int. J. Solids Structures*, 6, 553-568 (1970)
- Woodward, J.L., Mudan, K.S. 1991. Liquid and gas discharge rates through holes in process vessels. *J. Loss Prev. Process Ind.*, 4, .3, 161-165
- Woznica, K., Klosowski, P. 2000. Evaluation of viscoplastic parameters and its application for dynamic behaviour of plates. *Arch. App. Mech.*, 70, 561-570
- Woznica, K., Pennetier, O., Renard, J. 2001. Experiments and numerical simulation on thin metallic plates subjected to an explosion. *J. Eng. Mater. Technol.*, 123, 203-209

The Response of Materials and Structures Subjected to Blast Loading

D.D. Radford

*Dept. of Engineering, University of Cambridge, Trumpington St., Cambridge, CB2 1PZ, UK
(now at Chalk River Laboratories, AECL, Chalk River, ON., K0J 1J0, CANADA)*

Recently, there has been considerable interest in the use of novel sandwich panel designs for application as blast-resistant structures. Overall, sandwich structures offer superior strength and energy absorption characteristics as compared to monolithic panels of the same areal mass. In order to evaluate the dynamic response of structures, a new experimental technique was developed and used to test a variety of sandwich structures. In this paper, an overview of the methodology used to conduct blast loading experiments on structures is presented. Details of experiments recently performed on clamped circular sandwich plates with lattice-type core topologies are provided, and the results compared to three-dimensional finite element simulations.

INTRODUCTION

In a broad range of practical applications, structures are subjected to dynamic loading conditions, such that the applied loads far exceed the quasi-static collapse strength. The response of monolithic beams and plates to shock or blast type loading has been extensively investigated. For example, Wang and Hopkins (1954) and Symmonds (1954) analysed the impulsive response of clamped circular plates and beams, respectively. Recently, Xue and Hutchinson (2003) carried out a preliminary finite element (FE) investigation of the resistance of clamped circular sandwich plates with a foam-like core to shock loading with the effects of fluid-structure interaction neglected. Subsequently, Qui *et al.* (2005) proposed an analytical model for the shock response of clamped circular sandwich plates by modifying the Fleck and Deshpande (2004) sandwich beam model. These numerical and analytical models have indicated that circular sandwich plates offer a higher resistance to shock loading than monolithic plates of the same mass.

To date, there has been little experimental validation of these predictions as it is difficult to perform laboratory scale experiments with a prescribed dynamic loading history. In a recent study by Radford *et al.* (2005a), an experimental technique was developed to subject structures to high intensity pressure pulses using metallic foam projectiles. The applied pressure pulses attempt to mimic shock loading in air and in water, with peak pressures on the order of 100 MPa and loading times of approximately 100 μ s. This experimental technique has been employed by Radford *et al.* (2005b) and Rathbun *et al.* (2005) to investigate the blast resistance of clamped sandwich beams, and by Radford *et al.* (2005c) and McShane *et al.* (2005) to investigate the response on clamped circular plates, as depicted in Fig. 1. Overall, these studies have demonstrated that sandwich panels have a higher resistance to blast loads, when compared to monolithic plates of the same areal mass, and that core topology plays an important role on the response of the structure.

In this paper, an overview of the methodology used to conduct blast loading experiments on sandwich plate structures is presented. Details of experiments recently performed on clamped circular sandwich plates with lattice-type core topologies are provided, which includes a comparison with numerical predictions. The outline of the paper is as follows. The manufacturing route of sandwich plates with lattice-type cores is detailed and the experimental procedure for loading the plates at mid-span by metal foam projectiles is described. Experimental results from tests performed on sandwich plates are then presented and compared

with three-dimensional finite element predictions. The finite element calculations are used to determine the loading history experienced by the monolithic and sandwich plates, thereby allowing examination of the experimental method used to simulate blast loading.

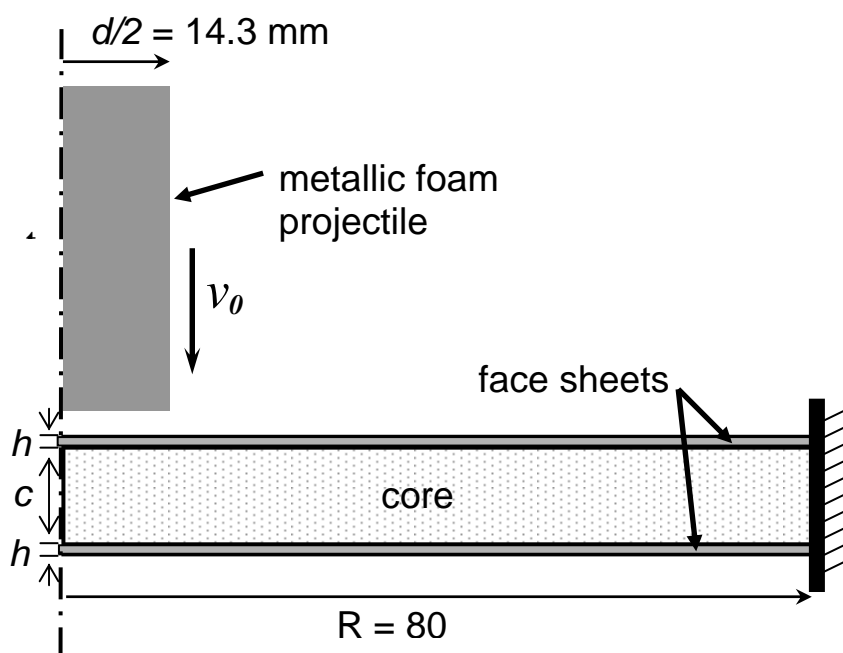


Figure 1: Specimen geometry and loading configuration used to study clamped circular sandwich plates.

SPECIMEN CONFIGURATION AND MANUFACTURE

In previous studies by Radford *et al.* (2005c) and McShane *et al.* (2005), circular sandwich plates comprising AISI type 304 stainless steel face-sheets and various core topologies were manufactured. McShane *et al.* (2005) considered two lattice-type core topologies; pyramidal and square-honeycomb cores, as shown in Fig. 2. In that study, the circular sandwich plates (radius $R = 80$ mm) comprised two identical AISI 304 stainless steel face-sheets of thickness $h = 1.18$ mm and density $\rho_f = \text{kg m}^{-3}$, and the pyramidal or square-honeycomb lattice cores of density $\rho_c \sim 430 \text{ kg m}^{-3}$ and thickness $c = 10$ mm. Thus, all sandwich plates had a common final areal mass of magnitude $m = 2h\rho_f + c\rho_c \approx 23.5 \text{ kg m}^{-2}$. The 10 mm thick pyramidal lattice core comprised struts of length 17 mm and cross-section 0.9 mm x 2.0 mm. These cores were manufactured from 0.9 mm thick AL-6XN stainless steel sheets by first laser cutting square-cells to obtain a perforated sheet and then folding this perforated sheet node row by node row to obtain regular pyramids, see Wadley *et al.* (2003) for details of the manufacturing route. The square-honeycomb core comprised square cells of side 10 mm, sheet thickness 0.3 mm and height $c = 10$ mm, manufactured from 0.3 mm thick AISI 304 stainless steel sheets using the slotting technique developed by Cote *et al.* (2004).

The sandwich plate specimens were manufactured as follows. Face-sheets of dimension 250 mm x 250 mm x 1.18 mm and the assembled pyramidal or square-honeycomb cores were clad with a thin layer of a braze powder of composition Ni-Cr 25-P10 (wt.%). Brazing was then conducted in a vacuum furnace at 1075 °C in a dry argon atmosphere at 0.03 – 0.1 mbar as described in Zupan *et al.* (2004). Eight equally spaced clearance holes for M8 bolts were then drilled in these plates on a pitch circle of radius 102 mm, to enable fastening to a clamping fixture. Plan and cross-section views of the clamped plate geometry are sketched in Fig. 3. Each sandwich plate was clamped between two annular steel rings of thickness 7 mm and of inner and outer radii, 80 mm and 125 mm, respectively. The assembly was then bolted down onto a rigid loading frame by M8 bolts, as sketched in Fig. 3.

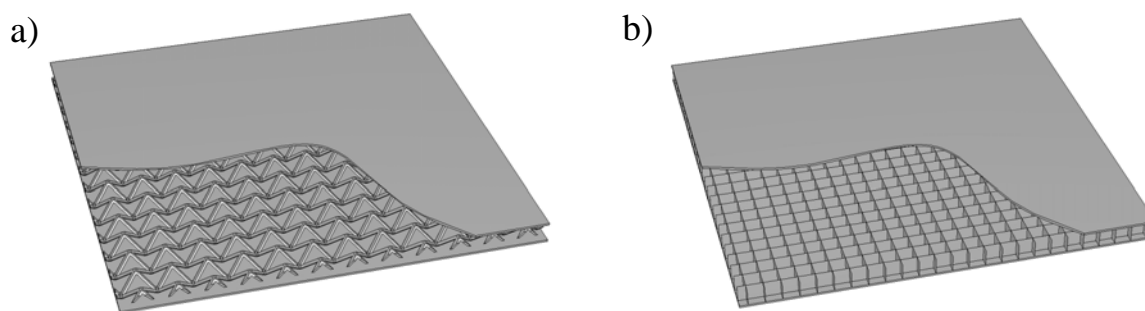


Figure 2: Schematics of the sandwich plates with a) pyramidal, and b) square-honeycomb cores.

In addition to the dynamic tests on two configurations of sandwich plates, dynamic tests were also performed on AISI 304 stainless steel monolithic circular plates of areal mass $m \sim 23.5 \text{ kg m}^{-2}$. These monolithic plates were also coated with the braze alloy and subjected to the thermal cycle used to braze the sandwich plates: this ensures that the monolithic plates have approximately the same mechanical properties as the face-sheets of the sandwich plates. The monolithic plates of radius $R = 80 \text{ mm}$ and thickness $h = 2.92 \text{ mm}$ were gripped using the apparatus described above.

MATERIALS

Cores

The uniaxial compressive responses of the pyramidal and square-honeycomb cores were measured quasi-statically at a nominal strain-rate of 10^{-3} s^{-1} using $50 \text{ mm} \times 50 \text{ mm}$ sandwich plate specimens. The measured compressive nominal stress versus nominal strain responses are plotted in Fig. 4a, and show that the pyramidal and square-honeycomb cores exhibit a peak compressive strength of approximately 5 MPa and 15 MPa, respectively at a nominal compressive strain of approximately 5%. Both cores show a sharp increase in strength at strain exceeding approximately 0.8 and which is referred to subsequently as the densification strain ε_D . The uniaxial compressive response of the Alporas metal foam of relative density $\bar{\rho} \sim 0.13$ is included in Fig. 4a; this foam is used to manufacture the foam projectiles for the dynamic experiments (the response of the foam was measured to determine the constitutive parameters used in the finite element simulations of the experiments). The quasi-static compressive response of the foam at a strain-rate of 10^{-3} s^{-1} was measured using a cylindrical specimen similar to that used as the projectile in the dynamic experiments (diameter 28.5 mm and length 50 mm). Unlike the lattices cores, the foam has no distinct peak strength, rather just a plateau strength of approximately 3.5 MPa and a nominal densification strain $\varepsilon_D \sim 0.8$.

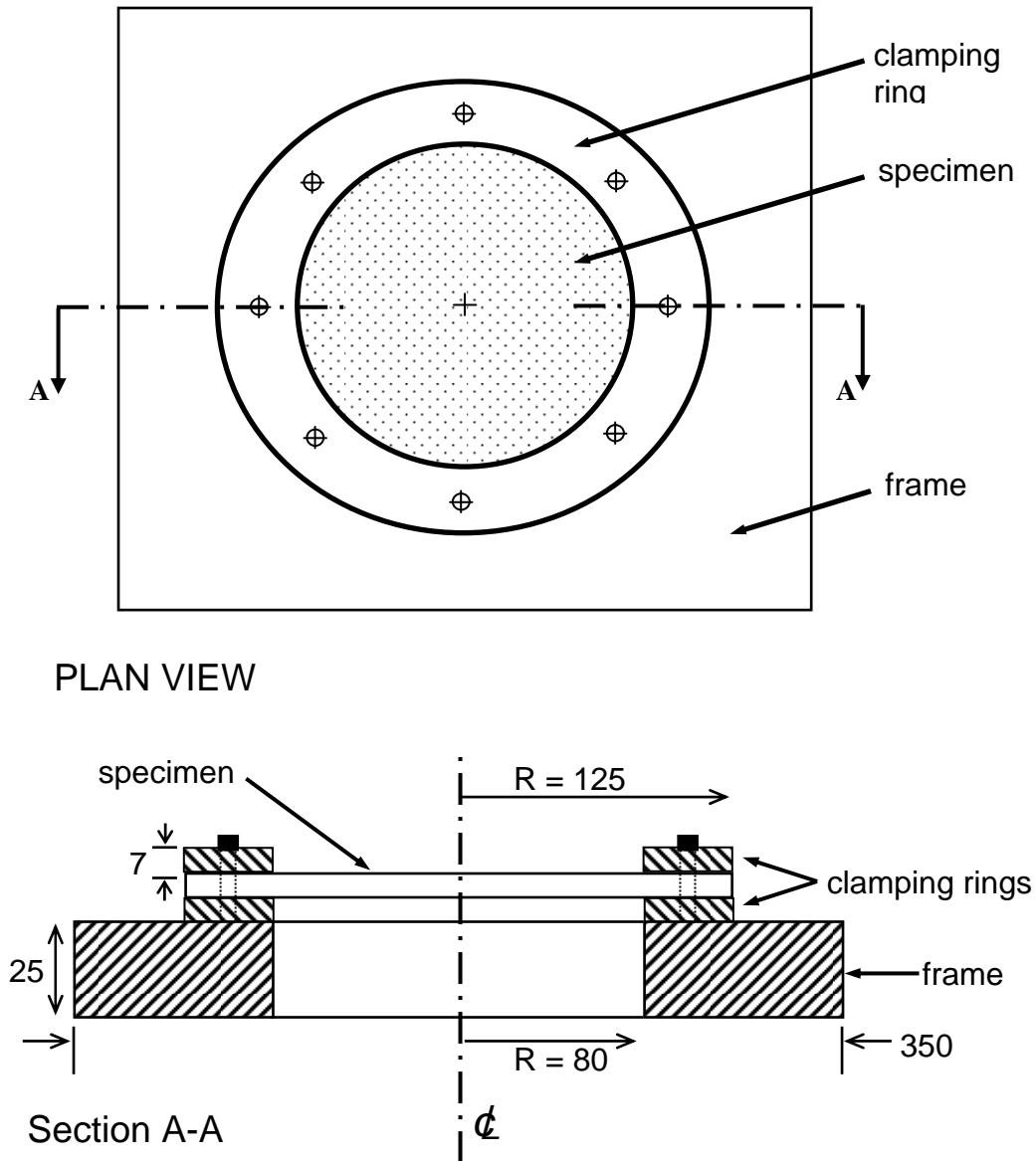


Figure 3: Sketch of the clamping arrangement. All dimensions in mm.

Face-Sheets

Recall that four types of stainless steel sheets were used to manufacture the sandwich and monolithic plates. The 1.18 mm and 2.92 mm thick 304 stainless steel sheets were used as the sandwich plate face-sheets and the monolithic plates, respectively, the 0.3 mm thick 304 stainless steel sheets were used to manufacture the square-honeycomb cores while the pyramidal core was manufactured from 0.9 mm thick AL-6XN sheets. Tensile specimens of dog-bone geometry were cut from each of the as-received steel sheets and then subjected to the same brazing cycle used to manufacture the sandwich and monolithic plates. The uniaxial tensile responses of the four types of stainless steel sheets (in their as-brazed condition) at an applied strain-rate 10^{-3} s^{-1} , are plotted in Fig. 4b, using axes of true stress and logarithmic strain. The AISI 304 and AL-6XN stainless steels have yield strengths of approximately 200 MPa and 290 MPa, respectively. Post yield, both the steels exhibit a linear hardening response with a hardening modulus $E_t \sim 2.1 \text{ Gpa}$.

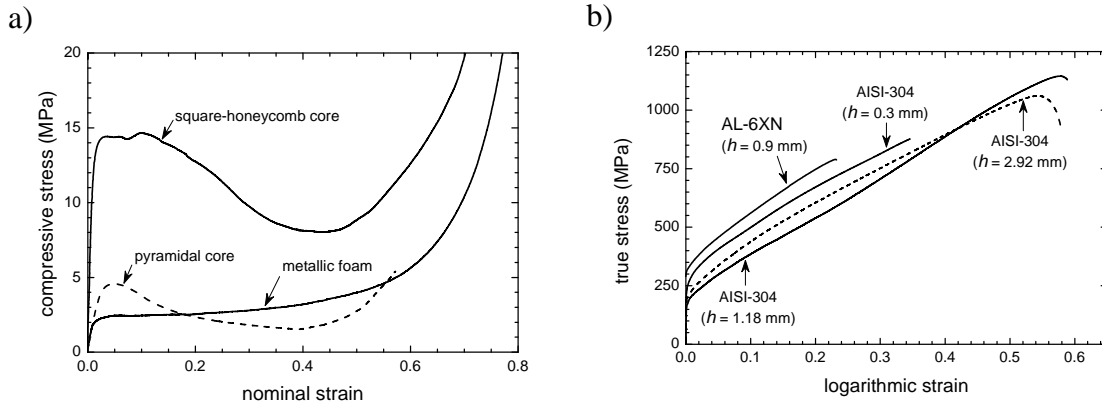


Figure 4: (a) Quasi-static compressive response of pyramidal and square-honeycomb cores. (b) Quasi-static tensile response of the annealed AL-6XN and AISI 304 stainless steels; results are shown for each sheet thickness, h .

The sandwich plates made from the stainless steel sheets were tested under dynamic loading conditions and thus knowledge of the high strain-rate behaviour of the stainless steel is critical. Stout and Follansbee (1986) and Nemat-Naser *et al.* (2001) have investigated the strain-rate sensitivity of the AISI 304 and AL-6XN stainless steels, respectively. Their data has been re-plotted in Fig. 5a, where the dynamic strength enhancement ratio R is plotted against the plastic strain-rate $\dot{\epsilon}^P$ for the range 10^{-3} to 10^4 s^{-1} . Here R is defined as the ratio of the stress $\sigma_d(\epsilon^P = 0.1)$ at an applied strain-rate $\dot{\epsilon}^P$ to the stress $\sigma_0(\epsilon^P = 0.1)$ at $\dot{\epsilon}^P = 10^{-3} \text{ s}^{-1}$. The measured stress versus strain histories presented in Stout and Follansbee (1986) and Nemat-Naser *et al.* (2001) indicate that the dynamic strength enhancement ratio R is reasonably independent of the choice of the plastic strain ϵ^P at which R is calculated. Thus, the dynamic strength σ_d versus plastic strain ϵ^P history can be estimated as

$$\sigma_d(\epsilon^P) = R(\dot{\epsilon}^P) \sigma_0(\epsilon^P) , \tag{1}$$

where $R(\dot{\epsilon}^P)$ is given in Fig. 5a.

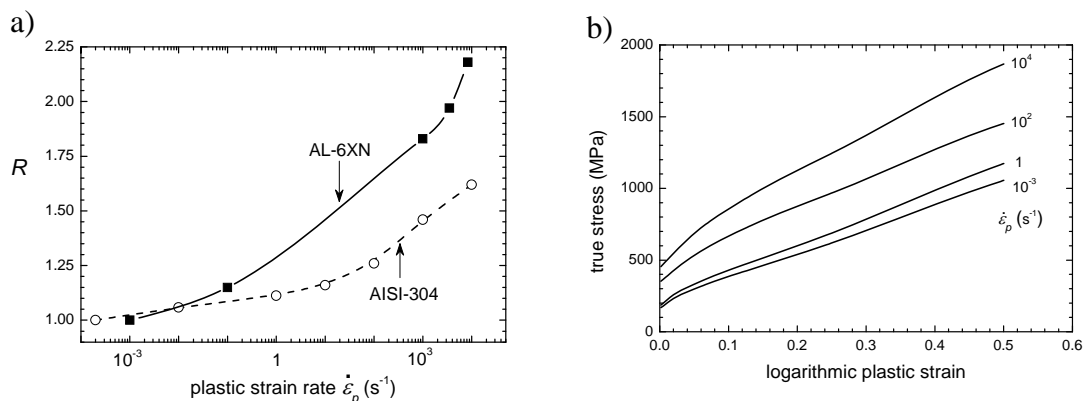


Figure 5: (a) The dynamic strength enhancement ratio R as a function of plastic strain-rate $\dot{\epsilon}^P$ for the AL-6XN and 304 stainless steels ($\epsilon_p = 0.1$). (b) Estimated tensile stress versus strain histories for 304 stainless steel ($h = 1.18 \text{ mm}$) at four selected values of the applied strain-rate.

In the dynamic finite element simulations of the experiments presented below, this prescription was employed for the strain-rate sensitivity of the stainless steels, with $\sigma_0(\dot{\epsilon}^p)$ given by the measured quasi-static stress versus strain histories for the different steels (Fig. 4b). As an example, the estimated true tensile stress versus logarithmic plastic strain histories of the 1.18 mm thick AISI 304 stainless steel at four selected values of applied strain-rate are sketched in Fig. 5b.

SIMULATED BLAST LOADING TECHNIQUE

The use of metallic foam projectiles as a means of providing well-characterised pressure versus time loading pulses has recently been developed by Radford *et al.* (2005a) and then subsequently employed to investigate the dynamic response of sandwich beams (Radford *et al.*, 2005b and Rathbun *et al.* 2005) and clamped circular plates (Radford *et al.*, 2005c and McShane *et al.* 2005). The method involves firing a circular cylindrical metal foam projectile of length l_0 and density ρ_p at an initial velocity v_0 , thereby imparting a pressure pulse of peak magnitude p_{peak} and duration τ that can be estimated by (Radford *et al.* 2005),

$$p_{peak} = \sigma_y + \frac{\rho v_0^2}{\epsilon_D}, \quad (2)$$

and

$$\tau = \frac{l_0 \epsilon_D}{v_0}, \quad (3)$$

respectively, where σ_y represents the plateau stress of the metallic foam during compression, and ϵ_D is the densification strain. Comparison of the experimentally measured values for p_{peak} and τ with theoretical predictions based on shock theory (Radford *et al.* 2005) are plotted in Fig. 6. In that study, the parameters were determined by impacting metal foam projectiles into a rigid target, which resulted in a pulse shape that closely approximated a square pulse. It was noted, however, that the pressure history imparted onto a structure is sensitive to the areal mass ratio of the foam projectile to the structure. This fact must be taken into account when using the technique to replicate blast loading.

In the recent studies on clamped circular plates (Radford *et al.*, 2005c and McShane *et al.* 2005), Alporas aluminium foam projectiles were used to provide a simulated blast loading on clamped monolithic and sandwich plates over a central circular patch of diameter d , as shown in Fig. 1. Specifically, circular cylindrical projectiles of length $l_0 \approx 50$ mm and diameter $d = 28.5$ mm were electro-discharge machined from Alporas foam blocks of density ρ_p in the range 350 kgm^{-3} to 460 kgm^{-3} . The projectiles were fired from a 28.5 mm diameter bore, 4.5 m long gas gun at velocities v_0 ranging from 110 ms^{-1} to 585 ms^{-1} , providing a projectile momentum per unit area $I_0 = \rho_p l_0 v_0$ of up to approximately 13 kNs m^{-2} .

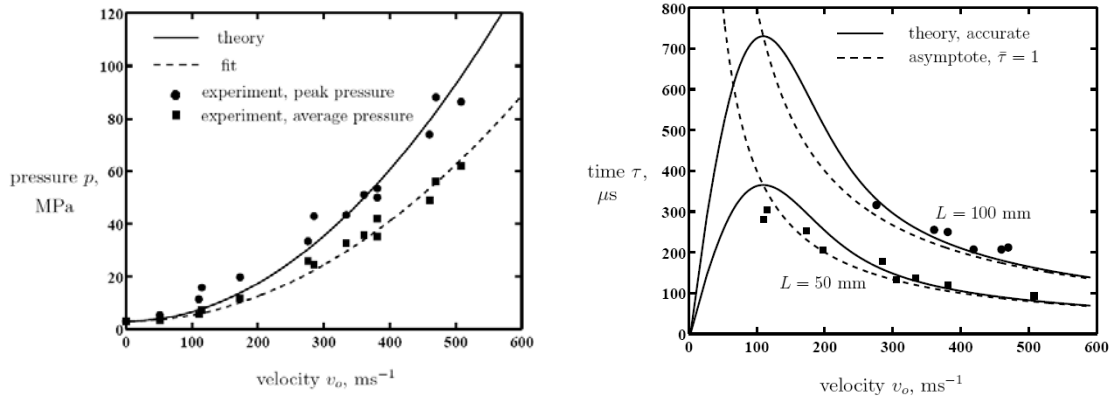


Figure 6: (a) The measured peak and mean contact pressures of the Alporas metal foams (relative density $\sim 11\%$) as a function of the impact velocity v_o from (Radford *et al.* 2005a), and (b) the measured pulse duration with results shown for two selected values of foam length (L). The theoretical predictions along with the asymptotes to the theory at large v_o are included.

EXPERIMENTAL RESULTS ON CLAMPED PLATES WITH LATTICE-TYPE CORES

The response of the clamped sandwich plates with lattice-type cores to shock loading is summarised in Fig. 7 as a plot of the permanent back-face deflections at the mid-span for each plate configuration as a function of the initial momentum of the foam projectile I_0 (McShane *et al.* 2005). Here, it is seen that both sandwich plate configurations deflect less than the monolithic plates of equal areal mass over the entire range of conditions investigated. The pyramidal and square-honeycomb core sandwich plates have similar responses up to $I_0 \sim 10 \text{ kNs m}^{-2}$. Above this value of projectile momentum, the square-honeycomb plates undergo smaller back face deflections.

The final core compressive strain is defined as $\varepsilon_c \equiv \Delta c / c$, where Δc is the reduction in core thickness at mid-span; the measured dependence of the ε_c upon I_0 is given in Fig. 8 for the two sandwich plate configurations. The strain ε_c increases with increasing I_0 , but is consistently less for the sandwich plates with the square-honeycomb core. For high impulses ($I_0 \geq 10 \text{ kNs m}^{-2}$), the core compression in the pyramidal core plates is approximately constant at its densification value of 0.8.

In order to gain insight into the deformation mechanisms, the monolithic and sandwich plates tested at $I_0 \sim 13 \text{ kNs m}^{-2}$ were sectioned along their diametrical plane. Photographs of the diametral sections are shown in Fig. 9a for the monolithic plate (specimen M7, back-face deflection of 17.7 mm), Fig. 8b for the sandwich plate with pyramidal core (specimen P4, back-face deflection of 14.4 mm), and Fig. 9c for the sandwich plate with square-honeycomb core (specimen SH4, back-face deflection of 11.7 mm). The diametrical profiles show that significant plastic deformation occurred in the vicinity of the foam impact and that the plates are continuously curved. It is deduced that the dynamic deformation of plates involves the formation of travelling hinges, analogous to the observed behaviour of monolithic and sandwich beams reported in (Radford *et al.*, 2005b). For $I_0 \sim 13 \text{ kNs m}^{-2}$, complete densification of the

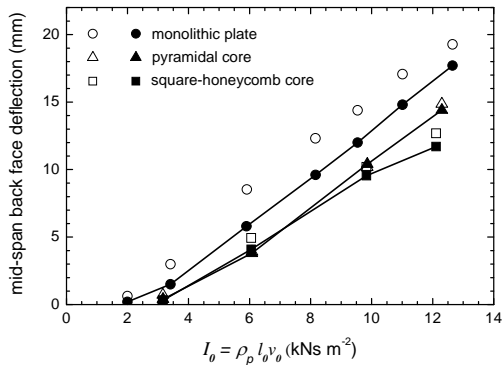


Figure 7: Comparison of the measured and predicted permanent back-face deflection at mid-span of the dynamically loaded monolithic and sandwich plates, as a function of the initial foam projectile momentum I_0 . Open symbols are the FE predictions and the filled symbols correspond to the experimental measurements.

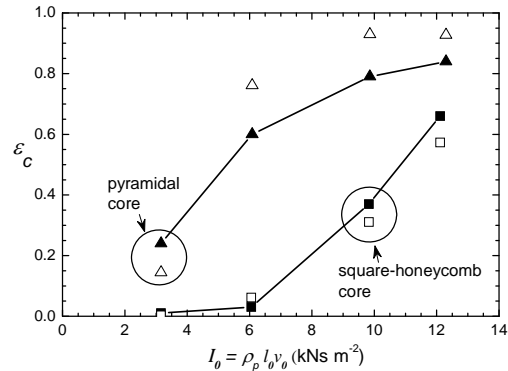


Figure 8: Measured permanent core compression ϵ_c at the mid-span of the dynamically loaded sandwich plates, as a function of the initial foam projectile momentum I_0 . Open symbols are the FE predictions and the filled symbols correspond to the experimental measurements.

pyramidal core occurs at the mid-span of the plate (Fig. 8b) while the square-honeycomb core only partially densifies at that impulse level. However, delamination of the square-honeycomb core from the face-sheets is evident at this impulse level, see Fig. 9c.

For comparison purposes, a clamped monolithic plate and the two configurations of sandwich plates were loaded quasi-statically over a central patch. These experiments were performed at a displacement rate of 10^{-5} m s^{-1} using a flat-bottomed steel cylindrical punch, of diameter 28.5 mm. The specimens were loaded until the permanent back-face deflection at the mid-span matched that obtained in the corresponding dynamic experiments with $I_0 \sim 13 \text{ kNs m}^{-2}$. Subsequently, the specimens were sectioned along their diametrical planes allowing for the comparison of the dynamic and quasi-static deflected profiles. Photographs of the quasi-static specimens are included in Fig. 10, and clearly show that the quasi-static response is dominated by membrane action with stationary plastic hinges at the edges of the indenter and the supports (as evidenced by the discontinuity in inclination of the plates at those locations).

FINITE ELEMENT PREDICTIONS OF BLAST LOADED CLAMPED PLATES WITH LATTICE-TYPE CORES

The recent studies on clamped sandwich plates by Radford *et al.* (2005c) and McShane *et al.* (2005) included finite element (FE) simulations of the experiments. The simulations were performed to determine the predictive capability of modelling the dynamic response of sandwich structures, and provide insight into the validity of the technique developed by Radford *et al.* 2005a to simulate blast loading using metal foam projectiles. The FE calculations conducted in these previous studies were performed using the explicit time integration version of the commercially available finite element code ABAQUS¹ (version 6.4).

Three-dimensional simulations of a quarter model of the sandwich plates and axisymmetric simulations of monolithic plates were performed. Dynamic loading of each plate was simulated

¹ Hibbit, Karlsson and Sorensen Inc.

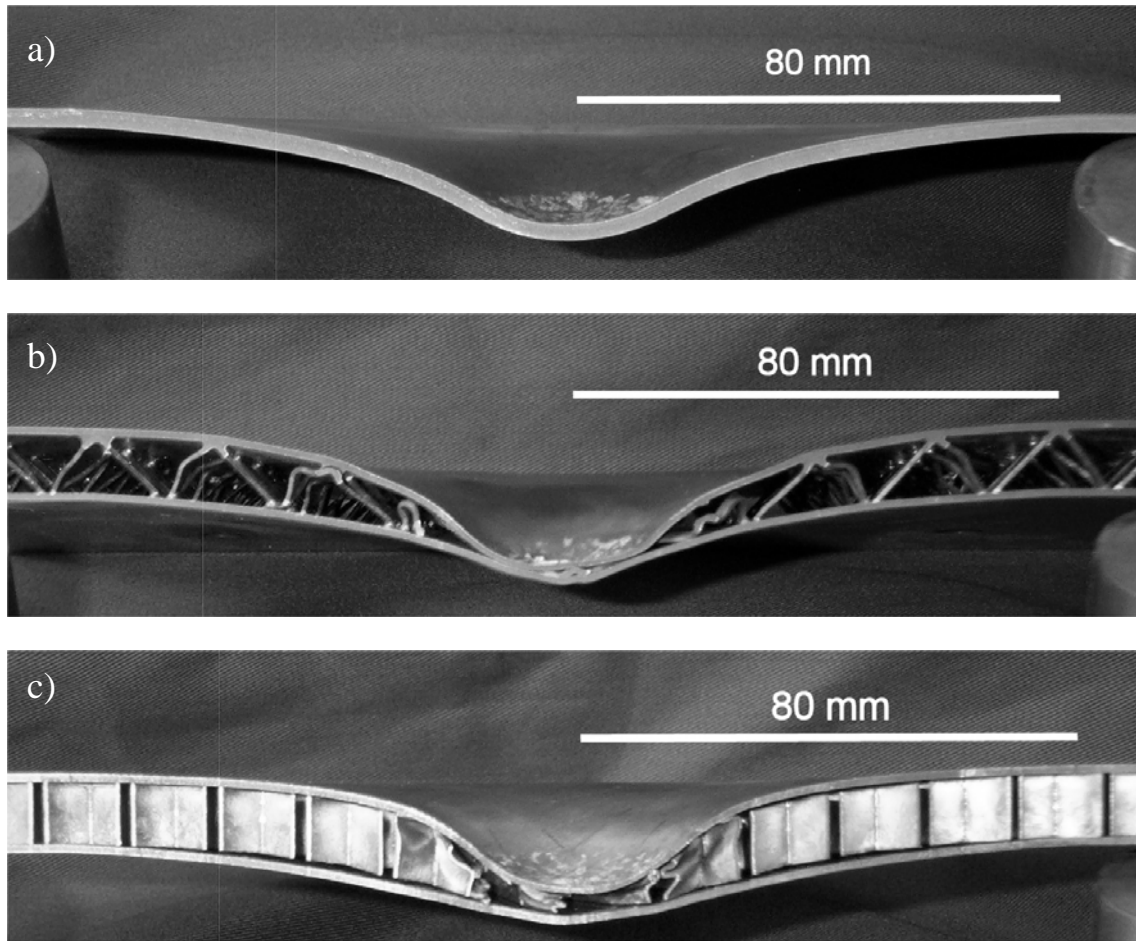


Figure 9: Photographs of the dynamically tested specimens (a) M7, (b) P4 and (c) SHC4. All these plates were tested at $I_0 \sim 13 \text{ kNs m}^{-2}$ and sectioned along their diametrical plane (McShane *et al.* 2005).

by the impact of a foam projectile: at the start of the simulation, the projectile was imparted with a uniform initial velocity v_o and was brought into contact with the plate at its mid-span. The “general contact” option in ABAQUS was employed to simulate contact between all possible surfaces including (i) the core and the face-sheets, (ii) self-contact of the core, (iii) contact of the two face-sheets, and (iv) contact between the projectile and front face-sheet. The cylindrical foam projectiles (diameter = 28.5 mm and length $l_o \approx 50 \text{ mm}$) were modelled using linear hexahedral and wedge elements (C3D8R and C3D6, respectively in the ABAQUS notation) with the elements swept about the cylindrical axis of the foam projectile.

The square-honeycomb plates were modelled using four-node shell elements (S4R in the ABAQUS notation) for both the face-sheets and the core. The pyramidal core sandwich plates were modelled using the four-node shell elements in the face-sheets and three dimensional linear beam elements (B31 in the ABAQUS notation) for the core struts. All dimensions (face-sheet thickness and core dimensions) were chosen to exactly match the experiments, and perfect bonding between the core and face-sheets was assumed. The monolithic plates were modelled using four-node axisymmetric quadrilateral elements with reduced integration (CAX4R in ABAQUS notation).

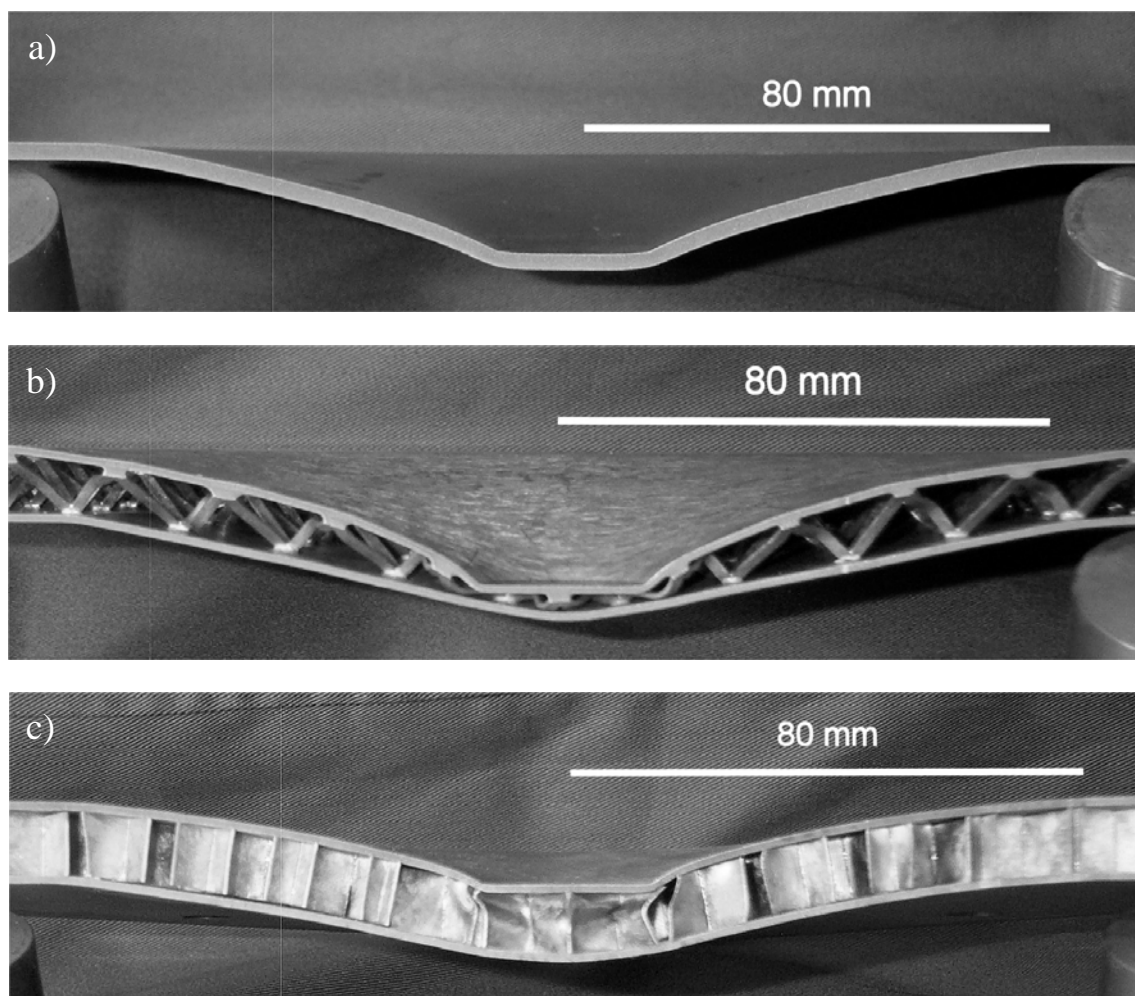


Figure 10: Photographs of the quasi-statically tested (a) monolithic plate (b) pyramidal core sandwich plate and (c) square-honeycomb sandwich plate. These plates were loaded until the permanent back-face deflection at the mid-span matched that obtained in the corresponding dynamic experiments of Fig. 9 and sectioned along their diametrical plane (McShane *et al.* 2005).

The various materials associated with the face sheets and cores were modelled as J2-flow theory rate dependent solids. The uniaxial tensile true stress versus equivalent plastic strain curves at plastic strain-rates $10^{-3} \text{ s}^{-1} \leq \dot{\epsilon}^p \leq 10^4 \text{ s}^{-1}$ were tabulated in ABAQUS using the prescription described above, and employing the data shown in Fig. 5. The projectiles were modelled as a compressible continuum using the metal foam constitutive model of Deshpande and Fleck (2000). Further details of the simulations performed on sandwich plates are provided in Radford *et al.* 2005c and McShane *et al.* 2005.

Comparison of finite element predictions and measurements

The predicted mid-span, back-face deflections of the monolithic and sandwich plates are included in Fig. 7 along with the experimental measurements. It was concluded that the FE model predicts the permanent deflection to reasonable accuracy for the sandwich plates, but slightly over-predicts the deflections of the monolithic plate. The FE predictions of the final core compression have been included in Fig. 8. The FE simulations predict the square-honeycomb measurements very well, but slightly over-predict the core compression in the pyramidal core sandwich plates. It was suggested by McShane *et al.* (2005) that this discrepancy

was a result of the fact that the beam elements used to model the pyramidal core do not accurately capture the dynamic collapse modes of the pyramidal core.

The pressure versus time history exerted by the foam projectile on a structure depends upon the foam projectiles density, length, compressive stress versus strain response, and projectile velocity v_0 . The analysis of Radford *et al.* (2005a) suggests that metal foam projectiles exert a rectangular pressure versus time pulse of magnitude and duration as described by equations 2 and 3 above, for impact on a rigid stationary target. This pressure versus time history, however, is sensitive to the structural response of the target: a decrease in the mechanical impedance of the target leads to a decrease in the applied pressure and to an increase in the pulse duration. Thus, it is unclear whether the observed differences in response of the various monolithic and sandwich plates for a given I_0 are due to differences in their intrinsic impact resistance, or a result of the application of different pressure time histories on the plates.

To clarify this ambiguity, Radford *et al.* (2005c) and McShane *et al.* (2005) employed the FE analysis as described above. The calculated pressure versus time histories exerted by the foam projectiles on the monolithic plate M7, the pyramidal core plate P4 and square-honeycomb core plate SH4 are plotted in Fig. 11. Here, $I_0 = 13 \text{ kN s m}^{-2}$ for each case, and the pressure versus time history exerted by the foam projectile on the plates was derived by

$$p(t) = \rho_p l_0 \dot{\bar{v}}(t), \quad (4)$$

where $\bar{v}(t)$ is the average axial velocity of the foam projectile at time t , and the over-dot denotes time differentiation. Momentum conservation implies that,

$$I_0 = \int_0^{\infty} p(t) dt. \quad (5)$$

It is seen that the differences between the pressure versus time histories are small confirming that the differences in response of the various monolithic and sandwich plates for a given I_0 are due to differences in their intrinsic impact resistance.

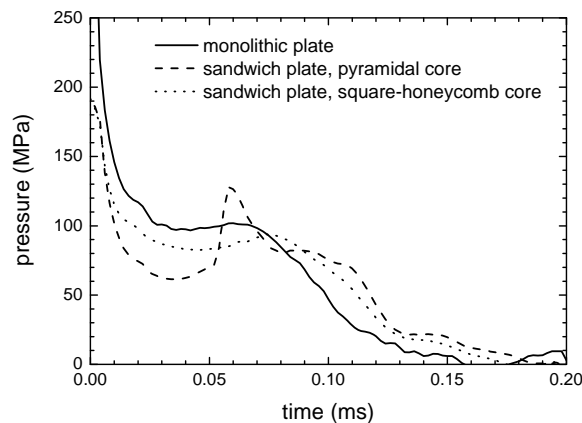


Figure 14: The predicted pressure versus time histories exerted by the foam projectiles on monolithic specimen M7 as well as the sandwich plate specimens P4 (pyramidal core) and SH4 (square-honeycomb core). $I_0 \sim 13 \text{ kNs m}^{-2}$ (McShane *et al.* 2005).

CONCLUDING REMARKS

This paper reviews the method of simulating blast loading on sandwich structures using metal foam projectiles. Details of this method as applied to impact clamped circular monolithic plates and sandwich plates with either pyramidal or square-honeycomb lattice cores were provided. The permanent deflections and core compression of the sandwich plates were measured as a function of the projectile momentum, and the measured responses compared with finite element simulations. It was found that the deformation mode due to dynamic loading is different to that observed in quasi-static loading due in part to the occurrence of travelling plastic hinges in the dynamic case. The sandwich plates outperform monolithic plates of equal mass with the square-honeycomb core plates having a higher shock resistance compared to the pyramidal core plates.

The finite element simulations capture the observed response with reasonable accuracy. These calculations show that the pressure versus time histories imparted on the clamped monolithic plates are similar to those imparted on the sandwich plates for projectiles with momentums $I_0 \geq 6 \text{ kN s m}^{-2}$. This confirms that the differences in the observed responses of the monolithic and sandwich plates for a given foam projectile momentum are due to differences in the intrinsic impact resistances of these plates.

References

- Cote F., Deshpande V. S., Fleck N. A., Evans A. G., 2004. The out-of-plane compressive behaviour of metallic honeycombs. *Materials Science and Engineering: A* 380, 272-280.
- Deshpande V. S., Fleck N. A., 2000. Isotropic constitutive models for metallic foams. *Journal of Mechanics and Physics of Solids* 48, 1253-1283.
- Fleck N. A., Deshpande V. S., 2004. The resistance of clamped sandwich beams to shock loading. *Journal of Applied Mechanics, ASME* 71(3), 386-401.
- McShane G. J., Radford D. D., Deshpande V. S., Fleck N. A., 2005. The response of clamped sandwich plates with lattice core. *European Journal of Mechanics A/Solids* (in print).
- Jones N., 1989. *Structural Impact*, Cambridge University Press.
- Nemat-Nasser S., Guo W.-G., Kihl D. P., 2001. Thermomechanical response of AL-6XN stainless steel over a wide range of strain-rates and temperatures. *J. Mech. Phys. Solids* 49, 1823-1846.
- Qiu X., Deshpande V. S., Fleck N. A., 2005. Impulsive loading over a central portion of clamped sandwich beams. *Journal of Mechanics and Physics of Solids* 53(5), 1015-1046.
- Radford D. D., Deshpande V. S., Fleck N. A., 2005a. The use of metal foam projectiles to simulate shock loading on a structure. *International Journal of Impact Engineering* 31(9), 1152-1171.
- Radford D. D., Fleck N. A., Deshpande V. S., 2005b. The response of clamped sandwich beams subjected to shock loading. *International Journal of Impact Engineering* (in print).
- Radford D. D., McShane G. J., Deshpande V. S., Fleck N. A., 2005c. The dynamic response of clamped circular sandwich plates with metallic foam cores. *International Journal of Solids and Structures* (in print).
- Rathbun H. J., Radford D. D., Xue Z., Yang J., Deshpande V. S., Fleck N. A., Hutchinson J. W., Zok F. W., Evans A. G., 2005. A dynamic probe for validating simulations of shock loaded metallic sandwich panels. *International Journal of Solids and Structures* (in print).
- Stout M. G., Follansbee P. S., 1986. Strain-rate sensitivity, strain hardening, and yield behaviour of 304L stainless steel. *Trans. ASME: Journal of Engineering Materials Technology* 108, 344-353.
- Symmonds P. S., 1954. Large plastic deformation of beams under blast type loading. *Second US National Congress of Applied Mechanics*.
- Wadley H. N. G., Fleck N. A., Evans A. G., 2003. Fabrication and structural performance of periodic cellular metal sandwich structures. *Composites Science and Technology* 63(16), 2331-2343.
- Wang A. J., Hopkins H. G., 1954. On the plastic deformation of built-in circular plates under impulsive load. *Journal of Mechanics and Physics of Solids* 3, 22-37.
- Xue Z., Hutchinson J. W., 2003. Preliminary assessment of sandwich plates subject to blast loads. *International Journal of Mechanical Sciences* 45, 687-705.
- Zupan M., Deshpande V. S., Fleck N. A., 2004. The out-of-plane compressive behaviour of woven-core sandwich plates. *European Journal of Mechanics - A/Solids* 23(3), 411-421.

Shock wave propagation in porous materials: the particular case of the syntactic foams

Jose Baranda Ribeiro, Jose Campos, Ricardo Mendes and Igor Plaksin

LEDAP – Laboratory of Energetics and Detonics – Mechanical Engineering Department – Faculty of Sciences and Technology – University of Coimbra, Pinhal de Marrocos – Polo II, 3030-788 Coimbra, Portugal

Microscale experiments, involved the use of an optical fiber strip with up to 64 independent channels with 250 μm of diameter each, which allows the observation of the light emitted during the shock wave [SW] propagation within syntactic foam samples with a temporal resolution in the order of the nanosecond and a spatial resolution in the order of few tens of μm were performed. The obtained results allow the observation of variations of the SW propagation velocity with the initial specific mass of the samples and with the intensity of the SW solicitation and also a non common variation arising from the differences in the characteristic size of the HGMS. It was observed that for the samples prepared with HGMS of medium and large sizes the intensity of the transmitted SW was well above what could be observed for the samples prepared with HGMS of small sizes or without any HGMS at all. It was also possible to find a characteristic propagation distance, resulting from the product of the SW velocity and the period of oscillation of the light intensity that was found very close to the characteristic values of the inter-particle distance for the samples with the smaller specific mass. All this experimental facts point to a pulsed propagation way of the SW ruled by the distribution of the HGMS in the polymeric matrix in which the collapse of the HGMS is determinant.

INTRODUCTION

The interest that is behind most of the studies on shock wave compression of porous materials is related with its usefulness in the attenuation of shock waves and in the determination of the Equations of State at very high pressures and temperatures. Actually to these subjects of interest were added the dynamic compaction of powders and the observation of very rare chemical reactions in mixtures of powders. Until few years ago [1] the majority of the work done in this area just looks for a relation between the initial porosity of the material and the Hugoniot Curve of the material. The well know $P-\alpha$ model [2] is an example of that situation. In that model, and in the models related, the initial porosity is taking into account through the α parameter but the material is considered to be homogeneous and the states of non-equilibrium are not considered. It is believed, however, nowadays that many aspects of the macroscale behaviour of the porous materials are due to the differences in the wave paths, sweeping around and closing the voids, but experimental and theoretic evidence of this still remains an open question in the study of porous solids. To answer to this question it is necessary to take the challenge of the direct observation and numeric simulation of the SW propagation process with a spatial resolution close to the characteristic length of the pores. This situation is addressing the investigation in the area to the study of porous materials presenting as an essential feature, the possibility to control, in wide limits, the size, the amount, the shape and even the relative position of the

pores. Among the materials presenting those characteristics are the ones resulting from the mixture of a thermoset resin with Hollow Glass Micro Spheres [HGMS], known in the literature as Syntactic Foams [SF] with the Greek origin word – *syntactic* – denoting precisely the ordered characteristic of the material, at least when compared with the kinds of porous materials.

During the bibliographic review made in the beginning of this work some papers were found referring about experiments carried out with this kind of materials, performed from a macroscopic/equilibrium point of view, but where its ordered character was already recognized [3, 4]. This characteristic, together with the ability to control the initial specific mass, is even referred in a more recent work [5] as one of the reasons for its use as reference materials for the benchmarking of Hydrocodes. Beyond that it was also found that this kind of materials has a wide and very interesting field of technologic applications. The use of HGMS, which are a fine, white, loose and very light powder of individual hollow spherical “glass” shells, as one of the components of polymeric matrix composites materials confers them a set of mechanical, acoustic and electromagnetic advantages over the polymer itself like, for example: less specific mass, bigger resistance to compression, bigger rigidity, bigger resistance to shear, bigger resistance to crack propagation, smaller thermal expansion coefficient, smaller dielectric constant, smaller magnetic permeability, smaller thermal conductivity, bigger ability for acoustic barrier and increase fire resistance [6]. To this set of outstanding properties is associated a very high technologic value that makes this kind of materials suitable for applications in areas ranging from aerospace to microelectronics going through the sea exploration and defence. As examples it can be referred that the SF are used in ablative coatings for rocket motors and turbo reactors, as core material for multi-laminated composites, coatings for radar and sonar invisible structures, deep immersion buoyancy in submarines and off-shore platforms, for electromagnetic and mechanic shielding in aero-space structures, potting of selected parts of electronic circuits and even for prosthetic applications [7-10].

The interest of the study of the propagation of SW in SF is then justified; from a fundamental point of view because it's a reference material in the area of the porous materials – with parameters easily characterized and controlled – and from a technologic point of view because of its wide range of applications. The global objective of this work is to contribute for the development of a model for the behaviour for porous materials when compressed by high amplitude SW, eventually extendable to the all group of heterogeneous materials, precise, physically sustained and including microscale information. That was done by the development of an experimental methodology which allows the access to information, at a microscale level, about the SW propagation process in the referred kind of materials, by the analysis of that information, and other, like the one resulting from the numeric simulation of the wave interaction with groups of HGMS, by the identification of the mechanism of propagation and by the suggestion of a phenomenological model that should be verified by the macroscale results. So what follows is a detailed description of the microscale experimental procedure and its results analysis to which follows a description of the macroscale experimental procedure and results analysis.

MICROSCALE EXPERIMENTS

Materials description and sample characterization

The HGMS used in the SF samples preparation were provided by the AKZO-Pennsylvania Quartz Corporation and have the commercial designation of Q-CEL 300. They are described by the manufacturer as a silicate glass spherical shell with approximately 1.5 μm of thickness and a characteristic particle size presenting a $d_{50} = 92 \mu\text{m}$, with 80% of the particles diameters between 30 and 167 μm , and a specific effective mass of 0.21 g/cm^3 . Prior to its utilization they

were sieved in three different granulometric classes characterized by the following values of d_{50} : 42, 92 and 135 μm . The polymer binder used in these particular experiments was the epoxy resin Araldite AY 103 with the curing agent Hardener HY 951, both obtained from Ciba-Geigy. Five different groups of SF samples have been prepared for the experiments being each one of them characterized by a unique pair of initial density and HGMS characteristic size (d_{50}). The main characteristics of the studied groups are presented in the Table 1 and their photos can be observed in Figure 1.

Designation	HGMS d_{50} [μm]	HGMS/Binder mass ratio [%]	Initial effective density [g/cm^3]	Characteristic distance between the HGMS [μm]	
				CFC	Hexagonal
EP-M-10	92	10	0.639	66	76
EP-M-7.5	92	7.5	0.812	74	85
EP-M-5	92	5	0.917	82	95
EP-S-10	42	38	0.631	28	33
EP-L-10	135	5	0.994	132	153
Binder	-	-	1.18	-	-

Table 1. Main characteristics of the studied SF groups.

Shock wave generators

All the samples were shock loaded using PBX, based on RDX, cylindrical explosive charges. For the EP-M-10 samples, Nitromethane [NM] cylindrical explosive charges were also used. The level of the SW pressure, in Kapton[®], evaluated at the end of an inert barrier that was always placed between the terminus of the explosive charge and the top surface of the samples was 20.0 and 9.6 GPa, respectively, for the PBX and for the NM charges.

Experimental set-up and diagnostic means

The observation of the light emitted by the samples during the SW propagation process was made using a modified version of the optical method developed by Plaksin *et al.* at the Laboratory of Energetics and Detonics of the University of Coimbra for the observation of the detonation wave propagation process [11-13]. The main element of this method is an optical fiber strip with 64 independent channels, each one of them with 250 μm of diameter, that carries the light, without any other intermediate optics, from the samples to a nanosecond resolution electronic streak camera (THOMSON TSN 506 N). A schematic representation of the used experimental set-up can be seen in Figure 2 a). As it is shown there, in each experiment the samples are placed below an inert barrier, at the end of the explosive charge, and below them, oriented toward the incoming SW, are positioned the referred optical fibers. In order to evaluate the intensity of the SW transmitted throughout the SF samples a set of Kapton[®] layers was placed between its bottom surface and the top of the fibers. A typical streak record obtained with the configuration shown in Figure 2 a) is shown in Figure 2 b). A temporal histogram of this streak record can be seen in the Figure 3 a). In both, the streak record and the temporal histogram, is possible to observe, for each one of the porous samples, an initial long, and non-homogeneous in intensity, light zone corresponding to the SW propagation in the SF samples, followed by almost equal spaced strips of light, corresponding to the SW propagation in the set of the output monitoring Kapton[®] layers. Measuring the time duration of the initial light zone is possible to evaluate the SW average velocity within the samples and measuring the time

propagation for each of the monitoring Kapton[®] layers is possible to evaluate the intensity of the transmitted SW. The characteristic period of the light intensity oscillations is evaluated by determining the autocorrelation function of several temporal histograms for each experimental situation. A typical result of the autocorrelation function evaluated for the temporal histograms shown in the Figure 3 a) can be seen in the Figure 3 b).

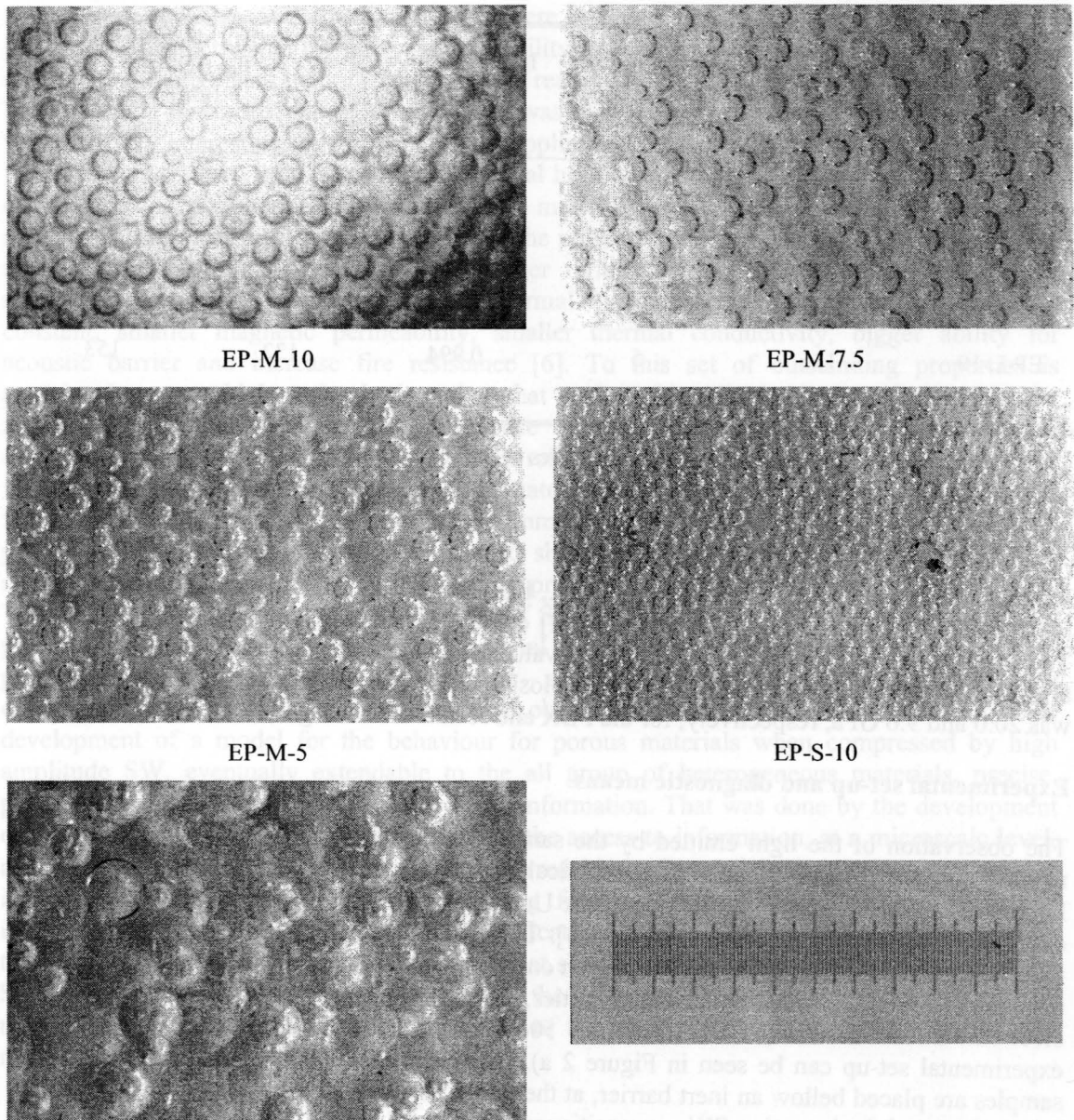


Figure 1. Photographs of the polymerisation surface of the different kind of samples used in the microscale experiments.

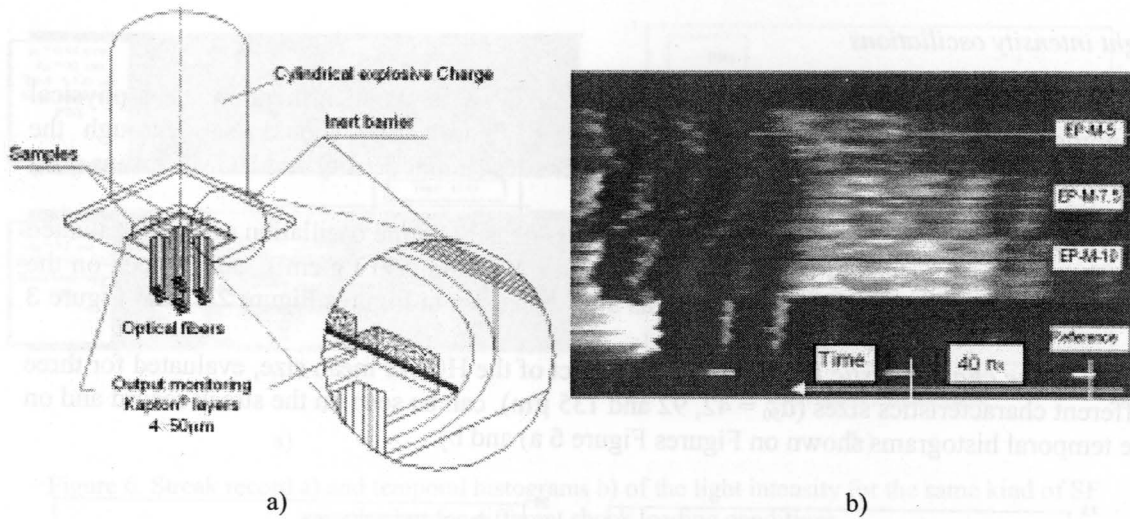


Figure 2. a) Schematic representation of the experimental set-up used in the obtainment of the presented results. b) Typical streak photochromogram .

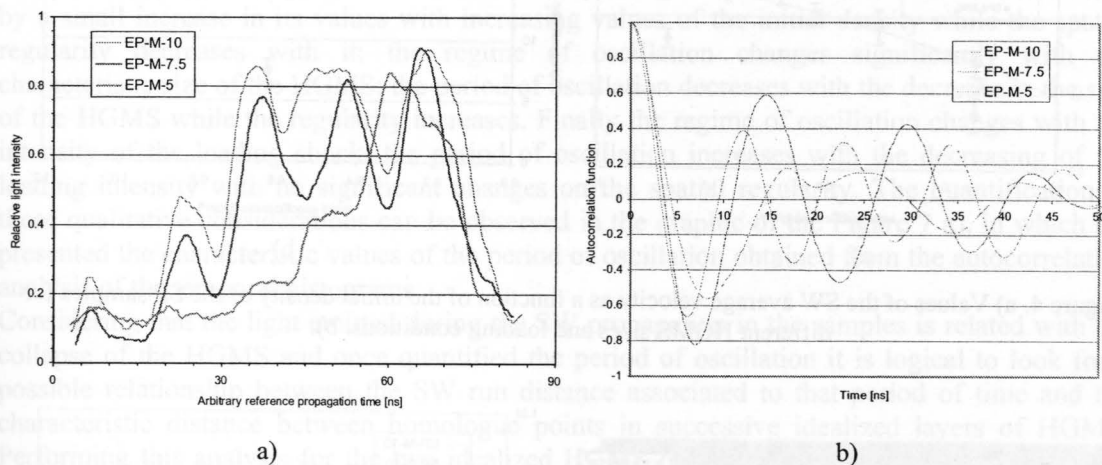


Figure 3. a) Typical temporal light intensity histogram corresponding to the streak record presented in the Figure 2b); b) Typical temporal autocorrelation function for the histograms presented in the Figure 3 a).

Experimental results

Average values of the SW velocity

The results of the SW average velocity, for SF samples with thicknesses ranging from 300 to 1050 μm , are presented in the Figure 4 a). It should be emphasise here that part of the dispersion in the result (related by the vertical error bars), observed for all the samples but in special for the EP-M-10 type, is a consequence of the use of different samples' thicknesses in the evaluation of the velocity. For the same loading conditions and for samples of the same kind a variation in the thickness from 300 to 1050 μm gives a variation in a the SW average velocity of 0.22 $\text{mm}/\mu\text{s}$. The obtained results show a significant variation with the initial density of the samples and a non-despicable differences arising from the HGMS sizes.

Light intensity oscillations

The first step in the light intensity oscillation analysis is its identification as a physical phenomena related to the SW propagation. This identification should pass through the evaluation of its sensibility to the samples characteristics (initial density and HGMS means size) and also to the loading conditions.

Effect of the initial density: The effect of the initial density on the oscillation regime, evaluated for three different values of that parameter (0.639, 0.812 and 0.917 g/cm³), can be seen on the streak record and in the temporal histograms already shown in Figures Figure 2 b) and Figure 3 a).

Effect of the characteristic HGMS size: The effect of the HGMS mean size, evaluated for three different characteristics sizes ($d_{50} = 42, 92$ and $135 \mu\text{m}$), can be seen on the streak record and on the temporal histograms shown on Figures Figure 5 a) and b).

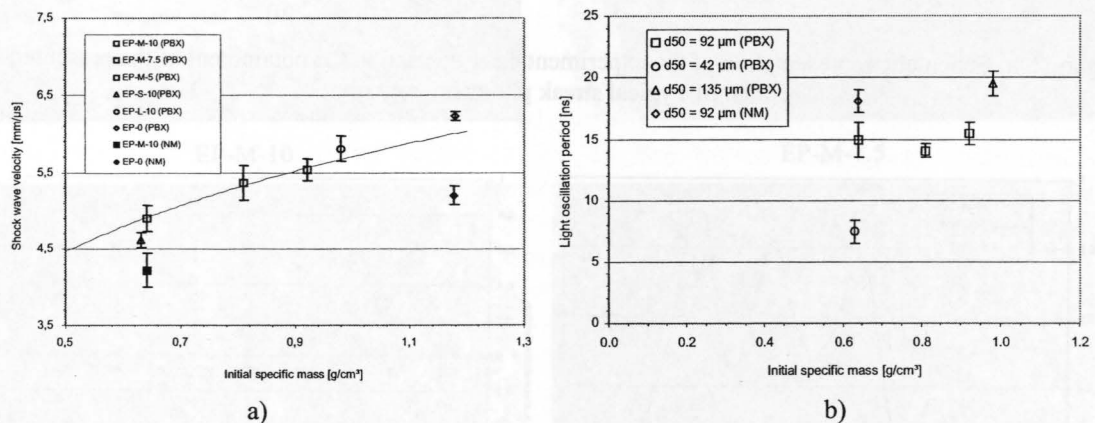


Figure 4. a) Values of the SW average velocity as a function of the initial density of the SF samples for different HGMS sizes and loading conditions. b).

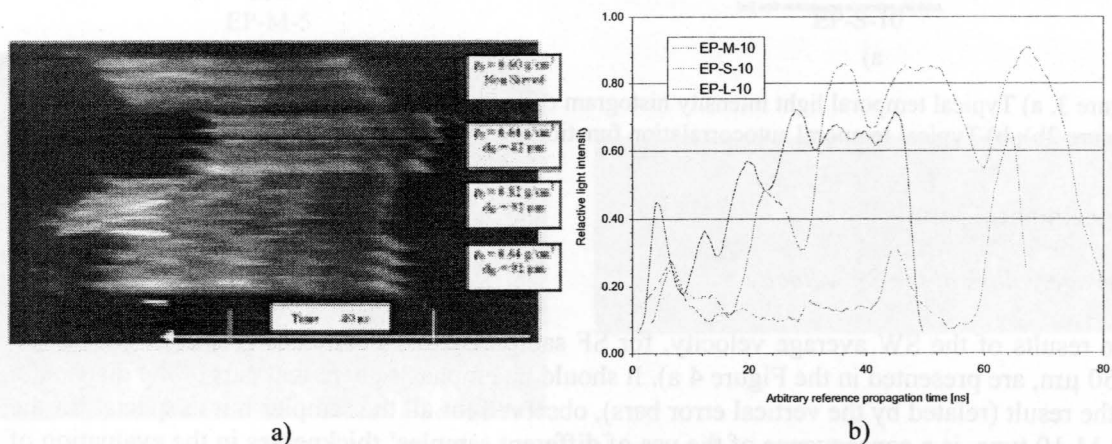


Figure 5. Streak record a) and temporal histograms b) of the light intensity for samples prepared with HGMS presenting different characteristics sizes.

Effect of the loading characteristics: The effect of the loading intensity on the oscillation regime, evaluated for two different loading intensity levels, is shown on the streak record and on the temporal histograms presented on Figures Figure 6 a) and b) respectively.

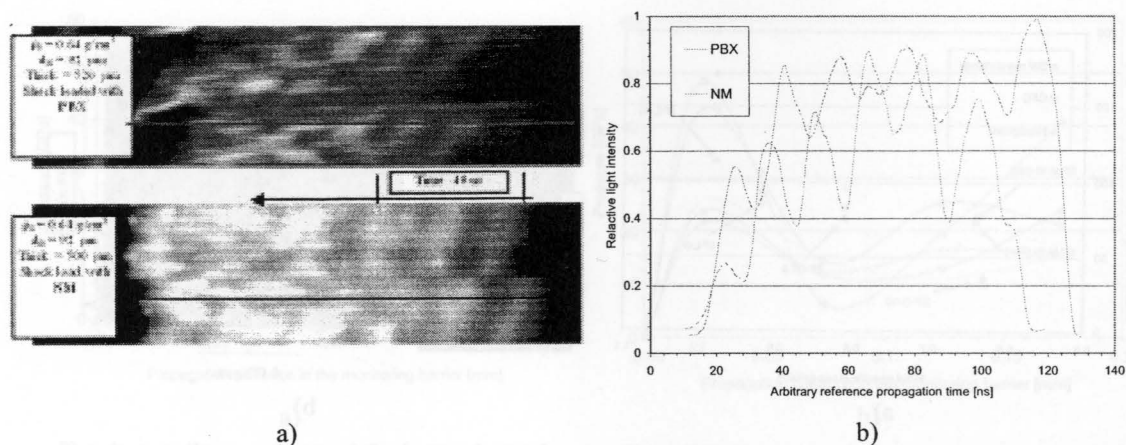


Figure 6. Streak record a) and temporal histograms b) of the light intensity for the same kind of SF samples but for different shock loading conditions.

The global analysis of the light intensity oscillations allow us to say the following: the regime of oscillation slightly changes with the initial density being the period of oscillation characterized by a small increase in its values with increasing values of the initial density while the spatial regularity decreases with it; the regime of oscillation changes significantly with the characteristic size of the HGMS; the period of oscillation decreases with the decrease in the size of the HGMS while the regularity increases. Finally the regime of oscillation changes with the intensity of the loading shock; the period of oscillation increases with the decreasing of the loading intensity with no significant changes on the spatial regularity. The quantification of these qualitative considerations can be observed in the graphic of the Figure 7 a), in which are presented the characteristic values of the period of oscillation obtained from the autocorrelation analysis of the temporal histograms.

Considering that the light emitted during the SW propagation in the samples is related with the collapse of the HGMS and once quantified the period of oscillation it is logical to look for a possible relationship between the SW run distance associated to that period of time and the characteristic distance between homologue points in successive idealized layers of HGMS. Performing this analysis for the two idealized HGMS distribution referred in the Table 1 we have reached to the values presented in the graphic of the Figure 7 a). In the Figure 7 b) is shown a streak record of the SW propagation in a 1050 μm thick SF sample ($d_{50} = 92 \text{ }\mu\text{m}$; $\rho_0 = 0.64 \text{ g/cm}^3$) side by side with an optical microscope photo of a transversal section of an identical sample. Overlaying this photo are placed the temporal histograms of the light captured by four adjacent optical fibers corresponding to a width distance of 1 mm. Despite of the impossibility to speak in a complete correspondence between the HGMS distribution in the matrix and the time histograms of the light, what can be observed in that Figure allow us to say that the concordance between the SW run distance during the period of an oscillation and the typical interparticle distance is an evidence of a pulsed propagation process dependent on the HGMS distribution in the polymeric matrix.

MACROSCALE EXPERIMENTS

Materials description and sample characteristics

As for the microscale experiments the HGMS used in the SF samples preparation for the macroscale experiments were provided by the AKZO-Pennsylvania Quartz Corporation and have the commercial designation of Q-CEL 300, however, on the contrary to what was done in

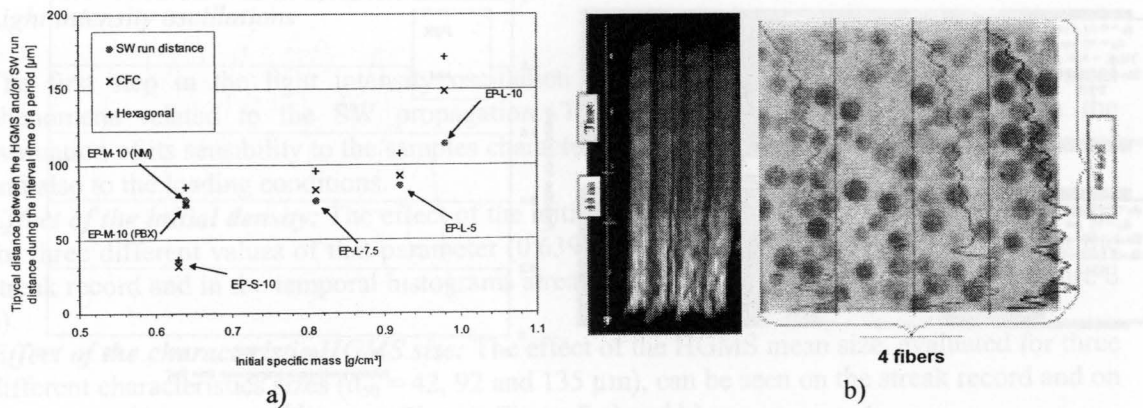


Figure 7. a) Typical values of the SW run distance for an interval of time corresponding to the characteristic period of the light oscillations compared with the distances between two homologue points for successive layers of HGMS admitting a CFC or Hexagonal distributions in the binder matrix. b) Typical streak record obtained for a SF prepared with HGMS presenting a mean diameter of 92 μm , an initial density of 0.64 g/cm^3 and a thickness of 1050 μm and corresponding optical microscope photograph of a transversal section of a SF identical to the one used to obtain the streak record.

Spatial profile of the intensity of the transmitted SW

The use of the output monitoring Kapton[®] barrier (4 layers of 50 μm of thickness each) allowed the evaluation of the spatial profile of the intensity of the transmitted (throughout the samples) SW. The results obtained are shown in the graphics of Figure 8. As it can be seen there the spatial profile of the wave transmitted through the porous sample change significantly with the porous size, however only small differences arise from the initial density values. For those SF samples prepared with HGMS with characteristic diameters of 135 μm (EP-L-10) and of 92 μm (EP-M-10, EP-M-7.5 and EP-M-5), the pressure values found for the first Kapton[®] layer are well above the pressure values found for the reference sample, prepared with any HGMS, while for the for the samples prepared with HGMS presenting a mean diameter of 42 μm those values are below the ones observed for the reference sample.

This overpressure values can only be explain by asymmetric collapse of the HGMS with jet formation which will act as a micro-shaped-charge and so the differences observed for the SW transmitted throughout the samples should be related with the ability of the HGMS to collapse asymmetrically forming micro-jets. The results show that bigger spheres collapse easier and produce more effective micro-jets. The independence of the results from the amount of spheres could be seen as a manifestation of the existence of different micro-jets intensities. The bigger number of micro-jets per unit of area that characterizes the samples with smaller initial specific mass when compared with the samples with bigger initial specific mass is compensated with its smaller intensity, for which should contributes the inability of the SW to sweep around the glass shell in order to produce an effective shaped charges.

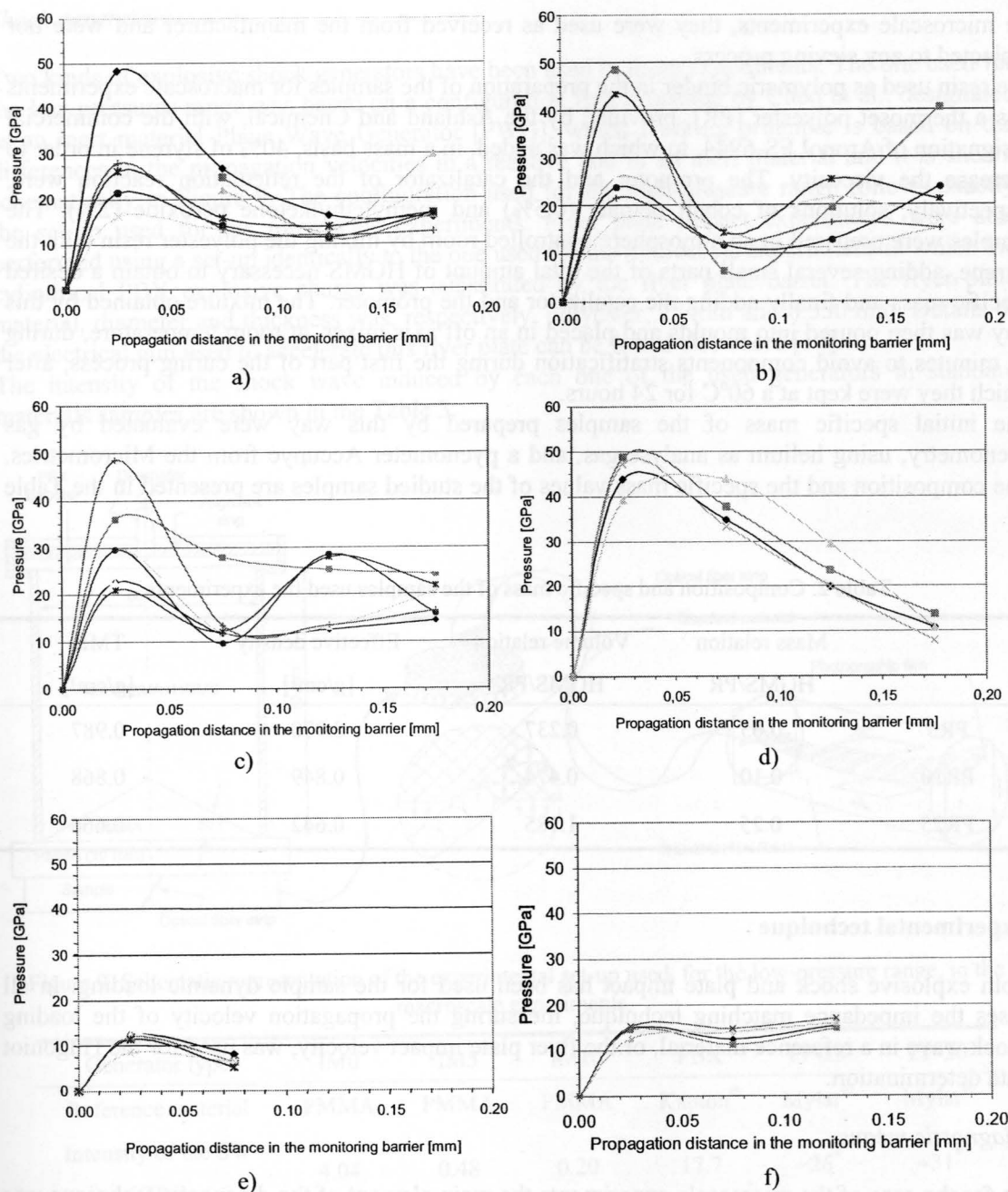


Figure 8. Spatial profiles of the intensity of the transmitted SW. a) EP-M-10; b) EP-P-7.5; c) EP-M-5; d) EP-L-10; e) EP-S-10; f) Reference sample (no HGMS, only binder).

MACROSCALE EXPERIMENTS

Materials description and sample characterization

As for the microscale experiments the HGMS used in the SF samples preparation for the macroscale experiments were provided by the AKZO-Pennsylvania Quartz Corporation and have the commercial designation of Q-CEL 300, however, on the contrary to what was done for

the microscale experiments, they were used as received from the manufacturer and were not subjected to any sieving process.

The resin used as polymeric binder in the preparation of the samples for macroscale experiments was a thermoset polyester [PR], provided by the Ashland and Chemical, with the commercial designation of Aropol FS-6944, to which was added, in a mass basis, 40% of styrene in order to decrease the viscosity. The promoter and the catalizator of the reticulation reaction were, respectively, solutions of cobalt octoate (0.5%) and methylethylketone peroxide (2%). The samples were prepared in an atmosphere controlled room by mixing the polyester resin with the styrene, adding several small parts of the total amount of HGMS necessary to obtain a desired specific mass and finally adding the catalizator and the promoter. The mixture obtained by this way was then poured into moulds and placed in an off axis mixer, at room temperature, during 60 minutes to avoid components stratification during the first part of the curing process, after which they were kept at a 60°C for 24 hours.

The initial specific mass of the samples prepared by this way were evaluated by gas pycnometry, using helium as analyse gas, and a pycnometer Accupyc from the Micrometrics. The composition and the specific mass values of the studied samples are presented in the Table 2.

Table 2. Composition and specific mass of the samples used the experiments

	Mass relation HGMS/PR	Volume relation HGMS/PR	Effective density [g/cm ³]	TMD [g/cm ³]
PR5	0.05	0.237	0.970	0.987
PR10	0.10	0.474	0.849	0.868
PR25	0.25	1.185	0.642	0.666

Experimental technique

Both explosive shock and plate impact has been used for the sample dynamic loading. In all cases the impedance matching technique, measuring the propagation velocity of the loading shock wave in a reference material, or the flyer plate impact velocity, was used for the Hugoniot data determination.

Diagnostic means

As for the case of the microscale experiments the main element of the diagnostic technique was an optical fiber strip with 64 independent channels with 250 μm of diameter each. This fiber can be inserted within the samples as it is shown schematically in the Figure 9 or placed under the samples and orientated toward the incoming shock wave in a similar way to what was done with the samples tested in the microscale experiments. In the first of the described configurations the simultaneous compression of the sample, the fibers and a light converter material placed between them allow the monitoring of the shock propagation and the evaluation of its velocity at each 250 μm of propagation as it is shown schematically in Figure 9. In the second case, used just for thin samples, with thickness' less than 1 mm, the semi-transparency of the samples and the emission of the light during the propagation of the shock wave within the samples is used to determine the propagation time in the samples and, by this way, once the thickness is known, the average propagation velocity. As for the microscale experiments the optical fiber strip is connected, without any intermediate optics to an electronic streak camera, Thomson TSN 506 N, which as a maximum temporal resolution of 1 ns.

Shock generators

Two kinds of explosive shock generators have been used in these experiments. The one used for the low pressures range was based on a configuration first proposed by Chen et al., designated as an inert material Plane Wave Generator [PWG], which working principle is based on the differences in the propagation velocities in a reactive and in an inert material and it is shown schematically in Figure 9. The configuration used for the high-pressure range follows exactly the set-up used for the microscale experiments. Flyer plate impact experiments were also performed using a set-up identically to the one used for the microscale experiments in which the cylindrical PBX explosive charge was substituted by the flyer plate barrel. The flyer plate material, diameter and thickness was, respectively, polyester, 25 mm and 0.350 mm. Details of the electrical gun used to accelerate this flyer plate can be found elsewhere [14].

The intensity of the shock wave induced by each one of the used generators in standard materials samples are shown in the Table 3.

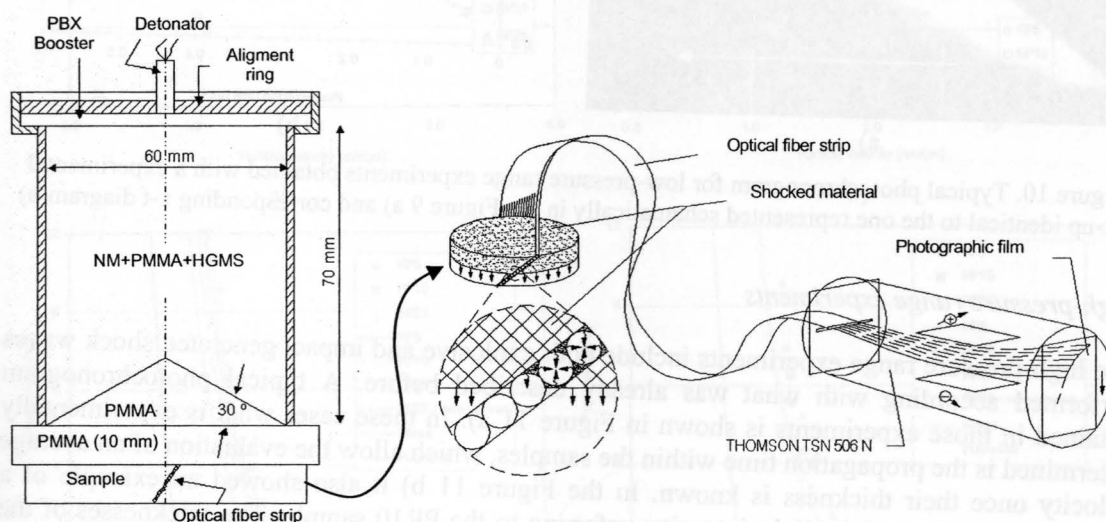


Figure 9. Schematic representation of the experimental set-up used, for the low-pressure range, in the macroscale experiments.

Generator type	IM0	IM5	IM10	PBX	FP-25	FP-30
Reference material	PMMA	PMMA	PMMA	Kapton [®]	Mylar [®]	Mylar [®]
Intensity of the SW [GPa]	4.04	0.48	0.20	17.7	≈26*	≈31*

Table 3. Scale of the intensity of the SW induced by each one of the used generator in reference material samples

Experimental results

Low-pressure range experiments

A typical photochronograms obtained with the low-pressure range experimental set-up is shown in Figure 10 a). From this kind of results x-t diagrams of the propagation process, like the one

* Depends on the flyer plate impact velocity, which is measured at each experiment.

that is presented in the Figure 10 b), can be obtain. Fitting a third order polynomial equation to the x-t points and take its derivative is possible to obtain a second order polynomial equation relating the propagation velocity with the propagation time. With these two equations x-t and v-t is possible determining the value of the propagation velocity for a propagation distance equal to zero and use that value for Hugoniot data determination.

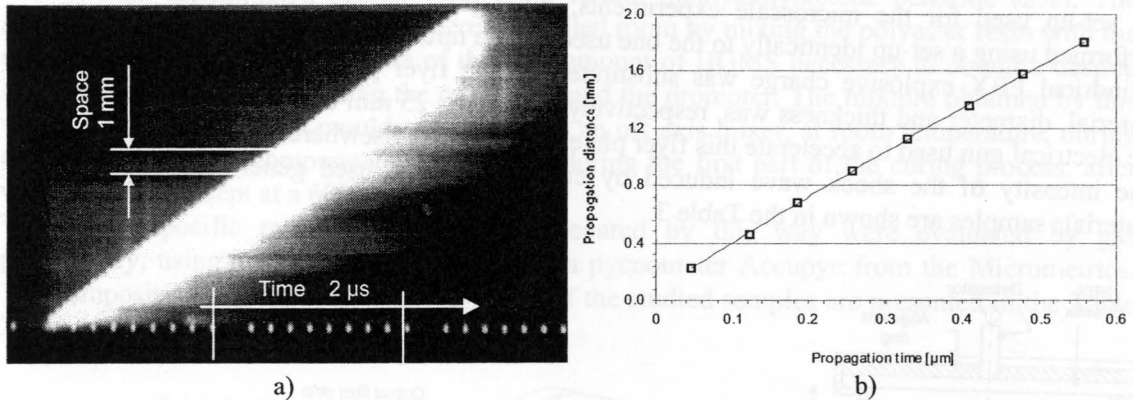


Figure 10. Typical photochronogram for low-pressure range experiments obtained with a experimental set-up identical to the one represented schematically in the Figure 9 a) and corresponding x-t diagram b)

High-pressure range experiments

The high-pressure range experiments include both explosive and impact generated shock waves performed according with what was already described before. A typical photochronogram obtained in those experiments is shown in Figure 11 a). In these cases what is experimentally determined is the propagation time within the samples, which allow the evaluation of an average velocity once their thickness is known. In the Figure 11 b) it also showed an example of a temporal histogram of the light intensity, referring to the PR10 sample. The thicknesses of the samples used in this kind of experiments were comprised between 500 and 1000 μm.

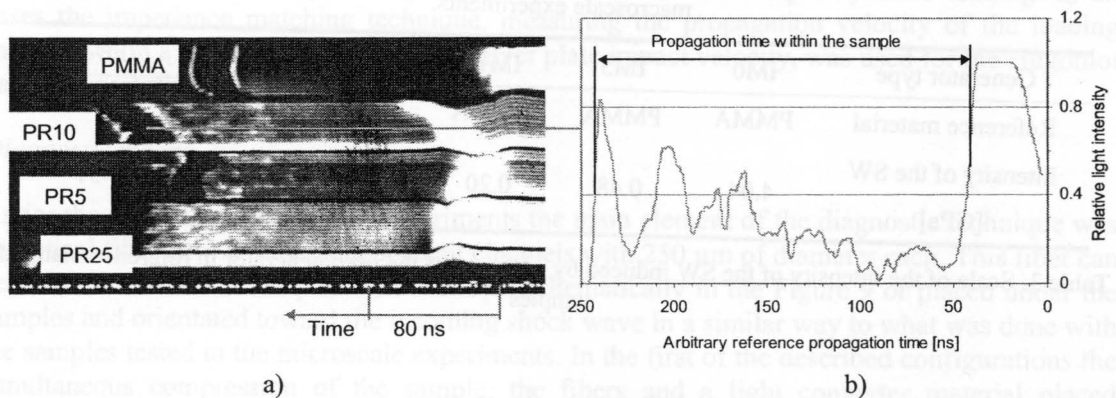


Figure 11. Typical photochronogram a) and corresponding light intensity histogram b) obtained for the high-pressure range experiments, for which the experimental set-up is shown schematically in Figure 2.

Hugoniot curves

Once the average shock propagation velocity in the samples and in a reference material (or/and the impact velocity of the 0.350 mm thick flyer plate) is known, is possible to determine their Hugoniot characteristics using the well know impedance matching technique. The results of

those calculations, performed with data from all the described experiments, are presented in the graphics of the Figure 12 in the P-up, us-up and P-v planes.

Differences in the results, arising from the initial specific volume values, can be observed in all the Hugoniot planes but are more significant for the P-up and us-up. In the first of the referred planes the results show a second order (parabolic) relation between the state variables and in the second of the referred planes (up-us), excluding the very low particle velocity range, a first order (linear) relation seems to match the experimental data very well.

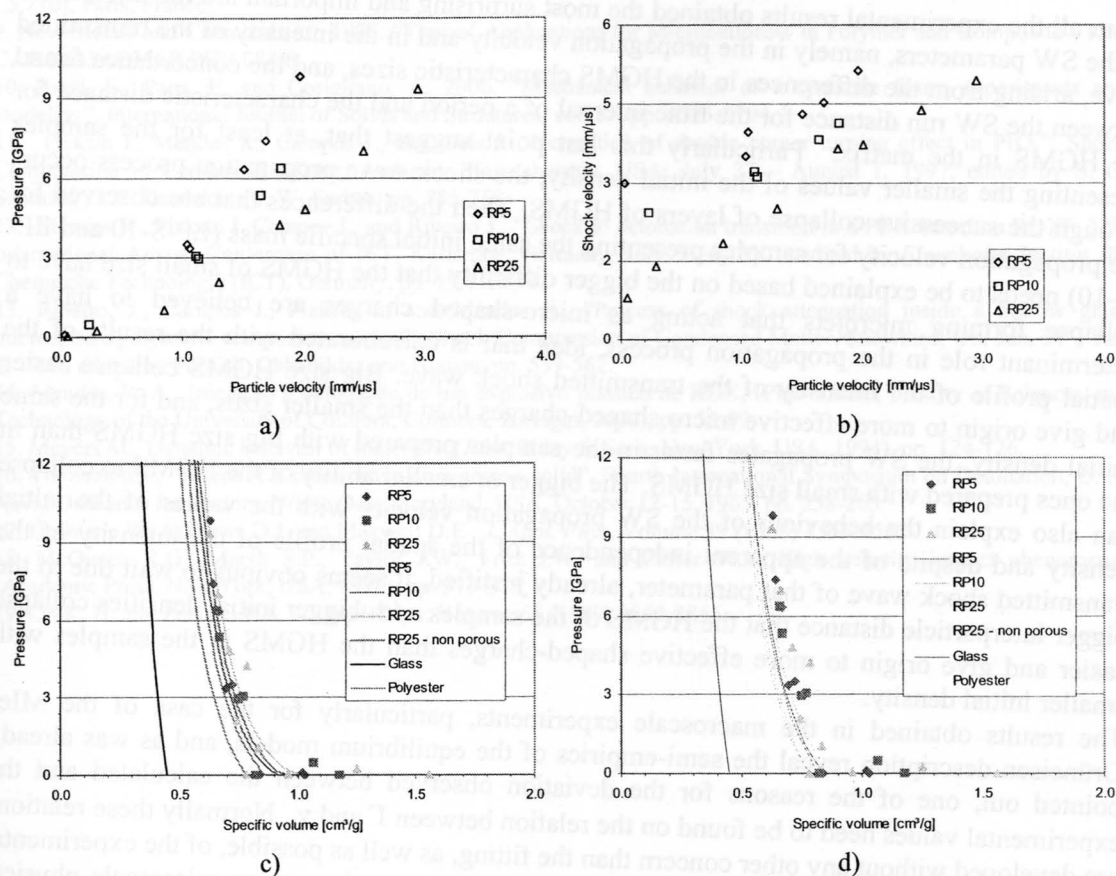


Figure 12. P-up a), us-up b) e P-v, (with results from Thouvenin/Hofmann c) and from Grüneisen d) models) Hugoniot planes.

Grüneisen and Thouvenin/Hofmann description of the experimental data

Together with the experimental data, in the graphics of the Figure 12, are also shown the Hugoniot curves of Glass, Polyester, and of an hypothetic solid, designated as RP25 – non porous, that should be considered resulting from the mixture of polyester and glass in a mass ratio of 100 to 25, respectively**. In those graphics are also shown the Hugoniot curves predicted by the Grüneisen and by the Thouvenin/Hofmann models.

Both models are very well known and detail descriptions of them can be found elsewhere [15-17]. Data description by the Thouvenin/Hofmann model can be considered good but data description by Grüneisen can not be considered so. One of the reasons for that can be related with the extreme dependence of the results obtained with this model on the Grüneisen coefficient values, as it is stated by Oh *et al.* [19], small errors in that coefficient can lead to big errors in the calculated pressure. In this case it was considered that $\Gamma/v = \Gamma_0/v_0$, where Γ is the

** The Hugoniot of this hypothetic material was evaluated using the method of mixtures [18]

Grüneisen coefficient, v is the specific volume and the index 0 denotes the initial conditions of the non-porous material corresponding to each one of the tested samples which could be not enough to "fit" the experimental data.

DISCUSSION OF THE RESULTS AND CONCLUSION

From all the experimental results obtained the most surprising and important are the differences in the SW parameters, namely in the propagation velocity and in the intensity of the transmitted wave, arising from the differences in the HGMS characteristic sizes, and the concordance found between the SW run distance for the time interval of a period and the characteristic distance for the HGMS in the matrix. Particularly this last point suggest that, at least for the samples presenting the smaller values of the initial density, the shock wave propagation process occurs through the successive collapse of layers of HGMS. Then the differences that are observed for the propagation velocity for samples presenting the same initial specific mass (EP-S-10 and EP-M-10) needs to be explained based on the bigger difficulty that the HGMS of small size have to collapse forming microjets that acting as micro-shaped charges are believed to have a determinant role in the propagation process, idea that is corroborated with the results of the spatial profile of the intensity of the transmitted shock wave. Big size HGMS collapse easier and give origin to more effective micro shaped-charges than the smaller sizes, and for the same initial density, the SW propagates faster in the samples prepared with big size HGMS than in the ones prepared with small size HGMS. The bigger or smaller ability of the HGMS to collapse can also explain the behaviour of the SW propagation velocity with the values of the initial density and despite of the apparent independence of the spatial profile of the intensity of the transmitted shock wave of that parameter, already justified, it seems obvious to wait due to the bigger interparticle distance that the HGMS of the samples with bigger initial densities collapse easier and give origin to more effective shaped-charges than the HGMS in the samples with smaller initial density.

The results obtained in the macroscale experiments, particularly for the case of the Mie-Grüneisen description reveal the semi-empirics of the equilibrium models, and as was already pointed out, one of the reasons for the deviation observed between the calculated and the experimental values need to be found on the relation between Γ and v . Normally these relations are developed without any other concern than the fitting, as well as possible, of the experimental data and that's way this model work despite of the complete absence on microscale physical basis. On the contrary, the Thouvenin/Hofmann model, despite of heuristic origin, incorporate one of the most important experimentally verified characteristics of the SW propagation process in porous materials: the pulsed, layer by layer, propagation process, and, without the necessity of any fitting parameters, is able of a very good description of the results.

References

1. Davison, L., Horie, Y. and Shahinpoor, M., 1997. "Response of highly porous solids to shock loading", High-Pressure Shock Compression of Condensed Matter IV, edition L. Davison, Y. Horie and M. Shahinpoor, Springer-Verlag, New York, USA.
2. Herrmann, W., 1969. "Constitutive equation for the dynamic compaction of ductile porous materials", Journal of Applied Physics, vol. 40, n° 6, pp. 2490-2499.
3. Linde, R., and Schmidt, D., 1966. "Shock propagation in nonreactive porous solids", Journal of Applied Physics, vol. 37, n° 8, pp. 3259-3271.
4. Maw, J., Withworth, N., and Holland, R., 1996. "Multiple shock compression of polyurethane and syntactic foams" Shock Compression of Condensed Matter-1995, edition S. Schmidt and W. Tao, AIP Conference Proceedings 370, New York, EUA, pp. 133-136.

5. Salisbury, D., Winter, R., Taylor, P., and Harris, E., 2000. "The response of foams to shock compression", Shock Compression in Condensed Matter-1999, edition M. Furnish, L. Chhabildas, and R. Hixson, AIP Conference Proceedings 505, New York, USA, pp.197-200.
6. New metals and chemicals ltd 1996 (1). "Advantages Arising From the Use of Microballons®", Ref. CAB/MB4TYPAP.PUB 08/96.
7. Verweil, H., de With, G., and Veeneman, D. 1985. "Hollow glass microsphere composites: preparation and properties", Journal of Material Science vol. 20, pp. 1069-107.
8. Radford, D., and Sadeh, W. 1994. "Role of volume fraction in composite EMI shielding", Proceedings of the 45th Congress of the International Astronautical Federation, edição da International Astronautical Federation (IAF-94-I.5.210), Paris, France.
9. New Metals and Chemicals ltd, 1996. "Typical Applications for Microballons® in Polymer and Composite", Ref. CAB/MB5ADVAR.PUB 08/96.
10. Rizzi, E., Papa, E. and Corigliano, A. 2000. "Mechanical behavior of a syntactic foam: experiments and modeling", International Journal of Solids and Structures, vol. 37, pp. 5773-5794.
11. Plaksin I., Mendes R., Campos J., and Gois J. "Interaction of double corner turning effect in PBX", Shock Compression in Condensed Matter, Amherst, Massachusetts, USA, July 27 – August 1, 1997, edited by S. C. Schmidt, D. P. Dandekar e J. W. Forbes, pp. 755-758
12. Mendes R., Plaksin I. Campos J., and Ribeiro J., "Shock to detonation transition in a PBX based on RDX", 32nd International Annual Conference of ICT, Karlsruhe, Germany, July 3 –6, 2001, edited by Fraunhofer Institut für Chemische Technologie (ICT), Germany, pp. 19.1-19.11.
13. Ribeiro, J., Campos J., Plaksin I., and Mendes R., "Process of shock attenuation inside a hollow glass microsphere/polymeric composite material", Shock Compression of Condensed Matter, Snowbird, Ut., Jun. 27 – Jul. 2, 1999, edited by Furnish, Chhabildas and Hixson, pp. 559-562.
14. Mendes, R. A., Iniciação e detonação de um explosivo plástico de RDX, (PhD Thesis, Faculty of Sciences and Technology of the University of Coimbra, Coimbra, Portugal, 2000), pp. 55-99.
15. Meyers M., Dynamic behavior of materials, (John Wiley & Sons, New York, USA, 1994), pp. 124-126.
16. Thouvenin J., "Effect of a shock wave on a porous solid", Fourth International Symposium on Detonation, U. S. Naval Ordnance Laboratory, White Oak, Maryland, USA, October 12-15, 1965, pp. 258-265.
17. Hofmann R., Andrews D.J. and Maxwell D.E., *J. Appl. Phys.* Volume 39 (1968) 4555-4562
18. McQueen R.G., Marsh S.P., Taylor J.W., Fritz J.W. and Carter W.J., High velocity impact phenomena, (Academic Press, New York, USA, 1970), pp. 373-377.
19. Oh K. H. and Persson P.A., *J. Appl. Phys.* Volume 65 (1989) 3852-3856.

A model for geologic materials (rock, soil and concrete), presentation and validation for a large range of dynamic loads

A. ROUQUAND¹, C. PONTIROLI²

¹ Centre d'Etudes de Gramat 46 500 Gramat (France)

² Communications & Systems, Av. Becquerel, Bât A. BP 19, 33072 Merignac (France)

A damage model has been developed at Centre d'Etudes de Gramat (CEG) to simulate the behavior of concrete under severe loading. This model includes two scalar damage variables that give respectively the loss of stiffness under tensile loading and the loss of stiffness under compressive loading. Strain rate effect allows to simulate the increase of the maximum tensile and compressive strength. The Hillerborg regularization concept is applied to limit the result dependency to the mesh size. A frictional stress can be included to simulate hysteresis loops for unloading and reloading paths. Furthermore, the elastic and plastic model proposed by Krieg has also been improved to include a non linear elastic behavior where the stiffness is now pressure dependent. According to the theory of effective stresses, this model can now take into account the water contents effect on the pressure volume relationship and on the shear yield stress. Recently these two models have been coupled.

The resulting elastic plastic and damage model have been tested on a large range of situations. Firstly we simulate simple stress strain paths like cyclic one dimensional tensile and compressive plane stress tests or cyclic compressive tests under one dimensional strain paths. The response under three axial compressive paths is also given. Finally we present comparisons between experiments and numerical simulations for a large number of tests on structure (quasi static and dynamic loading on reinforced concrete beams, impacts on reinforced concrete plates, side on explosion on a concrete slab, shock wave propagation in a earth media with different levels of water saturation). These results show the ability of the new model to predict the structure response for a large variety of situations.

1. INTRODUCTION

During the past decade, the Centre d'Etudes de Gramat (CEG) in France has mainly been involved in the vulnerability assessment of reinforced concrete structures against conventional weapons. The effectiveness of air to ground conventional warheads against concrete targets is also an other part of the CEG work. To achieve such work, numerical simulations, using engineering tools or physic codes, are extensively used. Most of the numerical simulations in physic codes take advantage of the explicit finite element method to simulate the behavior of structures under severe dynamic loading induced by conventional weapons. The accuracy of these finite element simulations is greatly dependent of the accuracy of the material model that describes the stress strain relation of concrete, rock and soil under highly dynamic and complex path loads. CEG has developed, during the last ten years, a material model expressly designed to simulate the behavior of complex structures under static loading, under far field or near field blast wave, under penetrating and perforating projectiles, etc.

2. THE TWO SCALAR DAMAGE MODEL

2.1 General considerations

For brittle materials like concrete and rock, the damage theory can be preferred to the well known elastic and plastic theory to model the crack propagation mechanism. In damage mechanic the damage parameter D , that describes the irreversible lost of material stiffness, takes more physical sense than the plastic strain which is itself more appropriate to simulate dislocation process in metallic media. Starting from a scalar damage model proposed by J. Mazars in 1984 [1] a modified two scalar damage model has been developed by C. Pontiroli in 1995 [2]. This model has been extensively used in the last ten years. It has been improved during all these years in order to become more and more effective as described by A. Rouquand in reference [3]. For the two scalar damage model, the stress tensor $\underline{\underline{\sigma}}$ is related to the strain tensor $\underline{\underline{\epsilon}}$ using the following relation :

$$\underline{\underline{\sigma}} = \alpha_t (1 - D_t) \left[\lambda_0 (\text{Trace} (\underline{\underline{\epsilon}} - \underline{\underline{\epsilon}}_{ft})) \underline{\underline{1}} + 2 \mu_0 (\underline{\underline{\epsilon}} - \underline{\underline{\epsilon}}_{ft}) \right] + \alpha_c (1 - D_c) \left[\lambda_0 (\text{Trace} (\underline{\underline{\epsilon}} - \underline{\underline{\epsilon}}_{ft})) \underline{\underline{1}} + 2 \mu_0 (\underline{\underline{\epsilon}} - \underline{\underline{\epsilon}}_{ft}) \right] + \underline{\underline{\sigma}}_{ft} \quad (1)$$

D_t and D_c represent the loss of stiffness for pure tensile loading and for pure compressive loading. α_t and α_c give the tensile part, and respectively the compressive part, of the loading ($\alpha_t + \alpha_c = 1$). λ_0 and μ_0 are the elastic Lamé coefficients. $\underline{\underline{\epsilon}}_{ft}$ and $\underline{\underline{\sigma}}_{ft}$ are respectively the closure strain and stress tensors. Figure 1 shows the relation between stress and strain for a one dimensional stress loading. As shown in figure 1, a tensile strain is applied in a first time. The corresponding stress is linearly increasing up to the maximum tensile stress σ_t . For higher tensile strain the tensile stress decreases due to the increasing of the tensile damage variable D_t . During the unloading phase (between points A and B), the stress strain slope is equal to $E_0 (1 - D_t)$. When the stress becomes compressive and equal to the closure stress σ_{ft} all the previous open cracks are closed and the original stiffness E_0 is recovered. At point B, the behavior becomes purely compressive. As the compressive load increases the compressive stress also increases linearly. Then some compressive damage D_c appears and the compressive behavior becomes more and more non linear. A softening stress is finally observed. During the second unloading phase (between points C and D) the stiffness is given by $E_0 (1 - D_c)$. At point D a tensile behavior is again recovered and the stiffness is now given by $E_0 (1 - D_t)$. Using the two scalar damage variables, cyclic loading can be easily simulated.

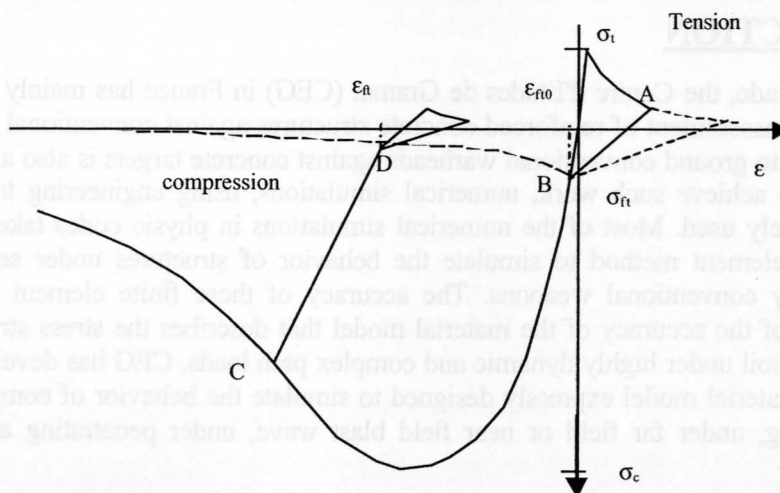


Figure 1 : Stress strain relation fore tensile or compressive loading.

The evolution of the tensile and compressive damage variables D_t and D_c are driven by an equivalent tensile strain $\tilde{\epsilon}_M$ which is itself computed from the sum of the principal strains :

$$\tilde{\epsilon}_M = \gamma_M \sqrt{\sum \langle \epsilon_i \rangle_+^2} \tag{2}$$

γ_M is a correction factor that becomes greater one when two stress components are simultaneously negative (compression). Damage variables D_t and D_c becomes positive when the equivalent tensile strain $\tilde{\epsilon}_M$ becomes greater than the tensile and respectively the compressive thresholds ϵ_{0t} and ϵ_{0c} .

2.2 Strain rate effects

It is well known that concrete is strain rate sensitive particularly for pure tensile loading. This effect is accounted using dynamic thresholds instead of static one's. The dynamic computed stresses are proportional to these dynamic strain thresholds. They are given by (for a compressive load) :

$$\epsilon_{0c}^d = \epsilon_{0c}^s \min(1.0 + a_c e^{bc}, 2.50) \tag{3}$$

and for tensile load :

$$\epsilon_{0t}^d = \epsilon_{0t}^s \min[\max(1.0 + a_t e^{bt}, 0.9e^{0.46}), 10.0] \tag{4}$$

In the two previous formula, exponent ^d and ^s refer respectively to dynamic and static values. a_c, b_c and a_t, b_t are user material coefficients. For high strain rate the dynamic increase factor is supposed to follow an empirical formula : $0.9\dot{\epsilon}^{0.46}$ that agrees very well with the experimental data obtained by Brara & Klepaczko [4] on a particular micro concrete. The dynamic increase factor, defined by the dynamic threshold divided by the static one, cannot become greater than 2.5 for a pure compressive loading, and cannot become greater than 10.0 for pure tensile loading. Figure 2 illustrates the evolution of the compressive (dashed line) and tensile (continuous line) increase factors versus the strain rate.

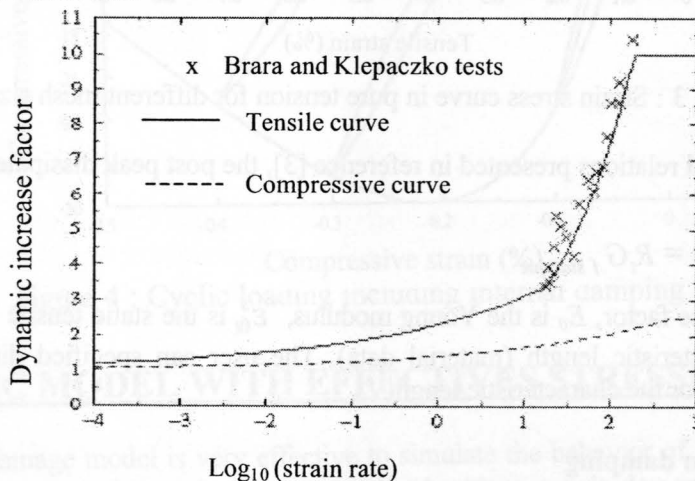


Figure 2 : Strain rate effects (two scalar damage model).

2.3 Hillerborg regularization concept

Concrete tensile behavior leads to a softening process. When the maximum tensile stress has been reached, the stress decreases as the strain increases (cf. figure 1). Such behavior induces numerical problems and the results become sensitive to the mesh size. In order to limit these disagreements, the regularization method proposed by Hillerborg [5] is used. In this method, the energy dissipated in a finite element mesh, when a crack propagates, is not related to the mesh size and remains a constant for a static loading. The post peak energy G_f is given by :

$$G_f = \int_{\varepsilon_p}^{\infty} \sigma(\varepsilon) dU = L_e \int_{\varepsilon_p}^{\infty} \sigma(\varepsilon) d\varepsilon = L_e A \quad (5)$$

U is the displacement of the crack lips, L_e is the mesh size and A represents the area under the strain stress curve. To keep the fracture energy constant G_f the area under the curve A has to decrease as the mesh size increases. Figure 3 shows the evolution of the strain stress curve for different mesh sizes.

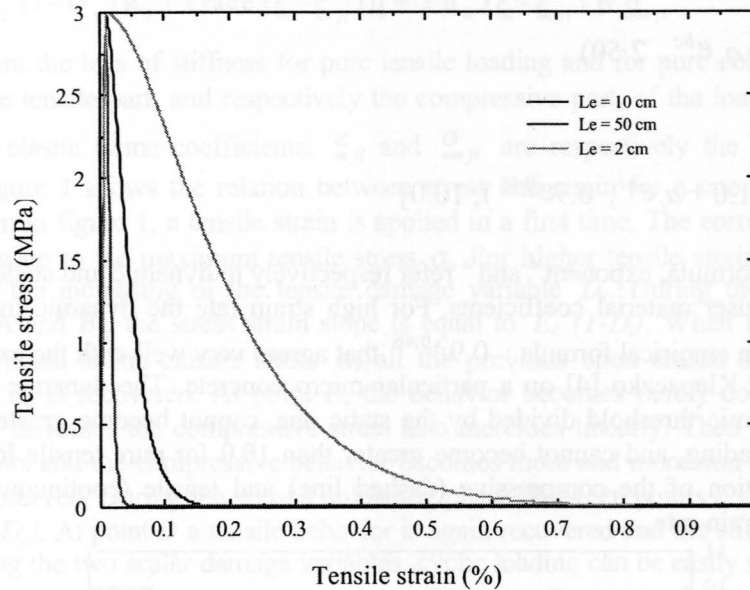


Figure 3 : Strain stress curve in pure tension for different mesh size.

According to the detailed relations presented in reference [3], the post peak dissipated energy G_f can be written as follow :

$$G_f = 4E_0 L_c \varepsilon_{0t}^s{}^2 R_t = R_t G_{f \text{ statique}} \quad (6)$$

R_t is the dynamic increase factor, E_0 is the Young modulus, ε_{0t}^s is the static tensile strain threshold. L_c is an internal characteristic length (material data). The user can specified directly the static fracture energy $G_{f \text{ statique}}$ or the characteristic length L_c .

2.4 Internal friction damping

In case of cyclic loading, like encountered during earthquake, friction stresses induce significant dissipated energy during unloading and reloading cycle. To account this important phenomena an additional damping stress is introduced in the model :

$$\underline{\underline{\sigma}} - \underline{\underline{\sigma}}_{fi} = (\underline{\underline{\sigma}} - \underline{\underline{\sigma}}_{fi})^{damage} + \underline{\underline{\sigma}}^{damping} \tag{7}$$

The damping stress generates hysteresis loop during the unloading and the reloading phase. The area under the closed loop defines the damping ratio :

$$\zeta = \frac{A_h}{E_0 (1-D) (\bar{\epsilon}_{max} - \bar{\epsilon}_{fi})} \tag{8}$$

A_h is the loop area under the stress strain curve, $E_0 (1-D)$ is the current material stiffness. The current damage variable D is a combination of the tensile damage D_t and of the compressive damage D_c .

$$D = \alpha_c D_c + \alpha_t D_t \tag{9}$$

ϵ_{max} is the maximum strain before unloading, ϵ_{fi} is the closure strain that defines the transition point between compression and tension. The damping stresses are computed in a such way that the damping ratio ζ is related to the damage D according to the following formula :

$$\zeta = (\beta_1 + \beta_2 D) \tag{10}$$

β_1 is a damping ratio for an undamaged and perfectly elastic material. $\beta_1 + \beta_2$ is the damping ratio for a fully damaged material. β_1 and β_2 are material parameters. Usually β_1 can be chosen equal to 0.02 and β_2 can be chosen equal to 0.05. Figure 4 shows, for cyclic tensile or compressive loading, the strain stress curve including damping stresses.

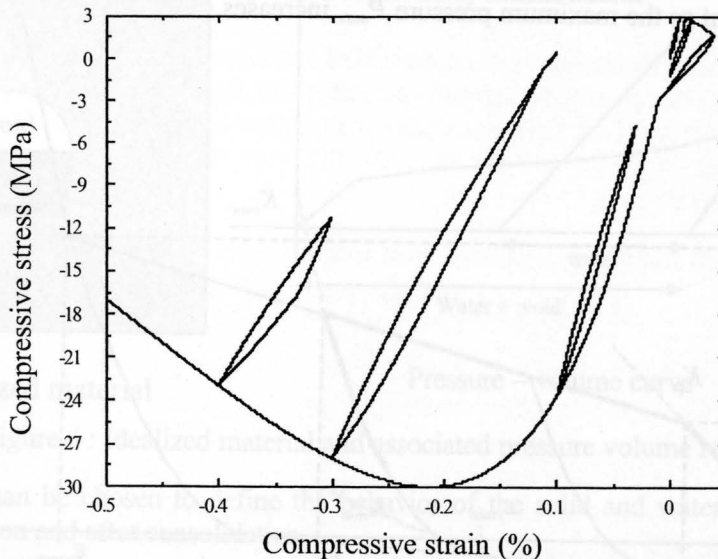


Figure 4 : Cyclic loading including internal damping stresses.

3. PLASTIC MODEL WITH EFFECTIVES STRESSES

The previous damage model is very effective to simulate the behavior of concrete and rock in case of unconfined loading with moderate pressure level with a magnitude comparable to the maximum compressive stress. For very high dynamic loads leading to higher pressure level, an elastic plastic

model is more appropriate. For example the impact of a projectile striking a concrete plate at 300 m/s induces local pressures of several hundred MPa. The previous damage model cannot simulate the pore collapse phenomena rising at this pressure level. It cannot also model the shear plastic strain occurring under high pressure. For an explosive charge detonating near a concrete plate the pressure level can reach very high values and the damage model is not designed to simulate these loads. The simple elastic and plastic model proposed by Krieg [6] can be preferred to simulate this kind of problem. CEG has improved the elastic and plastic Krieg model to account the non linear elastic behavior encountered during the unloading and reloading phase under high pressure regimes. Moreover an effective stress theory is introduced to account the effect of water in the porous media as described by C. Mariotti in reference [7]. This effect induces change on the pressure volume curve and on the plastic shear stress level.

3.1 Relation between pressure and volume for the modified Krieg model

Figure 5 shows a typical pressure volume curve used in the modified Krieg model. For pressure values under P_I the behavior between pressure and volume, is linear and elastic. For a maximum pressure greater than P_I , the pore collapse mechanism becomes effective. During the loading process, the pressure volume response follows a data curve. During the unloading, the behavior is elastic but non linear. The bulk modulus becomes pressure dependent. It is equal to K_{max} at the first unloading and decreases to K_{min} when the tensile pressure cutoff P_{min} is reached. This pressure cutoff becomes smaller and smaller as the maximum pressure P_{max} increases. When P_{max} is closed to P_I , K_{max} is close to K_{min} and also closed to the initial bulk modulus K_p . When P_{max} reach P_{cons} , K_{max} becomes equal to K_{grain} and K_{min} becomes equal to K_{0grain} . In a such way, the non linearity becomes more and more important as the maximum pressure P_{max} increases.

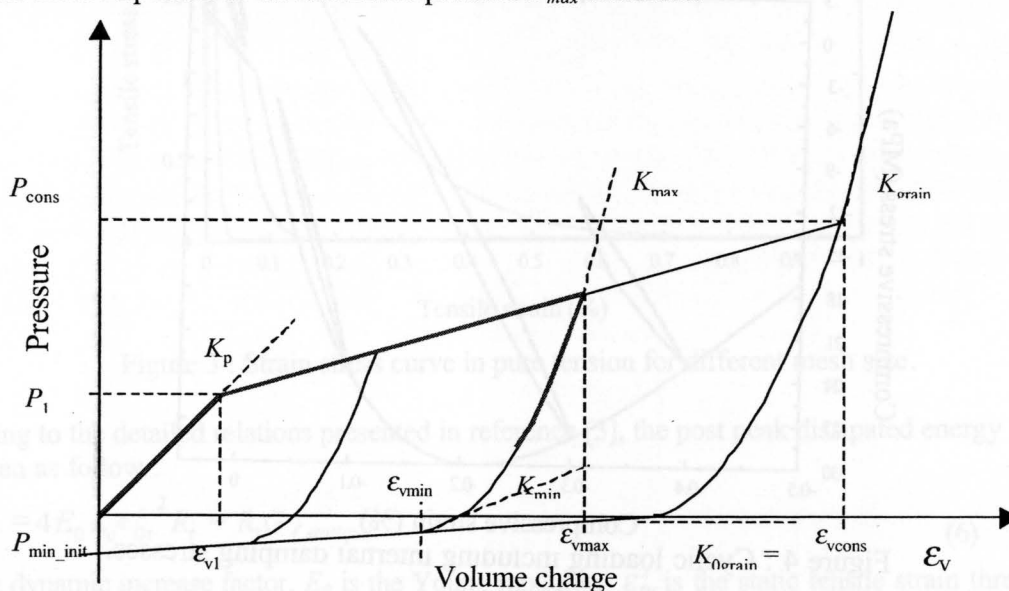


Figure 5 : Pressure volume behavior modified elastic and plastic Krieg model.

When P_{max} becomes greater than P_{cons} , the pore collapse phenomena is finished and the material is consolidated. At this state, the behavior becomes elastic and non linear. All the voids are removed from the material.

3.2 Water contents effect on pressure

Many concrete or geologic media have an open porous structure. The water can be moved through the porous media from one void to another. Consequently the void can be partially or totally filled of water. This induces significant change in the material response and particularly on the relation between the pressure and the volume. To understand more easily the water effect on a geologic medium, the material structure can be assimilated to a mixture of a solid media with a void partially filled with water like shown on the left part of figure 6.

The right part of figure 6 shows the generic response of a partially saturated material. This response is given in terms of pressure versus the volume change. For a dry material, the pressure volume response follows the dark blue curve. When the pressure is sufficient to remove all the voids, the response is given by the red curve. In case of a partially saturated material, the relation between pressure and volume is given by the response of the dry material until all voids are removed from the medium. Thereafter, the light blue curve gives the response of the solid and water mixture. The intersection of the red curve with the horizontal axis gives the porosity of the dry material. The intersection of the light blue curve with the horizontal axis gives the porosity of the partially saturated material. Consequently, when the material becomes more and more wet, the light blue curve moves on the left. In the modified plastic model presented here, the knowledge of the water contents ratio (water volume divided by the total volume) is sufficient to deduce all the improvements on the material behavior.

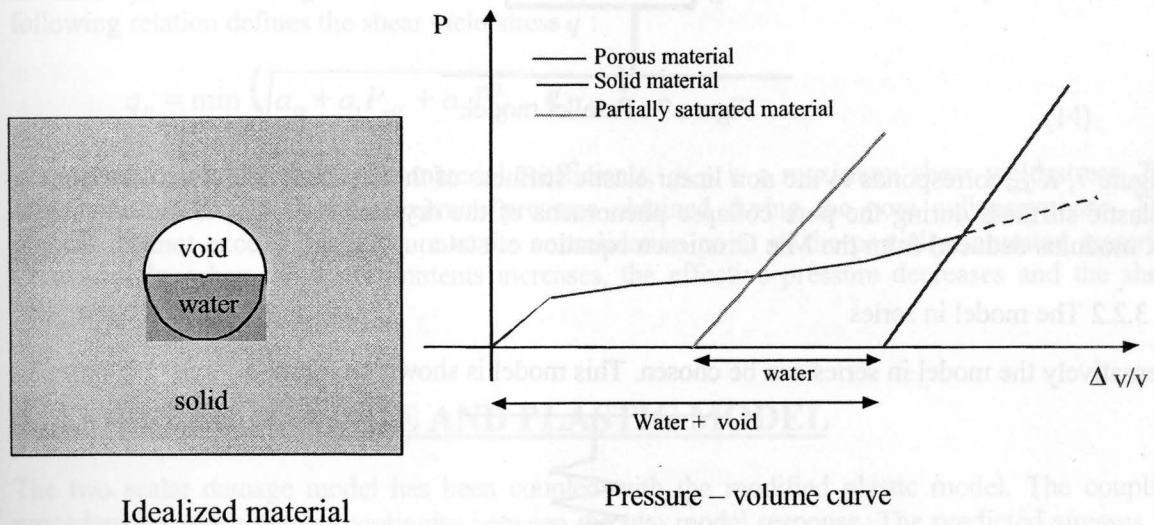


Figure 6 : Idealized material and associated pressure volume response.

Two solutions can be chosen to define the behavior of the solid and water mixture (blue curve) under compression and after consolidation.

3.2.1 The parallel model

The first choice is called the parallel model. In this model the pressure of the consolidated material can be written as the sum of two terms. The first is the pressure in the porous and dry medium and the second is the pressure in the water multiplied by the water volume ratio η . In the parallel model, we have the following relation :

$$P_{meg}(\epsilon_v) = P_{sec}(\epsilon_v) + \eta P_{eau}(\epsilon_v - \epsilon_{vps}) \tag{11}$$

P_{sec} is the pressure in the dry material given by the elastic and plastic model, P_{eau} is the pressure in the water. A Mie Gruniesen equation of state is used to define the pressure in water. This pressure is equal to zero when the volume change is equal to the porosity of the partially saturated material ϵ_{vps} . η is the volume of the water divided by the volume of the solid phase. The parallel model can be schematically represented as shown on figure 7.

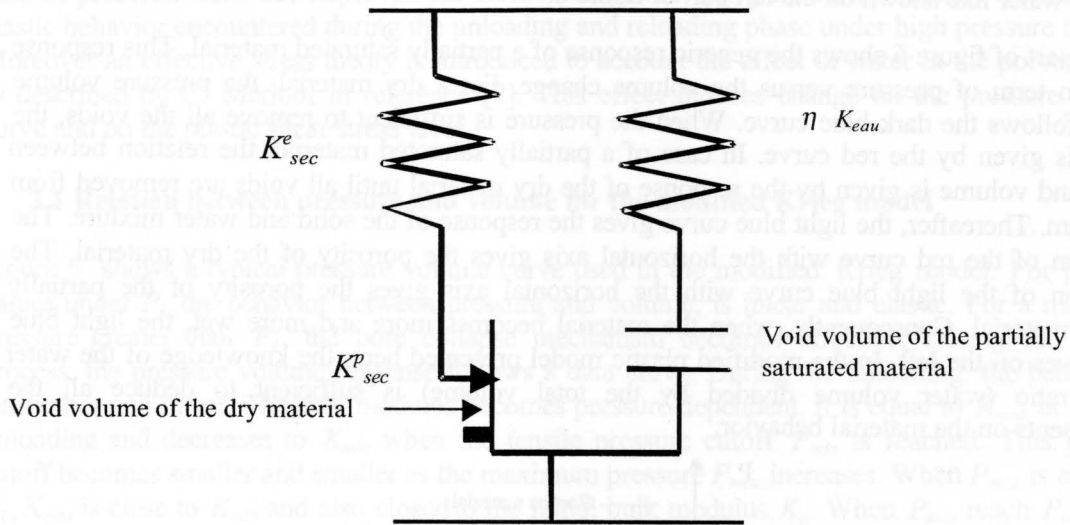


Figure 7 : Parallel model.

In figure 7, K^e_{sec} corresponds to the non linear elastic stiffness of the dry material, K^p_{sec} corresponds to plastic stiffness during the pore collapse phenomena of the dry material. K_{eau} is the non linear bulk modulus deduced from the Mie Gruniesen equation of state.

3.2.2 The model in series

Alternatively the model in series can be chosen. This model is shown on figure 8.

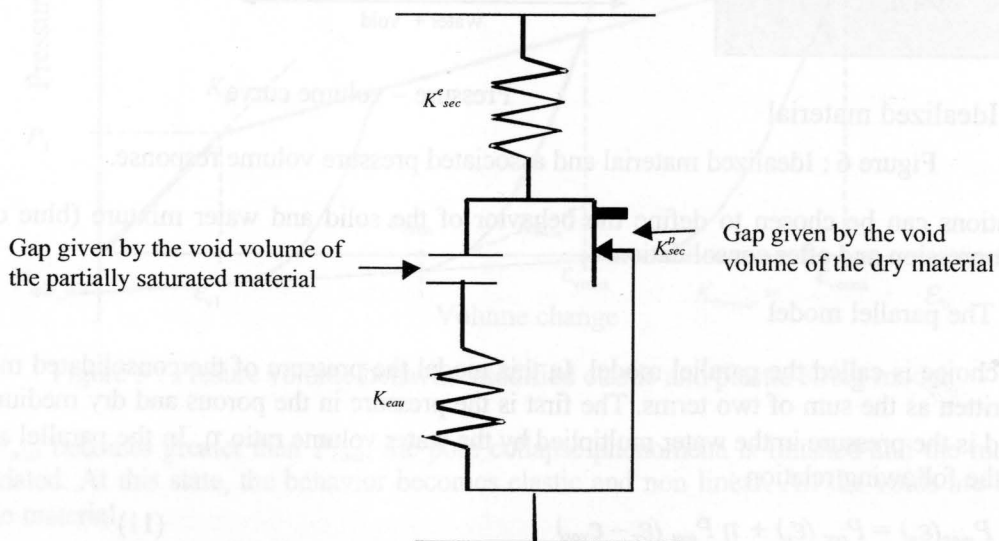


Figure 8 : Model in series.

In this model, the pressure after consolidation of the partially saturated material (pressure in the water and solid mixture) is given by :

$$P_{meg} = P_{sec}(\min(\epsilon_v - \epsilon_{vcons})) - P_l + P_{eau}(\epsilon_{veau}) \quad (12)$$

$P_{sec}(\min(\epsilon_v - \epsilon_{vcons}))$ is the pressure computed for a dry material. This pressure cannot exceed the consolidation pressure of the dry material. $P_{sec}(\min(\epsilon_v - \epsilon_{vcons})) - P_l$ corresponds to the pressure supported by the plastic slider. $P_{eau}(\epsilon_{veau})$ is the pressure in the water corresponding to a volume change ϵ_{veau} which is the difference between the total volume change ϵ_v and the volume change when the partially saturated material is consolidated ϵ_{vps} :

$$\epsilon_{veau} = \epsilon_v - \epsilon_{vps} \quad (13)$$

With the model in series, and for high pressure level, the total pressure minus the water pressure remains constant.

3.3 Water contents effect on the shear yield stress

In the original elastic and plastic Krieg model, the shear yield stress was pressure dependent. Now the shear yield stress depends on the effective pressure P_{eff} instead of the total pressure P . The following relation defines the shear yield stress q :

$$q_0 = \min \left(\sqrt{a_0 + a_1 P_{eff} + a_2 P_{eff}^2}, q_{max} \right) \quad (14)$$

Where a_0 , a_1 and a_2 are material coefficients, q_{max} is a maximum shear yield stress. The effective pressure P_{eff} is the maximum pressure obtained during the pore collapse phase. This pressure cannot exceed the pressure at the consolidation point of the partially saturated material. Consequently, when the water contents increases, the effective pressure decreases and the shear yield stress also decreases.

4. COUPLED DAMAGE AND PLASTIC MODEL

The two scalar damage model has been coupled with the modified plastic model. The coupling procedure ensures a perfect continuity between the two model response. The predicted stresses are given by the plastic model for loading without any equivalent tensile strain (no damage), and corresponds to the damage model response if the maximum pressure is too low to start the pore collapse phenomena or if the shear stress is too low to reach the shear yield stress. a_0 , a_1 and a_2 coefficients has to be chosen in order to obtain, for a pure tensile or a pure compressive static loading, the response given by the damage model. In dynamic problem these coefficients include strain rate effects in order to prevent any plastic strains in the material response for unconfined loading like in pure tensile or compressive tests. The figure 9 shows the static response obtained on a cylinder specimen for triaxial tests with increasing lateral pressure.

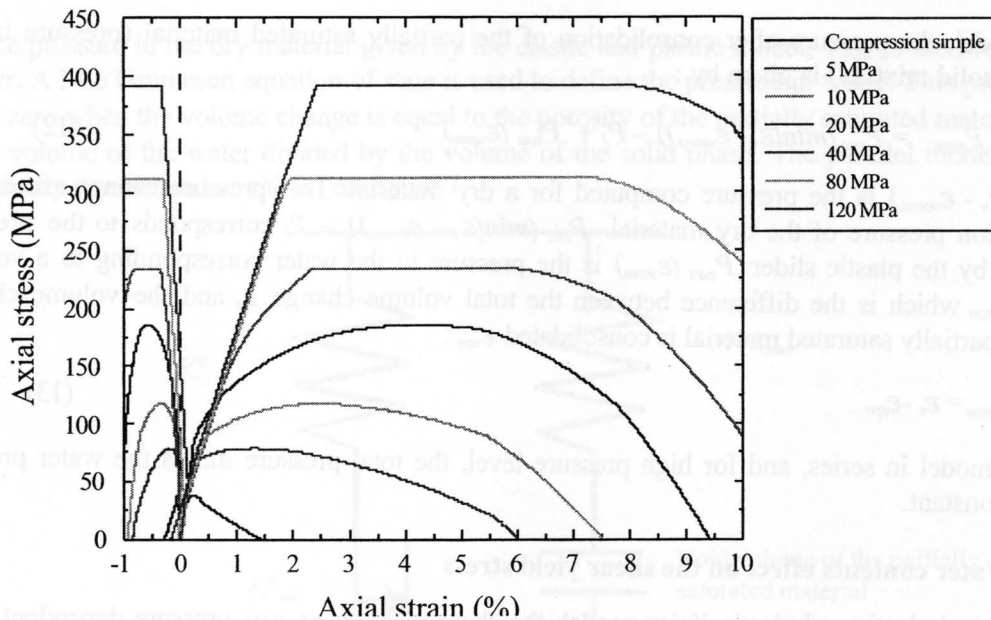


Figure 9 : Stress strain response given by the coupled damage and plastic model (triaxial tests with increasing lateral pressure).

Figure 9 gives the evolution of the material response with confining prescribed pressure for a regular concrete. The results shows that the concrete response is completely governed by the damage model at very low confining pressure. At higher lateral pressure, plastic strains appears and create a plateau in the stress response. For a confining pressure of 120 MPa and more, the material behavior is mainly driven by the modified plastic model.

5. NUMERICAL SIMULATIONS WITH THE COUPLED DAMAGE AND PLASTIC MODEL

This model has been implemented in the ABAQUS explicit finite element code and it has been extensively used to simulate a lot of complex problems. It can be used with most of the available finite elements (1D truss elements, beam elements, 2D plane strain elements, 2D axi symmetric elements, 3D solid elements, etc.). In order to show the capabilities of the coupled model some problems are presented here and numerical results are compared to experimental data.

5.1 Static four point bending test on a reinforced concrete beam

Figure 10 shows the experimental device and the beam characteristics. These tests have been conducted by Agardh, Magnusson and Hanson in sweden on a high strength reinforced concrete beam. The reference [8] gives all the details of the test device and all the details of the experimental results. Quasi static loading is applied in these tests.

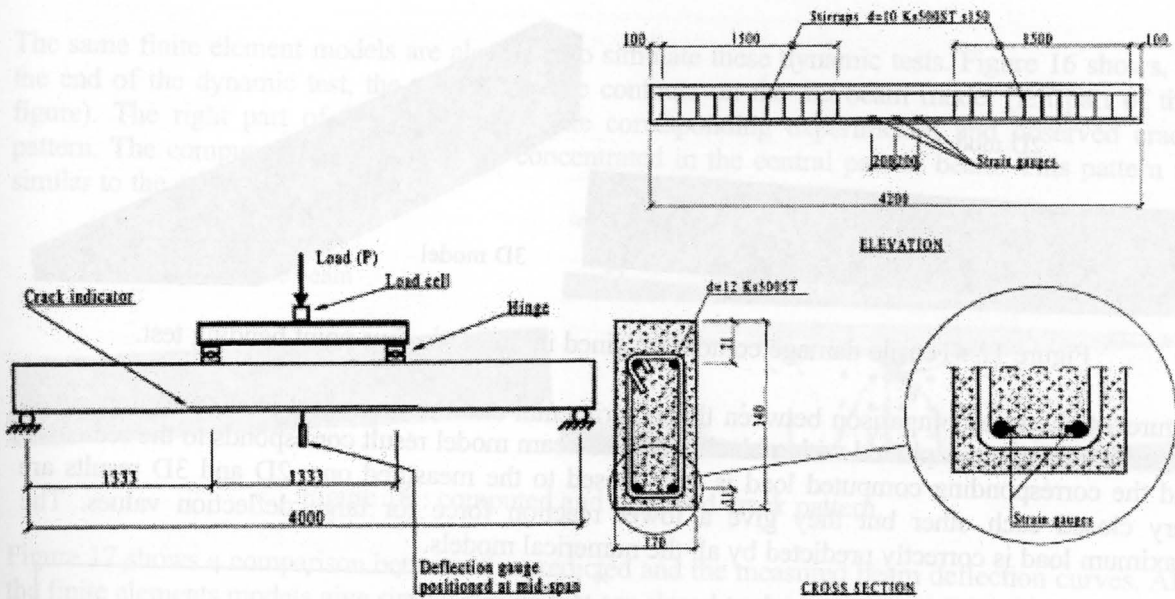


Figure 10 : Experimental device used for the four bending tests.

Figure 11 shows the 2D and 3D meshes used to model the beam. The reinforcement is shown with red lines. A single element is used in the depth of the beam with the 3D model, so the total number of finite elements is the same in the 2D and in the 3D model. Taking advantage of symmetry, only a half part of the beam is modeled.

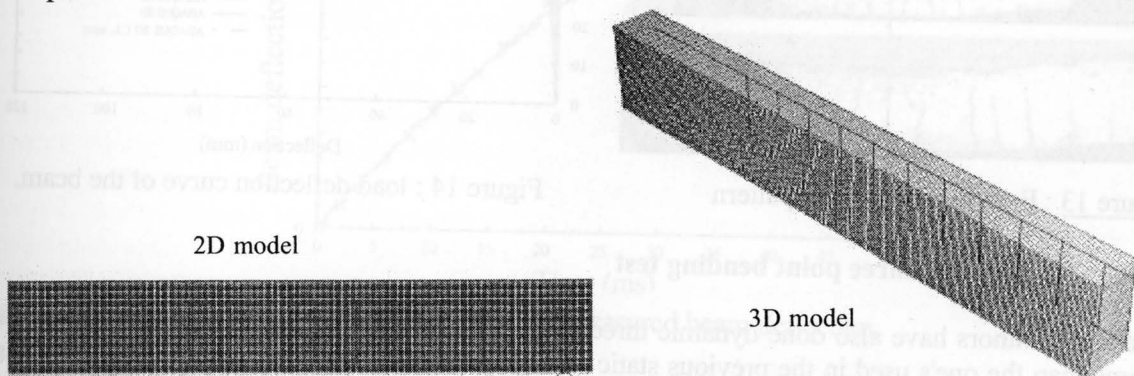


Figure 11 : 2D and 3D beam models (four point bending test).

Reinforcement is modeled with beam elements with a circular cross section. The reinforcement material model is the Johnson Cook plasticity model. All the material parameters are given in reference [3]. The concrete and the steel reinforcement are supposed to be perfectly bonded. Figure 12 gives the tensile damage contours when the beam deflection reach 80 mm. These contours show strain and damage localization along the lower and the upper reinforcement bars. Vertical crack pattern can easily be observed from the numerical results and it give a good idea of what we experimentally observe on figure 13.

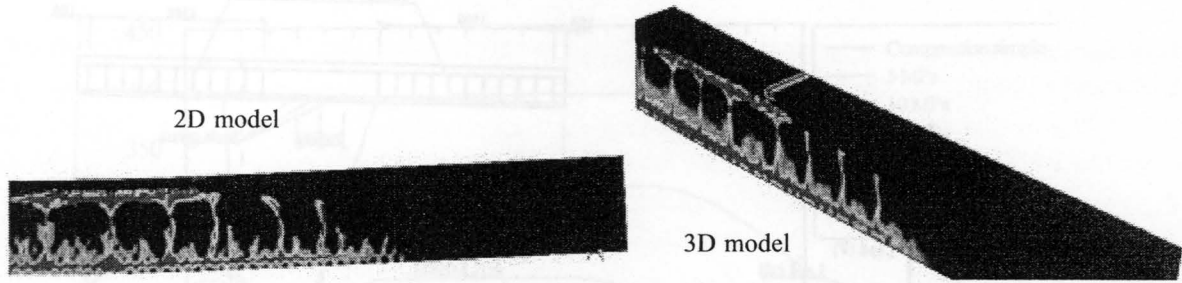


Figure 12 : Tensile damage contour obtained in the static four point bending test.

Figure 14 shows a comparison between the experimental and the numerical load deflection curve. Experimental curve is plotted with a black line. The beam model result corresponds to the red curve and the corresponding computed load is very closed to the measured one. 2D and 3D results are very closed each other but they give a lower reaction force for large deflection values. The maximum load is correctly predicted by all the numerical models.

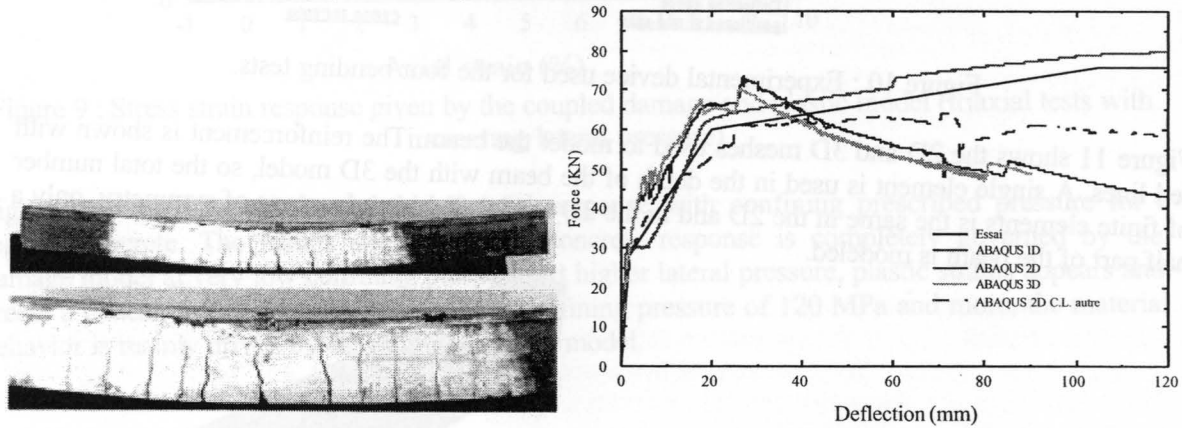


Figure 13 : Experimental crack pattern

Figure 14 : load deflection curve of the beam.

5.2 dynamic three point bending test

The same authors have also done dynamic three point bending tests on similar reinforced concrete beams than the one's used in the previous static tests. Figure 15 details the experimental apparatus. When the deflection becomes greater than 90 mm, shock absorbers damp the central part of the beam (see left part of figure 15).

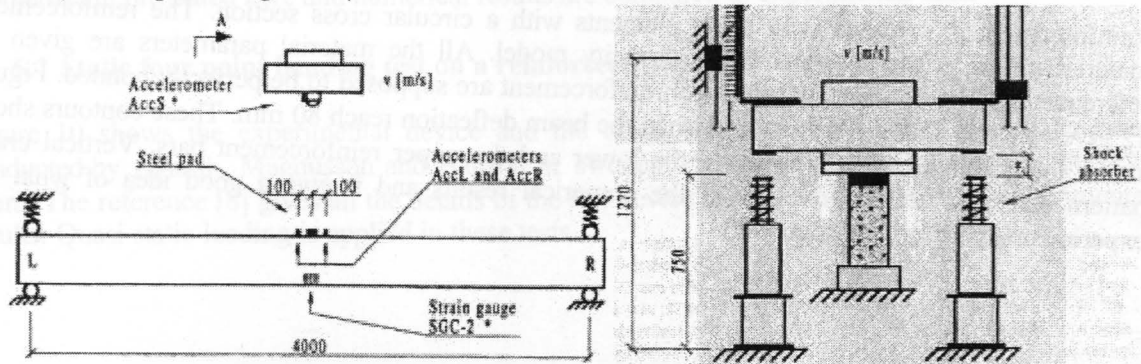


Figure 15 : Experimental apparatus (dynamic three point bending test).

The same finite element models are also used to simulate these dynamic tests. Figure 16 shows, at the end of the dynamic test, the tensile damage contours on the 3D beam model (left part of the figure). The right part of figure 16 shows the corresponding experimental and observed crack pattern. The computed cracks are mainly concentrated in the central part of beam. This pattern is similar to the experimental one.

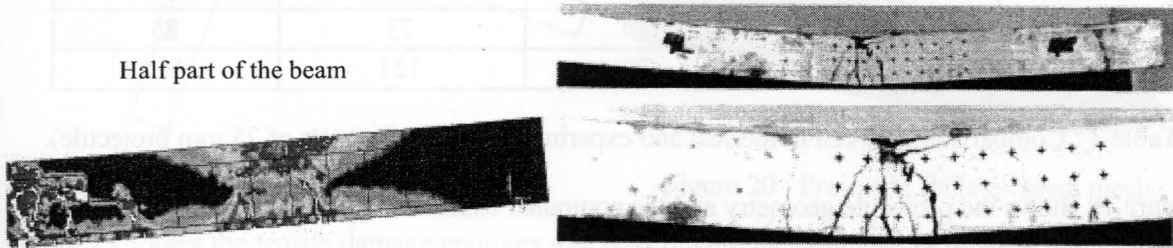


Figure 16 : computed and observed crack pattern.

Figure 17 shows a comparison between the predicted and the measured beam deflection curves. All the finite elements models give similar results that are closed to the experimental one.

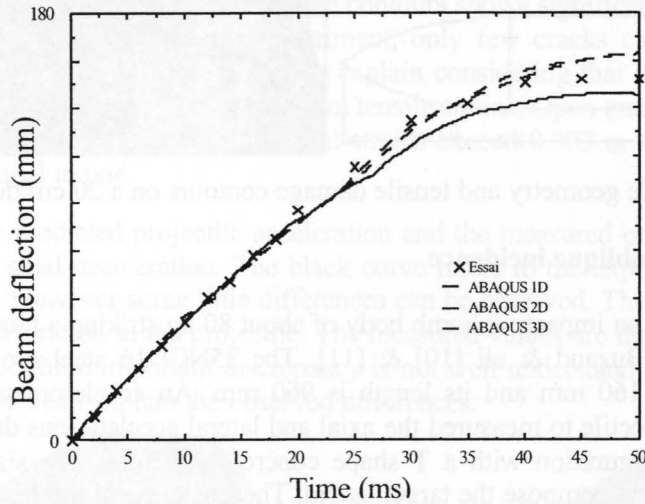


Figure 17 : Computed and measured beam deflection.

5.3 impact of a 25 mm diameter projectile on a micro concrete plate

Some years ago, experimental tests has been conducted at Centre d'Etudes de Gramat by E. Buzaud on a micro concrete material called MB 50 [9]. A steel projectile, with a diameter of 25 mm and a mass of 500 grams, impacts a concrete plate with initial velocities between 200 m/s and 600 m/s. The plate thickness is 10 cm or 20 cm and the size of the square plate is 800 mm. The angle of incidence and the angle of attack are very closed to zero. 2D axisymmetric simulations are performed with the ABAQUS explicit finite element code and with the coupled plastic and damage model. Table 1 gives a comparison between experimental and numerical results in terms of exit velocities or in terms of penetration depths. A good agreement is observed for all test conditions.

Test reference	Impact velocity (m/s)	Target thickness (cm)	Exit velocity or penetration depth (m/s ou cm)	
			Experimental	Numerical
DA539	333	10	210	222
DA540	600	10	500	530
DA541	214	10	73	35
DA543	292	20	123	140

Table 1.: Comparison between numerical and experimental result (impacts of 25 mm projectile).

Figure 18 shows the projectile geometry and the computed tensile damage contours for the test done on the 20 cm thick concrete plate.

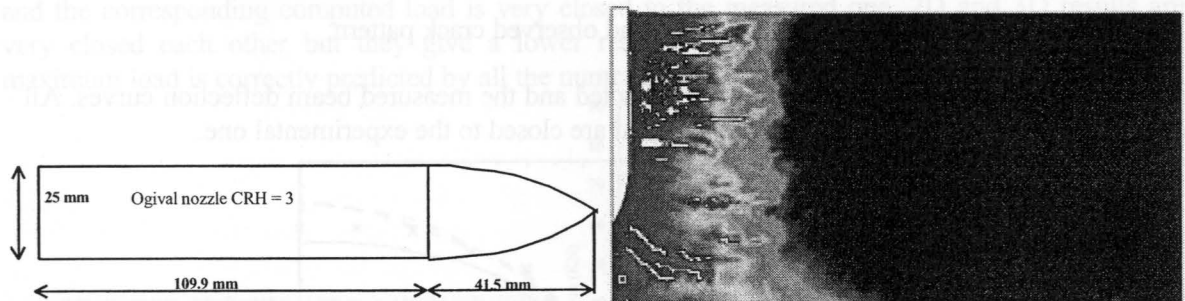


Figure 18 : Projectile geometry and tensile damage contours on a 20 cm thick concrete plate.

5.4 impacts under oblique incidence

Experimental tests with an impacting bomb body of about 80 kg striking a reinforced concrete plate have been done by E. Buzaud & all [10] & [11]. The 35NCD16 steel projectile has an ogival nozzle. Its diameter is 160 mm and its length is 960 mm. An accelerometer recorder system is mounted inside the projectile to measure the axial and lateral accelerations during the tests. Figure 19 shows the test configuration with a T shape concrete structure. The size of each reinforced concrete square plate, that compose the target, is 3m. The thickness of the front part of the concrete target is 400 mm and the thickness of the rear part is 300 mm. The reinforcement is composed of two steel layers (one on each side of the concrete plate) with 16 mm diameter bars. Other 10 mm diameter bars link each reinforcement mesh nodes of the face to face layers. The distance that separates each bar is 100 mm. The distance between the reinforcement layer and the top (or the bottom) plate surface is 50 mm.

Three dimensional numerical simulations have been done using the ABAQUS explicit finite element code. Figure 20 shows the mesh used for the projectile. The total number of the finite elements is about 530 000 for the entire model. The projectile material is simulated using an elastic and perfectly plastic model with a plastic yield stress of 1 300 MPa. The reinforcement is also modeled with an elastic and plastic model with isotropic hardening. The initial yield stress is 600 MPa and reach 633 MPa for a failure strain of 0.13. The concrete behavior is simulated with the coupled plastic and damage model. Material data are given in reference [3]. They correspond to a standard concrete.

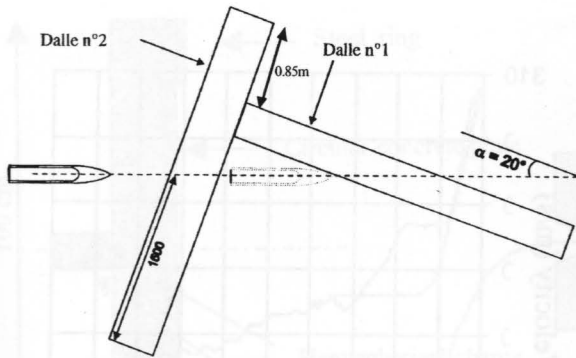


Figure 19 : T shape concrete structure.

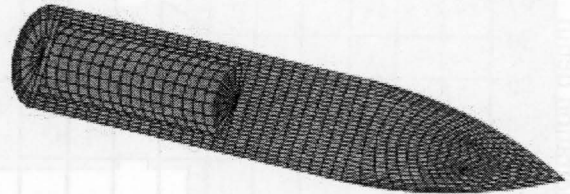


Figure 20 : Projectile finite element mesh.

Figure 21 shows the tensile damage contours and respectively the compressive damage contours at the end of the numerical simulation ($T = 20$ ms). The first part of the target is perforated then a ricochet is observed on the rear part. This has been observed experimentally. The projectile velocity, at the exit of the first impacted plate, is very closed to the measured one, as shown on figure 22. In this figure experimental data are plotted with a black curve. The steel projectile don't have any significant permanent strain. The damage contours shows significant damage observed on a large part of the concrete target. In the experiment, only few cracks can be seen around the impacted areas. This apparent discrepancy can be explain considering that damage parameters can reach important values even for moderate maximum tensile strains. Open cracks on the concrete can experimentally observed if the maximum principal strains exceed 0.003 or 0.004. At these values, the damage is nearly equal to one.

Figure 23 compare the predicted projectile acceleration and the measured one. The left part shows the comparison of the axial deceleration. The black curve refers to the experimental data. A good agreement is observed. However some little differences can be observed. The right part of figure 23 compare the lateral acceleration in the projectile. The measured values are three or four time greater than the computed one. These important discrepancy is not well understand. Probably vibration on the accelerometer support can explain the observed differences.

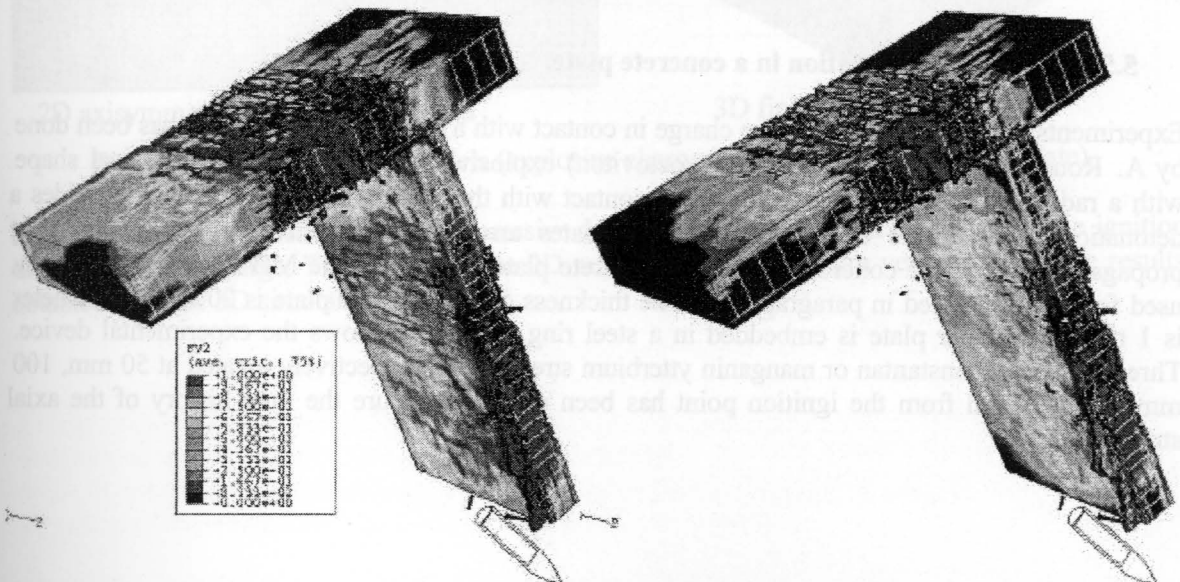


Figure 21 : Tensile and compressive damage contours on the T shape reinforced concrete target.

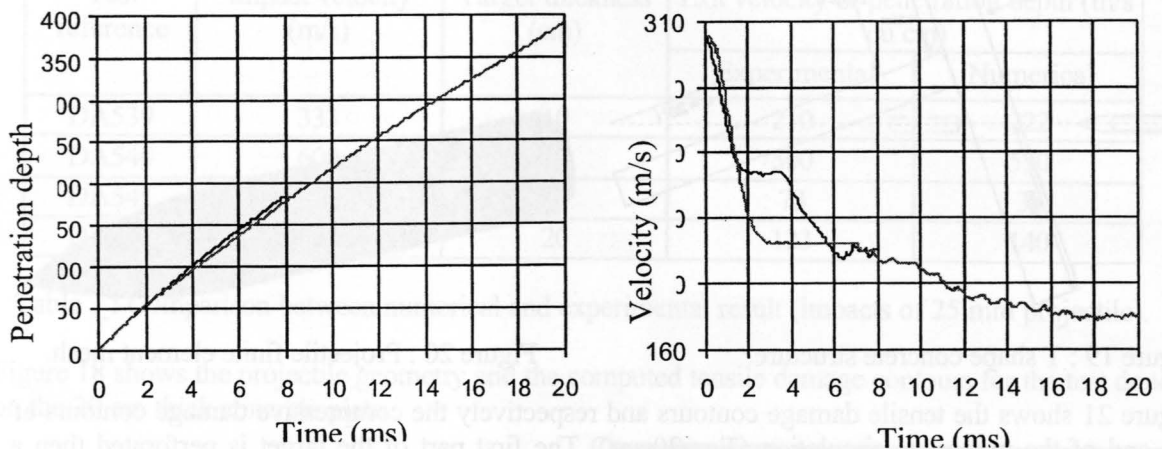


Figure 22 : Comparison between experimental and numerical results (depth and velocity).

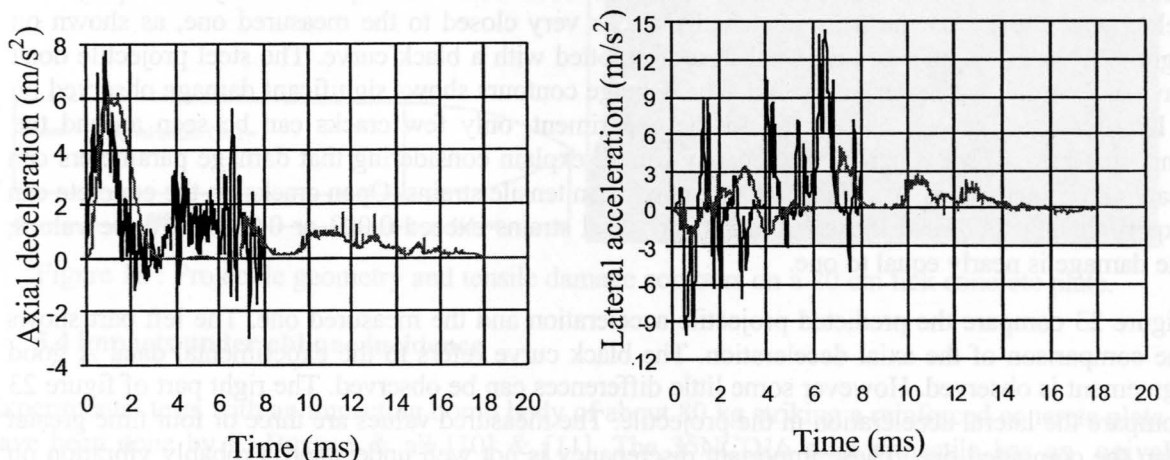


Figure 23 : Comparison between experimental and numerical results (axial & lateral accelerations).

5.5 shock wave propagation in a concrete plate.

Experiments with a bonded explosive charge in contact with a circular concrete plate has been done by A. Rouquand & all [12]. The V401 (octoviton) explosive charge has a hemispherical shape with a radius of 22.5 mm. The charge is in contact with the plate. The ignition device provides a detonation point at the charge center, and creates an expanding spherical shock wave that propagates through the concrete plate. The concrete plate is made of the MB 50 concrete already used for tests presented in paragraph 5.3. The thickness of the concrete plate is 20 cm. Its diameter is 1 m. The circular plate is embedded in a steel ring. Figure 24 shows the experimental device. Three manganin constantan or manganin ytterbium stress gages, respectively located at 50 mm, 100 mm and 150 mm from the ignition point has been used to measure the time history of the axial stress.

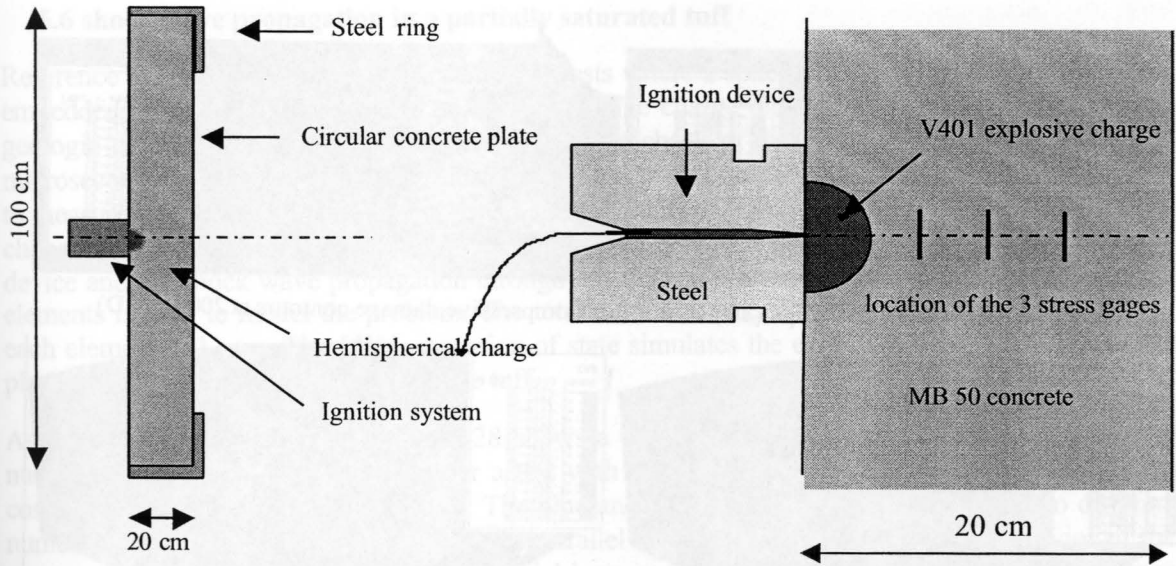


Figure 24 : Experimental device (explosive charge in contact with a concrete plate).

The behavior of the explosive charge is modeled with the J. W. L. equation of state. The concrete behavior is simulated with the coupled plastic and damage model. Both 2D and 3D meshes (see figure 25) are used to simulate the shock wave propagation through the concrete structure. A total of 516 000 finite elements compose the 3D model.

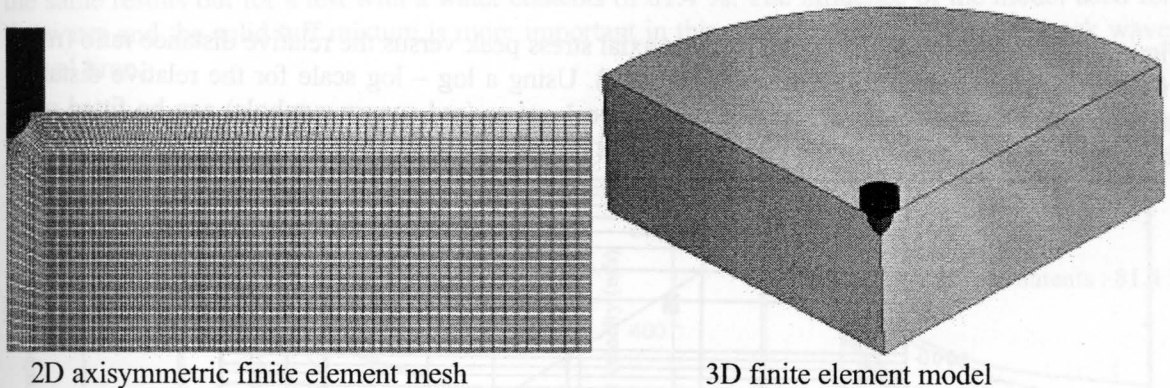


Figure 25 : Finite element models (explosive charge in contact with a concrete plate).

Figure 26 shows the tensile and the compressive damage contours obtained 200 μ s after the ignition of the explosive charge. The results of the 2D numerical simulation are very closed to the results obtained with the 3D simulation.

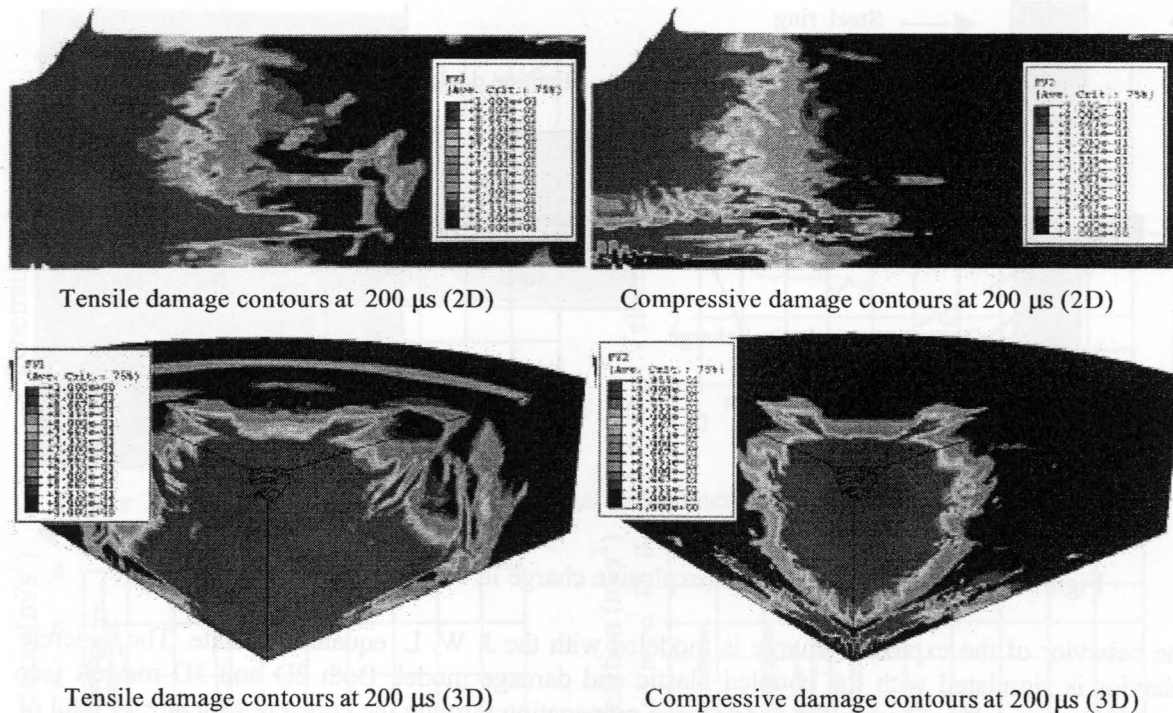


Figure 26 : Tensile and compressive damage contours (2D et 3D numerical simulations).

Figure 27 gives the evolution of the incident axial stress peak versus the relative distance ratio (ratio of the true distance divided by the charge radius). Using a log – log scale for the relative distance ratio axis and for the stress axis, the computed peak stress (red square symbols) can be fitted near the straight line defined from the measured values (black square symbols).

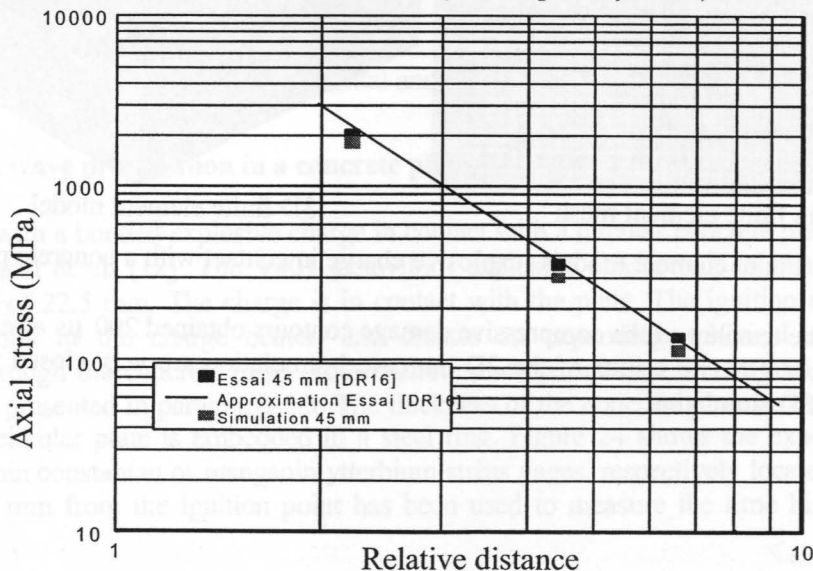


Figure 27 : Maximum axial stress versus the relative distance.

5.6 shock wave propagation in a partially saturated tuff

Reference [13] details a series of experimental tests where a spherical Lx – 0401 explosive charge, embedded in a geologic tuff specimen, detonates. The charge diameter is 2.5 cm. The size of the geologic material is enough large to prevent the comeback of the reflecting wave during the first microseconds. For each test, 3 electromagnetic velocity gages are incorporated into the tuff sample to measure the material velocity. Four tests have been done. Between each test, the water contents is changed. The ABAQUS explicit finite element code simulates the detonation of the pyrotechnic device and the shock wave propagation through the tuff material. A single row of 2D axisymmetric elements is used to model the problem. The total number of the finite elements is 550. The size of each element is 1 mm. The J.W.L. equation of state simulates the explosive behavior. The coupled plastic and damage model is used for the tuff.

As an example, the left part of figure 28 shows a comparison between the experimental and the numerical velocities. Here, we consider a test with a water contents of 51.8 %. The black curve corresponds to the experimental values. The blue and the green curves correspond to two different numerical simulations. For the blue line, the parallel model is used to simulate the behavior of the water and solid tuff mixture when the material becomes fully consolidated. While the green curve corresponds to the model in series. Three sets of curves are given. Each refers to a particular point (velocity transducer point). The amplitude of the peak velocity and the arrival time of the shock wave is correctly predicted in both cases. The parallel model gives a stiffer material response so the arrival time is a little bit overestimated. On the other hand, the model in series gives a lower stiffness and greater arrival times compare to the measured values. The right part of figure 28 shows the same results but for a test with a water contents of 81.4 %. The influence of the model used for the water and the solid tuff mixture is more important in this case, in particular for the shock wave arrival time.

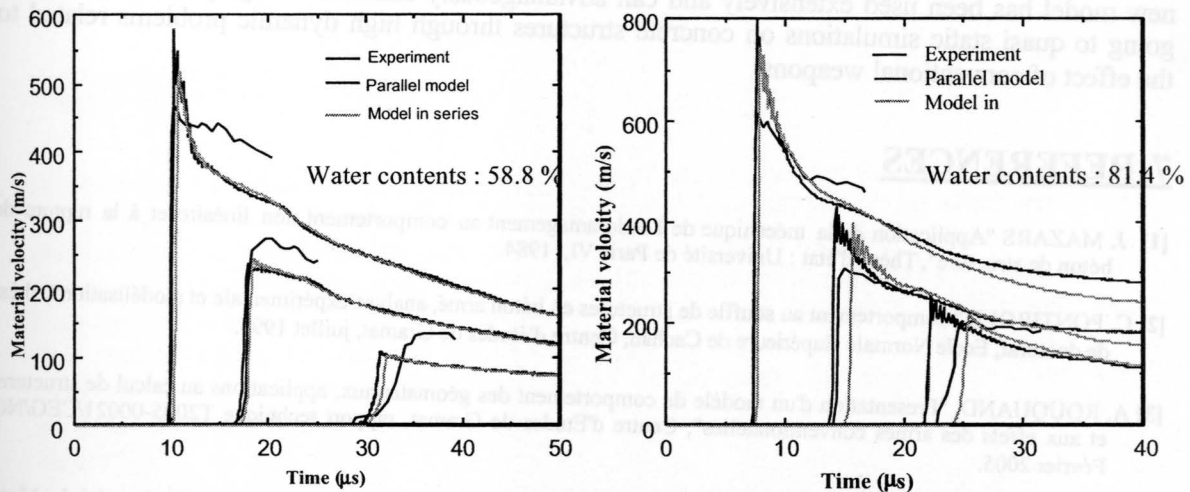


Figure 28 : Material velocity profiles (water contents of 58.8% and 81.4%).

Finally figure 29 shows a comparison between two numerical simulations. Both of these simulations use the parallel model. In the first, the water contents is taken equal to 58.8 %. This value is taken equal to 81.4% in the second simulation. These results shows clearly the great influence of the water contents on the shock wave characteristics.

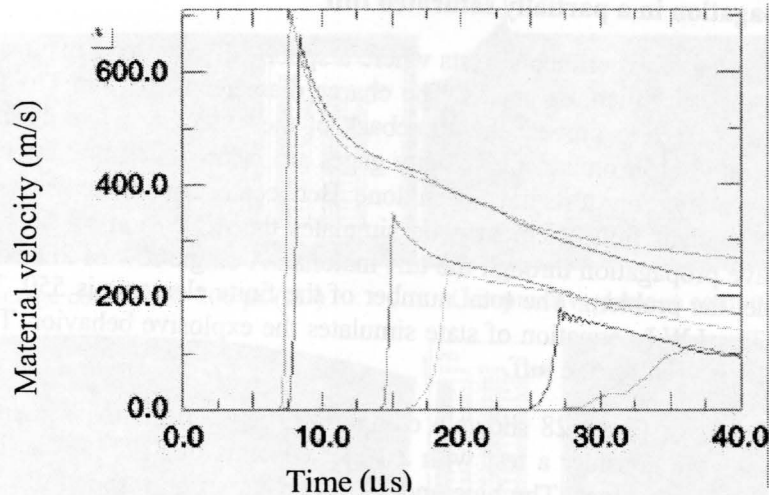


Figure 29 : Water contents effects on the propagating shock wave.

6. CONCLUSION

A general material model has been developed in the framework of the damage theory coupled with a plastic model that includes the effective stress concept. The proposed model can simulate a lot of physical mechanisms : the crack opening and the crack closure effect, strain rate effects, material damping induced by internal friction, compaction of porous media, shear plastic strains under high pressure, water contents effects on the pressure volume behavior and on the shear yield stress. The new model has been used extensively and can advantageously simulate a large panel of problems going to quasi static simulations on concrete structures through high dynamic problems related to the effect of conventional weapons.

7. REFERENCES

- [1] J. MAZARS "Application de la mécanique de l'endommagement au comportement non linéaire et à la rupture du béton de structure", Thèse d'état : Université de Paris VI, 1984.
- [2] C. PONTIROLI, "Comportement au souffle de structures en béton armé, analyse expérimentale et modélisation", thèse de doctorat, Ecole Normale Supérieure de Cachan, Centre d'études de Gramat, juillet 1995.
- [3] A. ROUQUAND, "Presentation d'un modèle de comportement des géomatériaux, applications au calcul de structures et aux effets des armes conventionnelles", Centre d'Etudes de Gramat, rapport technique T2005-00021/CEG/NC, Février 2005.
- [4] A. BRARA, "Etude expérimentale de la traction dynamique du béton par écaillage", thèse de l'université de Metz, Laboratoire de Physique et Mécanique des Matériaux, octobre 1999.
- [5] A. HILLERBORG, M. MODEER, P. E. PETERSSON, "Analysis of crack formation and growth in concrete beams of fracture mechanics and finite elements", Cement and Concrete Research, Vol. 6, pp 773-782, 1976.
- [6] R. D. KRIEG, "A simple constitutive description for soils and crushable foams", Sandia National Laboratories, SC-DR-72-0833, Albuquerque, New Mexico, 1978.

- Behaviour of metallic plates subjected to explosions.
- [7] C. MARIOTTI, J. P. PERLAT, J. M. GUERIN, A numerical approach for partially saturated geomaterials under shock", CEA/DAM Bruyères le Châtel, International Journal of Impact Engineering 28 (2003) 717 - 741, March 2002.
- [8] L. AGARDH, J. MAGNUSSON, H. HANSSON, "High strength concrete beams subjected to impact loading, an experimental study", FOA Defence Research Establishment, FOA-R-99-01187-311—SE, August 1999.
- [9] E. BUZAUD, S. CHAPELLE, "Essais de perforation de dalles en micro béton MB50", colloque GEO, 1-3 février 1999.
- [10] E. BUZAUD, "Rapports campagne expérimentale PCD et synthèse des calculs EVA3D", Dynalis, 1999.
- [11] E. BUZAUD, R. LAURENSOU, P. BELOUET, C. LISSAYOU, "An experimental investigation of corner effects resulting from vertical attack on hardened structures", 11 th International Symposium on Interaction of the Effects of Munitions with Structures", Mannheim, Germany - 05-09 May 2003.
- [12] A. ROUQUAND, "Shock propagation through a concrete plate subjected to a bonded explosive charge", 9 th International Symposium on Interaction of the Effects of Munitions with Structures, Berlin – Strausberg, Germany, 03 – 07 may 1999.
- [13] R. P. SWIFT, "Dynamic response of earth media to spherical stress waves", Final report, Physics International Company, May 1973.

INTRODUCTION

Metallic thin walled pressure vessels or pipes are of common use in the industrial field. They can contain fluids at various thermodynamic states (gas, liquid or liquefied gas). Some phenomena, e.g. explosion ignition, uncontrolled chemical reaction..., can drive a sudden pressure wave to travel across these vessels, to reflect on its walls and finally to result either in their bursting or in the splitting of the enclosure into big pieces. This event finally results, in the first case in two structures and fragments, while, in the second case, it can lead to the projections of entire parts of the vessel in its environment. The dynamics of the whole phenomenon, from its beginning to its final state, still remains very difficult to describe and explain.

For a better quantification of the potential effects of a capacity bursting on its environment, a preliminary characterisation of both the possible loading pressure and the structure response is required. Moreover, the load and the response seem to be generally coupled.

An underlying problem is to know whether two systems with similar initial conditions can produce the same response. If it was possible to show that the phenomenon is deterministic, it would be the proof that a real way of prediction is worth exploring.

Numerous experimental studies have already been done on the subject of circular metallic plates responses to dynamic loads. The first studies dealt with the permanent central deflection of circular plates. Florence (1966) compared his experimental results to those theoretically

Numerical analysis of the dynamic plastic instabilities in steel rings submitted to explosive radial expansion

A. Rusinek¹, R. Zaera²

¹ *Laboratory of Physics and Mechanics of Materials, UMR CNRS 75-54, University of Metz, Ile du Saulcy, 57045 Metz cedex, France*

² *Department of Continuum Mechanics and Structural Analysis, University Carlos III of Madrid, Avda. De la Universidad 30, 28911 Leganés, Madrid, Spain*

The expanding ring test permits to analyze the mechanical behavior of materials under high strain-rate loading, particularly strength and failure modes. This paper presents a numerical analysis of the expansion of a mild steel rings. A hardening relation which takes into account strain, strain rate and temperature is proposed to define precisely the thermoviscoplastic behaviour of the material. The constitutive equations were implemented in the commercial finite element code ABAQUS/Explicit. The effect of loading velocity and of the hardening behaviour of the material on the number of fragments and failure mode were analyzed. Moreover, the numerical predictions agree with the experimental results provided by other authors.

INTRODUCTION

The behaviour of materials at high strain rates could be determined by conventional dynamic tests such as tension, compression or shear, although only the last one allows to reach large deformations, close to $\gamma \approx 1$. Among other non-conventional tests, the impulsive expansion of a thin ring allows to reach also large plastic strains. In this test, the inertia effect provides a force resisting the localization of strain as a necking plastic flow instability tries to form. Moreover, the solid exhibits a dynamic uniaxial stress state along the circumference without the wave propagation problems arising in tensile tests. Thus, the failure strains reached with the ring expansion test seem to be higher than those observed in dynamic tensile tests and ductility increases monotonically with expansion velocity (Figure 1).

The experiment consists of loading a ring of radius R expanding at a roughly constant velocity V_0 which commonly varies from 50 to 300 m/s, leading to strain rates $\dot{\epsilon}_0 = V_0/R$ within the range $10^3 \leq \dot{\epsilon}_0 \leq 10^4 \text{ s}^{-1}$. Currently, the materials used in the experimental tests are aluminium [2,3,4] or copper [2]. The dynamic loading is commonly procured by the use of explosives (Figure 2), although electro-magnetic field has also been used [2,5]. The test is specifically used to determine the number of fragments and the failure mode which appear at very high expansion rates. After testing the ring, the fragments are recovered, counted and examined to establish the effect of applied velocity V_0 on the number of fragments.

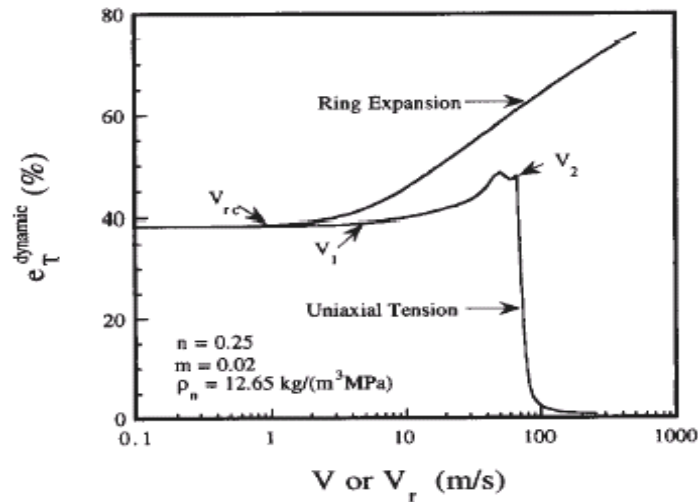


Figure 1: Evolution of the failure strain in dynamic loading, comparison between dynamic tensile test and ring expansion [1]. Steel with Hollomon-type hardening law and power-law strain rate sensitivity $\bar{\sigma} = K\bar{\varepsilon}^n \dot{\bar{\varepsilon}}^m$, $K=570$ MPa, $\rho_n = K/\rho$, $\rho=7800$ kg/m³.

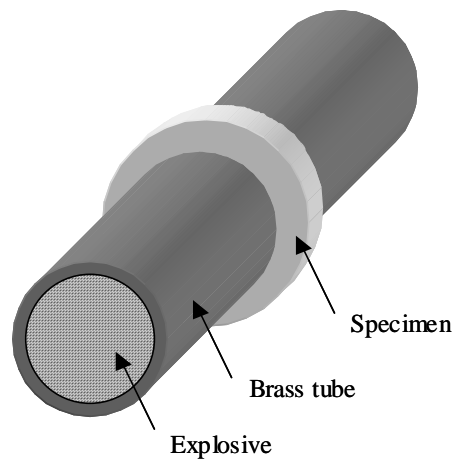


Figure 2: Experimental configuration for explosively loaded rings.

The fragmentation phenomena occurring during the test is the consequence of the interaction between elasto-plastic wave propagation and failure modes, such as shear banding, void growth, fracture nucleation and necking, which strongly depend on the constitutive equation of the material. In order to determine the influence of the mechanical behaviour of the material into the number of fragments and fragmentation type, 3D Finite Element numerical simulations of ring expansion test were made by varying the parameters of the thermoviscoplastic constitutive equation proposed by Rusinek and Klepaczko [6]. This equation was implemented into the commercial FE code ABAQUS/Explicit [7] through the fully-implicit integration algorithm described in [8]. These results were compared with experimental data, as well as those of an analytical model proposed in [9], which uses a linear perturbation technique to capture the dynamic necking, and of a numerical approach which considers elements with a cohesive law to predict the failure of the ring [3].

THERMOVISCOPLASTIC CONSTITUTIVE EQUATION

To simulate the process of ring expansion, a reference material with well-known mechanical behaviour was used: a mild steel ES, commonly used in the automotive industry. The steel is annealed to reduce the rolling effect that causes residual stresses and anisotropy; elements such as aluminium and titanium are added in small proportion (< 0.1 wt%) to produce fine-grained material and formation of carbide to increase the failure stress level. A number of different tests -tensile, double shear, perforation- have been performed during the last decade over a broad range of strain rates and temperatures to characterise this material, with special attention to the precise reciprocity effects between the strain rate and temperature, the quantities defining the process of thermal activation [10,11]. Its chemical composition is given in the Table 1.

<i>Mn</i>	<i>Al</i>	<i>Cr</i>	<i>C</i>	<i>Ni</i>	<i>S</i>	<i>Cu</i>	<i>Si</i>	<i>P</i>	<i>N</i>	<i>Ti</i>
0.203	0.054	0.041	0.03	0.018	0.011	0.009	0.009	0.008	0.0063	0.002

Table 1 : Chemical composition of mild steel ES (% weight).

In order to describe more precisely of high strain rate behavior of materials is assumed that the yield σ_Y is the sum of two stress components σ_μ and σ^* which are respectively the internal and the effective stress. The first component is directly related to the strain hardening of the material and the second defines the contribution due to the thermal activation (combination of temperature and strain rate). The constitutive relation can be written in one-dimensional stress or as equivalent quantities:

$$\sigma_Y(\bar{\varepsilon}^p, \dot{\varepsilon}^p, T) = \frac{E(T)}{E_0} [\sigma_\mu(\bar{\varepsilon}^p, \dot{\varepsilon}^p, T) + \sigma^*(\dot{\varepsilon}^p, T)] \quad (1)$$

where E_0 is the Young's modulus at $T = 0$ K and $E(T)$ is the evolution of the modulus as a function of temperature. Eq. 1 is based to some extent on physical considerations, [6]. The explicit expressions for both stress components are given below:

$$\sigma_\mu(\bar{\varepsilon}^p, \dot{\varepsilon}^p, T) = B(\dot{\varepsilon}^p, T) (\varepsilon_0 + \bar{\varepsilon}^p)^{n(\dot{\varepsilon}^p, T)} \quad (2)$$

where $B(\dot{\varepsilon}^p, T)$ and $n(\dot{\varepsilon}^p, T)$ are respectively the modulus of plasticity and the strain hardening exponent. These quantities, defined respectively by Equations 3 and 5, take into account the experimental observations that the strain hardening itself depends on temperature and strain rate.

$$n(\dot{\varepsilon}^p, T) = \left\langle n_0 \left(1 - D_2 \left(\frac{T}{T_m} \right) \log \left(\frac{\dot{\varepsilon}^p}{\dot{\varepsilon}_{\min}^p} \right) \right) \right\rangle \quad (3)$$

where n_0 and D_2 are material constants, T_m is the melting point, and $\langle \bullet \rangle$ are the MacCauley brackets

$$\langle \bullet \rangle = \begin{cases} \bullet & \text{if } \bullet \geq 0 \\ 0 & \text{if } \bullet < 0 \end{cases} \quad (4)$$

such that negative values of the hardening exponent are not allowed. The plastic strain rate is limited by $\dot{\varepsilon}_{\min}^p \leq \dot{\varepsilon}^p \leq \dot{\varepsilon}_{\max}^p$, $\dot{\varepsilon}_{\min}^p$ being the minimum strain rate which defines the quasi-static stress-strain relation, and $\dot{\varepsilon}_{\max}^p$ the maximum limit of strain rate.

For the ES steel analyzed in this paper, the strain-hardening exponent n substantially changes with strain rate and temperature, particularly in the adiabatic conditions [6,12]. Moreover, the effective strain rate $\dot{\bar{\epsilon}}^p$, which corresponds to the complete transition into adiabatic conditions of deformation is estimated as $\dot{\bar{\epsilon}}^p \approx 10 \text{ s}^{-1}$. For strain rates higher or equal to 10^2 s^{-1} , a significant temperature increase ΔT is observed during plastic deformation and at the same time an intensification of the thermal softening of the material occurs. The process of plastic deformation is then coupled with temperature as it will be shown later. The formula for $B(\dot{\bar{\epsilon}}^p, T)$ is a function of the homologous temperature modified by strain rate [6]

$$B(\dot{\bar{\epsilon}}^p, T) = \left\langle B_0 \left(\left(\frac{T}{T_m} \right) \log \left(\frac{\dot{\epsilon}_{\max}}{\dot{\bar{\epsilon}}^p} \right) \right)^v \right\rangle \quad (5)$$

where B_0 is the material constant and v is the temperature sensitivity (usually negative).

Explicit form of the effective stress σ^* , given by Eq. 6, is similar to the Arrhenius relation which describes the kinetics of thermally activated processes.

$$\sigma^*(\dot{\bar{\epsilon}}^p, T) = \left\langle \sigma_0^* \left(1 - D_1 \left(\frac{T}{T_m} \right) \log \frac{\dot{\epsilon}_{\max}}{\dot{\bar{\epsilon}}^p} \right)^{1/m} \right\rangle \quad (6)$$

where σ_0^* is the effective stress at $T = 0 \text{ K}$, D_1 is the material constant and $m^* = 1/m$ is the coefficient characterizing the temperature and strain rate sensitivity. In adiabatic conditions the quantities that are functions of temperature are coupled via Eq. 7, which gives the increment of temperature $\Delta T_{\text{adiabatic}}$ due to the plastic work converted into heat [14].

The adiabatic increase of temperature triggers the thermal softening phenomenon and reduces the rate of strain hardening.

$$T_{\text{adiabatic}} = T_0 + \frac{\beta}{\rho c} \int_{\epsilon_c}^{\bar{\epsilon}^p} \sigma(\xi, \dot{\bar{\epsilon}}^p, T) d\xi \quad (7)$$

where β is the Taylor-Quinney coefficient of plastic work converted into heat, ρ is the density of material and c is the specific heat.

It is interesting to highlight its capability to fit experimental data over a broad range of strain rates. Figure 3 shows how the strain rate sensitivity is well defined in a range of strain rates from 10^{-4} to 10^3 s^{-1} and covering both isothermal and adiabatic conditions. The hardening equation also shows a high strain rate sensitivity at strain rates above $\dot{\bar{\epsilon}}^p > 10^4 \text{ s}^{-1}$, which is in agreement with the current experimental observations for mild steels. Thus, the constitutive relation allows a study of a number of dynamic load processes such as perforation, shear, tension or crash box test. The model is suitable for metals with BCC structure, which show an additive dependence on the flow stress. It also accounts for the large strain rate sensitivity observed in BCC metals at very high strain rates, much higher than that of FCC metals exhibiting a lower movement of screw dislocations.

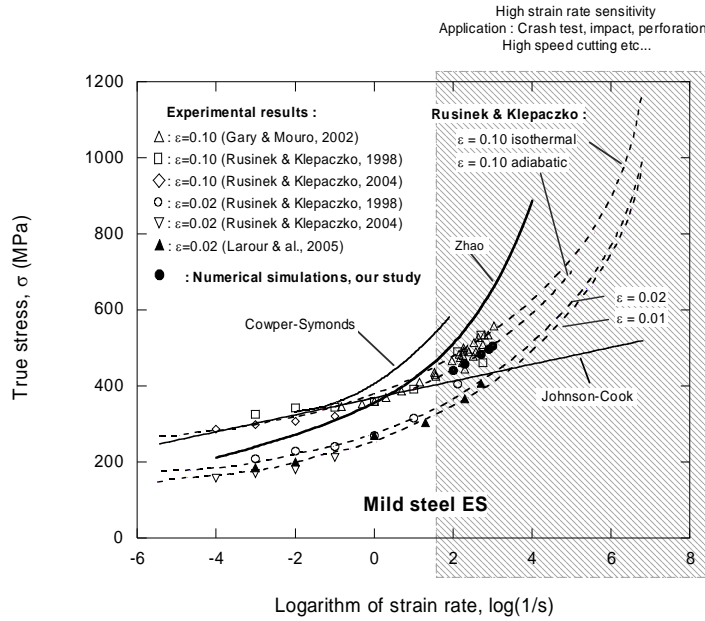


Figure 3: Analytical prediction of the model for mild steel ES, comparison with several constitutive relations and experimental results.

IMPLICIT INTEGRATION ALGORITHM

In order to complete the constitutive description of the material, the following equation should be added to the model. In this approach, we consider the additive decomposition of the rate of deformation tensor $\underline{\underline{d}}$, generally assumed for hypoelastic-plastic materials

$$\underline{\underline{d}} = \underline{\underline{d}}^e + \underline{\underline{d}}^p + \underline{\underline{d}}^\theta \tag{8}$$

$\underline{\underline{d}}^e$, $\underline{\underline{d}}^p$ and $\underline{\underline{d}}^\theta$ being tensors associated with elastic deformation, plastic deformation and thermal deformations. Considering isotropic hypoelastic behaviour, the objective stress rate could be related to the elastic rate of deformation tensor

$$\underline{\underline{\dot{\sigma}}}^e = \underline{\underline{C}} : \underline{\underline{d}}^e \tag{9}$$

where $\underline{\underline{C}}$ is the isotropic elastic stiffness fourth order tensor. A J_2 yield criteria would define the yield function as follows

$$f = \bar{\sigma} - \sigma_y \tag{10}$$

$\bar{\sigma}$ being the equivalent stress. The following equation relates the plastic flow direction to the deviatoric stress tensor $\underline{\underline{s}}$

$$\underline{\underline{d}}^p = \lambda \frac{\partial f}{\partial \underline{\underline{s}}} = \lambda \frac{3}{2} \frac{\underline{\underline{s}}}{\bar{\sigma}} \tag{11}$$

where λ is the plastic multiplier and $\underline{\underline{s}}$ the deviatoric stress. The last term in Eq. 8 is given by an isotropic law of thermal deformations:

$$\underline{\underline{d}}^\theta = \alpha \dot{T} \underline{\underline{I}} \tag{12}$$

where α is the coefficient of thermal expansion.

To integrate the rate equations, incremental objectivity is achieved by rewriting them in a neutralized or corrotational configuration. Moreover, the rate equations defined above are form-identical in the neutralized configuration and a small deformation formulation could be used to integrate the thermoviscoplastic constitutive model. To solve this system of incremental equations, we used the algorithm proposed in [17]. The stress update is in two steps an elastic predictor driven by an elastic increment in total strain leading to a trial stress state

$$\sigma_{n+1}^{\text{trial}} = \sigma_n + C : \Delta \varepsilon_{n+1} \quad (13)$$

and a plastic corrector which projects iteratively the trial stress onto the revised yield surface in the direction specified by the plastic flow. The principal feature of the algorithm is the possibility of expressing all the arguments of the yield condition in terms of the plastic multiplier increment $\Delta \lambda$

$$f \left(\bar{\sigma}_{n+1}^{\text{trial}} - 3G\Delta\lambda, \lambda_n + \Delta\lambda, \frac{\Delta\lambda}{\Delta t}, T_n + \frac{\beta}{\rho_{n+1} C_p} (\Delta\lambda \bar{\sigma}_{n+1}^{\text{trial}} - 3G\Delta\lambda^2) \right) = 0 \quad (14)$$

To solve this equation, a Newton-Raphson iterative procedure is used. The linearization of the consistency condition leads to the following expression

$$\delta \lambda_k = \frac{f_k}{3G - \left. \frac{\partial f}{\partial \bar{\varepsilon}^p} \right|_k - \frac{1}{\Delta t} \left. \frac{\partial f}{\partial \dot{\varepsilon}^p} \right|_k - \left. \frac{\partial f}{\partial T} \right|_k \frac{\beta}{\rho_{n+1} C_p} (\bar{\sigma}_{n+1}^{\text{trial}} - 6G\Delta\lambda_k)} \quad (15)$$

which is a generalization of the well known radial return algorithm to update the plastic multiplier, including viscosity and thermal effects.

DESCRIPTION OF THE FINITE ELEMENT MODEL

The numerical simulation of the ring expansion process was done with the Finite Element commercial code ABAQUS/Explicit. A mesh with 300 8-node trilinear reduced integration (C3D8R in ABAQUS notation) brick elements including hourglass control (see Figure 4) and 900 nodes was used. The inner radius of the ring is equal to $R_0 = 16$ mm, with 1 mm thickness and 1 mm width (1 mm² square cross section). The effect of radial expansion was simulated by imposing a constant radial velocity V_0 on the inner face of the ring, varying within the range 1 to 500 m/s. The ring was assumed to be initially at room temperature.

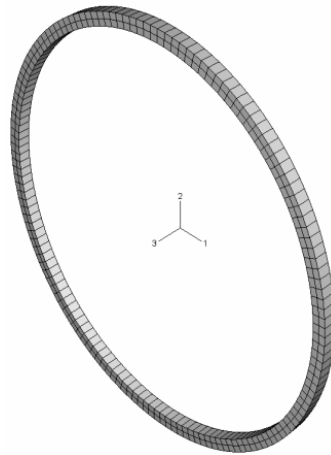


Figure 4: Picture of the reference mesh used for the numerical simulations of ring expansion.

In order to determine the influence of the type of element and the mesh refinement on the results of the numerical simulations, three additional models were completed with 6-node triangular prisms following the work of Pandolfi et al. [3] (Figure 5).

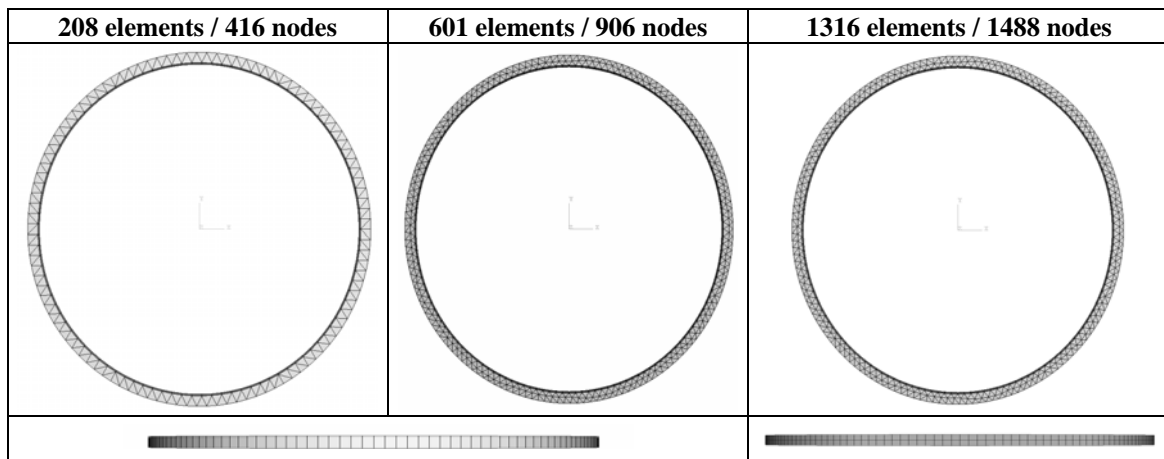


Figure 5: Picture of the meshes with triangular prisms used for the numerical simulations of ring expansion.

Also different inner radius of the ring were considered - 20, 32 and 50 mm - to analyze the influence of the geometry, keeping constant thickness and width.

PROPOSAL OF A FAILURE CRITERION

No geometrical or material imperfections were introduced in any of the models, so that necking starts as a result of the decay in the slope of the strain hardening curve, thus avoiding artificial triggering of the necking process. The Considère criterion

$$\frac{\partial \sigma}{\partial \varepsilon} = \sigma \quad (16)$$

applied to the constitutive equations 1 to 6, allows to estimate the strain level ε_{neck} corresponding to the loss of homogeneous plastic deformation at the ring. Figure 6-left shows these values for different values of n_0 (see Equation 3); low values of the strain hardening

exponent will lead to a early initiation of the necking process. Moreover, when increasing the radial velocity (and consequently the strain rate), both the adiabatic heating and the decrease of n (Equation 3) give rise to a premature loss of homogeneity at the ring.

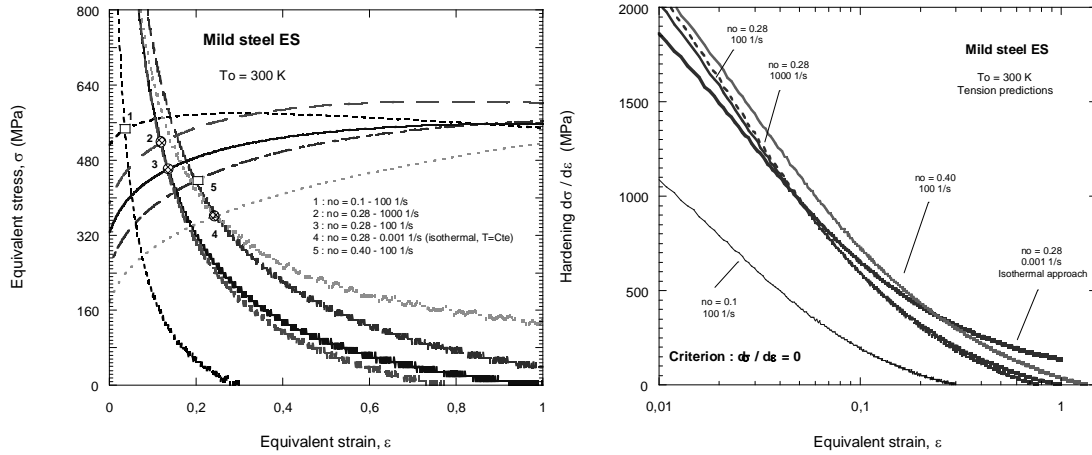


Figure 6: Evaluation of the strain corresponding to loss of homogeneous plastic deformation (left) and corresponding to failure (right) for different values of n_0 and at different strain rates

To arrive to the development of fragments after necking, a failure criterion based on a critical values of the equivalent plastic strain $\bar{\epsilon}^p = \epsilon_c$ was included in the model. Elements reaching this condition at their Gauss point are removed from the mesh. The failure condition

$$\frac{\partial \sigma}{\partial \epsilon} = 0 \tag{17}$$

applied to Equations 1 to 6 now allows to evaluate ϵ_c (Figure 6-right). This criterion doesn't perturb the solution and the process of growing necking caused by the lost of homogeneity, Fig. 7. Again, a lower value of n_0 or a higher value of the radial velocity should give rise to an earlier fragmentation of the ring. Thus, the following relation was proposed to determine ϵ_c as a function of n_0

$$\epsilon_c = \lambda n_0 \tag{18}$$

with $\lambda \approx 4$ (Table). A similar value (between 3 and 4) was used by Triantafyllidis et al. [5].

n_0	ϵ_c
0.10	0.40
0.28	1.20
0.35	1.40
0.40	1.60

Table 2: Failure strain for different values of n_0 .

A secondary effect of the strain exponent on the onset and evolution of the necking process comes through the modification of the plastic wave speed, which directly depends on the slope of the strain hardening curve

$$c_p = \sqrt{\frac{1}{\rho} \frac{\partial \sigma}{\partial \epsilon}} \tag{19}$$

Thus, low values of n_o favours the localization of plastic deformation leading to an increase of the number of fragments. For the same reason, a low value of the density ρ serves to stabilize the homogeneous deformation.

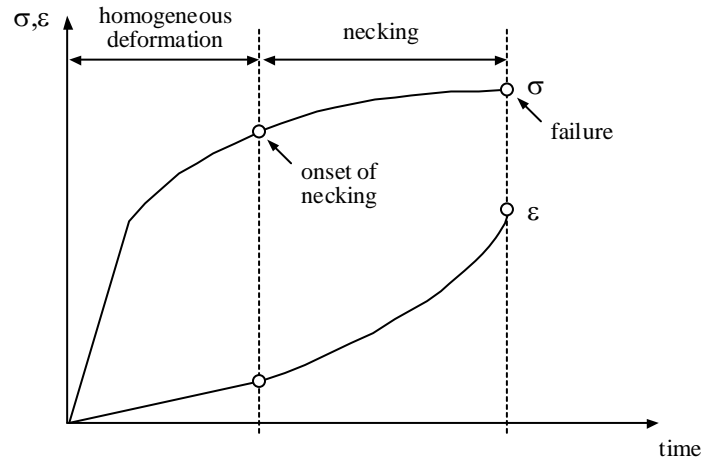


Figure 7: Process of deformation and fragmentation of the ring.

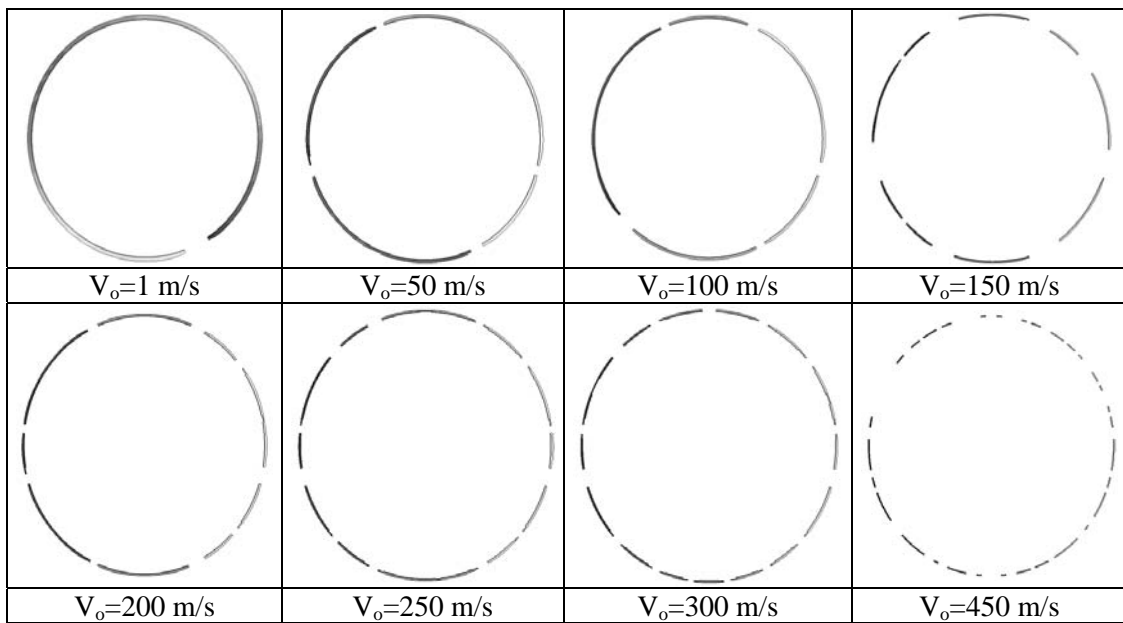


Figure 8: Evolution of the number of fragments with the radial velocity for the reference geometry and mesh (Figure 4). $n_o=0.28$.

RESULTS OF THE SIMULATION

Effect of the radial velocity

As stated above, a higher radial velocity induces higher strain rates on the material and an increase in the number of fragments N is expected. This was confirmed by the simulations: Figure 8 shows the results for $n_0=0.28$ and the reference ring geometry $R_0 = 16$ mm and mesh of Figure 4. Plotting N versus V_0 in Figure 9, three regions appear: a first one with a small increase at $1 \leq V_0 \leq 100$ m/s, a linear increase at $100 \leq V_0 \leq 300$ m/s and a quick increase at $300 \text{ m/s} \leq V_0$. The same trend was observed by Diep et al. [18] for a 34CrNiMo6. Since the adiabatic strain rate transition is similar in both metals (close to 100 s^{-1}), there is a good agreement in the evolution of the number of fragments with the velocity. The size of the ring was observed to have little effect, as could be seen also in Figure 14.

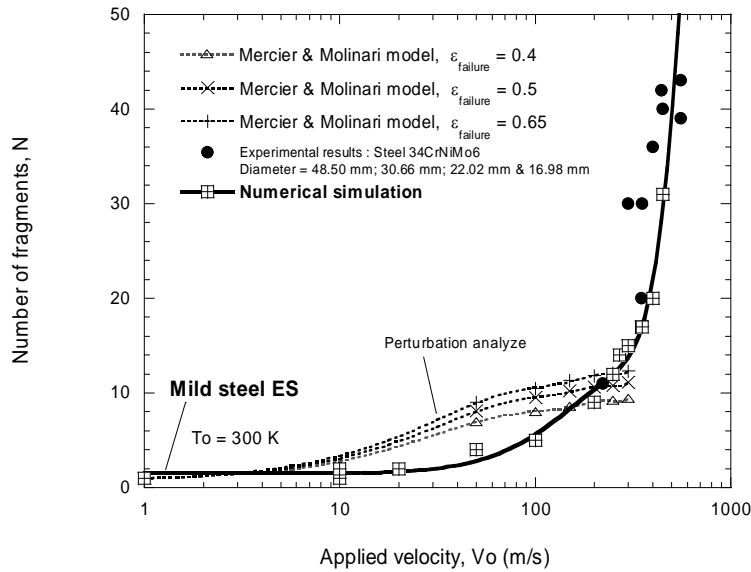


Figure 9: Numerical predictions of the number of fragments with applied velocity and different initial geometries. Comparison with experimental results [18].

Effect of the strain hardening exponent and density

Differences in the number of fragments were analyzed in relation to two material properties: hardening and density. As anticipated previously, low values of n_0 lead to a larger number of fragments (Figure 10). Also the prediction of the failure mode agree the experimental results observed for brittle [3] and ductile alloys [19]. When a small value of n_0 was used, brittle failure of the ring was observed, whereas large necking develops for large values of n_0 . Regarding the effect of density, it was artificially decreased (3900 and 5200 kg/m^3) or increased (11700 kg/m^3) to analyse its influence on the number of fragments through the variation of the plastic wave velocity. As shown in Figure 10, large values of the density lead to a higher number of fragments and brittle-like failure.

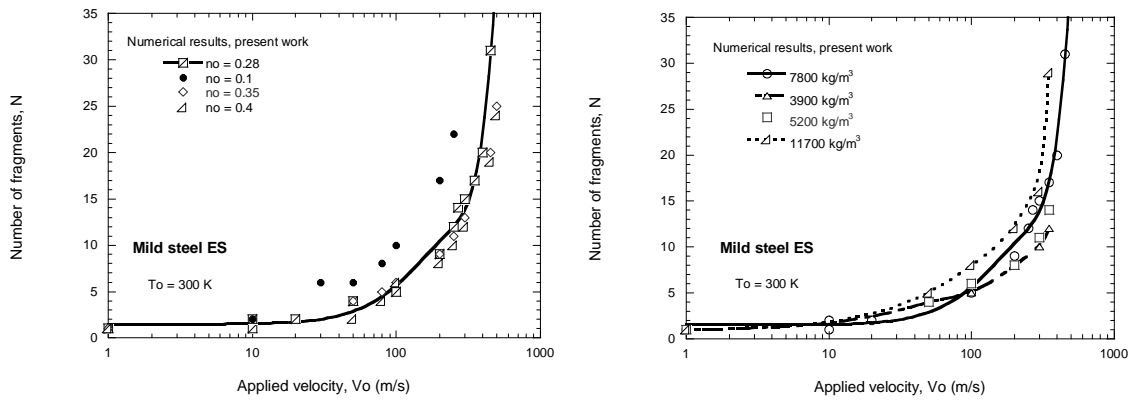


Figure 10: Effect of n_0 (left) and density (right) on the number of fragments. Reference geometry and mesh (Figure 4).

Mesh dependence solution

An analysis of the influence of the mesh in the results was additionally made, changing element type and refinement. Besides the 8-node linear brick elements, 6-node linear triangular prisms were used (Figure 5) following the work of Pandolfi et al. [3]. The results were consistent with the experimental results and those obtained with the reference mesh, with a sudden increase of N at velocities $V_o \geq 300 \text{ m/s}$ (Figure 11). However, triangular elements seem to be better able to define failure of brittle materials and brick element reproduced with more reliability the necking process of ductile alloys.

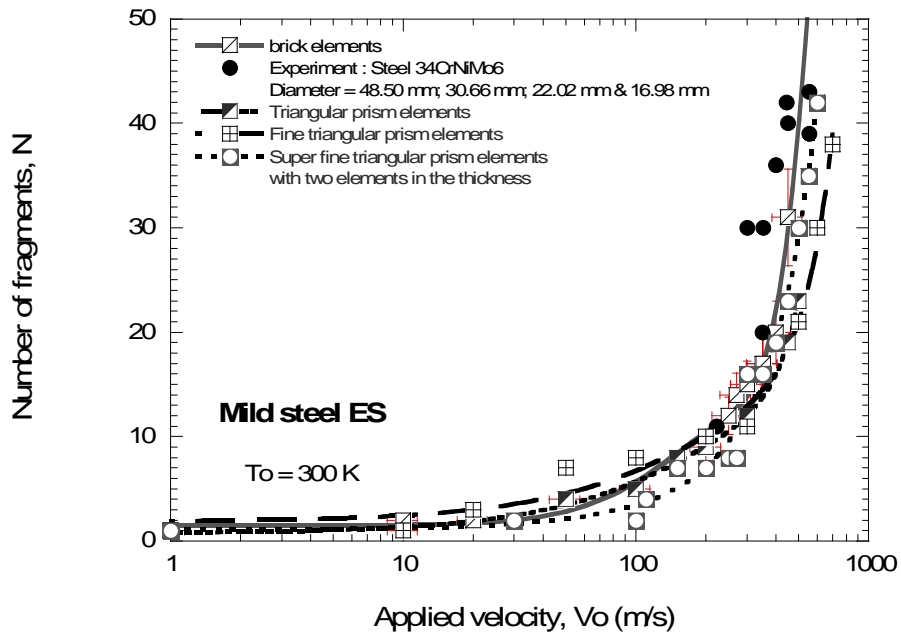


Figure 11: Effect of the element type and mesh refinement on the number of fragments.

CONCLUSIONS

The problem of a ring expanding under explosive load was analyzed. An original thermoviscoplastic constitutive equation coupled to an integration algorithm allowed to simulate accurately this problem using a relatively simple finite element model, and to obtain a good prediction of the number of fragments as a function of imposed radial velocity.

Some material parameters, such as strain hardening exponent and density, also showed their influence in the fragmentation process. Both of them define the value of the velocity of propagation of plastic waves, being thus strongly connected to the phenomenon of stagnation plastic deformation in dynamic applications. This phenomenon also appears during the dynamic tensile test of metallic alloys (Critical Impact Velocity).

The analysis confirmed the validity of the constitutive equation and the algorithm to model other dynamic processes such as dynamic tension, perforation, shear and buckling. Complementary to the effort made on the development sophisticated elements or mesh refinement, it is clear that a strong point of an appropriate simulation is the constitutive relation used to define the thermoviscoplastic behaviour of the material.

References

1. X. Hu & G.S. Daehn, "Effect of velocity on flow localization in tension", *Acta Mater.*, 44, 1021-1033, (1996).
2. D.E. Grady, D.A. Benson, "Fragmentation of metal rings by electromagnetic loading", *Experimental mechanics*, 12, 393-400, (1983).
3. A. Pandolfi, P. Krysl, M. Ortiz, "Finite element simulation of ring expansion and fragmentation", *Int. J. of Fracture*, 95, 279-297, (1999).
4. M. Altinova, X. Hu, G.S. Dahren, "Increased ductility in high velocity electromagnetic ring expansion", *Metall. Trans. A*, 27, 1837-1844, (1996).
5. N. Triantafyllidis, J.R. Waldenmyer, "Onset of necking in electro-magnetically formed rings", *J. of the Mechanics and Physics of Solids*, 52, 2127-2148, (2004).
6. A. Rusinek, J.R. Klepaczko, "Shear testing of a sheet steel at wide range of strain rates and a constitutive relation with strain-rate and temperature dependence of the flow stress", *Int. J. of Plasticity*, 17, 87-115, (2000).
7. ABAQUS/Explicit v6.4, User_s Manual, ABAQUS Inc., Richmond, USA, 2003.
8. R. Zaera, J. Fernández-Sáez, "An implicit consistent algorithm for the integration of thermoviscoplastic constitutive equations in adiabatic conditions and finite deformations", *Int. J. Solids and Structures*, (in press, 2005).
9. S. Mercier, A. Molinari, "Predictions of bifurcation and instabilities during dynamic extension", *Int. J. of Solids and Structures*, 40, 1995-2016, (2003).
10. A. Rusinek, "Modélisation thermoviscoplastique d'une nuance de tôle d'acier aux grandes vitesses de déformation. Etude expérimentale et numérique du cisaillement, de la traction et de la perforation", PhD Thesis, University of Metz, (2000).
11. J.R. Klepaczko, "Modelling of structural evolution at medium and high strain rates, FCC and BCC metals, in : *Impact : Effects of fast transient loading*", A.A. Balkema, Rotterdam-Brookfield, Denmark, 3-35, (1988).
12. A. Rusinek, J.R. Klepaczko, "Etude numérique de la propagation des ondes dues à un chargement par impact", *Revue Française de Mécanique*, 1, 55-62, (2001).
13. C. MacGregor, J.C.Fisher, "A velocity modified temperature for the plastic flow of metals", *J. Appl. Mech.*, 13, 11-16, (1946).

14. H. Quinney, G.I. Taylor, "The emission of latent energy due to previous cold working when a metal is heated", Proc. Roy. Soc. (London), 163, 157-181, (1937).
15. D.R. Stull, G.C. Shink, "Thermodynamic properties of elements", American Chemical Society (1956).
16. N. Mouad, "Etude expérimentale et modélisation du comportement viscoplastique de l'acier 316 LN aux grandes déformations et vitesses de déformation; simulation numérique du cisaillement adiabatique", Thesis, University of Metz (1999).
17. R. Zaera, J. Fernández-Sáez, "An implicit consistent algorithm for the integration of thermoviscoplastic constitutive equations in adiabatic conditions and finite deformations", accepted for publication in Int. J. Solids Struct., (2005)
18. Q.B. Diep, J.F. Moxnes, G. Nevstad, "Fragmentation of projectiles and steel rings using numerical 3D simulations", 21th International Symposium on Ballistics, Adelaide, Australia.
19. M. Singh, H.R. Suneja, M.S. Bola, S. Prakash, "Dynamic tensile deformation and fracture of metal cilindres at high strain rates", Int. J. Impact Engng, 27, 939-954, (2002).

Static and dynamic response of fibre-metal laminates

Martin Simmons, Graham Schleyer, Wesley Cantwell and Robert Birch

*Impact Research Centre, Department of Engineering, University of Liverpool, Brownlow Hill,
Liverpool, L69 3GH, UK*

This paper reports some results of a series of pressure tests on clamped Fibre Metal Laminate (FML) plates with a 0.3m x 0.3m pressurised area. Quasi-static pressure loads of up to 780 kPa were applied to these plates using a pressure differential device recently commissioned at the University of Liverpool Impact Research Centre. The FML plates were manufactured using aluminium alloy 2024-0 grade and two different thermoplastic based composites (Curv and Twintex). Pressure tests and quasi-static tensile tests have been carried out on these FMLs using various lay-up configurations. The quasi-static tensile test results indicated that the Curv based FMLs have a slightly lower ultimate tensile strength but are significantly more ductile than equivalent Twintex based FMLs. Quasi-static pressure loading succeeded in achieving rupture of aluminium, Twintex and Curv plates of approximate thicknesses 0.6mm, 1mm and 0.9mm, respectively. However, all of the FML plates failed by large inelastic deformation, without rupture. The Curv based FML plates deformed significantly more than the Twintex FML plates under the same level of loading.

INTRODUCTION

More damage to property and injury to people are caused by a bomb attack than any other criminal act. The damage to buildings caused in the Manchester bomb attack in 1996 ran into hundreds of millions of pounds. The emergence of terrorist threats to the built environment and the public is of major concern as a bomb blast in a shopping centre, an office block or an airport could be responsible for a substantial amount of damage and injury. Therefore it is necessary to develop methods of blast mitigation to reduce the risk of damage to property, serious injury and loss of life. It is often the case that the only practical means of achieving this is by improving the blast resistance of the structure into which the explosive device has been placed.

Steel structures are often used to mitigate blast effects as steel has excellent stiffness and ductility properties at low cost, compared to other metals. However, the relatively high density of steel makes it unsuitable when it is desirable that the structure is lightweight, as may well be the case if it is situated within an aircraft. Fibre Metal Laminates (FMLs) are multi-layered materials consisting of stacked arrangements of sheets of metal and fibre-reinforced composites. These materials are lightweight and have been shown to exhibit excellent impact properties [1,2]. They also have the potential to be used as blast resistant materials. A recent study [3] has investigated the response of FMLs manufactured with an aluminium alloy and two thermoplastic based composite materials, to localised blast loading. However, in order to develop a better understanding of the blast response of these materials it is also necessary to investigate their behaviour when subjected to uniform pressure loading. This paper presents some initial results of an investigation into uniform pressure loading of two types of FML panel, manufactured from aluminium alloy and thermoplastic based composite materials.

The overall aim of this work is to test develop a lightweight, blast-resistant material using the FML concept. However, as with many studies of engineering materials and structures, the ultimate aim is to develop methods of modelling which reduce the need for expensive, time consuming experiments. Therefore, a long term objective of this project is to model the response of FML structures using the Finite Element (FE) technique. However, in order to

obtain reasonable results using FE methods it is critical to have knowledge of FML material properties and consequently, a number of quasi-static and dynamic tensile tests have been conducted on some FMLs and their constituent materials as part of this investigation. The results of some of these experiments are presented in this paper.

TEST PLATES

Tests were carried out on FML plates that were manufactured from 0.025 in. (approximately 0.6 mm) thick aluminium alloy grade 2024-0 and two different thermoplastic-based composite materials; Twintex, (manufactured by Saint-Gobain Vetrotex) consisting of woven glass fibres in a polypropylene matrix and Curv (manufactured by BP) which consists of polypropylene fibres, self-reinforced by a polypropylene matrix. The mechanical properties of the composite materials are given in Table 1. Tests were also conducted on panels made purely from the aluminium and composite materials in order to assess their contributions to the performance of the FMLs.

In order to manufacture the FML panels, the aluminium alloy and composite were cut to size (400mm x 400mm) and laid up in an aluminium mould, using various stacking sequences. Plates were identified by a code (based on the stacking sequence) of the form **AXTYZ-#** for Twintex based FMLs and **AXCYZ-#** for Curv based FMLs, where:

A	Aluminium
T	Twintex
C	CURV
X	Number of layers of aluminium. One aluminium layer is placed on the front face, and one on the back face. The aluminium layers are spaced equally through the thickness of the laminate.
Y	Number of layers of composite (Twintex or Curv) material. The layers of composite are all of equal thickness, and each composite layer is placed between the aluminium layers.
Z	Number of separate sheets of composite in each layer of composite
#	Plate number

The FML lay-up construction is illustrated in Figure 1.

For the Twintex based FMLs, a chromate coating was applied to the aluminium alloy sheets prior to manufacture and a thin layer of thermoplastic adhesive (XIRO 2310 from Collano AG) was placed between the layers of aluminium alloy and composite material, in order to promote better adhesion. In the case of the Curv based FMLs, a different adhesive film was used (Glucos from Gluco Ltd.) and no pre-treatment of the aluminium was required. Once the layers had been stacked in the required sequence, the mould and stack were placed in a fan-assisted oven and then heated to the processing temperature of the composite material (165°C for Curv and 185°C for Twintex). Once this temperature had been reached, the mould was removed from the oven and rapidly transferred to a hydraulic press where it was cold stamped under a pressure of approximately 130 kPa. This was to ensure a rapid rate of cooling and a low degree of crystallinity within the semi-crystalline polypropylene matrix. Once the laminate had cooled to room temperature, the pressure was released, the mould removed from the press and, finally, the laminate removed from the mould.

EXPERIMENTAL PROCEDURES

Quasi-static tensile tests

Quasi-static tensile tests were carried out in order to determine tensile properties of Aluminium 2024-0 and various types of FML. For the aluminium, a 'dogbone' shape specimen with a gauge length of 100mm, gauge width of 10mm and thickness of 0.64mm was used. Specimens were loaded at a rate of 1mm/min up until yield and then at 2mm/min from yield to rupture. An extensometer was used to measure elastic displacement in order to more accurately determine the Young's modulus. Tests were performed in both the longitudinal and transverse direction with respect to material grain orientation.

In the case of the FML specimens, straight-sided specimens with an overall length of 300mm and a width of 30mm were used. The gripped length at each end of the specimen was 50mm, leaving an ungripped length of 200mm, which was taken as the gauge length. The specimens were loaded at a rate of 1mm/min until the entire cross section had ruptured. Since these specimens were too wide for the extensometer, a strain gauge was bonded to one of the outer metal surfaces and used to measure elastic strain for the purpose of determining a stiffness modulus.

Pressure tests

Tests were carried out using a new Pulse Pressure Loading Rig (PPLR), recently commissioned at the University of Liverpool. This facility is capable of producing repeatable, uniform loads with various pressure-time histories. A similar test rig has been used extensively, in the past, to assess the response of numerous materials and structures [4-7] to pulse pressure loads. However, the new facility has a number of advantages, in particular, the ability to apply higher pressure loads at faster rates of loading. The maximum pressure that can be applied is 800 kPa and the rate of loading is typically within the range 10 MPa/s – 30MPa/s. The test rig, shown schematically in Figure 2, consists of two pressure loading chambers, which clamp around a central support plate. The test rig is enclosed inside an acoustic chamber, which reduces noise levels transmitted to the surrounding areas. The support plate contains a 500mm x 500mm aperture over which the test specimens are clamped in place using a clamping frame. However, in this study, manufacturing constraints meant that the largest panels that could be constructed had only a 300mm x 300mm pressurised area and therefore, a reduction plate was required as shown in Figure 3. A displacement transducer (LVDT) was also attached to the centre of the plate in order to measure transient and permanent displacement. However, when rupture of the test panel was likely, the LVDT was removed in order to prevent damage.

The PPLR has two principal modes of operation; quasi-static and dynamic. The vast majority of the tests that have been conducted in the initial phase of this study have utilised the quasi-static mode. In this mode, both of the chamber nozzles are covered with steel end plates. Only one chamber is pressurised, with the other vented to atmosphere via a safety valve and therefore a differential pressure acts on the plate. The test procedure involved slowly increasing the pressure acting on the plate until (a) rupture of the panel occurred or (b) the maximum working pressure of the vessel (approximately 800 kPa) was reached. Tests were also conducted at lower pressures in order to determine elastic limits and yield pressures.

RESULTS AND DISCUSSION

Tensile properties of constituent materials

The experimentally determined properties of aluminium 2024-0 are summarised in Table 2. In general, the results showed that the longitudinal direction exhibited higher yield (0.1% proof) stress, UTS and Young's modulus but lower rupture strain, compared to the transverse direction.

FML Tensile Properties

The results of the tests to determine FML tensile properties are summarised in Table 3 and sample stress-strain curves for each specimen type are shown in Figure 4. Each curve exhibited a very small, approximately linear region at low strain, from which the elastic modulus was derived. In general, the Twintex based FMLs were stiffer and exhibited significantly greater UTS than the Curv based FMLs, which reflects the influence of the composite material on the overall properties of the FML. The specific strength is included in the table in order to compare the potential of these materials for lightweight applications. Specimen types A2T14 and A2C12 have similar thicknesses, but A2T14 has significantly higher (approximately 30%) specific strength, suggesting that Twintex based FMLs have an advantage on strength.

During the tensile tests, the Twintex FMLs generally exhibited debonding of the metal and composite layers as the load was increased, whereas in the case of the Curv FMLs, delamination occurred within the composite layers themselves. For most of the specimens tested, tensile failure occurred in a number of stages as successive aluminium and composite layers failed. In most cases, an entire composite layer usually failed first, resulting in a distinctive drop in applied load and hence average stress, which can be seen in the plots shown in Figure 4. The strain at which this occurred is referred to as the 'initial failure strain'. In the case of the Twintex FMLs this was approximately 3%, whereas for the Curv FMLs it was within the range 15-20%. These failure strains correspond well with those quoted in Table 1 for the separate composite materials, which emphasises the strong influence of the composite material on the performance of the FML. The values also suggest that although Curv FMLs are not as strong as Twintex FMLs, they have the potential to absorb more energy.

Quasi-Static Pressure Tests

The results of all the pressure tests are summarised in Table 4. In general, the failure modes are specified using the descriptions first adopted by Menkes and Opat [8] for explosively loaded clamped beams and subsequently by numerous other researchers [4,9,10] for dynamically loaded plates:

Mode I: Large inelastic deformation.

Mode II: Tearing (tensile failure) in the outer fibres or over the support.

When Mode I failure occurred in a panel, elastic recovery was observed since the central displacement of the panels decreased when the pressure was reduced, as shown in Figure 5. This reduction in displacement was taken as an approximation to the elastic limit of a panel and the pressure at that displacement was defined as the yield pressure. Figure 6 shows photographs of typical failures of the various types of panel that were tested.

Panels made from constituent materials

Three tests were conducted on single sheets of aluminium 2024-0. Mode II failure was obtained for panels A1-1 and A1-2 at pressures of 540 kPa and 530 kPa respectively. Panel A1-1 ruptured at the top and side edges with the lower edge remaining largely intact whereas A1-2 completely ruptured. A photograph of panel A1-1 in its failed state is shown in Figure 5 (a). The

plates were orientated so that the rolling (longitudinal) direction was vertical (i.e. from top to bottom edge). Therefore it is suggested that in the case of panel A1, tearing initiated at the centre of the top edge due to the lower ductility in the longitudinal direction. The tearing then progressed to the upper corners and along the vertical edges before ceasing at the bottom edge.

Four tests were conducted on double-layered Twintex specimens with an approximate thickness of 1mm. One panel (T2-1) failed at a pressure of 490 kPa due to formation of a crack close to the centre. Twintex is quite brittle in its processed state and therefore it is possible that a small defect may have been accidentally induced in panel T2-1, prior to testing. Panels T2-2 and T2-3 generally exhibited Mode II type failure at pressures of 660 kPa and 570 kPa respectively. However both panels also displayed evidence of slippage in the clamped regions, which resulted in shear pullout failure at the locating holes, as can be seen in Figure 5 (b).

The Curv panels that were tested were single sheets with a thickness of approximately 0.9mm. Rupture of all edges was achieved (Figure 5 (c)) for panels C1-1 and C1-2 at pressures of 610 kPa and 620 kPa respectively. Although slightly lower than the highest failure pressure achieved with Twintex (660 kPa), these results compare favourably, since the Curv failure pressures were more consistent and the thickness of the Curv panels was at least 7% lower than that of the Twintex panels. However, the Twintex panels had lower densities, which may mean that Twintex is preferable for lightweight applications. It is also possible that the Twintex panels would fail at higher pressures if the edge slippage were reduced.

Although the composite panels exhibited only slightly higher failure pressures than those of the aluminium, their densities were significantly lower, giving them a clear advantage in terms of potential use for lightweight applications. However, the aluminium plates were significantly thinner than the composites, which may be advantageous in some applications where space is restricted. By combining a metal and composite as an FML it may be possible to develop a blast proof, lightweight material that is practical in size.

FML panels

A number of different FML lay-up configurations were examined although most panels tested so far have been of the A2T12-# variety. In all cases failure was of type mode I and rupture could not be achieved despite applying pressure loads up to 780 kPa. The final deformed shapes of the panels exhibited uniform curvature as shown in Figure 5 (d). It could be argued that this was to be expected given the failure pressure loads of the constituent materials. A number of panels were also sectioned and indicated no evidence of debonding or delamination, suggesting that the behaviour of the FML panels in the pressure tests was similar to that of monolithic panels.

Figure 6 shows sample pressure-central displacement curves for each type of FML panel, subjected to pressure loads of approximately 750 kPa. In each case the panels exhibited elastic recovery since displacement at the centre of the panel decreased when the pressure load was released. This reduction in displacement was taken as an approximation of the elastic limit of the panel. Clearly, the Curv based FML exhibits significantly lower stiffness than the Twintex FMLs due to the lower stiffness of the Curv itself. This suggests that Curv FML panels have potential to absorb more energy under uniform pressure loading conditions. However, it is also more likely that rupture of the aluminium layers will occur in Curv FMLs due to the larger deflections and subsequent larger strains induced.

CONCLUSIONS

Initial results of the response of thermoplastic based FML panels to pulse pressure loading have been presented. Material tests showed that Curv-based FMLs exhibit a lower ultimate strength than Twintex FMLs, but are significantly more ductile indicating potential for greater energy absorption. In the quasi-static pressure tests, Mode II failure was achieved for panels made from the FML constituent materials. However, for the FMLs themselves, only Mode I failure could be induced with pressures of approximately 750 kPa. Dynamic loading may result in more plastic deformation in the FML panels but is unlikely to cause rupture.

Acknowledgments

The authors are grateful to the EPSRC for providing financial support for this project. The support and advice given by the project collaborators, The Blast Impact and Survivability Research Unit (BISRU) at the University of Cape Town, BP (Amoco Fabrics GmbH), LINPAC Environmental, GLUCO Ltd, Westminster Council and The Home Office is gratefully acknowledged. Thanks are also due to Cornelious Group for providing materials used in the manufacture of test specimens. Finally, many thanks are due to Mr. P.J. Smith and Mr. C.W. Eyre for providing technical assistance.

References

1. Reyes, G. and Cantwell, W. J., The mechanical properties of fibre-metal laminates based on glass fibre reinforced polypropylene, 200010851094 *Composite Science and Technology* 60
2. Reyes, G. and Cantwell, W. J., The high velocity impact of composite and FML-reinforced sandwich structures, 2003120 *Composite Science and Technology* 63
3. Langdon, G. S., Cantwell, W. J., and Nurick, G. N., The blast response of novel thermoplastic-based fibre-metal laminates - some preliminary results and observations, 2004 *Composite Science and Technology*
4. Langdon, G. S. and Schleyer, G. K., Inelastic deformation and failure of clamped aluminium plates under pulse pressure loading, 200311071127 *International Journal of Impact Engineering* 28
5. Langdon, G. S. and Schleyer, G. K., Inelastic deformation and failure of profiled stainless steel blast walls. Part I: experimental investigations, 2005341369 *International Journal of Impact Engineering* 31
6. Goodfellow, A. M. and Schleyer, G. K., Experimental investigation of corner-supported architectural glazing under pulse pressure loading, 2003113 *Journal of Strain Analysis* 38
7. Schleyer, G. K., Hsu, S. S., White, M. D., and Birch, R. S., Pulse pressure loading of clamped mild steel plates, 2003223247 *International Journal of Impact Engineering* 23
8. Menkes, B. and Opat, H. J., Broken beams, 1973480486 *Experimental Mechanics*
9. Teeling-Smith, R. G. and Nurick, G. N., The deformation and tearing of thin circular plates subjected to impulsive loads, 19917791 *International Journal of Impact Engineering* 11
10. Nurick, G. N. and Shave, G. C., The deformation and tearing of thin square plates subjected to impulsive loads - an experimental study, 200499116 *International Journal of Impact Engineering* 18
11. Saint-Gobain Vetrotex (website), 2004
12. MatWeb: Material Property Data (website), 2004

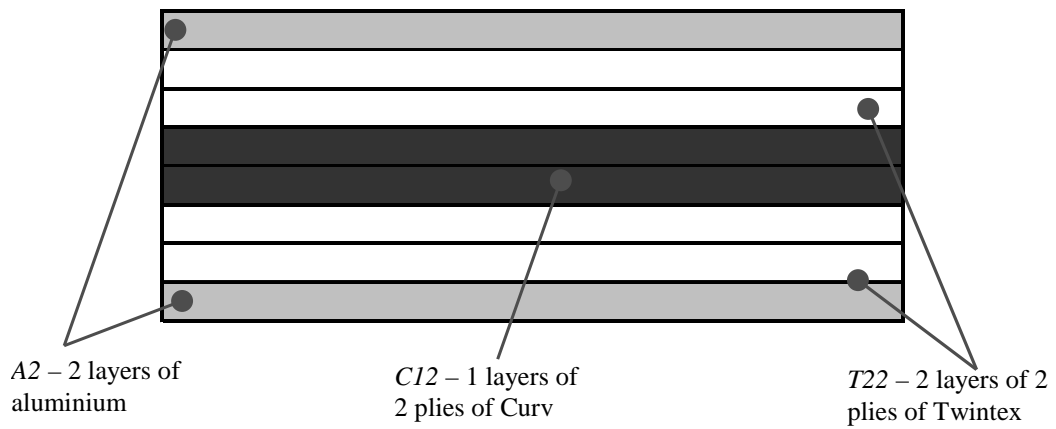


Figure 1: FML panel lay-up description (e.g. A2T22C12)

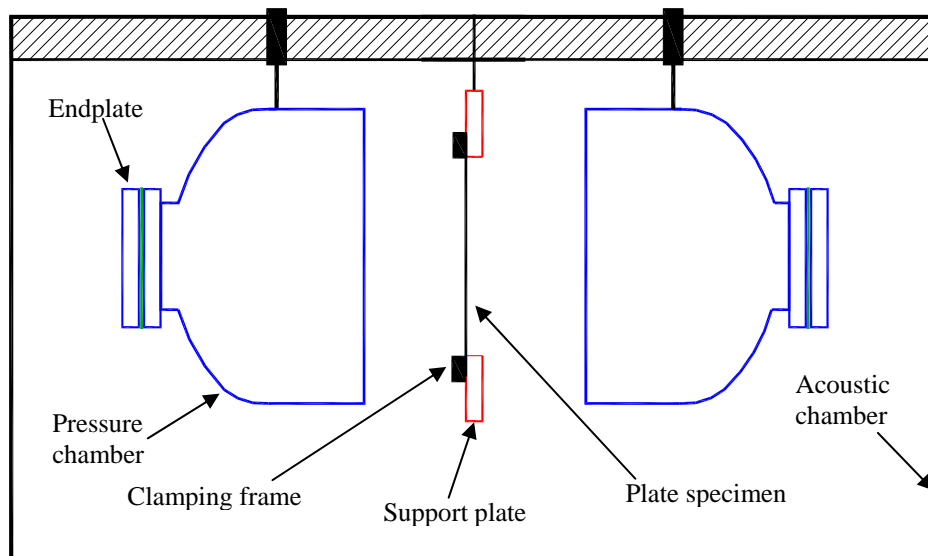


Figure 2: Schematic of PPLR (quasi-static mode)

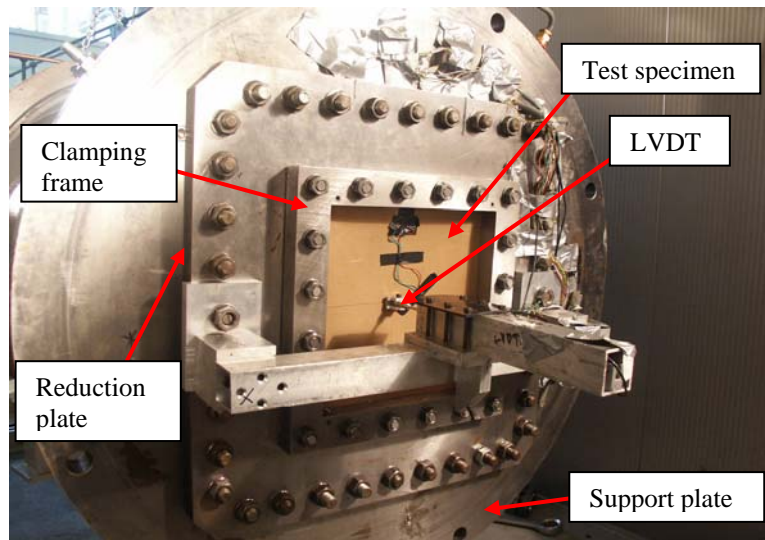


Figure 3: Panel mounting in pulse pressure rig

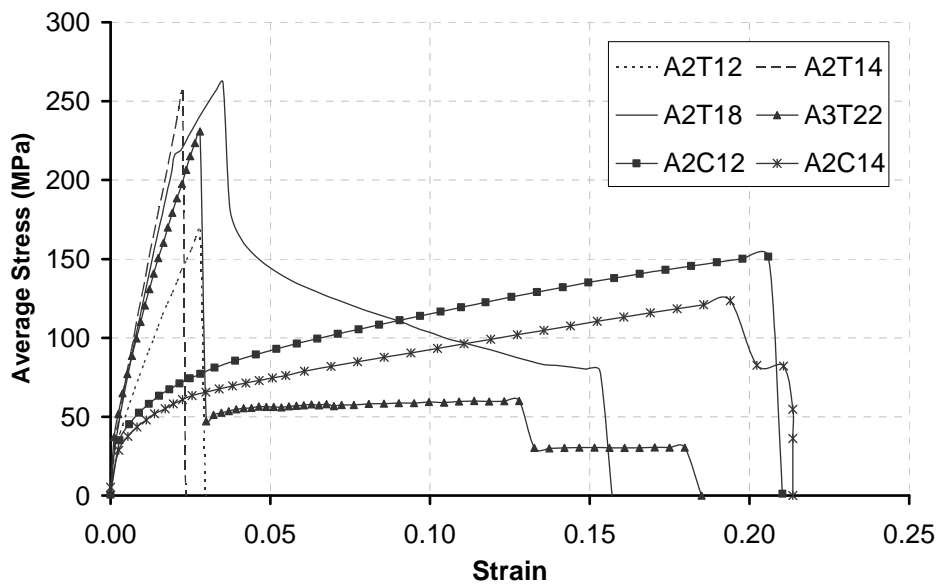


Figure 4: Sample tensile stress-strain curves for various FMLs

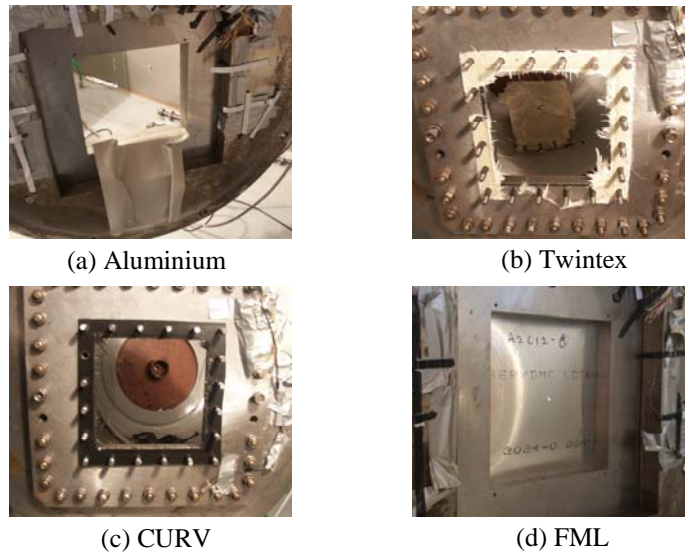


Figure 5: Photographs showing failure modes of pressure tested panels

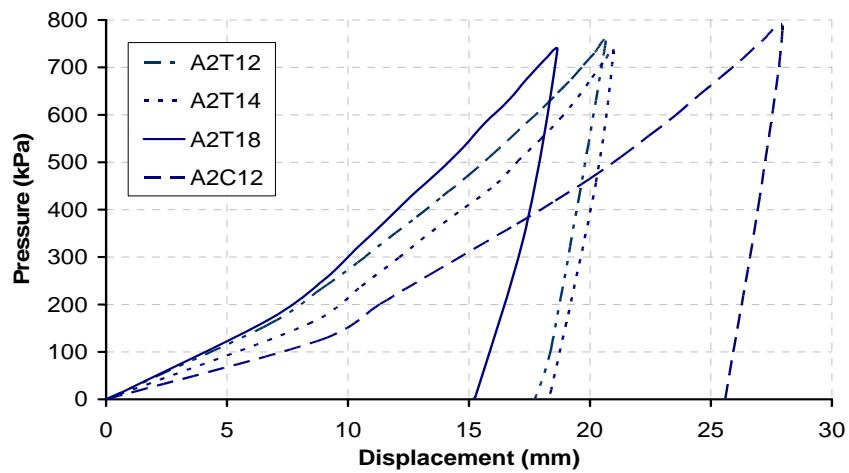


Figure 6: Sample pressure-displacement curves for pressure tested FML panels

Composite	Density (kg/m ³)	Mass/Area (kg/m ²)	UTS (MPa)	Elongation (%)	Elastic modulus (GPa)
Twintex [11]	-	745	300	2.9	13
Curv [12]	920	-	180	20.0	5

Table 1: Mechanical properties of composite materials (mean average values)

Grain Orientation	Density (kg/m ³)	Yield (0.1% Proof) Stress (MPa)	UTS (MPa)	Specific Strength (kNm/kg)	Elongation (%)	Young's Modulus (GPa)
Longitudinal	2780	88.2	198.8	71.5	14.0	74.7
Transverse	2780	86.0	190.6	68.6	15.2	72.5

Table 2: Quasi-static mechanical properties of Aluminium 2024-0

Specimen type	Mean thickness (mm)	Density (kg/m ³)	Modulus (GPa)	UTS (MPa)	Specific strength (kNm/kg)	Initial failure strain (%)
A2T12	2.39	2042	30.7	175.5	85.9	2.6
A2T14	3.34	1883	35.7	264.5	140.5	2.6
A2T18	5.36	1693	29.9	260.4	153.8	3.2
A3T22	4.08	1987	51.9	234.9	118.2	2.9
A2C12	3.26	1609	25.0	150.9	93.8	20.5
A2C14	5.24	1347	16.7	110.5	82.0	15.7

Table 3: Quasi-static properties of various FMLs (mean average values)

Test Reference	Thickness (mm)	Density (kg/m ³)	Mass/Area (kg/m ²)	Peak Pressure (kPa)	Max. Disp. (mm)	Perm. Disp. (mm)	Elastic Limit (mm)	Yield Pressure (kPa)	Failure Mode
A1	0.64	2725	1.74	540	-	-	-	-	II
A2	0.64	2744	1.76	530	-	-	-	-	II
A3	0.64	2783	1.78	390	33.0	31.4	1.6	30	I
T2-1	1.07	724	0.78	490	15.8	15.8	-	-	I (cracked)
T2-2	0.96	788	0.76	660	-	-	-	-	II
T2-3	1.01	780	0.79	570	-	-	-	-	II
T2-4	1.08	723	0.78	380	26.3	16.5	9.8	64	I
C1-1	0.87	912	0.79	610	-	-	-	-	II
C1-2	0.89	899	0.80	620	-	-	-	-	II
C1-3	0.86	952	0.82	380	-	30.4	-	-	I
A2T12-6	2.38	2012	4.78	240	9.1	6.8	2.3	36	I
A2T12-11	2.35	2023	4.75	>730	-	25.2	-	-	I
A2T12-12	2.35	2076	4.88	760	20.7	17.8	3.0	45	I
A2T14-8	3.32	1873	6.22	740	21.0	18.2	2.8	34	I
A2T18-7	5.36	1724	9.24	740	18.7	15.2	3.5	95	I
A3T22-7	4.00	2002	8.01	>710	-	16.8	-	-	I
A2C12-9	3.17	1609	5.09	440	19.9	17.5	2.3	25	I
A2C12-10	3.16	1632	5.16	780	28.0	25.6	2.4	21	I

Table 4: Summary of pressure test results

